University of Alberta

Development of a CFD Model for Predicting Disinfection in a Large UV Reactor

by

Alex Munoz ©

A thesis submitted to the Faculty of Graduate Studies and Research in partial fulfillment of the requirements for degree of Master of Science in Environmental Engineering

Department of Civil and Environmental Engineering

Edmonton, Alberta

Fall, 2004

Library and Archives Canada

Published Heritage Branch

395 Wellington Street
Ottawa ON K1A 0N4
Canada

Bibliothèque et Archives Canada

Direction du Patrimoine de l'édition

395, rue Wellington
Ottawa ON K1A 0N4
Canada

Your file Votre référence
ISBN: 0-612-95822-1
Our file Notre référence
ISBN: 0-612-95822-1

The author has granted a non-exclusive license allowing the Library and Archives Canada to reproduce, loan, distribute or sell copies of this thesis in microform, paper or electronic formats.

L'auteur a accordé une licence non exclusive permettant à la Bibliothèque et Archives Canada de reproduire, prêter, distribuer ou vendre des copies de cette thèse sous la forme de microfiche/film, de reproduction sur papier ou sur format électronique.

The author retains ownership of the copyright in this thesis. Neither the thesis nor substantial extracts from it may be printed or otherwise reproduced without the author's permission.

L'auteur conserve la propriété du droit d'auteur qui protège cette thèse. Ni la thèse ni des extraits substantiels de celle-ci ne doivent être imprimés ou aturement reproduits sans son autorisation.

In compliance with the Canadian Privacy Act some supporting forms may have been removed from this thesis.

Conformément à la loi canadienne sur la protection de la vie privée, quelques formulaires secondaires ont été enlevés de cette thèse.

While these forms may be included in the document page count, their removal does not represent any loss of content from the thesis.

Bien que ces formulaires aient inclus dans la pagination, il n'y aura aucun contenu manquant.

Canada

This thesis is dedicated to my wife Dr. Stephanie Young and my parents Luis and Ana for their limitless love.

Acknowledgements

I would like to express my deep appreciation to Dr. Stephen Craik and Dr. Suzanne Kresta for their valuable guidance, encouragement and financial support throughout the course of this research. I would also like to thank my committee, Dr. Mohamed Gamal El-Din for his suggestions, comments and questions, which improved the quality of my thesis.

I would like to express my appreciation and thanks to Dr. Jim Bolton (Bolton Photosciences Inc.), and Mr. Craig Bonneville (Epcor Water Services of Edmonton, AB) for providing comments and necessary technical information related to the study. My appreciation and thanks are also extended to Ms. Vesselina Roussinova, Mr. Bob Barton, and Mr. Nick Chernuka for assisting with this research.

Finally, I would like to give special thanks to my wife, Dr. Stephanie Young, for her encouragement and support.

Table of Contents

1 LITERATURE REVIEW AND COMPONENTS OF THE MODEL 1

1.1 UV use in water treatment 2
1.1.1 UV for Disinfection of Drinking Water 3
1.1.2 UV for Microorganism Reduction in Wastewater 5

1.2 Determining UV Dose 6
1.2.1 Dose Distribution 8

1.3 Models Reported in the Literature to Date 10

1.4 Components of UV Reactor Models 14

1.5 Ultraviolet Radiation 17
1.5.1 Source, Generation and Propagation of UV Radiation 17
1.5.2 Ultraviolet Fluence Rate Model 21
1.5.3 Germicidal Efficiency 25
1.5.4 UVCalc3D_200 26

1.6 Turbulent Flow Modeling 27
1.6.1 Reynolds Averaged Navier Stokes (RANS) Equations 28
1.6.2 Turbulence Models 29
1.6.2.1 The k-ε Models 30
1.6.2.2 The Reynolds Stress Model 32
1.6.2.3 Large Eddy Simulation Model 35
1.6.2.4 Turbulence Models -Summary 36

1.7 Discrete Phase Model 38
1.7.1 Lagrangian Approach to Discrete Phase 38
1.7.2 Discrete Random Walk (DRW) Model 41
1.7.3 Simulation of the Particle Trajectories 43
1.7.4 Limitations of the DRW Model 44
1.7.5 Integration of the Dose 47

1.8 Microorganism Response to UV Radiation 48
1.8.1 Microorganism Inactivation Models 48
1.8.2 Equivalent Dose 51

1.9 Problem Statement 54

2 CFD METHODOLOGY AND VALIDATION 56

2.1 Ultraviolet Reactor Description 57

2.2 Simulation Conditions 59
2.2.1 Mesh Generation 59
2.2.2 Numerical Procedure 64

2.3 Boundary Conditions 65
2.3.1 Inlet 66
2.3.1.1 Velocity at the Inlet 66
2.3.1.2 Turbulent Kinetic Energy at the Pipe Inlet 70
2.3.1.3 Rate of Dissipation of the Turbulent Kinetic Energy at the Inlet 71
2.3.2 Solid Wall Treatment 72
2.3.3 Outlet 73

2.4 Validation of the CFD Code for Pipe Flow 74
2.4.1 Laminar Flow in a Straight Pipe 75
2.4.2 Turbulent Flow in a Straight Pipe 76
2.4.3 Summary of the CFD Validation for Empty Pipe Flow 79

2.5 Boundary Conditions for the Discrete Phase Model 80
2.5.1 Initial Conditions 80
2.5.1.1 Starting Position of the Particles in Laminar Pipe Flow 81
2.5.1.2 Starting Position of the Particles in Turbulent Pipe Flow 82
2.5.2 Particle Diameter 84
2.5.3 Wall Treatment 86

2.6 Verification of the UDF Used to Compute the UV Dose 86
2.6.1 Verification of the UDF Used to Compute Dose in Laminar Flow 88
2.6.2 Verification of the UDF Used to Compute Dose in Turbulent Flow 89
2.6.3 Summary of the Verification of the UDF Used to Compute Dose 91

2.7 Verification of the Fluence Rate Distribution 94
2.7.1 Bolton Model Validation 94
2.7.2 UVCalc Inputs 95
2.7.3 Numerical Verification of the Fluence Rate Distribution 98
2.7.4 Fluence Rate Distribution 99

2.8 Verification of the Inactivation Program 102

2.9 Summary of the Validated Protocol 103

3 SIMULATIONS AND SENSITIVITY STUDY RESULTS 105

3.1 Preliminary Analysis 106
3.1.1 Steady-State Analysis 107
3.1.2 Unsteady State Analysis 112
3.1.3 Summary 123

3.2 Optimum Number of Particles 124

3.2.1 Effect of Number of Particles on the Dose Prediction 127
3.2.2 Effect of the Number of Simulations on the Dose Prediction 131
3.2.3 Effect of the Total Number of Particles on the Dose Prediction 133
3.2.4 Effect of the Lagrangian Empirical Constant on the Dose Prediction 135

3.3 Sensitivity Analysis of the UV Disinfection Predictions 138
3.3.1 Evaluation of EED, UVT and C_L in a Full Factorial Experiment 140
3.3.2 Effect of UVT, EED and C_L on the UV Dose Prediction 142
3.3.3 Effect of the Lamps on the UV Dose Prediction 147
3.3.4 Effect of the Baffles on the UV Dose Prediction 149
3.3.5 Additional Simulations 151
3.3.6 Effect of the Mesh Type on the UV Dose Prediction 153
3.3.7 Effect of the Turbulence Model on the UV Dose Prediction 154
3.3.8 Effect of the Simulation Mode on the UV Dose Prediction 155
3.3.9 Effect of the Lamp Shadow on the UV Dose Prediction 155

3.4 Investigation of Modified UV Reactor Designs Using CFD 156

4 CONCLUSIONS 172

5 RECOMMENDATIONS 176

REFERENCES 177

List of Tables

Table 1.1: Summary of UV reactor models.....13
Table 1.2: Values of the constants in the k- ε model.....32
Table 1.3: Values of the constants in the RSM model.....35
Table 1.4: Summary of general characteristics of various turbulence models.....36
Table 1.5: Reported values of the Lagrangian time scale in homogeneous turbulence (from MacInnes and F.V. Bracco, 1992).....42
Table 1.6: Kinetic inactivation constants for series event model from batch data.....50
Table 2.1: UV Reactor specifications (Sentinel™ Calgon Carbon Corporation, Pittsburgh, PA, USA).....57
Table 2.2: Number of elements for different mesh types of the UV reactor.....61
Table 2.3: Under relaxation factors used for all the simulations.....65
Table 2.4: Fluid properties used to predict laminar flow in a pipe.....75
Table 2.5: Fluid properties used for simulation of turbulent flow in a pipe.....77
Table 2.6: Particle tracking parameters for laminar pipe flow.....88
Table 2.7: Particle tracking parameters for turbulent pipe flow.....90
Table 2.8: Inputs for the calculation of the fluence rate distribution for the SUVR.....95
Table 2.9: Lamp orientation and coordinates of the SUVR.....96
Table 2.10: Input data for the calculation of a single MP lamp.....96
Table 2.11: Fluence rate received by a point, located at x = 2.0099 m, y = 0.0 m, z = 0.0 m, estimated using UVCal3D_200 and Excel worksheet with the inputs given in Table 2.8 2.9 and 2.10. Reflection and refraction was neglected.....98
Table 2.12: Summary of the validation protocol.....104
Table 3.1: Simulation conditions to evaluate the number of particles required.....128
Table 3.2: Confidence intervals and standard deviation expected for the SUVR reactor under the conditions given in Table 3.1 with 55000 particles and C_L = 0.15.135
Table 3.3: Confidence intervals and standard deviation expected for the SUVR reactor under the conditions given in Table 3.1 with 55000 particles and C_L = 0.30.136
Table 3.4: Factors and levels used for investigating the Sentinel UV reactor.....139
Table 3.5: Simulation conditions to evaluate the effect of EED, UVT and C_L on the performance of the SUVR.....140
Table 3.6: Matrix design and UV performance estimation for the Sentinel UV reactor under the conditions given in Table 3.5.....141
Table 3.7: Matrix design and UV performance predictions for the SUVR operated with 2 lamps at 20kW.....141
Table 3.8: Calculated effects for results of the 2^3 factorial design in Table 3.6.....143
Table 3.9: Correlation between EED and equivalent dose.....147
Table 3.10: Effect of the Baffles on the prediction of the SUVR performance.....149
Table 3.11: Additional simulations used to predict the SUVR performance.....152
Table 3.12: Factors and level used for the comparison of the SUVR and MUVR.....156
Table 3.13: Matrix design and UV performance estimation for both UV reactors: the equivalent dose was estimated using the kinetic inactivation constant for MS2 coliphage 159
Table 3.14: Microorganism inactivation kinetic constants.....163

List of Figures

Figure 1.1: Typical dose distribution in a wastewater UV reactor (Chiu et al., 1999).....8
Figure 1.2: Flow chart of the procedure to evaluate the inactivation of microorganisms in a UV reactor.....16
Figure 1.3: 3-D UV reactor, A_1 and A_3 are the cross sectional areas needed to calculate the fluence rate (Adapted from Bolton, 2000).....23
Figure 1.4: Germicidal factor relative to the DNA absorbance and relative lamp emission as function of the UVC radiation, courtesy of Bolton Photosciencies Inc....26
Figure 1.5: Flow chart for computing particle trajectories in a discontinuous random walk model (Adapted from MacInnes and F.V. Bracco, 1992).....46
Figure 1.6: Typical UV dose response curves.....49
Figure 2.1: Elevation view of the Sentinel™ UV reactor 6x20 kW.....58
Figure 2.2: Cross-sectional view of the Sentinel™ UV reactor 6x20 kW.....58
Figure 2.3: Cross-sectional view of the mesh generated to simulate pipe flow.....61
Figure 2.4: Cross-section of the coarse unstructured hexahedral mesh generated to simulate the SUVR.....62
Figure 2.5: Cross-section of the fine unstructured hexahedral mesh generated to simulate the SUVR.....62
Figure 2.6: Cross-section of a coarse structured hexahedral mesh generated to simulate the SUVR.....63
Figure 2.7: Cross-section of the fine structured hexahedral mesh generated to simulate the SUVR.....63
Figure 2.8: Cross-section of the unstructured tretrahedral mesh generated to simulate the SUVR.....64
Figure 2.9: Universal turbulent velocity distribution at $Re = 1.8x10^6$.....68
Figure 2.10: Velocity defect plot in the outer region as a function of the normalized distance from the wall at $Re=1.8x10^6$.....69
Figure 2.11: Profile of the turbulent kinetic energy as a function of the normalized distance from the wall at the pipe inlet.....70
Figure 2.12: Profile of the rate of dissipation of turbulent kinetic energy as a function of the normalized distance from the wall at the pipe inlet.....72
Figure 2.13: Comparison of the user defined velocity profile at the inlet for laminar flow with the velocity predicted by Fluent 6.1 at 3.5 m along the pipe for r = 0.5985 m.....76
Figure 2.14: Comparison of the user defined velocity profile at the inlet with the k-ε and RSM model predictions at the outlet for $Re = 1.8x10^6$.....78
Figure 2.15: Comparison of the user defined TKE profile at the inlet with the k-ε and RSM turbulence model predictions at the outlet for $Re = 1.8x10^6$.....78
Figure 2.16: Comparison of the user defined dissipation profile at the inlet with k-ε and RSM model predictions at the outlet for $Re = 1.8x10^6$.....79
Figure 2.17: Distribution of particles as a function of radius for laminar pipe flow.....82
Figure 2.18: Distribution of particles as a function of distance from the wall in turbulent pipe flow.....84
Figure 2.19: Predicted dose received by 9999 particles in laminar flow (mean = 399.4 J/m^2, s_D = 10.40 J/m^2).....89

Figure 2.20: Predicted dose received by 9999 particles in turbulent flow u = U (mean = 399.9 J/m^2, s_D = 3.4 J/m^2).....92
Figure 2.21: Particle tracks colored by UV dose (J/m^2) with C_L = 0.15.....92
Figure 2.22: Dose received by 9999 particles C_L = 0.15 Δl = 2.0x10^{-4} m (mean = 400.2 J/m^2, s_D = 10.8 J/m^2).....93
Figure 2.23: Particle tracks colored by UV dose (J/m^2) with C_L = 0.30.....93
Figure 2.24: Dose received by 9999 parcels C_L = 0.30 Δl = 2.0x10^{-4} m (mean = 400.1 J/m^2, s_D = 13.4 J/m^2).....94
Figure 2.25: Scaled UV spectra based on the UV spectra of chlorinated filter water effluent from the E.L Smith plant, Edmonton, Alberta, provided by Epcor Water Services.....97
Figure 2.26: Contour of fluence rate (W/m^2) in an x-y plane with z = 0 m (UVT 93%, shadow effect ON and refractive effect ON).....100
Figure 2.27: Fluence rate profile at the reactor x-axis and at the middle of the lamps 1, 3, and 5, UVT 93% shadow effect ON and refractive effect ON).....100
Figure 2.28: Contour of fluence rate (W/m^2) in an x-y plane with z = 0 m, UVT 80% shadow effect ON and refractive effect ON).....101
Figure 2.29: Fluence rate profile at the reactor x-axis and at the middle of the lamps 1, 3, and 5, UVT 80% shadow effect ON and refractive effect ON. 101
Figure 3.1: Velocity magnitude contours (m/s) in a vertical plane through the central axis of the reactor. Generated using the steady-state k-ε model and the UHCM. Re = 1.83x10^6.....109
Figure 3.2: Velocity magnitude contours (m/s) in a vertical plane through the central axis of the reactor. Generated using the steady-state RSM model and the UHCM. Re = 1.83x10^6.....109
Figure 3.3: Axial velocity profiles in a plane through the central axis of the reactor and at various x-distances from the inlet of the reactor. Generated using the steady-state k-ε or RSM turbulence models and the UHCM. 110
Figure 3.4: Axial velocity profiles in a plane through the central axis of the reactor and at various x-distances from the inlet of the reactor. x shows the location of these traverses on the reactor geometry. 111
Figure 3.5: y-velocity as a function of the time using the SHFM at a point located three lamps diameters downstream of the first lamp. Unsteady-state k-ε model, , Re = 1.8x10^6 Time step = 0.01 s.....114
Figure 3.6: y-velocity as a function of the time using the UHFM at a point located three lamps diameters downstream of the first lamp. Unsteady-state k-ε model, Re = 1.8x10^6, time step = 0.01 s.....114
Figure 3.7: Velocity magnitude contours (m/s) in a vertical plane through the central axis of the reactor. Generated using the unsteady-state k-ε model and the SHFM, Re = 1.8x10^6 time = 1.04s.....116
Figure 3.8: Velocity magnitude contours (m/s) in a vertical plane through the central axis of the reactor. Generated using the unsteady-state k-ε model and the SHFM, Re = 1.8x10^6 time = 1.12s.....116
Figure 3.9: Axial velocity profiles in a plane through the central axis of the reactor and at various x distances from the inlet of the reactor. Generated using the

unsteady-state k-ε model and the SHFM, Re = 1.83×10^6. Left column: time = 1.04s. Right column: time = 1.12s. 117
Figure 3.10: Velocity magnitude contours (m/s) in a vertical plane through the central axis of the reactor. Generated using the LES model and the SHFM at time step = 1.20s, Re = 1.83×10^6 119
Figure 3.11: Velocity magnitude contours (m/s) in a vertical plane through the central axis of the reactor. Generated using the LES model and the SHFM at time step = 1.60s, Re = 1.83×10^6 119
Figure 3.12: Axial velocity profiles in a plane through the central axis of the reactor and at various x distances from the inlet of the reactor. Generated using the LES model and the SHFM, Re = 1.83×10^6. Left column: time step = 1.2s. Right column: time step = 1.6s. 120
Figure 3.13: Velocity magnitude contours (m/s) in a vertical plane through the central axis of the reactor. Generated using the LES model and the UHFM at time step = 1.20s, Re = 1.83×10^6 121
Figure 3.14: Velocity magnitude contours (m/s) in a vertical plane through the central axis of the reactor. Generated using the LES model and the UHFM at time step = 1.60s, Re = 1.83×10^6 121
Figure 3.15: Axial velocity profiles in a plane through the central axis of the reactor and at various x distances from the inlet of the reactor. Generated using the LES model and the UHFM, Re = 1.83×10^6. Left column: time step = 1.2s. Right column: time step = 1.6s. 122
Figure 3.16: Distribution of the dose received by 163 particles for the Sentinel UV reactor under the conditions given in Table 3.1 ($\overline{D}$ = 837.3 J/m^2, D_{eqv} = 508.0 J/m^2, and s_D = 632.6 J/m^2) 129
Figure 3.17: Distribution of the dose received by 2003 particles for the Sentinel UV reactor under the conditions given in Table 3.1: ($\overline{D}$ = 847.0 J/m^2, D_{eqv} = 492.7 J/m^2, and s_D = 1254.5 J/m^2) 129
Figure 3.18: Simulation mean dose, $\overline{\overline{D}}$, (top) simulation equivalent dose, $\overline{D}_{eqv}$, (middle) and simulation mean time, $\overline{\overline{t}}$, (bottom) as a function of the number of particles per simulation. The bar represent 95% confidence intervals at the UV reactor outlet resulting from 30 repeated simulations with C_L = 0.15.. 130
Figure 3.19: Simulation mean dose, $\overline{\overline{D}}$, (top) simulation equivalent dose, $\overline{D}_{eqv}$, (middle) simulation mean dose, $\overline{\overline{t}}$, (bottom) as a function of the number of particles per simulation. The bars represent the 95% confidence intervals at the UV reactor outlet resulting from n_s repeated simulations using a 1000 particles with C_L = 0.15 132
Figure 3.20: Size of the Confidence Interval of particle mean dose, $\overline{D}$, (top) simulation equivalent dose, D_{eqv}, (middle) simulation particle time dose, $\bar{t}$, (bottom) as a function of the total number of particles (n_p x n_s) with C_L = 0.15. The lines represent the linear least square regression for each set of the simulations 134

Figure 3.21: Simulation mean dose, $\overline{\overline{D}}$, (top) simulation equivalent dose, $\overline{D}_{eqv}$, (middle) and simulation mean time, $\overline{\overline{t}}$, (bottom) as a function of the number of particles per simulation. The bar represent 95% confidence intervals at the UV reactor outlet resulting from 30 repeated simulations with $C_L = 0.30$..136
Figure 3.22: Effect of UVT and EED on Equivalent Dose.....145
Figure 3.23: Dose received by 57,668 particles for SUVR with baffles under the conditions of run ID 1: EED = 0.0192, UVT = 93 % and $C_L = 0.15$ ($\overline{D}$ = 849 J/m^2, D_{eqv} = 492 J/m^2, D_{min} = 201 J/m^2, and s_D = 914 J/m^2).....145
Figure 3.24: Dose received by 57,684 particles for SUVR with baffles under the conditions of run ID 7: EED = 0.0128, UVT = 80% and $C_L = 0.15$ ($\overline{D}$ = 289 J/m^2, D_{eqv} = 114 J/m^2, D_{min} = 8 J/m^2, and s_D = 664 J/m^2).....146
Figure 3.25: Effect of EED on the equivalent dose, theoretical dose and hydraulic efficiency for SUVR under the conditions of runs ID 1 and 5.....147
Figure 3.26: Dose received by 58,397 particles for the SUVR **without baffles** under the conditions of run ID 1. EED = 0.0192, UVT = 93% and $C_L = 0.15$ ($\overline{D}$ = 807.2 J/m^2, D_{eqv} = 267.1 J/m^2, D_{min} = 47.3 J/m^2 and s_D = 895.9 J/m^2)...150
Figure 3.27: Cumulative relative frequency for the residence time of the SUVR **with baffles** ($\bar{t}$ = 2.61 s, t_{min} = 1.68 s and s_t = 0.939 s) and **without baffles** ($\bar{t}$ = 2.73 s, t_{min} = 2.12 s and s_t = 0.363s) under the conditions of run ID 1. EED = 0.0192, UVT = 93% and $C_L = 0.15$.....150
Figure 3.28: Elevation view of the Modified UV reactor (scale in meters).....157
Figure 3.29: Cross sectional view of the alternative UV reactor.....157
Figure 3.30: Dose received by 58,327 particles for the Modified UV reactor **with baffles** under the conditions of run ID 18: flowrate of 6,250 m^3/h, eight lamps operating, lamps output power at 100%, water transmittance 93% UVT and $C_L = 0.15$ ($\overline{D}$ = 864.3 J/m^2, D_{eqv} = 452.0 J/m^2, D_{min} = 161.2 J/m^2, and s_D = 729.8 J/m^2).....162
Figure 3.31: Dose received by 58,398 particles for the Modified UV reactor **without baffles** under the conditions of run ID 22: flowrate of 6,250 m^3/h, eight lamps operating, lamps output power at 100%, water transmittance 93%UVT and $C_L = 0.15$ ($\overline{D}$ = 847.3 J/m^2, D_{eqv} = 441.7 J/m^2, D_{min} = 181.96 J/m^2, and s_D = 851.7 J/m^2).....162
Figure 3.32: Effect of microorganism resistance on the inactivation using a first order inactivation curve for the Sentinel UV Reactor.....164
Figure 3.33: Effect of microorganism resistance on the inactivation using a first order inactivation curve for the Modified UV Reactor.....164
Figure 3.34: Effect of microorganism resistance on the inactivation using a tailing inactivation curve for the Sentinel UV Reactor.....166
Figure 3.35: Effect of microorganism resistance on the inactivation using a tailing inactivation curve for the Modified UV Reactor.....166
Figure 3.36: Effect of microorganism inactivation response to UV radiation on the predicted inactivation for the MUVR operated under the conditions of run ID 18 and the kinetic inactivation constants given in Table 3.13 for

Cryptosporidium parvum. The sub indices beside the equivalent dose stands for linear (l) and non-linear (nl) model.....168
Figure 3.37: Effect of microorganism inactivation response to UV radiation on the predicted inactivation for the MUVR operated under the conditions of run ID 19 and the kinetic inactivation constants given in Table 3.13 for *Cryptosporidium parvum*. The sub indices beside the equivalent dose stands for linear (l) and non-linear (nl) model.....168
Figure 3.38: Effect of microorganism resistance on the hydraulic efficiency using a first order inactivation curve for the Sentinel UV Reactor.....170
Figure 3.39: Effect of microorganism resistance on the hydraulic efficiency using a first order inactivation curve for the Modified UV Reactor.....170
Figure 3.40: Effect of microorganism resistance on the hydraulic efficiency using a tailing inactivation curve for the Sentinel UV Reactor.....171
Figure 3.41: Effect of microorganism resistance on the hydraulic efficiency using a tailing inactivation curve for the Modified UV Reactor.....171

Nomenclature

Upper-case Roman

A	cross-sectional area of a sphere, cm^2
A_i	area of cylinder i perpendicular to the flow, m^2
A_t	cross sectional area of the UV reactor
A_θ	cross sectional area of a circular segment between angle θ and $\theta+d\theta$ at a distance of interest from the lamp, cm^2
A_λ	absorbance at a given wave length λ
A_1	the projected area perpendicular to the beam subtended between the internal and external angles between the lamp and the beam in the air medium
A_3	projected area perpendicular to the beam subtended between the internal and external angles between the sleeve and the beam in the water medium.
C_{ls}	model parameter of the length scale
C_D	drag force coefficient
C_{ij}	convection term
C_k	intercept with the y-axis of a logarithmic data fit kinetic
C_L	Lagrangian empirical constant
C_l	$C_\mu^{0.75}/\kappa$
C_1	constant in the model equation for Π_{ij}
$C_{1\varepsilon}$	constant in the model equation for ε
C_2	constant in the model equation for Π_{ij}
$C_{2\,\varepsilon}$	constant in the model equation for ε
C_3	constant in the model equation for Π_{ij}
C_μ	turbulent viscosity constant in the k-ε model
D	UV dose, Wm^{-2} s
$\overline{D}_i$	particle-mean dose of the ith simulation
D_{eqv}	equivalent dose, Wm^{-2} s
$\overline{D}_{eqv,i}$	equivalent dose of the ith simulation
$\overline{D}_{eqv}$	simulation-mean equivalent dose, Wm^{-2} s
D_{ij}	diffusion term
D_l	lamp diameter, m
D_{min}	minimum dose absorbed by a particle, Wm^{-2} s
D_p	effective diffusivity of the particles
D_{th}	theoretical dose, Wm^{-2} s
$\overline{D}$	particle-mean dose, Wm^{-2} s
$\overline{\overline{D}}$	simulation-mean dose, Wm^{-2} s
E	energy state (J)
E_f	hydraulic efficiency
$E_{\overline{D}}$	size of the confidence interval of the particle-mean dose
$E_{D_{eqv}}$	size of the confidence interval of equivalent dose

$E_{\bar{t}}$	size of the confidence interval of particle-mean time,
E'	fluence rate, Wm^{-2}
E'_{max}	maximum fluence rate for a hypothetical case test, Wm^{-2}
E'_λ	transmitted irradiances
E^o_λ	incident irradiances
F_D	drag force between the particle and fluid
F_G	gravitational force
F_{AM}	added mass force
F_{LF}	lift force
H	vertical distance from the central plane of the lamp to the irradiated volume, cm
I	radiant intensity
I'	turbulent intensity
L	distance from the particle staring position to the outlet
L_i	staring position of a particle
N	number of organisms
N_e	number of steps
N_i	number of organisms in the level i on the series event model
N	number of live organisms after exposure to UV light
N_o	number of live organisms prior to exposure to UV light
$(N/N_o)_i$	survival ratio in each particle
(N/N_o)	overall survival ratio
P	mean pressure vector
P_{ij}	stress production term
$Pr(z_o < z)$	probability that z is greater than z_o
Q_t	total flow rate, $m^3\ s^{-1}$
Q_i	flow rate in the cylinder i, $m^3\ s^{-1}$
R	pipe radius, m
R^+	ratio between the length scales associated with the inner region and the outer region
$R(\tau)$	correlation function of the particle velocity
Re	Reynolds number
Re_p	relative Reynolds number between the two phases
R_f	the ratio of reflected intensity to incident intensity
S_{tr}	Strouhal number
U	mean velocity vector
U_1	x -component of the mean velocity, m s^{-1}
U_2	y-component of the mean velocity, m s^{-1}
U_3	z-component of the mean velocity, m s^{-1}
$\hat{U}$	absorption attenuation factor of the beam
$\bar{U}$	average "bulk velocity", m s^{-1}
U_{cl}	centerline velocity, m s^{-1}
U_{max}	Maximum velocity for laminar flow m s^{-1}
U_n	normal component of velocity to the area (A), m s^{-1}
U_∞	flow free stream velocity, m/s

Lower-case Roman

a	intercept of the exponential region of the dose-response with the y-axis
c	speed of light (2.997×10^8 m/s)
c_i	molar concentration of the absorbing species, M
d	the normal distance to the wall
d_p	particle diameter of size i, m
$e(\lambda)$	molar absorption coefficient at wavelength λ, M^{-1} cm^{-1}
e_{ijk}	alternating symbol
f_f	friction factor
f	frequency, Hz
g	gravitational force, m s^{-2}
h	Planck's constant (6.626×10^{-34} Js)
k	turbulent kinetic energy, m^2 s^{-1}
k_{df}	data fit inactivation constant
k_r	kinetic rate constant, m^2 $W^{-1}s^{-1}$
k_{nw}	turbulent kinetic energy near the wall,
k_{cl}	turbulent kinetic energy at the centerline,
l	length scale, m
l	the path length or distance of transmittance, cm
m	number of cylinders
n	number of point sources
n_a	refractive index of first media
n_b	refractive index of second media
n_c	number of discrete critical target
n_i	number of particles in the cylinder i
n_k	the x_k component of the unit normal to the wall
n_d	microorganism threshold of damage
n_p	number of particles per simulation
n_s	number of simulations
n_t	total number of particles entering the UV reactor
n_1	refractive index of air
n_2	refractive index of lamp sleeve
n_3	refractive index of water
q	quartz absorption factor
r	radius, m
r_i	internal radius of cylinder i, m
r_{i+1}	external radius of cylinder i, m
$r_k(t)$	microorganism kinetic inactivation
r_{Ni}	rate at which a microorganism passes from one event level to the next
$r_{\parallel}$	amplitude of light parallel to the plane of incidence based on Fresnel Law
$r_{\perp}$	amplitude of light perpendicular to the plane of incidence based on Fresnel Law
s	perpendicular distance from the lamp (cm)
s_D	standard deviation of the particle-mean dose

s_t	standard deviation of the particle-mean time
$s_{\bar{D}}$	standard deviation of the simulation-mean dose
$s_{\bar{t}}$	standard deviation of the simulation-mean time
$s_{D_{eqv}}$	simulation equivalent dose standard deviation
T_λ	transmittance
t	time of exposure (s)
t_q	the thickness of the quartz at $\theta = 0$
$t_{Nr-1,0.025}$	the *t*-distribution at 95 confidence limit
$\bar{t}$	particle-mean time
$\bar{t}_i$	particle-mean time of the ith simulation
$\bar{\bar{t}}$	simulation-mean time
$\mathbf{u}$	velocity vector
$\mathbf{u'}$	fluctuating component of the velocity vector
u_i,	*x*, *y* or *z*-instantaneous component of the velocity
u_i	*x*, *y or z*- fluctuating component of the velocity
u_p	instantaneous velocity of the particles
u^+	characteristics velocity
u_τ	mean velocity by the shear velocity
x	perpendicular distance between the lamp and the irradiated volume, cm
x_i	*x*, *y or z* -Cartesian coordinate
$\overline{y^2}$	particle dispersion
y	perpendicular distance from the reactor wall
y^+	characteristic length at the reactor wall

Upper-case Greek

$\Delta E'_\theta$	fluence rate for any volume element in the reactor volume, $mWcm^{-2}$
Δl	space increment along the particle path, m
ΔV	spherical volume element, cm^3
Δt	time increment, s
Δx	grid spacing, m
$\Delta\theta_1$	delta of angle between the internal and external angles between the lamp an the beam in the air medium
$\Delta\theta_3$	delta of angle between the internal and external angles between the sleeve an the beam in the water medium
Φ	the radian power of the lamp (W)
κ	von Karman constant (0.4187)
E_{ij}	dissipation term
Π_{ij}	Pressure strain term
$\Pi_{ij,1}$	interaction of fluctuations velocities
$\Pi_{ij,2}$	interaction of mean strain fluctuating velocities
$\Pi_{ij,w}$	correction for the influence of wall proximity on the pressure strain term
Ω	solid angle

Ω_{ij}	rotation term
Ψ	mean component of the flow property ψ

Lower-case Greek

$\alpha_e(\lambda)$	napierian absorption coefficient (cm^{-1})
$\alpha_q(\lambda)$	the absorption coefficient of the quartz at the wavelength λ
$\alpha_{10}(\lambda)$	Decadic absorption coefficient (cm^{-1})
δ	boundary layer thickness
δ_{ii}	kronecker delta (δ_{ij}=1 if i=j and δ_{ij}=0 if i≠j)
ε	dissipation rate of turbulent kinetic energy, m^2/s^3
λ	wave length, nm
η	population mean
μ	dynamic viscosity, kg/m s
μ_t	turbulent viscosity, kg/m s
μ_{eff}	effective viscosity, kg/m s
ω_k	rotational vector
θ_a	angle of incident
θ_b	angle of refraction
θ_c	angle of reflection
θ	angle measured from the vertical axis, deg
θ_1	the average angle between the internal and external angles between the lamp an the beam in the air medium
θ_3	average angle between the internal and external angles between the sleeve an the beam in the water medium,
ϕ	azimuthal angle about the radial axis
ρ	density of the fluid
ρ_p	density of the particle
σ^2	population variance
σ_k	turbulent Prandtl number for kinetic energy
σ_ε	turbulent Prandtl number for dissipation
τ_{ii}	normal Reynolds stress
τ_{ij}	shear Reynolds stress
τ_w	wall shear stress
τ_e	eddy lifetime
τ_p	particle relaxation time
τ_L	Lagrangian integral time scale
ν	velocity scale, m/s
ζ	standard Gaussian distribution
ψ	instantaneous flow property
ψ'	time-varying fluctuating component of the flow property φ

Subscripts

-	lower level of a design or computational factor
+	higher level of a design or computational factor

Subscripts

i,j or k = 1	x- Cartesian coordinate
i,j or k = 2	y- Cartesian coordinate
i,j or k = 3	z- Cartesian coordinate
p	particle number
q	event level occupied for the microorganism

Symbols

∇	gradient operator
$\nabla \circ$	divergence operator
∇^2	Laplacian operator

Abbreviations

AWWARF	American Water Works Association Research Foundation
CFD	Computational Fluid Dynamics
CBBR	Continuous Beam Batch Reactor
CLT	Central Limit Theorem
CSTR	Continuous Stirred Tank Reactor
DNS	Direct Numerical Simulation
DRW	Discrete Random Walk Model
EED	Electrical Energy Dose
MUVR	8 x 15 kW Modified UV Reactor
LSI	Linear Source Integration
LES	Large Eddy Simulation
MPSS	Multiple Point Sources Summation
NLO	Number of lamps operating
NWRI	National Water Research Institute
PSS	Point Source Summation
RANS	Reynolds Averaged Navier-Stokes
RED	Reduction Equivalent Dose
RMS	Root Means Squares
RSM	Reynolds Stress Model
RTD	Residence Time Distribution
RWM	Random Walk Model
SHCM	Structured Hexahedral Coarse Mesh
SHFM	Structured Hexahedral Fine Mesh
STFM	Structured Tetrahedral Fine Mesh
SUVR	6 x 20 kW Sentinel UV Reactor
UDF	User Defined Function
UHCM	Unstructured Hexahedral Coarse Mesh
UHFM	Unstructured Hexahedral Fine Mesh
USEPA	United States Environmental Protection Agency
UVT	Ultraviolet Transmittance

1 Literature Review and Components of the Model

Ultraviolet (UV) inactivation of microorganisms in drinking water began in France in 1906, and was abandoned in the late 1930s, because chlorine disinfection was more affordable and easier to operate and maintain than UV equipment. UV technology was revived in Europe after the end of the Second War World; however, widespread application of UV technology in centralized municipal water treatment facilities was delayed in North America until experimental results of protozoan inactivation proved that UV could be used for inactivation of *Giardia lamblia* and *Cryptosporidium parvum* (Bolton and Dussert, 1998).

UV radiation refers to the electromagnetic waves in the actinic wavelength range (10 to 400 nm). UV lamps typically consist of a quartz tube filled with an inert gas, such as argon, and small quantities of mercury. UV radiation is generated when ionized mercury atoms return to their initial energy level after activation by electrical discharges. For the inactivation of pathogens in drinking water facilities, actinic wavelengths can be emitted either in a broad range of 200 to 400 nm (medium pressure lamps) or in a narrow band around 254nm (low pressure lamps). Although medium pressure lamps emit over a wide range of wavelengths, they yield 50 to 80 times higher output than lower pressure lamps.

A UV reactor is a combination of one or more UV lamps arranged in a pipe or a channel with associated electrical, cooling, cleaning and monitoring systems. The majority of UV reactors for drinking water are built with medium pressure lamps oriented either parallel or perpendicular to the flow. UV lamps are mounted within a quartz tube to moderate the effect of cooling by water, to facilitate removal or replacement of lamps,

and to avoid mercury spills into the water if a lamp should happen to break. Some UV reactors include mechanical cleaning systems which remove deposits from lamp sleeves. UV reactors are also equipped with UV radiation sensors and UV transmittance monitors to measure 1) the intensity of UV radiation delivered by the lamps and 2) the clarity of the water. UV reactors are usually designed to promote high radial mixing with minimum axial mixing within the irradiation zone. Ideally, UV reactors are installed in such a way that inlet conditions promote a uniform velocity profile and the outlet conditions do not affect the hydrodynamic patterns inside the equipment.

The mathematical analysis of a UV reactor involves the use of several models, including: 1) continuous phase hydrodynamic model, 2) discrete phase particle transport model, 3) spatial UV fluence rate distribution model, and 4) microorganism inactivation model. The first three models are used to generate a dose distribution by simulating the transport of microorganisms through the velocity and UV fluence rate fields. The dose distribution is then combined with the microorganism inactivation response to estimate the level of inactivation.

1.1 UV use in water treatment

UV radiation is used to inactivate pathogens in drinking water or wastewater treatment plants. However, the regulatory measures of UV reactor performance differ according to the treatment application. In wastewater treatment the reduction of the total number of coliforms in the water effluent is used as an indicator of performance whereas in drinking water facilities UV intensity and UV transmittance are used to estimate the level of inactivation. The following section describes the basic UV radiation concepts for

drinking water and wastewater treatment. The problems faced by operators of drinking water treatment facilities, manufacturers of UV equipment, and drinking water agencies demanding better or more reliable methods for predicting UV reactor performance, are reviewed to place the work done in this project in a broader context.

1.1.1 UV for Disinfection of Drinking Water

UV disinfection in drinking water has been widely applied to small point-of-use facilities such as campgrounds, households, hospitals, schools, recreational facilities, and remote areas, as well as in boats, ships, trains, food industries and groundwater treatment. The extension of UV technology to centralized municipal drinking water treatment facilities with surface water feed has been limited by:

1. a belief that UV is unable to inactivate *Giardia* and *Cryptosporidium*
2. lack of a secondary disinfectant in the water distribution system,
3. possibility of high operational cost due to replacement of the lamps,
4. possible latent reactivation of microorganisms after treatment,
5. lack of well established and accepted guidelines for performance estimation,
6. potential formation of photochemical by-products,
7. need for strict operational control of the UV equipment.

The first unknown was addressed by Bolton and Dussert (1998). They proved that UV could be used for inactivation of *Giardia* and *Cryptosporidium*. This study addresses the need for a well-established guideline to estimate UV reactor performance with CFD. The remaining unknowns required further research. Despite these development needs,

UV technology provides some significant advantages over chlorine-based technology including:

1. inactivation of *Cryptosporidium parvum* at low doses,
2. production of few chemical by-products,
3. reduction of chemical risk and associated safety precautions, and
4. reduction of the installation space required.

UV radiation alters the nucleic acids of a microorganism and thus inhibits its ability to multiply and cause disease. Specifically, UV radiation causes damage to the nucleic acid of microorganisms by forming covalent bonds between certain adjacent bases of the DNA (thymine or cytosine) or RNA (uracil or cytosine). Formation of such bonds prevents the DNA from being "unzipped" during replication, and as a result the microorganism is unable to replicate. The effectiveness of the UV radiation depends on its wavelength and energy. The highest germicidal effectiveness is at 260nm, which is close to the wavelength emitted by low pressure lamps (Jagger, 1967).

The increasing number of water facilities using UV equipment has forced governmental agencies to provide guidance for the use of UV technology in drinking water treatment. Among these agencies are the United States Environmental Protection Agency (USEPA), the National Water Research Institute (NWRI) and the American Water Works Association Research Foundation (AWWARF). These agencies have published guidelines that focus on the validation and minimum acceptable design of UV disinfection systems (USEPA, 2003 and Batchley et al. 2000).

In addition, the United States Environmental Protection Agency (USEPA) has proposed two rules that have forced water utilities to implement UV technology in order

to reduce disease associated with pathogens in drinking water and to minimize the chlorine dosage added to the water. The first rule is the Long Term 2 Enhanced Surface Water Treatment Rule (LT2ESWTR) which aims to reduce disease associated with *Cryptosporidium* and other microorganisms in drinking water. The second rule is the Stage 2 Disinfectants and Disinfection By Product Rule (D/DBPR), which aims to protect public health by limiting the exposure to disinfectant by products such as trihalomethanes (THM) and Haloacetic acids (HAA) both byproducts of chlorine disinfection. These new regulations will accelerate the implementation of UV reactors in municipal drinking water facilities throughout North America.

1.1.2 UV for Microorganism Reduction in Wastewater

In contrast with drinking water treatment, the use of UV reactors for disinfection of secondary effluent is more common in North America than in Europe because 1) chlorine is toxic to aquatic microorganisms in receiving water; 2) wastewater reclamation is viewed as a solution for the heavy irrigation demands in the some geographical areas of the United States. Therefore, many states have adopted regulations that limit the maximum concentration of total coliforms in the wastewater effluent. UV technology is able to meet these regulatory requirements while reducing the discharge of chemicals to the receiving water.

UV reactors for wastewater consist of banks of lamps in a channel, where the lamps are parallel or perpendicular to the flow. These UV reactors deliver a higher UV dose to overcome the shielding effect exerted by the high concentration of Total Suspended Solids (TSS) and lower water UV transmittance (UVT). UV reactors for wastewater

differ from the ones for drinking water not only in the configuration and lamp system implemented, but also in monitoring. The performance of a UV reactor for wastewater is monitored by directly measuring the microorganism reduction of an indicator microorganism (i.e. total coliforms).

1.2 Determining UV Dose

The performance of a UV reactor for drinking water cannot be measured directly since the concentrations of both pathogens and indicator microorganisms in drinking water are below the detection limits of current microbial assays. Full-scale implementation of UV inactivation for drinking water is currently limited by the lack of a sound method for determining the level of UV disinfection.

The level of microorganism inactivation is in general proportional to UV dose (J/m^2), where the UV dose, D, is defined as:

$$D = E' * t \qquad (1.1)$$

where E' stands for the UV fluence rate (W/m^2) and t stands for the exposure time of microorganisms to be treated (s). The UV fluence rate is defined as the radiant power passing from all directions through an infinitesimally small sphere of cross-sectional area dA, divided by dA. The term UV fluence rate will be used in this document instead of the term UV irradiance, which is defined as the total radiant power incident on an infinitesimal element of surface of area dS containing the point under consideration, divided by dS (Bolton, 2000). The UV dose defined in Equation (1.1) indicates that a high UV fluence rate over a short period of time would provide the same inactivation as a lower UV fluence rate at a proportionally longer period of time.

The UV dose received by a microorganism is a function of several factors:

1. the radiant intensity emitted by the lamps,
2. the water quality, which determines the water transmittance and the degree of UV radiation absorbed by the water, and
3. the exposure time, which depends on both the mean residence time as determined by the UV reactor volume and flowrate, and the hydrodynamic characteristics of the reactor.

Quantification of the UV dose depends on the ability to determine all three of these factors, which at present is difficult to do. The UV fluence rate varies spatially within the UV reactor and depends on the distance from the lamp, the water transmittance, the lamp output, the number of lamps and the spacing between them. At present there are no instruments capable of measuring fluence rate distribution directly. UV sensors measure the UV irradiance at one point and thus provide only partial information about the fluence rate field. Additional complications to the estimation of the UV fluence rate are the lamp aging and the lamp and sensor fouling. Water quality parameters play a significant role in the dose received by microorganisms. The amount of UV radiation reaching the target microorganism may be diminished due to 1) shielding and scattering and absorbance caused by suspended solids, 2) UV absorbance by dissolved chemicals, and 3) lamp sleeve fouling by inorganic constituents. The residence time is not a unique value in continuous flow UV reactors due to the hydrodynamic characteristics of the unit. Ideally, the flow regime in a UV reactor should be plug flow with perfect radial mixing and no axial dispersion, where each microorganism entering the reactor receives the same UV dose regardless of the spatial fluence rate distribution. Perfect plug flow does not exist in

a real UV reactor. As a result, microorganisms receive a distribution of doses rather than a single well defined dose.

1.2.1 Dose Distribution

The complex interaction between the hydrodynamic field and the non-uniform UV fluence rate profile means that a UV reactor delivers a distribution of UV doses. A dose distribution is typically represented as a histogram of probability that a microorganism receives a given UV dose (Figure 1.1). The shape of the histogram indicates the hydraulic efficiency of the reactor. A UV reactor with a narrow dose distribution is hydraulically more efficient and provides the greatest inactivation for the same power input.

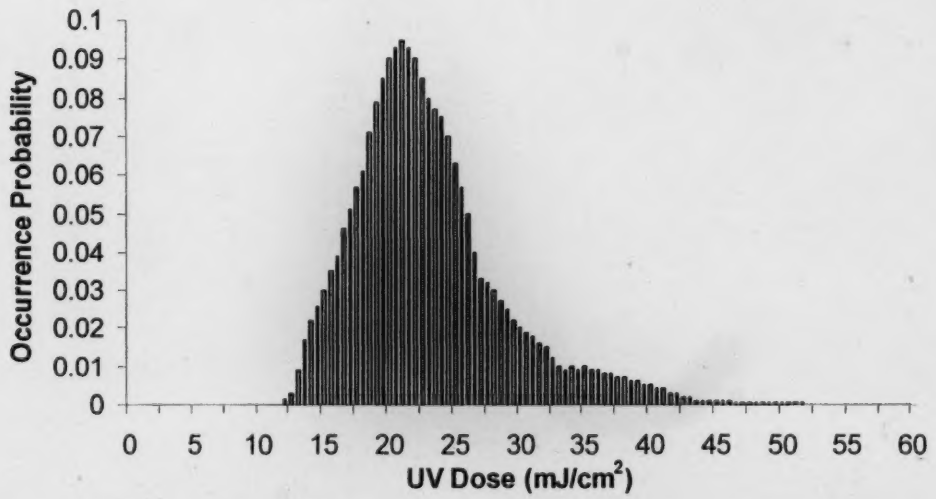

Figure 1.1: Typical dose distribution in a wastewater UV reactor (Chiu et al., 1999).

The dose distribution in large UV reactors cannot be directly measured. Tracer studies provide a description of the hydrodynamic field but do not characterize the UV fluence rate field. Conversely, actinometrical tests can provide the average dose but

cannot characterize the hydrodynamic field. As a result, computational modeling has been proposed as a way to estimate the dose distribution.

An alternate method, called biodosimetry, determines the level of inactivation experimentally. Challenge microorganisms are used in biodosimetry due to the reasonable public objection to the release of pathogens in drinking waters. First, the inactivation of the challenge microorganism is related to a UV dose response curve as determined in a Collimated Beam Batch Reactor (CBBR). A collimated beam is a uniform parallel beam of UV radiation that is used to irradiate a suspension of microorganisms in a Petri dish or another suitable container. Then inactivation of the challenge microorganism is measured after exposure in a UV reactor under fixed operating conditions. The result of the biodosimetry is expressed in terms of the Reduction Equivalent Dose (RED), which is set equal to the UV dose that achieves the same level of inactivation of the challenge microorganism in a collimated beam test as measured for the flow-through UV reactor during biodosimetry testing (Cabaj et al. 1996).

Biodosimetry presents several limitations:

1. it cannot be used as a design tool,
2. it does not provide any insight into the phenomena occurring inside the reactor,
3. it gives results that depend on the challenge microorganism,
4. it provides results that cannot be extrapolated beyond the conditions of the test,
5. it is expensive, complicated and logistically difficult to perform. It requires large installations, full equipment, a water supply, and permits to release the challenge microorganism in wastewater from the test.

An alternative test method that will lead to improved design of UV reactors is needed. Therefore, a large incentive to develop reliable computational models

1.3 Models Reported in the Literature to Date

The mathematical analysis of a UV reactor involves four major models. These are:

1. continuous phase hydrodynamic model,
2. discrete phase particle transport model,
3. discrete random walk model,
4. spatial UV fluence rate distribution model, and
5. microorganism inactivation kinetics model.

The first attempts at modeling UV fluence rate were carried out by Jacob and Dranoff (1970); Scheible et al. (1985); and Suidan and Severin (1986); who divided the lamp into independent sources of equal intensity. This is called the multiple point source summation (MPSS). Irozoqui et al. (1993) later expanded the MPSS to three-dimensional space and accounted for the spectral distribution of the lamp emission. Blatchley et al. (1997) integrated the MPSS to the limit of an infinite number of sources (Line Source Integration (LSI)). Finally, Bolton (2000) improved the MPSS by including absorption, reflection, refraction and a germicidal factor to account for photon effectiveness for broadband MP lamps. Fluence rate models can be used to estimate a theoretical dose by multiplying the spatial average fluence rate by the theoretical residence time (Bolton, 2000). This approach assumes ideal plug flow with perfect radial mixing inside the reactor, neglecting any effects of local hydrodynamics.

Blatchley et al. (1997) address the hydrodynamics and used CFD to calculate the velocity field. Their model did not, however, combine the flow and fluence rate characterization to permit complete description of the dose distribution. Lin et al. (1999) applied a CFD code restricted to the central region of a wastewater UV reactor where the lamps are perpendicular to the flow. The fate and transport of the microorganisms through the reactor was modeled by solving two-dimensional differential equations for advection, diffusion and reaction.

Chiu et al. (1999) used a different approach to model disinfection efficacy for a similar wastewater UV reactor. Their model integrated dose response information from batch studies with a dose distribution that was generated by combining experimental flow field data with the UV fluence rate field predicted using the MPSS model. This model used the random walk model to simulate particle transport through the fluence rate field. The authors found that particles moving near the wall received lower doses than the ones in the core region due to the low fluence rate near the wall.

Wright and Hargreaves (2001) applied 3-dimensional CFD analysis to four UV reactor configurations. This work compared the relative efficiencies of different UV reactor designs through the use of a commercial CFD code. The objective of their study was to optimize the location of the inlet and outlet in the main body of a single lamp reactor. The authors performed a sensitivity analysis of the computational variables and found that different turbulence models predicted similar inactivation efficiency. The main limitations of this work are that radiation energy attenuation by the water was not considered, and the number of particles used in the simulations was not provided, which it makes difficult to interpret or replicate the results.

Table 1.1 summaries the UV inactivation models currently available in the literature, All of these models were used in wastewater treatment except for the model developed by Lem (2002), which was used in drinking water. All those models were applied to small UV reactors. Six out of eight models used CFD, except for Severin et al (1983) and Chiu et al. (1999). Chiu's model provided better prediction of the inactivation than the other models due to the use of the random walk model to simulate the motion of individual microorganisms through the UV reactor. To achieve better prediction for a large UV reactor, it is essential to combine CFD and the random walk model, which was the focus of this study.

Table 1.1: Summary of UV reactor models

Characteristics	Severin et al. 1983	Blatchley et al. 1998	Downey et al. 1998	Lyn et al. 1988	Chiu et al. 1999	Wright & Hargreaves 2001	Rokjer et al. 2002	Lem 2002
Geometry								
Open channel	×	✓	×	✓	✓	×	×	×
Closed pipe	✓	×	✓	×	×	✓	✓	✓
Size: width, length (m)	0.14x0.27	0.3x0.3	0.07x0.4	0.04x0.82	0.45x9.6	0.24x1.4	0.9x1.9	0.3x1.0
Lamps parallel to flow	✓	✓	✓	×	×	✓	×	×
Lamps perpendicular to flow	×	×	×	✓	✓	×	✓	✓
Number of lamps	1	4	1	5	25	1	72	4
Lamp type	LP	LP	NR	LP	LP	NR	LPHI	MP
Hydrodynamics	none	2 Ph	1 Ph	2-Ph	2-Ph	2-Ph	2-Ph	2-Ph
Velocity measurements	×	×	×	×	✓	×	×	×
2 or 3D simulation	×	2	3	2	×	3	3	3
Turbulence model	×	k-ε	k-ε	k-ε	×	k-ε	k-ε	k-ε
Microorganism transport model	×	×	×	CP	DP	×	DP	DP
Residence time distribution	×	×	✓	×	×	×	×	×
Head loss Consideration	×	✓	×	×	×	✓	×	×
UV fluence rate model	B-L	LSI	×	LSI	LSI	I	B	B
Disinfection								
Dose distribution	×	×	×	×	✓	×	✓	✓
Equivalent Dose	×	×	×	×	✓	×	✓	✓
Disinfection kinetics	✓	✓	×	✓	✓	×	✓	✓
Hydraulic efficiency	×	×	×	×	×	×	✓	×

✓ stands for Yes, × stands for None, LPHI Low Pressure High Output, CP Continuous phase, DP Discrete phase, B-L Beer-Lambert law, LSI Light Source Integration, I intensity proportion, NR Not reported, B Bolton Model, Ph Number of phase,

1.4 Components of UV Reactor Models

The inactivation of microorganisms in the reactor is estimated by combining the dose distribution with the microorganism inactivation response, as shown in Figure 1.2. In order to estimate the dose distribution, it is necessary to generate both velocity and UV fluence rate fields. In this study, the velocity field was computed using FLUENT 6.1, a commercial Computational Fluid Dynamics package. This code applies the finite volume method to solve the Reynolds Averaged Navier-Stokes (RANS) equations in conjunction with a turbulence model. The distribution of UV fluence rate generated by the UV lamps is computed with a commercial code (UVCalc 3D-200, developed by Bolton Photosciences Inc.) which uses the Multiple Point Source Summation (MPSS) to estimate the UV radiation emitted and adsorbed by the reactor components. In this method, each lamp was divided into a series of one thousand equally spaced point sources along the axis of the lamp, and the contribution of each point source over an infinitesimal sphere was computed.

The particle trajectory was simulated with a discrete phase model (DPM), and the discrete random walk (DRW) model. This describes the movement of a single microorganism referred to as fluid particle in this study through the reactor. The UV dose received by a particle is computed by summation of the fluence rate along the path traveled by the particle through the UV reactor.

$$D = \sum_{t=0}^{t=t} E_t' \Delta t \qquad (1.2)$$

The dose received by each fluid particle is converted to survival ratio, $(N/N_o)_i$, using a microorganism inactivation model. In each simulation, thousands of fluid particles were

uniformly distributed by volume at the inlet of the UV reactor ensure a statistically robust and repeatable UV dose distribution at the outlet. The overall survival ratio, N/N_o, was computed by summation of the survival ratio $N/N_{o,i}$ of each fluid particle as given in Equation (1.3) (see Appendices A and B).

$$\frac{N}{N_o} = \sum_{i=0}^{i=n_t} \frac{1}{n_t} \left(\frac{N}{N_o} \right)_i \tag{1.3}$$

Where

N is the number of organisms viable at the outlet after exposure to UV radiation

N_o is the number of organisms viable at the inlet before exposure to UV radiation

n_t is the total number of particles.

Inactivation was expressed as the negative logarithm in base 10 of the survival ratio, $-\log_{10} (N/N_o)$. The procedure used to estimate the overall survival ratio assumes that there is no exchange of microorganisms between fluid particles. Therefore, the microorganism on a fluid particle does not change its carrier throughout the UV fluence rate field.

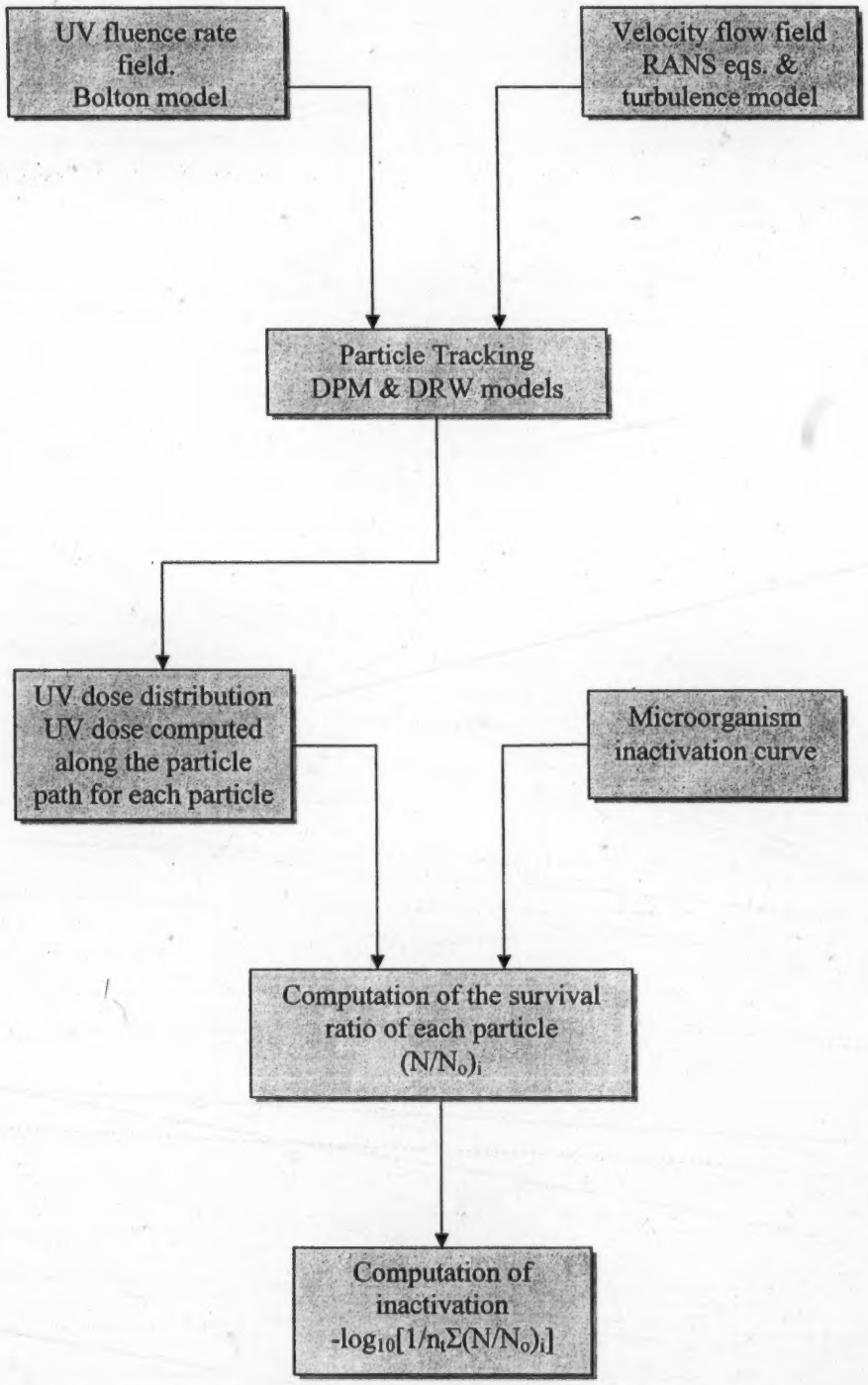
UV fluence rate field, Bolton model
Velocity flow field RANS eqs. & turbulence model
Particle Tracking DPM & DRW models
UV dose distribution UV dose computed along the particle path for each particle
Microorganism inactivation curve
Computation of the survival ratio of each particle $(N/N_o)_i$
Computation of inactivation $-\log_{10}[1/n_t\Sigma(N/N_o)_i]$

Figure 1.2: Flow chart of the procedure to evaluate the inactivation of microorganisms in a UV reactor

1.5 Ultraviolet Radiation

The UV fluence rate inside a UV reactor is highly non-uniform due to the absorption, reflection and refraction of UV radiation by water constituents or reactor components. These phenomena create spatial UV fluence rate profiles, which show that the fluence rate decreases as the distance between the irradiated volume and the UV radiation source increases. It is essential for UV reactor designers to have a complete understanding of the generation, propagation and absorption of UV radiation by the reactor components (i.e. air, quartz, water, and stainless).

1.5.1 Source, Generation and Propagation of UV Radiation

Ultraviolet radiation is defined as the portion of the electromagnetic wave spectrum between x-rays and visible light (40 to 400 nm). The UV radiation is divided into vacuum UV (40-190nm), far UV (190 – 220 nm), UVC (220 -290nm) and UVA (320 – 400nm). Germicidal lamps are designed to emit UVC radiation because of the high microorganism inactivation in this range. Mercury arc UV lamps emit radiation due to the flow of current through a mercury vapor between electrodes. The specific wavelengths of radiation produced by the photon discharge depend on the power supplied to the lamp, the gas composition and the mercury concentration. Three types of mercury arc UV lamps are commercially available: low-pressure low-intensity lamps, low-pressure high-intensity lamps, and medium-pressure high-intensity lamps.

The low-pressure low-intensity lamps generate monochromatic radiation at a wavelength of 254 nm, which is close to the wavelength of maximum germicidal effect (Jagger, 1997). These lamps require a maximum temperature of 40°C at the wall of the

lamp to avoid reduction of UV output, where the UV lamp output is defined as the number of photons emitted per unit length of lamp. Instead of using mercury alone, low-pressure high-intensity UV lamps use mercury–indium amalgam, which allows greater UVC output, usually two to four times the output of conventional low-intensity lamps. Medium-pressure high-intensity UV lamps generate polychromatic radiation with only 7 to 15% of the output near 254 nm and 27 to 44% of the total energy in the germicidal UVC range. However, medium-pressure high-intensity UV lamps generate approximately 50 to 100 times the UVC output of low-pressure low-intensity UV lamps. In addition, they allow modulation of the UV output without changing the spectral distribution of the lamp.

UV radiation is generated after a current applied to a gas increases the energy state of the electrons. When the electrons return to their initial energy state, a discrete amount of energy is released as photons of radiation at a particular wavelength, λ, (Equation 1.4). If sufficient energy is applied to an electron, it can be removed from the atom, leading to a positive charged atom, or cation, and a negatively charged free electron. This ionization process provides a rapid increase in the number of free electrons and cations, which in turn causes an increase in lamp current and a drop in the voltage across the lamp.

$$E_2 - E_1 = \frac{hc}{\lambda} \qquad (1.4)$$

E_1= Lower energy state (J)

E_2= Higher energy state (J)

h = Planck's constant (6.626×10^{-34} Js)

c = Speed of light (2.997×10^{8} m/s)

λ = Wavelength (m)

Among the materials used to generate UV radiation, mercury is preferred since it requires a relatively low voltage to create the gas discharge (a combination of non-excited atoms, excited atoms, cations, free electrons and filling gas) and has a lower vapor pressure relative to other metals. In addition, mercury at high vapor pressure provides high intensity polychromatic UV radiation with reasonably high efficiency and minimal reaction between mercury and the electrode materials or the lamp envelope.

Once the UV radiation is generated by the lamps in a UV reactor, it propagates through three media: air, quartz and water (recall from Section 1.1 that a UV lamp is usually encased in a quartz sleeve and air fills up the gap within the lamp wall and the sleeve). These materials affect the radiation propagation by factors of scattering, absorption, reflection, and refraction. Scattering of UV radiation is the change in direction of radiation propagation caused by interaction with a particle. Absorption is the reduction of radiation as it passes through a solution. The UV radiation attenuation factor is quantified by the Beer Lambert Law :

$$T_\lambda = \frac{E_\lambda^t}{E_\lambda^o} = 10^{-A_\lambda} = 10^{-\alpha_{10} l} = 10^{-\sum \varepsilon_i c_i l} = e^{\alpha_\varepsilon l} \qquad (1.5)$$

where

T_λ = the UV transmittance at a given wavelength λ (unitless),

E_λ^t = the transmitted irradiance (W/m^2),

E_λ^o = the incident irradiance (W/m^2),

A_λ = the UV absorbance at a given wavelength λ (unitless),

α = the absorption coefficient[1] at a given wavelength λ (cm^{-1}),

[1] The absorption coefficient can be expressed Naperian (α_ε)or Decadic base(α_{10})

l = the distance traveled by the UV radiation through the solution (cm),

e_i = the molar absorption coefficient ($M^{-1}cm^{-1}$),

c_i = the molar concentration of the component i (M).

In water and wastewater treatment, UVT is defined as the percentage of radiation passing through a water sample over a path length of 1cm and is related to UV absorbance at a wavelength of 254 nm (A_{254}) by Equation (1.6).

$$\%UVT = 100 * 10^{-A_{254}} \tag{1.6}$$

Refraction refers to the change in the direction of radiation propagation as it passes from one medium to another. Refraction is described by Snell's law

$$n_a \sin\theta_a = n_b \sin\theta_b \tag{1.7}$$

where n_a and n_b are the refractive indices of the two media and θ_a and θ_b are the angles of incidence and refraction, respectively.

Reflection is the change in the direction of radiation propagation as it is deflected backwards by the interface between two media. The degree of reflection depends on the roughness of the surface. If the surface roughness is smaller than the wavelength of the radiation the reflection is called specular and is governed by Fresnel's Law

$$R_f = \frac{1}{2}\left[r_{\parallel}^2 - r_{\perp}^2\right] = \frac{1}{2}\left[\left(\frac{n_b \cos\theta_a - n_a \cos\theta_c}{n_a \cos\theta_c + n_b \cos\theta_a}\right)^2 + \left(\frac{n_a \cos\theta_a - n_b \cos\theta_c}{n_a \cos\theta_a + n_b \cos\theta_c}\right)^2\right] \tag{1.8}$$

where

R_f = the ratio of reflected irradiance to incident irradiance (unitless),

$r_{\parallel}$ = the amplitude of radiation parallel to the plane of incidence,

$r_{\perp}$ = amplitude of radiation perpendicular to the plane of incidence

θ_a = the angle of incidence,

θ_c = angle of reflection

1.5.2 Ultraviolet Fluence Rate Model

The design of a UV reactor requires characterization of the UV radiation emitted and adsorbed by the reactor components. The UV radiation model should account for reflection, refraction, and media absorption (i.e. air/quartz/water). Several UV radiation models have been developed (Jacob and Dranoff, 1970; Scheible et al. 1995; Suidan and Severin, 1986; Blatchley et al. 1997 and Bolton, 2000).

The Multiple Point Source Summation (MPSS) model developed by Jacob and Dranoff 1970 assumes:

1. The lamp is composed of n point sources spaced equally along the axis of the lamp.
2. Each point source is considered a spherical source that emits equal intensity in all the direction in 3 dimensions and independently from the others.
3. Radiation properties such as the total output power Φ are equal to the sum of Φ_i from i to *n* point sources, where Φ_i is the power at each point source.
4. The UV radiation is absorbed by the media (air/quartz/water) according to the Beer Lambert Law (Equation 1.5).
5. The total fluence rate at each point in the reactor is the sum of the fluence due to each of the *n* point sources.

Bolton (2000) improved and generalized the Jacob-Dranoff model by including 1) reflection and refraction that take place at the interfaces of each media (air/quartz/water), 2) absorption in the air space between the lamp envelope and the quartz sleeve, 3) a

germicidal correction factor to account for UV photon effectiveness in the range from 200-300nm, 4) radiation sources that emit radiation in all directions and 5) radiation energy received by infinitesimally small spheres within the reactor. Bolton (2000) found that the UV fluence rate can be underestimated by as much as 25% if reflection and refraction are not taken into account. The significance of reflection and refraction increases as the distance from the lamp increases.

The derivation of the fluence rate equation is based on the radiant intensity concept, which states that the radiant intensity, I, does not diminish with distance if there is no absorption or reflection. The model considers a beam of radiant energy emitted from a source in certain direction within an element of solid angle[2], $d\Omega$, where differential radiant power, $d\Phi$, is equal to radiant intensity, I, times the element of solid angle, $d\Omega$. Equation (1.9) represents the differential of radiant power, $d\Phi$, as a function of the solid angle, $d\Omega$, expressed in polar coordinates and the radiant intensity, I.

$$d\Phi = I * d\Omega = I \sin\theta d\theta d\phi = \frac{\Phi}{4\pi} \sin\theta d\theta d\phi \qquad (1.9)$$

In Equation (1.9), θ is the angle measured from the vertical axis and ϕ is the azimuthal angle about the radial axis, as shown in Figure 1.3. The UV fluence rate, E', defined as the radiant power incident from all directions onto an infinitesimally small sphere of cross-sectional area dA, of a circular segment between angle θ and $\theta+d\theta$ at a distance of interest from the lamp, can be mathematically expressed as:

$$dE'_\theta = \frac{d\Phi}{dA_\theta} = \frac{\Phi}{4\pi dA_\theta} \sin\theta d\theta d\phi \qquad (1.10)$$

[2] solid angle refers to the angle subtended at the center of a sphere by an area on its surface numerically equal to the square of the radius $d\Omega=A/r^2$

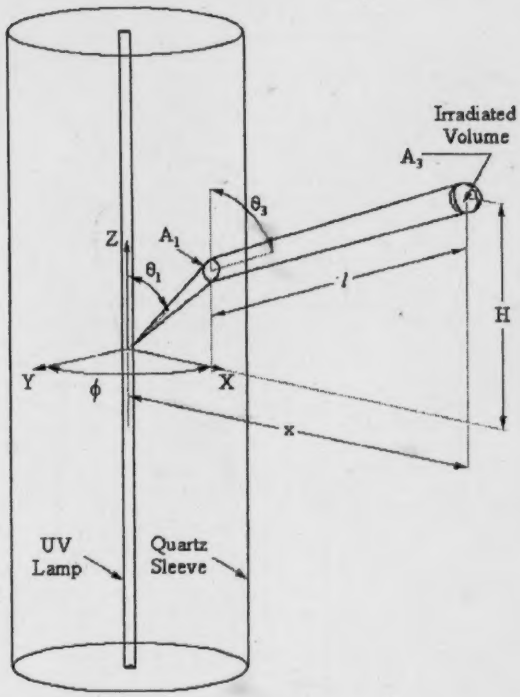

Figure 1.3: 3-D UV reactor, A_1 and A_3 are the cross sectional areas needed to calculate the fluence rate (Adapted from Bolton, 2000).

Since the UV lamp has cylindrical symmetry, it is possible to integrate over the azimuthal angle to obtain:

$$dE'_\theta = \frac{\Phi}{4\pi dA_\theta}\sin\theta d\theta \int_0^{2\pi} d\phi = \frac{\Phi}{2dA_\theta}\sin\theta d\theta \qquad (1.11)$$

To compute the fluence rate at the quartz sleeve, Equation (1.11) can be written in finite difference form:

$$\Delta E'_\theta = \frac{\Phi \sin\theta_1 \Delta\theta_1}{2A_1} \qquad (1.12)$$

where

θ_1 is the average angle between the internal and external angles between the lamp and the beam in the air medium,

$\Delta\theta_1$ is the delta of angle between the internal and external angles between the lamp an the beam in the air medium, and

A_1 is the projected area perpendicular to the beam subtended between the internal and external angles between the lamp and the beam in the air medium.

To compute the fluence rate after the beam has propagated through water, Equation (1.11) is expanded to account for refraction, reflection and absorbance of the water as giving in Equation (1.13).

$$\Delta E'_\theta = (1 - R_f)T_\lambda \frac{\Phi \sin\theta_3 \Delta\theta_3}{2A_3} \tag{1.13}$$

where

T_λ is given by Equation 1.5,

R_f is given by Equation 1.8,

θ_3 is the average angle between the internal and external angles between the sleeve and the beam in the water medium,

$\Delta\theta_3$ is the delta of angle between the internal and external angles between the sleeve and the beam in the water medium, and

A_3 is the projected area perpendicular to the beam subtended between the internal and external angles between the sleeve and the beam in the water medium.

The trigonometric relations that define *l*, A_1, A_3 as a function of angle, θ, the irradiated volume located at radial distance, x, and at longitudinal distance, H, from the lamp centroid to the irradiated volume are given in Bolton (2000).

Equations (1.12) and (1.13) do not account for absorption by the quartz, which can be quantified by adding the factor, q, into these equations

$$q = \exp\left[\frac{\alpha_q(\lambda)t_q}{\sin\theta}\right] \tag{1.14}$$

where

q is quartz absorption factor,

$\alpha_q(\lambda)$ the absorption coefficient of the quartz at the wavelength λ (cm^{-1}), and

t_q the thickness of the quartz at $\theta = 0$ (cm).

The UV fluence rate is computed with either Equation (1.12) or (1.13) for a spherical volume element ΔV in the reactor. The fluence rate for a medium pressure lamp is corrected by the germicidal efficiency for the wavelength range between 200-300nm. The summation of the UV fluence rate contribution from each point source gives the total UV fluence rate received at this volume element for one lamp. The number of point sources used by the MPSS model is 1001, because Bolton (2000) proved that this number results in less than 1% error (Bolton, 2000).

1.5.3 Germicidal Efficiency

The fluence rate model can be used for any photochemical process. However, for the case of microorganism inactivation with medium pressure UV lamps, a germicidal correction factor has to be implemented to account for UV photon effectiveness in the range 200-300nm. This is because the UV photons must first be absorbed by the DNA before it can alter the DNA. The UV radiation damages the DNA or RNA of microorganisms by forming covalent bonds between certain adjacent bases of the DNA (thymine or cytosine) or RNA (uracil or cytosine). This reaction is termed dimerization. The germicidal efficiency curve is a measure of relative UV-absorbance and dimerization of the DNA as a function of the wavelength. Figure 1.4 shows the emission and the

germicidal efficiency curve of a medium pressure lamp, clearly illustrating that the UV effectiveness is highest in the 260 nm wavelength range.

1.5.4 UVCalc3D_200

The UVCalc3D_200 code is a numerical tool developed to solve the fluence rate equations (1.12) and (1.13). This code accounts for:

1. the 3 dimensional UV radiation emitted by the point sources,
2. the fluence rate contribution for multiple lamps,
3. absorption, reflection and refraction of UV radiation, and
4. the **shadow effect** generated by the interception of the radiation by other lamps.

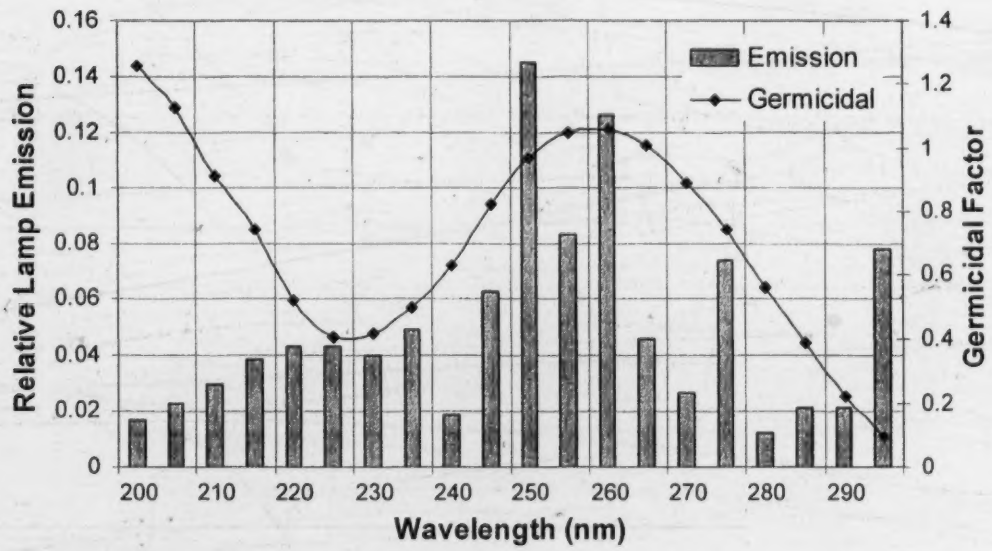

Figure 1.4: Germicidal factor relative to the DNA absorbance and relative lamp emission as function of the UVC radiation, adapted from (Bolton 2001).

1.6 Turbulent Flow Modeling

The flow regime in a UV reactor is turbulent due to the high flow rates required in water treatment facilities and the low viscosity of water. In turbulent flow, the fluid motion is chaotic[3] and random, and the velocity and the pressure change with time at each point in the flow. Visualization of the turbulent flow reveals rotational structures called turbulent eddies or vortices with a wide range of length and time scales. Eddies play an important role in a UV reactor as they carry microorganisms to the lamps and move microorganisms from the lamps to the reactor walls. This radial mixing increases the microorganism inactivation efficiency relative to what could be achieved in laminar flow.

Full simulation of the wide range of eddy lengths and timescales would require an extremely fine mesh with massive amounts of computing time. For many engineering purposes this level of detail is not necessary: the time averaged properties of the flow are sufficient. The time averaged properties are generated from a description of the instantaneous properties (ψ) as average values (Ψ) plus fluctuations (ψ'). For instance, in the case of velocity, the instantaneous velocity vector (**u**) is equal to the sum of the average velocity vector (**U**) plus the fluctuating velocity vector (**u'**):

$$\mathbf{u} = \mathbf{U} + \mathbf{u}' \tag{1.15}$$

The introduction of time averaging, or Reynolds averaging, of the instantaneous Navier–Stokes equations discards all the details contained in the instantaneous fluctuations but creates six new unknowns: the Reynolds Stresses.

---

[3] New models describe the turbulent flow as chaotic with underlying structure

1.6.1 Reynolds Averaged Navier Stokes (RANS) Equations

The instantaneous continuity and Navier-Stokes equations for incompressible flow can be solved directly by Direct Numerical Simulation (DNS). However, this technique demands a very fine grid resolution as the Reynolds number increases, which in turn demands large computer resources (Speziale, 1991). Time averaging is a procedure used to solve the Navier-Stokes equations for the mean velocity field with time averaged fluctuations, which for most engineering purposes is acceptable. In order to simplify the notation, suffix notation has been used here. The convention of this notation is that i (or any other suffix) takes the values 1, 2, or 3, which correspond to the x, y or z directions, respectively.

The time averaged continuity equation is

$$\nabla \bullet \mathbf{U} = \frac{\partial U_1}{\partial x_1} + \frac{\partial U_2}{\partial x_2} + \frac{\partial U_3}{\partial x_3} = 0 \tag{1.16}$$

The time averaged momentum equations are written as

$$\frac{\partial(\rho U_i)}{\partial t} + \nabla \bullet (\rho U_i \mathbf{U}) = -\frac{\partial P}{\partial x_i} + \mu \nabla^2 U_i + \nabla \bullet \left(-\rho \overline{u_i' \mathbf{u}'}\right) \tag{1.17}$$

where **u** is a velocity vector with x-component u_1, y-component u_2, and z-component u_3. The time-averaged equations, called the Reynolds Averaged Navier-Stokes (RANS) equations; contain six additional terms called Reynolds stresses. Three of these are the **normal stresses**, $\tau_{ii} = \rho \overline{u_i' u_i'}$ and the others are **shear stresses**, $\tau_{ij} = \rho \overline{u_i' u_j'}$. The degree of difficulty of modeling the Reynolds stress terms depends on the complexity of the turbulence.

1.6.2 Turbulence Models

A turbulence model is a set of semi-empirical equations used to determine the turbulent transport terms and thus close the system of RANS equations to obtain the mean flow field properties and the Reynolds Stresses. During the last half century many models have been developed. The most common of these are implemented in commercial CFD codes: 1) the Spalart-Allmaras model, 2) the k-ε model with variants including: the Renormalization Group (RNG) k- ε model, realizable k-ε model, the k-ω model 3) Reynolds Stress Model (RSM) and 4) the Large Eddy Simulation (LES) model.

The Spalart-Allmaras model is a one equation model, which solves just one turbulent quantity, the turbulent kinetic energy, k, and specifies the mixing length *l*. The turbulent viscosity ($\mu_t \approx k^{0.5} l$) and the Reynolds Stresses are then determined using the turbulent viscosity hypothesis[4]. The k-ε model is considered a two equation model since it solves both the turbulent kinetic energy k and the turbulent energy dissipation rate ε. These two quantities are used to calculate a length scale ($l \approx k^{1.5}/\varepsilon$) and the turbulent viscosity ($\mu_t \approx k^2/\varepsilon$). The Reynolds Stresses are then obtained from the turbulent viscosity hypothesis. Extensions of the k-ε model have been developed to simulate more complex flows. Examples include the RNG k-ε model to describe swirling flow, the realizable k-ε model to predict jet flow, and the k-ω model to account for boundary-layer flow. In the eight equation Reynolds stress model, transport equations are solved for the individual Reynolds stresses and for the dissipation rate ε. Thus, the Reynolds stress model accounts

[4] The turbulent viscosity or Boussinesq hypothesis relates the Reynolds Stresses to the mean velocity gradients. The advantage of the Boussinessq hypothesis is the lower computational cost required to calculate the turbulent viscosity. The disadvantage of the turbulent viscosity hypothesis is that it assumes the turbulent viscosity is isotropic.

for the anisotropy of the flow since it does not require the turbulent-viscosity hypothesis. Finally, Large Eddy Simulation (LES) describes the large-scale unsteady motions, where the energy and anisotropy are simulated directly, and models the smaller scales, which are considered isotropic. LES uses a set of filtered equations derived from the Navier-Stokes equations to compute the large scale motion. The filtered equations have been treated to remove the eddies that are smaller than the size of the filter, usually taken as the mesh size which is in the inertial convective range. The filtering process generates new terms that are modeled to achieve closure.

Since a considerable number of models are available in CFD codes, a preliminary selection of the turbulent model is required. Selection of a model most suitable for UV reactor simulation was made using the following criteria:

1. Accurate description of similar flows,
2. Numerical stability and convergence,
3. Compatibility with the discrete phase model, DPM,
4. Implementation available with unstructured and structured grids,
5. Computer resources required in terms of memory and data storage, and
6. Time required for the simulation.

1.6.2.1 The k-ε Models

The standard k-ε model, developed by Launder and Spalding (1974), makes use of the eddy-viscosity, μ_{eff}, concept (Equation 1.18), and the approximation of Boussinesq (1877) (Equation 1.19), where the Reynolds Stresses, τ_{ij}, are linked to the mean rate of deformation. The k-ε model approximates the turbulent viscosity (Equation 1.23), as the

product of the velocity scale, u, (Equation 1.21), and the length scale, *l*, (Equation 1.22). The relevant equations are:

$$\mu_{eff} = \mu + \mu_t \tag{1.18}$$

$$\tau_{ij} = -\rho\overline{u_i' u_j'} = \mu_t\left(\frac{\partial U_i}{\partial x_j} + \frac{\partial U_j}{\partial x_i}\right) - \frac{2}{3}\delta_{ij}k \tag{1.19}$$

$$k = \frac{1}{2}\left(\overline{u_i'^2} + \overline{u_j'^2} + \overline{u_k'^2}\right) \tag{1.20}$$

if $u_i'^2 = u_j'^2 = u_k'^2$ then

$$u = \frac{2}{3}k^{1/2} \tag{1.21}$$

$$l = \frac{C_{ls}k^{3/2}}{\varepsilon} \tag{.122}$$

$$\mu_t = C_\mu \rho k^{1/2} l = C_\mu \rho \frac{k^2}{\varepsilon} \tag{1.23}$$

where

μ_{eff} = effective viscosity (kg/m s),

μ = dynamic viscosity (kg/m s),

C_μ = model parameter (= 0.09),

C_{ls} = model parameter (= 0.1) for isotropic turbulence, and

δ_{ii} = the Kronecker delta (δ_{ij}=1 if i=j and δ_{ij}=0 if i≠j).

The k-ε model relates the turbulent viscosity to the turbulent kinetic energy and the rate of dissipation of the turbulent kinetic energy per unit mass. The turbulent kinetic energy k (Equation 1.24) is derived from the Navier-Stokes equations:

$$\underbrace{\frac{\partial(\rho k)}{\partial t}}_{\text{rate of change}} + \underbrace{\nabla \bullet (\rho k \mathbf{U})}_{\text{convection}} = \underbrace{\nabla \bullet \left[\frac{\mu_t}{\sigma_k}\nabla k\right]}_{\text{diffusion}} + \underbrace{\mu_t\left(\frac{\partial U_i}{\partial x_j} + \frac{\partial U_j}{\partial x_i}\right)\frac{\partial U_i}{\partial x_j}}_{\text{production}} - \underbrace{\rho\varepsilon}_{\text{dissipation}} \qquad (1.24)$$

The rate of dissipation of the turbulent kinetic energy ε (Equation 1.25) is a semi-empirical equation, which assumes that the production and destruction terms in the ε equation are proportional to the production and destruction terms of the k equation.

$$\underbrace{\frac{\partial(\rho\varepsilon)}{\partial t}}_{\text{rate of change}} + \underbrace{\nabla \bullet (\rho\varepsilon \mathbf{U})}_{\text{convection}} = \underbrace{\nabla \bullet \left[\frac{\mu_t}{\sigma_\varepsilon}\nabla\varepsilon\right]}_{\text{diffusion}} + \underbrace{C_{1\varepsilon}\mu_t\frac{\varepsilon}{k}\left(\frac{\partial U_i}{\partial x_j} + \frac{\partial U_j}{\partial x_i}\right)\frac{\partial U_i}{\partial x_j}}_{\text{generation}} - \underbrace{C_{2\varepsilon}\rho\frac{\varepsilon^2}{k}}_{\text{destruction}} \qquad (1.25)$$

The k and ε equations enable us to evaluate the turbulent viscosity μ_t (Equation 1.23) in conjunction with the values for the constants in table 1.2. These values were determined by fitting experimental data from basic turbulent flows according Launder and Spalding (1974).

Table 1.2: Values of the constants in the k- ε model

C_μ	$C_{1\varepsilon}$	$C_{2\varepsilon}$	σ_k	σ_ε
0.09	1.44	1.92	1.0	1.3

The k-ε model has been used to simulate flow in a pipe and around a circular cylinder. The model gives good predictions of the flow in a pipe; and is capable of resolving the unsteady mean characteristics of vortex dominant flow around bodies (Koobus et al. 2000)

1.6.2.2 The Reynolds Stress Model

Prediction of flows with complex strain fields, where the local state of turbulence cannot be characterized by one velocity scale and where the individual Reynolds stresses

(Equation 1,19) cannot be related to a single velocity scale, demands solution of the Reynolds stress transport equations to account for the directional effects of the Reynolds stress field. Rodi (1984) presented the Reynolds stress equations to account for different velocity scales and for their proper transport:

$$\underbrace{\frac{\partial \overline{u_i' u_j'}}{\partial t}}_{\text{rate of change}} + \underbrace{U_k \frac{\partial \overline{u_i' u_j'}}{\partial x_k}}_{C_{ij}=\text{convection}} = \underbrace{\nabla \bullet \left(\frac{\mu_t}{\rho \sigma_k} \nabla \left(\overline{u_i' u_j'} \right) \right)}_{D_{ij}=\text{diffusion}} - \underbrace{\left(\overline{u_i' u_k'} \frac{\partial U_j}{\partial x_k} + \overline{u_j' u_k'} \frac{\partial U_i}{\partial x_k} \right)}_{P_{ij}=\text{stress production}}$$
$$+ \underbrace{\overline{\frac{p}{\rho} \left(\frac{\partial u_i'}{\partial x_j} + \frac{\partial u_j'}{\partial x_i} \right)}}_{\Pi_{ij}=\text{pressure strain}} - \underbrace{\frac{2}{3} \varepsilon \delta_{ij}}_{E_{ij}=\text{disspation}} \underbrace{- 2\omega_k \left(\overline{u_j' u_m'} e_{ikm} + \overline{u_i' u_m'} e_{jkm} \right)}_{\Omega_{ij}=\text{rotation}} \tag{1.26}$$

Equation (1.26) expresses six partial differential equations: one for the transport of each of the six independent Reynolds stresses. A comparison between the transport equation for the turbulent kinetic energy (Equation 1.24) and the above equation shows that there are two additional terms in the Reynolds stress equations: the pressure strain correlation and the rotation term. In order to solve Equation (1.26), it is necessary to provide models for the dissipation, diffusion and pressure correlation terms. At high Reynolds numbers, the model assumes local isotropy for the small dissipative eddies, so that the anisotropy affects only the normal component of the Reynolds stresses. In this case the dissipation term reduces to $E_{ij} = 2/3\varepsilon\delta_{ij}$. The diffusion term D_{ij} is modeled using the assumption that the rate of transport of Reynolds stresses by diffusion is proportional to the gradients of Reynolds stresses.

The pressure strain interaction is the most important term in Equation (1.26). Its overall effect is to re-distribute energy amongst the normal Reynolds stresses. This effect on the Reynolds stresses is caused by three distinct physical processes: interaction of the fluctuation velocities $\Pi_{ij,1}$, interaction of the mean strain and fluctuating velocities $\Pi_{ij,2}$

and correction for the influence of wall proximity on the pressure strain term $\Pi_{ij,w}$.

Launder et al. (1975) introduced the following models that account for the effects of the pressure strain terms:

$$\Pi_{ij,1} = -C_1 \frac{\varepsilon}{k}\left(\overline{u_i' u_j'} - \frac{2}{3}k\delta_{ij}\right) - C_2\left(P_{ij} - \frac{2}{3}P\delta_{ij}\right) \tag{1.27}$$

$$\Pi_{ij,2} = -C_2\left[\left(P_{ij} + \Omega_{ij} - C_{ij}\right) - \frac{2}{3}\delta_{ij}\left(\frac{1}{2}P_{kk} - \frac{1}{2}C_{kk}\right)\right] \tag{1.28}$$

$$\begin{aligned}\Pi_{ij,w} = {} & C_1' \frac{\varepsilon}{k}\left(u_k' u_m' n_k n_m \delta_{ij} - \frac{3}{2}u_i' u_k' n_j n_k - \frac{3}{2}u_j' u_k' n_i n_k\right)\frac{k^{0.5}}{C_l \varepsilon d} \\ & + C_2'\left(\Pi_{km,2} n_k n_m \delta_{ij} - \frac{3}{2}\Pi_{ik,2} n_j n_k - \frac{3}{2}\Pi_{jk,2} n_i n_k\right)\frac{k^{0.5}}{C_l \varepsilon d}\end{aligned} \tag{1.29}$$

where

n is the unit normal to the wall,

d is the normal distance to the wall, and

$C_l = C_\mu^{0.75}/\kappa$ and κ is the von Karman constant (0.4187).

The rotation term is given by:

$$\Omega_{ij} = 2\omega_k\left(\overline{u_j' u_k'} e_{ikm} + u_i' u_m' e_{jkm}\right) \tag{1.30}$$

where

ω_k is the rotational vector, and e_{ijk} is the alternating symbol,

e_{ijk}=+1 if i,j and k are different and in cyclic order, e_{ijk}=-1 if i,j and k are different and in anti-cyclic order and e_{ijk}=0 if any two indices are the same.

The turbulent kinetic energy k for this model is obtained by adding the three normal stresses together, Equation (1.20).

The closure problem for the RANS is solved with the six equations for the Reynolds stress transport Equations (1.26) to (1.30), the turbulent kinetic energy Equation (1.20)

and the scalar dissipation rate ε, Equation (1.25). The constant values required for this model are presented in Table 1.3.

Table 1.3: Values of the constants in the RSM model

C_μ	$C_{1\varepsilon}$	$C_{2\varepsilon}$	σ_k	σ_ε	C_1	C_2	C'_1	C'_2
0.09	1.44	1.92	0.82	1.3	1.8	0.6	0.5	0.3

The Reynolds stress model has been used successfully to reproduce experimental data for flow in a 90° and 180° pipe bend (Sierra-Espinoza et. al., 2000 and Kumar and Pavithran, 1999). The model is also able to predict the correct mean drag coefficient, but under predicts the length of the circulation region of a flow passing bluff bodies (Franke and Rodi, 1993)

1.6.2.3 Large Eddy Simulation Model

Large eddy simulation is based on the explicit computation of large scale motions, where the smallest scales are represented by a model. LES decomposes the instantaneous velocity vector **u** into the sum of filtered component **U** (the mean velocity plus large scale fluctuations) and the residual component **u'** (the small scale fluctuation velocity). To filter the fluid velocity, a filter must be selected. Fortunately, several filters have been proposed. Their mathematical descriptions are beyond the purpose of this research. However, general comments can be made about the filtering process. Once a filter function is selected, the mean velocity U is a weighted average of u about the physical point x. As the averaging radius of the filter tends to zero the points near x are weighted more and more heavily so that **U** tends to **u**.

Filtration of Navier-Stokes equations gives rise to unknown terms similar to the ones discussed in the RANS equations. The general approach to the closure problem is again based on an eddy viscosity model. The most commonly used eddy viscosity model in LES is the Smagorinsky model (Pope, 2000), which is improved through the Kolmogorov-Prandtl relation to provide a much less dissipative model.

Large Eddy Simulation has been shown to be more suitable for describing the very complex unsteady behavior of flow passing bluff bodies than any of the RANS calculations; however, the cost of better simulation of the details of the flow was 36 times the computational time required for RANS calculations (Rodi, W., 1998). Large Eddy Simulation has also been applied to pipe flow with accurate prediction of the turbulent intensity and Reynolds Stresses (Yang, Z.Y., 2000)

1.6.2.4 Turbulence Models -Summary

Recalling the selection criteria from section 1.7.2, the properties of the various turbulence models are summarized in Table 1.4

Table 1.4: Summary of general characteristics of various turbulence models

Criteria	SA	k-ε	RSM	LES
Accurate description of similar flows	No	Yes	Yes	Yes
Numerical Stability & convergence	Yes	Yes	No	Yes
Compatibility with DPM	No	Yes	Yes	No
Implementation available with unstructured & structured grids	Yes	Yes	No	Yes
Computer resources required in terms of memory and data storage	Yes	Yes	No	No
Time required for the simulation	Yes	Yes	No	No

The Spalart Allmaras model is a one-model equation that solves for the turbulent kinetic energy k. This model is restricted to high Reynolds number flows and is not

applicable to the viscous sublayer near walls (Rodi 1984). This model is incapable of describing flows with separation and recirculation. Moreover, the discrete phase model cannot be applied if the continuous phase is solved by the Spalart Allmaras model. Therefore, the Spalart Allmaras model cannot be used for simulation of UV reactors.

The k-ε model and its variants describe the turbulence in more detail through two transport equations: one for the rate of dissipation of the turbulent kinetic energy ε and another for the turbulent kinetic energy k. This model is built under the assumption that the turbulent viscosity μ_t is locally isotropic[5] at high Reynolds numbers. The k-ε model will be considered as a potential model for UV reactor simulation in the next section.

In the RSM model, each of the Reynolds stress is modeled separately. The resulting partial differential equations (PDEs) are solved in conjunction with the transport equation for the rate of dissipation of the turbulent kinetic energy, ε. The solution of these seven PDEs increases the computational time of the simulation. Several researchers have reported numerical diffusion in the RSM model when it is used with an unstructured triangular mesh (Slack M, Prasad R 2000, Mori G & Razore S, 2001). Nonetheless, the RSM model will be used in this research to solve the velocity field in UV reactors because anisotropy in the flow field may impact the microorganism trajectory and thereby the dose received by each microorganism.

LES is a model where the time dependent flow equations are solved for the mean flow of the largest eddies and where the effect of the small eddies are modeled. LES is too costly in terms of calculations and computer resources to be considered as a potential model for hydrodynamic characterization of large UV reactor. In addition the LES model

[5] local isotropy occurs when fluctuations have no directional preferences at limited range of eddy sizes, Kresta and Brodkey (2003).

is not compatible with the discrete phase models available in Fluent 6.1. Nevertheless, the LES model will be used in a limited way in this study in order to contrast the flow field results between models.

1.7 Discrete Phase Model

The Discrete Phase Model (DPM) is used to simulate particle dispersion due to turbulent motion in the carrier fluid. The movement of a particle is estimated through a Lagrangian equation, which uses the previous computed mean flow velocity and a random fluctuation velocity in the continuous phase to estimate the instantaneous velocity of the particle. The core of the model is the specification of the fluctuating continuous fluid velocity and the drag force on the particle, since these determine the extent of particle dispersion by establishing the relative velocity between the two phases. Therefore, the velocity history indirectly fixes the exchange of momentum between the dispersed and continuous phases since the fluid properties surrounding the particle depend on where in the continuous flow field the particle was transported by the instantaneous velocity of the fluid in previous time steps.

1.7.1 Lagrangian Approach to Discrete Phase

The Lagrangian approach considers the discrete phase as single spherical particles, subjected to a volume fraction less than 0.1%. Under this assumption the particle–particle interaction can be neglected (Tanka, T and Tsuji Y., 1991). Therefore, the main governing equations for the Lagrangian description of particle motion start with the equation for a single particle (Chen X. Pereira J. 2000) of the i^{th} class:

$$\frac{d\mathbf{u}_p}{dt} = F_D + F_G + F_{AM} + F_{LF} \tag{1.31}$$

The drag force between the particle and fluid, F_D, accounts for the flow force exerted on a particle in the direction of the flow:

$$F_D = \frac{1}{\tau_p}\left(\mathbf{u} - \mathbf{u}_p\right) \tag{1.32}$$

The gravitational force, F_G, accounts for the acceleration associated with external forces:

$$F_G = g\left(1 - \frac{\rho}{\rho_p}\right) \tag{1.33}$$

The added mass force, F_{AM}, accounts for the inertia of the fluid which a particle displaces as it is accelerating:

$$F_{AM} = \frac{\rho}{2\rho_p}\frac{d}{dt}\left(\mathbf{u} - \mathbf{u}_p\right) \tag{1.34}$$

The lift force, F_{LF}, accounts for the force induced on a particle by a gradient in local carrier-fluid velocity:

$$F_{LF} = \frac{3.0884}{\rho_p d_p}\sqrt{\rho\mu\left|\frac{\partial u_j}{\partial x_m}\right|}\left(\mathbf{u} - \mathbf{u}_p\right)\delta_{mi}\left(1 - \delta_{mi}\right) \tag{1.35}$$

The particle relaxation time τ_p accounts for the drag response time of a particle:

$$\tau_p = \frac{4}{3\mu}\frac{\rho_p d_p^2}{Re_p C_D} \tag{1.36}$$

The drag force coefficient C_D is determined as follows:

$$C_D = \frac{24}{Re_p}\left(1 + 0.15 Re_p^{0.687}\right) \tag{1.37}$$

The relative Reynolds number between the two phases, Re_p, is defined as:

$$Re_p = \frac{\rho_p D_p |\mathbf{u} - \mathbf{u}_p|}{\mu} \tag{1.38}$$

In Equations 1.34 to 1.41

d_p = particle diameter of size i

$\mathbf{u}_p$ = the instantaneous velocity vector of the particles

μ = the molecular viscosity

$\mathbf{u}$ = the instantaneous velocity vector of the continuous phase

ρ_p = density of the particle

ρ = density of the fluid

g = gravitational force

δ_{ij} = Kronecker delta ($\delta_{ij} = 1$ if $i = j$ and $\delta_{ij} = 0$ if $i \neq j$)

In the above equations, the added mass accounts for the inertia of the fluid which a particle displaces as it is accelerating. The lift force accounts for the force induced on a particle by a gradient in local carrier-fluid velocity.

Two approaches have been proposed to estimate the flow field velocity experienced by a particle; the random walk and the stochastic differential models. The random walk model computes the velocity as the sum of the mean fluid velocity and a random fluctuating velocity which is evaluated either from the local turbulent kinetic energy or the Reynolds stresses. The stochastic differential model computes the fluctuation and mean fluid velocities through a stochastic differential equation. It has been found that the stochastic differential model provides a better representation of the particle dispersion and uniform particle distribution than the random walk model for inhomogeneous flows (MacInnes and Bracco, 1992). However, the stochastic differential model has not yet

been implemented in commercial CFD codes, thus UV reactor designers are typically forced to use the Discrete Random Walk (DRW) model.

1.7.2 Discrete Random Walk (DRW) Model

The random walk model was designed to describe the velocity history of a particle transported by a turbulent flow. The first version of the random walk model proposed random increments in space for particles in addition to the convection increments due to mean motion in a three-dimensional numerical solution of the flow field. The fluctuation in each coordinate direction was sampled for each time step, δt, from a Gaussian distribution, with a zero mean and a standard deviation $\sigma_{\delta t}=(2D_p\delta t)^{0.5}$. D_p is the effective diffusivity of the particles in turbulent flow. Thus the characteristic velocity, equal to $\sigma_u=(2D_p/\delta t)^{0.5}$, becomes infinite as the time step, δt, approaches zero. This result is clearly non-physical.

Yuu et al. (1978) considered that since the instantaneous fluid velocity, u, given by Equation (1.15) is the sum of the local mean fluid velocity, U, and the fluctuating velocity, u', a new fluctuation velocity should be used only after a finite time called the Lagrangian integral time scale, τ_L has elapsed[6]. Each of the fluctuation velocities are sampled independently from a Gaussian distribution, ζ, having zero mean and variance corresponding to the particular component and recalculated for every eddy breakup.

In turbulent anisotropy, the local Reynolds stresses are used to evaluate the velocity fluctuations

$$u'_i = \zeta\sqrt{\overline{u_i'^2}} \qquad (1.39)$$

[6] Discrete Random Walk (DRW) model estimates a fluctuating velocity that is discontinuous in time because a sample velocity fluctuation remains fixed until the eddy time has elapsed.

Whereas in turbulent isotropic flow

$$u'_i = \zeta\sqrt{\overline{u_i'^2}} = \zeta\sqrt{\frac{2}{3}k} \qquad (1.40)$$

It should be stressed that careful selection of the time step is the key to obtaining reasonable and accurate particle tracking results. Generally, the time step selected must be smaller than the particle relaxation time, τ_p, (Equation 1.36) and the eddy lifetime, τ_e, which is given by the k-ε turbulence model;

$$\tau_e = 2\tau_L = 2C_L\frac{k}{\varepsilon} \approx 2*0.15\frac{k}{\varepsilon} \qquad (1.41)$$

where, τ_L is the Lagrangian time, C_L is the Lagrangian empirical constant (in the range 0.03-0.63), and k and ε are the turbulent kinetic energy and its dissipation rate, respectively. It should be emphasized that the particle is not allowed to pass through a computational volume in one time step. The reported values of the Lagrangian empirical model constant (C_L) vary by one order of magnitude (Table 1.5)

Table 1.5: Reported values of the Lagrangian time scale in homogeneous turbulence (from MacInnes and F.V. Bracco, 1992)

Theoretical Studies	$C_L = \tau_L/(k/\varepsilon)$
Boysan et al. (1982)	0.06
Shuen et al (1993)	0.10
Zhou and Leschziner (1991)	0.16
Haworth and Pope (1987)	0.63
Experimental studies	
Snyder and Lumley (1971)	0.45
Calabrese and Middleman (1979)	0.36
Mostafa and Elghobashi (1986)	0.35
Wells and Stock (1983)	0.16

Ormancey and Martinon (1984) suggested that an eddy time determination according to the Poisson process has an average eddy change frequency of $1/\tau_L$. This model is

implemented with good accuracy by selecting a random number, r, with uniform distribution on [0, 1]:

$$\tau_e = -\tau_L \log(r) \qquad 0 < r < 1 \tag{1.42}$$

1.7.3 Simulation of the Particle Trajectories

Simulation of the particle trajectory implies integration in time of the force balance on the particle (Equation 1.31). The trajectory equations in Fluent are solved by stepwise integration over discrete time steps. Integration of Equation (1.31) in time yields the velocity of the particle at each point along the trajectory, with the trajectory itself predicted by:

$$\frac{d\mathbf{x}_p}{dt} = \mathbf{u}_p \tag{1.43}$$

Discretized forms of Equations (1.31) and (1.43) are solved in each coordinate direction to predict the trajectory of the discrete phase.

Assuming that the term containing the body force remains constant over each small time interval, and linearizing any other forces acting on the particle, the trajectory equation can be written as:

$$\frac{d\mathbf{u}_p}{dt} = \frac{1}{\tau_p}\left(\mathbf{u} - \mathbf{u}_p\right) \tag{1.44}$$

Fluent uses a trapezoidal scheme for integrating Equation (1.44):

$$\frac{\mathbf{u}_{p,n+1} - \mathbf{u}_{p,n}}{\Delta t} = \frac{1}{\tau_p}\left(\mathbf{u}_{\cdot} - \mathbf{u}_{p,n+1}\right) \tag{1.45}$$

where n represents the iteration number and

$$\mathbf{u}_{\bullet} = \frac{\mathbf{u}_n + \mathbf{u}_{n+1}}{2} \tag{1.46}$$

$$\mathbf{u}_{n+1} = \mathbf{u}_n + \Delta t \mathbf{u}_{p,n} \bullet \nabla \mathbf{u}_n \tag{1.47}$$

Equations (1.45) and discretized form of Equation (1.43) are solved simultaneously to determine the velocity position of the particle at a given time. The steps used for the integration of the particle trajectory are summarized in Figure 1.5. The accuracy of the discrete phase computation depends on the time step used for the integration. Therefore, the time step, Δt, is selected from the lowest of the eddy time, the relaxation time, and the time estimated through the Courant number, Co, defined as the time for a particle to move only a fraction of the grid spacing, Δx, in a time step (Pope S.B. 2000):

$$\mathrm{Co} = \frac{k^{1/2}\Delta t}{\Delta x} = \frac{1}{20} \tag{1.48}$$

An additional numerical control is implemented in Fluent to abort the particle trajectory calculation when the particle never exits the domain. This numerical control is called the maximum number of time steps, n_{max}. The calculation is stopped once this number of calculations has been executed.

1.7.4 Limitations of the DRW Model

Despite the use of the Lagrangian approach in UV reactor design, the adequacy of the model for estimation of microorganism inactivation is not known. Two questions can be asked: 1) Can the DRW model predict the particle dispersion rate realistically in a UV reactor? and 2) Can the DRW model maintain a uniform particle distribution in inhomogenuous flow?

To address the first question MacInnes and Bracco (1992) conducted a comprehensive study of the dispersion rate for several discrete phase models. Their study used the expression for the dispersion rate in turbulent flow derived by Taylor:

$$\frac{dy^2}{dt} = \int_0^t R(\tau)d\tau \tag{1.49}$$

$$R(\tau) = \frac{\overline{u_p(t)u_p(t+\tau)}}{\overline{u_p}^2} \approx e^{-\tau/\tau_L} \tag{1.50}$$

where

y^2 = dispersion,

dy^2/dt = dispersion rate,

$R(\tau)$ = correlation function of the particle velocity, and

τ_L = integral time scale.

The correlation function was approximated by Taylor with an exponential function that describes the dispersion rate of various particles, as tested by Snyder and Lumley (1971).

MacInnes and Bracco (1992) found that for the random walk models which determine the eddy lifetime according to Equation (1.41), the correlation function, $R(\tau)$, decreases linearly towards zero at the maximum possible correlation time of τ_e. Therefore, the linear function (Equation 1.52) overestimates the dispersion unless the Lagrangian time is reduced:

$$R(\tau) = \begin{cases} 1-(\tau/2\tau_L) & 0 \le \tau \le 2\tau_L = \tau_e \\ 0 & \tau > 2\tau_L = \tau_e \end{cases} \tag{1.51}$$

$$\overline{y^2} = \begin{cases} \overline{u_p^2}t^2(1-t/6\tau_L) & 0 \le \tau \le 2\tau_L = \tau_e \\ 2\overline{u_p^2}\tau_L(t-2\tau_L/3) & \tau > 2\tau_L = \tau_e \end{cases} \tag{1.52}$$

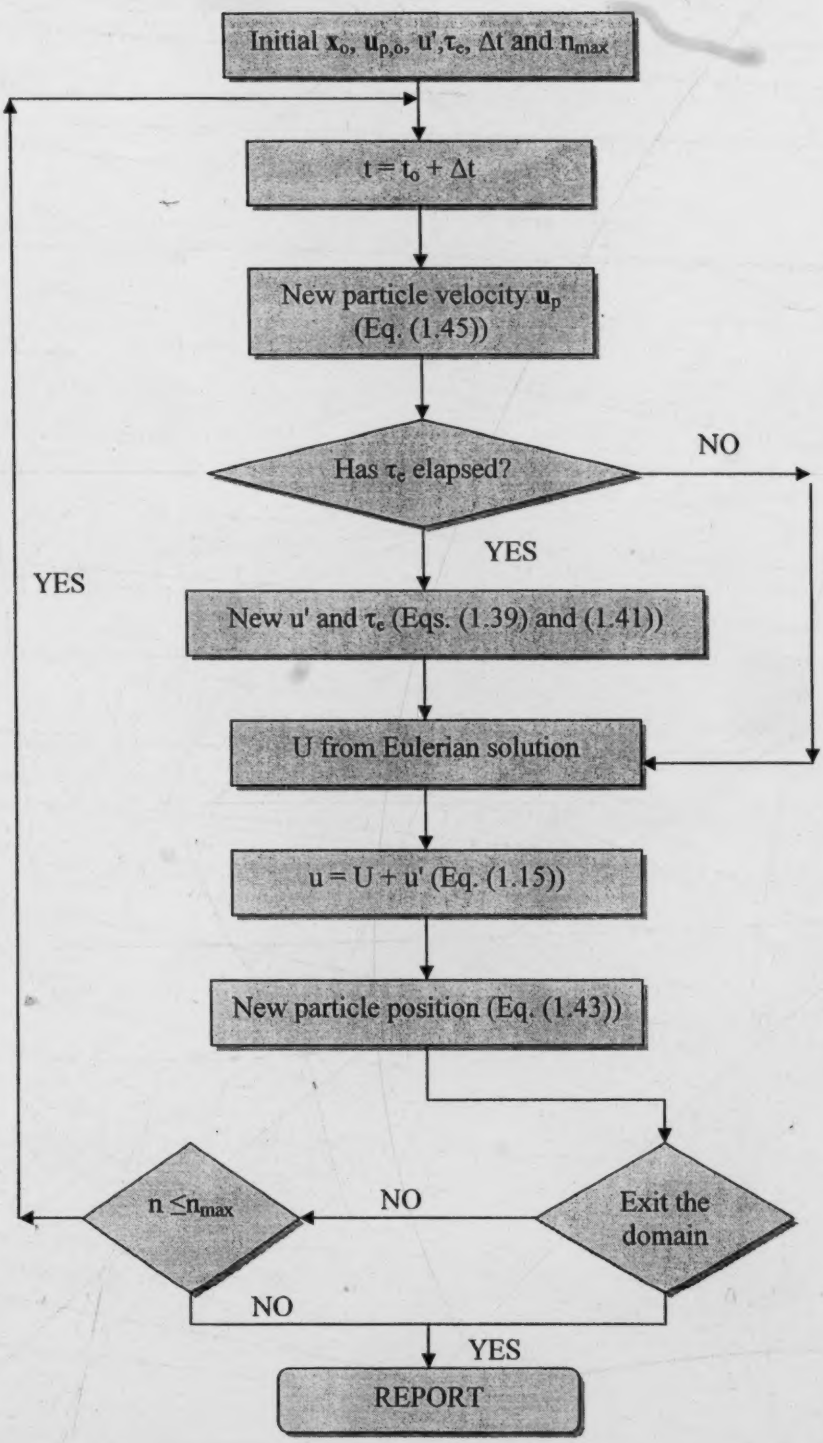

Figure 1.5: Flow chart for computing particle trajectories in a discontinuous random walk model (Adapted from MacInnes and F.V. Bracco 1992)

For the Random Walk Model, which determines the eddy lifetime according to the random eddy time τ_e (Equation 1.42), the correlation function is exponential, and underestimates the dispersion (Equation 1.53).

$$\overline{y^2} = \overline{u_p^2}\left[2\tau_L t - 2\tau_L^2\left(1 - e^{-t/\tau_L}\right)\right] \tag{1.53}$$

The greatest difference between the two correlation functions occurs at time, $t = 2\tau_L$, where the variance of the exponential function is about 20% less than that for the linear correlation. MacInnes and Bracco (1992) emphasized the relevance of the integral time scale in the dispersion rate estimation; a model with same correlation function but a different Lagrangian time yields a different dispersion rate.

With respect to the second question, MacInnes and Bracco (1992) found that the random walk model reproduces the mean velocity distribution with reasonable accuracy; however, it is unable to predict uniform mass density distribution. Therefore, the random walk model cannot accurately predict the particle momentum distribution in a mixing layer or in an axisymmetric jet, although the normalized fluctuation component is taken into account in the model. In other words, the DRW model accumulates particles in regions of low turbulence intensity and depletes particles from regions of high intensity.

1.7.5 Integration of the Dose

The discrete phase model predicts only the spatial and temporal position of a particle or microorganism, not the accumulated dose received. To compute the total radiant energy passing from all directions through a microorganism as it is moved along its trajectory, it is necessary to implement a function that combines the microorganism position information with the fluence rate field. This function integrates the product of

the average UV fluence rate and the time step at each step over the residence time of the microorganism.

$$D = \sum_{t=0}^{t=\infty} \frac{(E'_{t-1} + E'_t)}{2}(\Delta t) \qquad (1.54)$$

Equation (1.54) is implemented in Fluent through a User Defined Function (UDF). This function allows a C code to be dynamically loaded with the Fluent solver (Appendix B). This UDF is called at the start of the particle integration and then after each time step for a particle trajectory calculation. For steady state simulations, particle trajectories are estimated one at a time; whereas for unsteady state simulations, all the particle trajectories are advanced at the end of each time step of the continuous phase solution.

A UV dose distribution is generated after computing a large number of particle trajectories. The dose histogram is created by ranking the dose data in ascending order. To estimate the overall survival ratio is normalized by the total area under the curve.

1.8 Microorganism Response to UV Radiation

The predicted UV dose only represents the total energy passing through a given microorganism in the wavelength range of 200 to 300 nm, not the level of microorganism inactivation. It is necessary to develop a relationship between the inactivation and UV dose for a particular microorganism.

1.8.1 Microorganism Inactivation Models

The UV dose response curve of a microorganism may follow one of three typical shapes including first order, tailing and shoulder as shown in Figure 1.6. Frequently, the

microorganisms' response to UV radiation is first order, and the microorganisms undergo an exponential inactivation:

$$\frac{N}{N_o} = e^{-k_r D} \tag{1.55}$$

where k_r is the first order inactivation coefficient of the microorganism.

Other microorganisms present a slow response to UV radiation, producing a shoulder at low UV doses followed by near-exponential inactivation. The multi-target and the series event models were proposed by Severin et al. (1983) to describe this type of UV dose response.

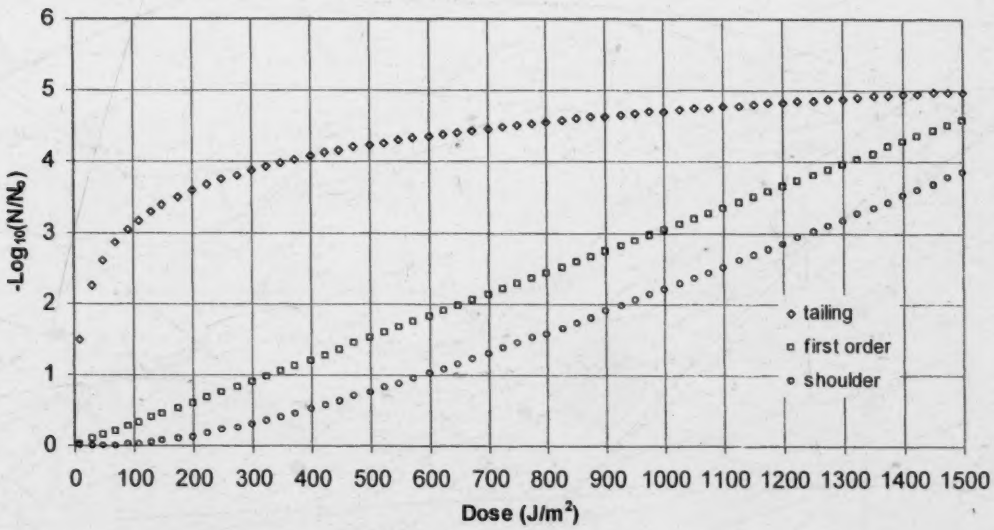

Figure 1.6: Typical UV dose response curves

The multi-target model assumes that a particle contains a finite number of discrete targets, n_c, each of which must be hit prior to full inactivation of the particle. Since the number of targets is finite, the probability of attaining a hit on the particle is decreased as the reaction proceeds. For a batch reactor, the multi-target model is given by:

$$\frac{N}{N_o} = \left[1 - \left(1 - e^{-k_r D}\right)^a\right] \tag{1.56}$$

where k_r is the multi-target inactivation coefficient of the microorganism, and a is the intercept of the exponential region of the dose-response with the y-axis.

The series-event model assumes that a microorganism collects discrete units of damage, called events, as it is exposed to a UV fluence rate field. If a microorganism collects a number of events higher than the threshold of damage, n_d, it is inactivated. In contrast, if the microorganism receives less than the threshold number of damage, n_d, it may retain its reproducibility. For a batch reactor, the series event model is given by:

$$\frac{N}{N_o} = e^{-k_r D} \sum_{i=0}^{n-1} \frac{(k_r D)^i}{i!} \tag{1.57}$$

where, i is the index for the event level, and k_r is the series event inactivation coefficient of the microorganism.

The series-event and the multi-target models become the first-order model if the number of events or targets is equal to one. Table 1.6 summarizes the kinetic inactivation constants reported for some microorganisms used to test the series event model. Severin et al. (1983) concluded that although both models agree with experimental data, there was not sufficient proof to conclude that mechanistically one model is better than the other.

Table 1.6: Kinetic inactivation constants for series event model based on batch data

Study	Microorganism	Number of events (n)	kr (m2 W-1s-1)	Regression coefficient
Severin, 1983	E. coli	9	0.1538	$r^2 = 0.967$
Severin, 1983	C parapsilosis	15	0.0891	$r^2 = 0.965$
Severin, 1983	f2 virus	1	0.00724	$r^2 = 0.986$
Chiu, 1999	Fecal Coliform	1	0.1107	RSS = 1.045

Other microorganisms present a decrease in the inactivation rate after a certain degree of inactivation has been reached. This is termed tailing. Equation (1.56) was proposed by Craik et al. (2001) to provide an empirical relationship for this type of UV dose response. These empirical relationships were developed for *Cryptosporidium parvum* and *Giardia muris*:

$$-\log_{10}\frac{N}{N_o} = \log_{10} C_k + k_{df} \log_{10} D \tag{1.58}$$

where

k_{df} = empirical curve-fit parameter

C_k = intercept with the y-axis of the logarithmic data fit kinetic

In addition, Craik et al. (2001) provided potential explanations of the tailing effect. These are: 1) the presence of a very resistant parasite subpopulation, 2) an artifact of the experimental conditions, 3) the high concentration of microorganisms increases the absorbance of the suspension, and 4) formation of microorganism aggregates that shield UV radiation.

1.8.2 Equivalent Dose

The concept of an equivalent dose[7], D_{eqv}, can be defined by relating the computed inactivation in the UV reactor to the UV dose-inactivation relationship. The equivalent dose can be expressed mathematically for a first-order microorganism response by substituting Equation (1.55) into Equation (1.3):

$$\frac{N}{N_o} = e^{-k_r D_{eqv}} = \sum_{i=0}^{\infty} f_i \, e^{-k_r D_i} \tag{1.59}$$

[7] This document considers the Equivalent Dose as the weighted average of the dose distribution and the RED as the experimental average dose determined from biodosimetry

where f_i stands for the fraction of particles receiving dose D_i. Since the area under the dose distribution curve must be equal to one, $\sum_{i=0}^{i=\infty} f_i = 1$. The equivalent dose delivered by the reactor can be determined by solving Equation 1.59:

$$D_{eqv} = -\frac{1}{k_r} \ln\left[\sum_{i=0}^{\infty} f_i \, e^{-k_r D_i}\right] \tag{1.60}$$

A similar procedure can be used to express the equivalent dose for a non-linear equation like Equation (1.58).

$$\log_{10} D_{eqv} = \frac{1}{k_{df}} \log_{10}\left(\frac{1}{\sum_{i=1}^{\infty} \frac{f_i}{D_i^{k_{df}}}}\right) \tag{1.61}$$

Equations (1.60) and (1.61) show that the equivalent dose is a function of UV dose and the inactivation rate constant k_r or k_{df}. This means the D_{eqv} depends on the microorganism unless the dose distribution is very narrow (Wright and Lawryshyn, 2000). Since the equivalent dose varies with the microorganism selected for the calculation, the results of this study will be reported based on a commonly used challenge microorganism in order to provide comparison with potential future biodosimetry testing. The F-specific RNA coliphage MS2 is often selected for biodosimetry because:

1. MS2 is a single-strand RNA virus and consequently its dose response curve for UV inactivation follows first order kinetics (Harm, 1980).
2. The structure and size of MS2 is similar to the human enteroviruses.
3. MS2 has a relatively high UV resistance, comparable to that of bacterial spores (Harm, 1980).

4. MS2 is not pathogenic to humans, so it can be used for calibration of full-scale reactors without additional safety measures.
5. The organism is easily cultivable in titres up to 10^{12} pfu/ml, which makes it useful for calibration of full-scale reactors over other recommended microorganism such us *Bacillus subtilis* spores. The later can only be cultured up to 10^{8} cfu/ml (Qualls and Johnson, 1983).
6. The microorganism is easy to seed and enumerate, and provides consistent and reproducible results.

In order to standardize the use of MS2 coliphage as a challenge microorganism in validation tests, the NWRI and the AWWARF specified that the UV dose response of the MS2 phage should fall between the limits of Equation (1.62) and (1.64) in the UV dose range from 200 to 1500 J/m^2. This region was established after regression analysis of compiled data showed that an appropriated experimental protocol should yield a dose-response curve that meets this criterion, (Blatchley et al. 2000).

$$-\log_{10}\left(\frac{N}{N_o}\right) = 0.0040D + 0.64 \qquad (1.62)$$

$$-\log_{10}\left(\frac{N}{N_o}\right) = 0.0033D + 0.20 \qquad (1.63)$$

where D must be expressed in J/m^2.

The equivalent dose results presented in the next chapter were estimated with Equation (1.64), which is an average of Equations (1.62) and (1.63)

$$-\log_{10}\left(\frac{N}{N_o}\right) = 0.00365D + 0.42 \qquad (1.64)$$

1.9 Problem Statement

UV disinfection has proven to be a feasible method for reduction of pathogens in drinking water under controlled laboratory conditions. However, a current limitation of UV technology in drinking water facilities is the complexity of UV dose prediction or measurement in large UV reactors. As a result, computer modeling has been proposed as an alternative technique to evaluate the performance of UV reactors. One approach is to use Computational Fluid Dynamic (CFD) codes to predict microorganism trajectories in the UV fluence rate field and thus to estimate the UV dose received by each microorganism.

CFD analysis may provide a better understanding of the critical issues that affect the performance of UV reactors, such as short circuiting of microorganisms and excessive head loss. CFD analysis suits the needs of UV equipment designers since the large flow rate in drinking water facilities makes it very expensive and time consuming to perform experimental testing. In addition, CFD analysis allows simulation of the actual size of the UV reactors, which is virtually impossible to scale down to a lab scale model due to the non-uniform fluence rate and hydrodynamic characteristics. Another advantage of CFD analysis is the flexibility it provides for predicting the performance of a UV reactor under changing hydrodynamic conditions, fluence rate distributions, or UV dose microorganism responses.

The main drawback to the acceptance of CFD analysis in the water treatment industry is the need for validation of the CFD approach. Although manufacturers and consultants working with UV equipment use CFD as a design tool, they do not publish the CFD results in open literature because the detailed work is proprietary. Therefore,

independent assessment of CFD has not been done due to the lack of technical information.

Adoption of CFD analysis by regulatory agencies has been delayed due to the uncertainty of the UV dose prediction, the lack of objective validation studies of CFD predictions, limited awareness of the inherit limitations of CFD modeling, and a scarcity of information about the sensitivity of the results to the adjustable parameters in the CFD models. Consequently, a critical study of the use of CFD for prediction of UV reactor performance is needed in order to standardize this technique and prove or disprove the validity of CFD analysis as a design and validation tool.

This investigation aims to

1. Develop a 3-D computational model to calculate the UV dose for large UV reactors.
2. Evaluate the performance of a commercial UV reactor (Sentinel™ UV disinfection System 6 x 20kW, 48 inch diameter manufactured by Calgon Carbon Corporation) using the model.
3. Use the CFD analysis to understand the effect of hydrodynamics on the performance of UV reactors.
4. Identify the critical design and computational factors affecting the UV dose calculations.
5. Investigate alternative reactor designs to achieve higher efficiency than the Sentinel UV reactor, and to maximize lamp performance and lifetime.

2 CFD Methodology and Validation

One of the problems in the study of large UV reactors is how to assess the accuracy of CFD simulations. Despite the use of CFD to simulate small UV reactors, there is almost no information on how CFD solutions were verified or validated (i.e. Wright and Hargreaves 2001, Rokjer et al. 2002 and Lem 2002). Here the term '**verification**' is used for testing the ability of the discrete computational scheme to provide an accurate solution of the underlying differential equations. The term '**validation**' is used for testing the plausibility of the model as whole (Hardy et al. 2003) as an accurate representation of physical reality. Verification involves eliminating coding errors as well as errors associated with spatial discretization and numerical solution. Once these errors are eliminated validation concentrates on boundary conditions, initial conditions, and key model equations (e.g. turbulence closure and fluence rate distribution). Ideally, all of these elements of the models are directly compared with experimental data. The credibility of a CFD solution for a large UV reactor is difficult to evaluate due to the difficulty in measuring the flow field and the inactivation. In this work the CFD solutions were validated in an empty pipe before the more difficult semi-implicit calculation in a large UV reactor was attempted. The accuracy of the flow field predicted in an empty pipe was assessed by comparison with reliable experimental results. Validation of the User Defined Function (UDF) used to calculate the dose distribution was performed by comparison with appropriate analytical solutions. Verification of the fluence rate distribution predicted with UVCalc3D_200 was completed by comparison with a calculation for a single point.

2.1 Ultraviolet Reactor Description

The geometry selected for the CFD analysis, shown in Figures 2.1 and 2.2, is similar to a Sentinel 6x20 kW Reactor (Sentinel™ Calgon Carbon Corporation, Pittsburgh, PA, USA). The Sentinel UV Reactor (SUVR) is an enclosed pipe reactor, 1.219 m in diameter and 2.591 m long, with six 20 kW, medium pressure UV lamps oriented perpendicular to the flow. The reactor contains six baffles located on the inside wall of the reactor at the top and bottom and 0.1524 m in front of each set of lamp in the x-direction. Other specifications are reported in Table 2.1 and Figures 2.1 and 2.2. For this work, the x-axis is oriented in the direction of the bulk flow, the y-axis is oriented perpendicular to the lamps, and the z-axis is oriented in the direction of the lamp axes as shown in Figure 2.1.

Table 2.1: UV Reactor specifications (Sentinel™ Calgon Carbon Corporation, Pittsburgh, PA, USA).

Reactor Specifications	**Value**
Internal diameter	1.1971 m
Length	2.591 m
Reactor weight	1500 kg
Electrical Utilities Current (60Hz)	480 V 3 phase 160 A
Total power	120 kW
Design UV dose	400 J/m^2
Maximum design flow rate	6469 m^3/h at 40 mJ/cm^2 and 93% UVT
Maximum system pressure	690 kPa (100 psi)
Maximum Pressure Drop at max flow rate	14 kPa (2.0 psi)
Inlet/Outlet	1.219 m 75 kg flange
Entrance length	1.1971 m
Exit length	1.1911 m
Lamp Specifications	
Type	Medium pressure
Lamp configuration	Perpendicular to the flow
Number of lamps per module	2
Number of modules	3
Total number of lamps	6
Lamp Quartz Sleeve diameter	0.06756m

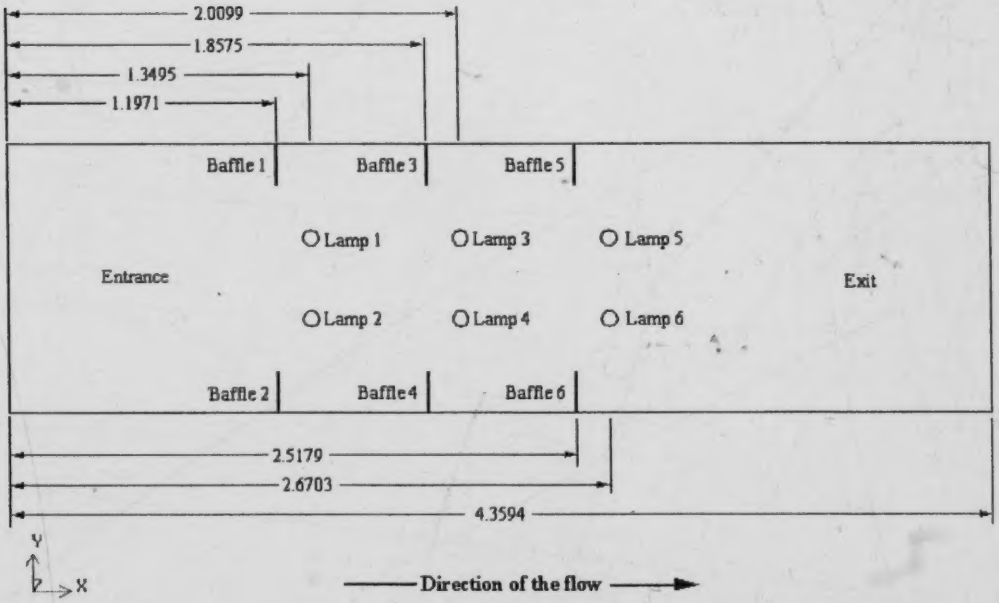

Figure 2.1: Elevation view of the Sentinel™ UV reactor 6x20kW (scale in meters).

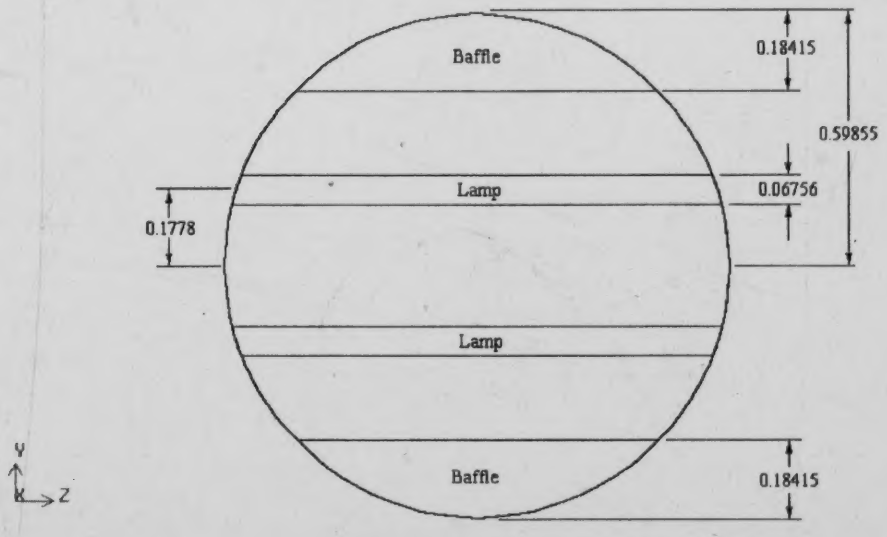

Figure 2.2: Cross-sectional view of the Sentinel™ UV reactor 6x20kW (scale in meters).

2.2 Simulation Conditions

The flow field in the Sentinel UV reactor was simulated using Fluent 6.1 (FLUENT INC. Lebanon, New Hampshire). Solution of the flow field requires specification of the mesh, the inflow and outflow boundary conditions, and model parameters. The following sections describe the mesh generation, numerical procedure, boundary conditions and turbulence model selected, and how each of these parts of the model were validated.

2.2.1 Mesh Generation

The first step in the solution of a flow field is to divide the domain into discrete control volumes or elements. In general, the accuracy of the solution increases as the number of elements increases. However, the cost of increasing the number of elements is an increase in calculation time and the output file size. Therefore, an optimal mesh should be fine where the velocity gradients are high and coarse where the velocity gradients are small.

A second factor to consider in mesh design for complex geometries, like a UV reactor, is the time consumed on the definition of the domain geometry and the mesh refinement around complex surfaces. The development of unstructured tetrahedral meshing has partially solved this problem because tetrahedral meshes can be generated quickly. Unstructured tetrahedral meshes also require fewer cells than unstructured hexahedral meshes in regions where the flow variation is low. However, unstructured tetrahedral meshes increase numerical diffusion and create other numerical problems because the mesh faces are not aligned with the flow. In this study, both structured and unstructured hexahedral and tetrahedral meshes were tested.

For the empty pipe, two three-dimensional meshes were constructed using Gambit 2.0 (FLUENT INC. Lebanon, New Hampshire). Figure 2.3 shows a cross section of the mesh with 4,618 elements on the face and a total of 798,914 elements after projection onto the x-Cartesian coordinate. The mesh presented is an unstructured hexahedral mesh, 1.197 m in diameter and 3.5052 m in long. The mesh was refined in the region near the wall (ten cells were located between 0.0 m and 0.0575 m from the wall). The second mesh is an unstructured tetrahedral mesh with a total of 817,180 elements (not shown).

For the SUVR, the mesh study was more extensive. Five three-dimensional meshes were used to evaluate the effect of the mesh type and refinement on the flow field prediction. Table 2.2 lists the five meshes and summarizes the resolution for each mesh. The meshes were constructed using GAMBIT 2.0. The mesh generation journal files are referenced in Appendix J. In Table 2.2 "**Entrance**" refers to the volume between the inlet and the first baffle ($0 < x < 1.1971$ m), "**Lamps**" refers to the volume between the first baffle and an imaginary plane located at 3.17m from the inlet, ($1.1971 \text{ m} < x < 3.1783$ m), and "**Exit**" refers to the volume between the imaginary plane and the outlet ($3.1783 \text{ m} < x < 4.3594$ m). The fine meshes contain approximately 60% more elements than the coarse meshes.

Figures 2.4 to 2.8 show transverse sections of the SUVR for each mesh. The fine unstructured hexahedral meshes have more elements surrounding the lamps and extending from the lamps to the baffles than the coarse unstructured hexahedral mesh. The fine structured hexahedral mesh was constructed with a progressive reduction of the number of elements between the lamps and baffles in order to provide better resolution around the flow obstacles (Figure 2.6 and 2.7). The unstructured tetrahedral mesh (Figure

2.8) is composed of hexahedral elements in the Entrance and Exit sections and tetrahedral elements in the Lamps section.

Table 2.2: Number of elements for different mesh types of the UV reactor

Mesh type	Entrance	Lamps	Exit	Total
Coarse unstructured hexahedral	141120	303939	138462	583521
Fine unstructured hexahedral	197904	555168	273936	1027008
Coarse structured hexahedral	122910	257299	143640	523844
Fine structured hexahedral	204624	560922	246024	1011570
Fine unstructured tetrahedral	152010	687315	148544	987869

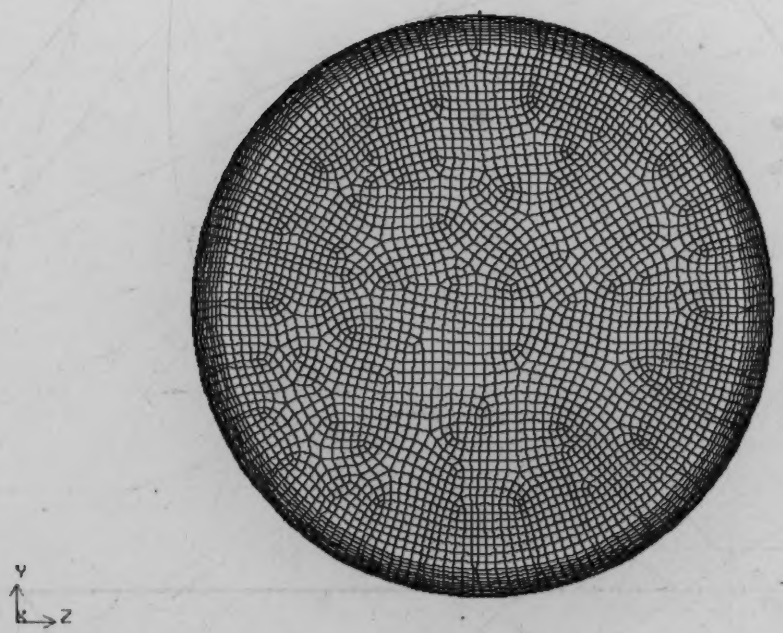

Figure 2.3: Cross-sectional view of the mesh generated to simulate pipe flow.

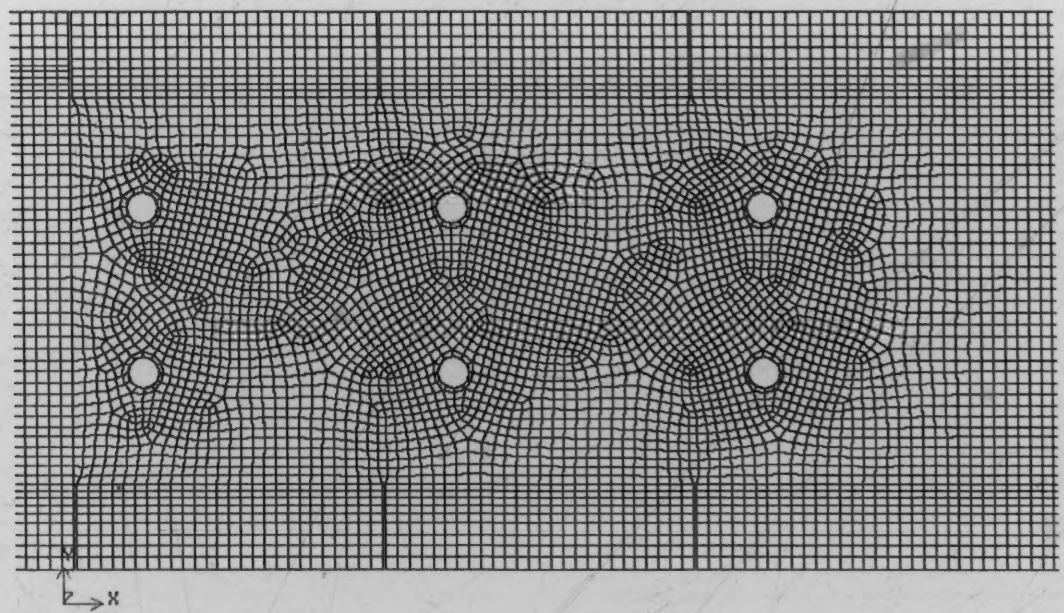

Figure 2.4: Cross-section of the coarse unstructured hexahedral mesh generated to simulate the SUVR.

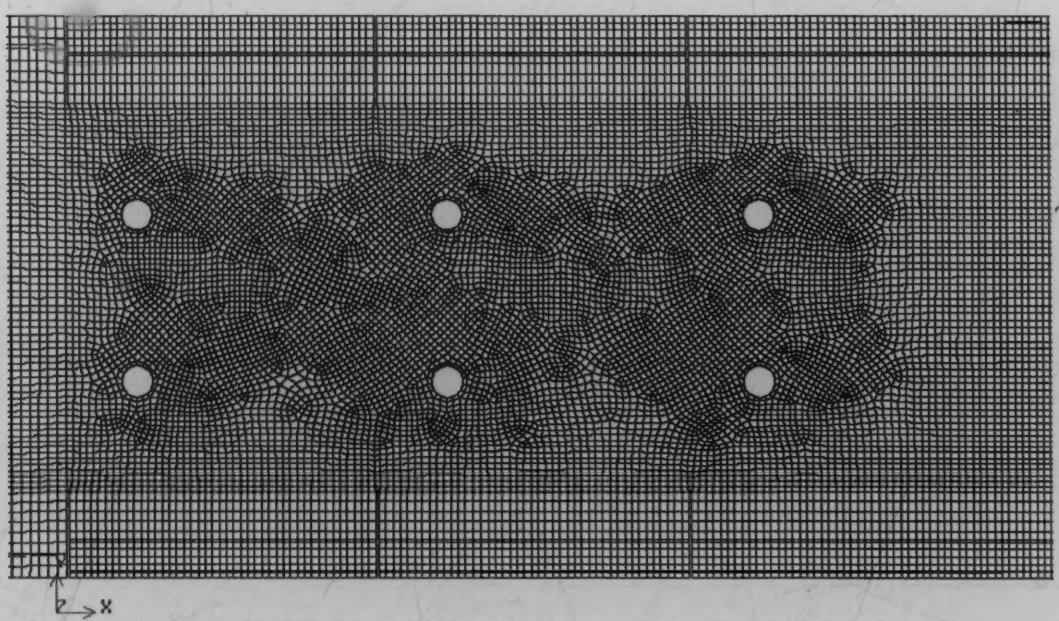

Figure 2.5: Cross-section of the fine unstructured hexahedral mesh generated to simulate the SUVR.

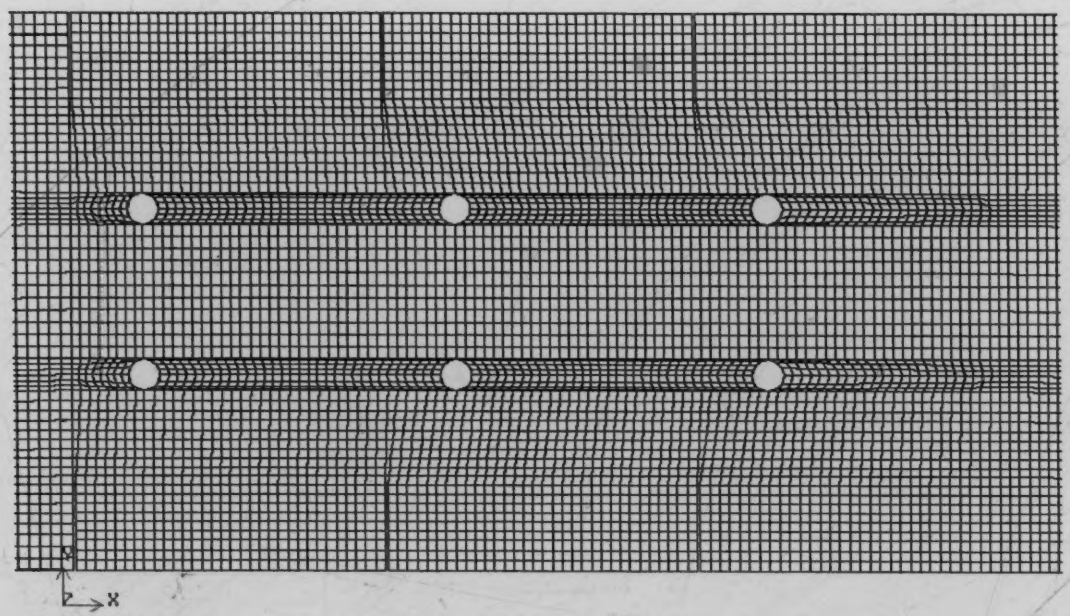

Figure 2.6: Cross-section of a coarse structured hexahedral mesh generated to simulate the SUVR.

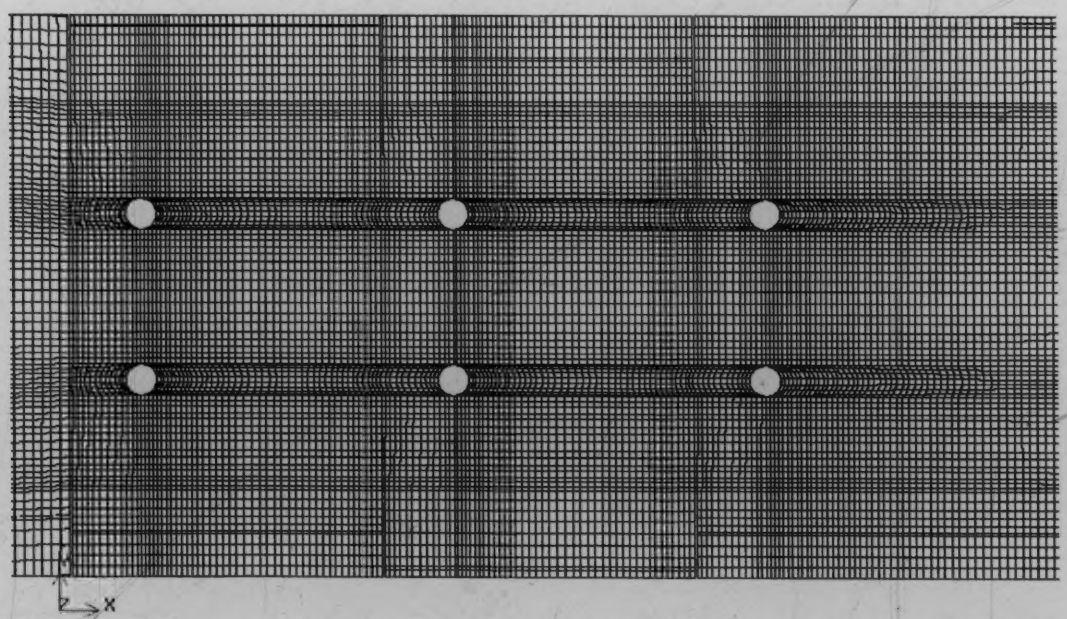

Figure 2.7: Cross-section of the fine structured hexahedral mesh generated to simulate the SUVR.

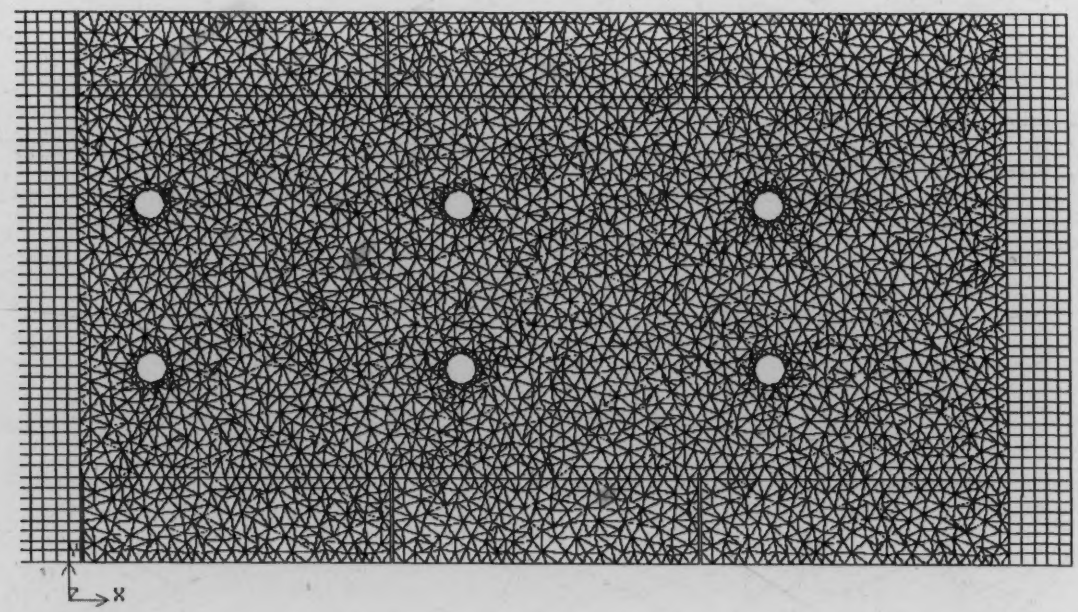

Figure 2.8: Cross-section of the unstructured tetrahedral mesh generated to simulate the SUVR.

2.2.2 Numerical Procedure

Fluent 6.1 solves the velocity field using the finite volume method. This numerical algorithm consists of the following steps (Versteeg and Malalasekera, 1995):

1. Formulation of the governing equations in their integral form over a control volume to yield discretized equations.
2. Substitution of the unknown variables by means of simple functions into the discretized equations. This converts the discretized equations into a system of algebraic equations.
3. Solution of the algebraic equations by an iterative method.

The algebraic equations for the pipe flow were solved using the SIMPLEC algorithm by van Doormal and Raithby (1984). SIMPLEC is one of several alternatives that Fluent

6.1 offers for solving the algebraic equations. This algorithm computes not only the velocity field (**U**) but also the pressure field (**p**) and is discussed thoroughly by Versteeg and Malalasekera (1995). The SIMPLEC algorithm requires under-relaxation factors to ensure stability of the iteration process because the pressure correction equation is susceptible to oscillations or divergence unless a relaxation factor is used. In addition, SIMPLEC uses the upwind differencing scheme to discretize the convective term of the flow. This scheme sets the accuracy of the solution by selecting either a first or second order Taylor series truncation error. The under relaxation factors used for the empty pipe flow and for simulation of the SUVR are summarized in Table 2.3. These factors provided a fast and smooth convergence of the normalized residuals of the equations for continuity, velocity, turbulent kinetic energy and the rate of dissipation of the turbulent kinetic energy. The discretization scheme selected was second order upwind.

Table 2.3: Under relaxation factors used for all the simulations.

Variable	Under relaxation factors
Pressure	0.7
Density	1
Body forces	1
Momentum	0.7
Turbulent kinetic energy	0.7
Turbulent dissipation rate	0.7
Turbulent viscosity	1
Reynolds Stresses	0.7

2.3 Boundary Conditions

Boundary conditions are required at the inlet and outlet of the reactor, as well as at solid surfaces. They have a significant impact on the solution of the flow. The boundary conditions for either a pipe or a UV reactor include: 1) specification of all variables

(except pressure) at the inlet of the flow domain, 2) specification of the pressure at one location inside the flow domain (the pressure was specified at the outlet), and 3) specification of all variables (except pressure and density) or their normal gradients at solid walls. In addition, the outlet should be located where the gradient of all the variables is equal to zero in the direction of the flow.

2.3.1 Inlet

The variables that must be specified at the inlet for the simulation of turbulent pipe flow are the x-y and z velocities, turbulent kinetic energy, k, and the rate of dissipation of turbulent kinetic energy, ε. These variables were approximated using an experimental correlation in some cases, and gross approximation of the expected profiles in others, as discussed below. Appendix E, presents the User Defined Function (UDF) that was used to implement these profiles.

2.3.1.1 Velocity at the Inlet

Velocity profiles in fully developed pipe flow have been study extensively by Schlichting (1979) and by Zagarola and Smits (1997). At high Reynolds numbers, viscous effects are confined to a thin layer of fluid next to the pipe wall. Therefore, the flow in a pipe is divided in two main regions: 1) the inner region and 2) the core region.

The velocity profile in the inner region nearest to the wall is given by the self-similar relation:

$$u^+ = \frac{U}{u_\tau} = f\left(\frac{u_\tau y}{\nu}\right) = f\left(y^+\right) \qquad (2.1)$$

Equation (2.1) is called the law of the wall, which defines the characteristic velocity, u^+, as a function of the characteristic distance from the wall, y^+. The characteristic velocity is obtained by dividing the local mean velocity, U, by the friction velocity, $u_\tau = (\tau_w/\rho)^{1/2}$, where τ_w is the wall shear stress and ρ is the fluid density. The characteristic distance from the wall, y^+, is obtained by dividing the product of the friction velocity and the perpendicular distance from the wall, y, by the kinematic viscosity, ν.

The outer region is characterized by the self-similar relation:

$$u^+ = \frac{U_{cl} - U}{u_\tau} = g\left(\frac{y}{\delta}\right) \tag{2.2}$$

Equation (2.2) is called the velocity deficit law, which defines the velocity deficit (U_{cl} – U) as a function of the distance from the wall, y, divided by the boundary layer thickness, δ, where U_{cl} is the center-line velocity.

These self similar relations (Equations 2.1 and 2.2) are used to establish a number of limiting solutions for specific areas, as shown in Figure 2.9.

In the **viscous sublayer** it is assumed that turbulence is negligible and that the shear stress is equal to that at the wall. Equation 2.1 becomes

$$u^+ = y^+ \qquad y+ \leq 12 \tag{2.3}$$

In the **inertial sublayer**, beyond the area immediately adjacent to the wall, it is assumed that the viscous forces are negligible and the local shear stress remains essentially equal to that at the wall. Equation 2.1 becomes:

$$u^+ = \frac{1}{0.436}\ln y^+ + 6.15 \qquad 500 < y^+ \leq 0.07R^+ \tag{2.4}$$

The values 0.436 and 6.15 were determined by Zagarola and Smits (1998) at high Reynolds numbers.

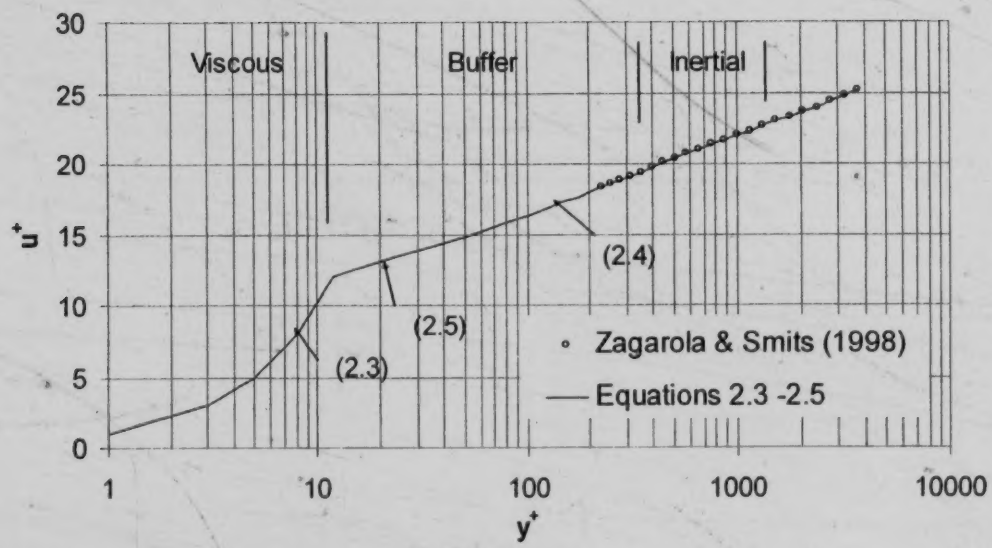

Figure 2.9: Universal turbulent velocity distribution at Re = 1.8×10^6.

The **buffer layer** connects the viscous and the inertial layers, and its velocity profile as determined by Zagarola and Smits (1998) is:

$$u^+ = 8.70\left(y^+\right)^{0.137} \qquad 12 < y^+ \leq 500 \qquad (2.5)$$

Zagarola and Smits (1998) developed a new theory to explain the scaling in the outer region at high Reynolds numbers. They selected as the outer velocity scale the velocity deficit in the pipe (U_{cl}-$\bar{U}$), where U_{cl} is the center-line velocity and $\bar{U}$ is the volume flow velocity (superficial velocity). They found that the velocity deficit in the pipe was a better velocity scale than the friction velocity, u_τ, in Equation (2.2), which is a velocity scale associated with the near wall region. They used the velocity deficit scale to normalize the velocity profiles in the outer region from $y/R = 600/R^+$ to $y/R = 1$, as shown in Figure 2.10, where R^+ is the ratio between the length scales associated with the inner region and the core region ($R^+ = Ru_\tau\rho/\mu$).

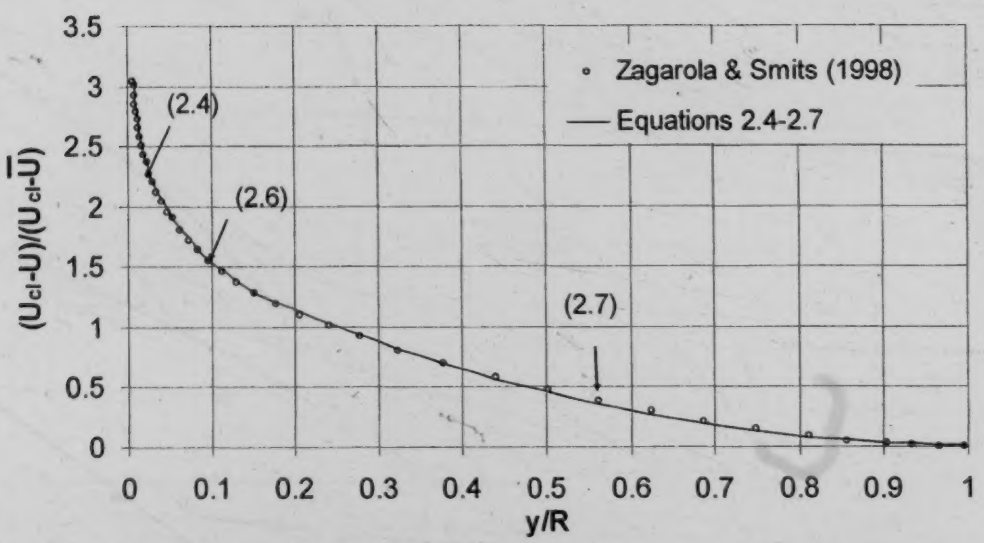

Figure 2.10: Velocity defect plot in the outer region as a function of the normalized distance from the wall at $Re=1.8x10^6$.

The outer velocity scale proposed by Zagarola and Smits (1998) was used to generate the fully developed turbulent flow velocity profiles in the outer region. The Zagarola and Smits' data were selected because: 1) they provided a complete data set (from the center to the wall of a pipe), 2) they were obtained at high Reynolds numbers, and 3) they are available online (www.princeton.edu/~gasdyn/Superpipe_data). The velocity profiles were estimated by fitting empirical equations to the Zagarola and Smits' data for the Reynolds number range ($7.5x10^5$ to $1.8x10^6$) using least squares. The resulting equations were:

$$\frac{U_{cl}-U}{U_{cl}-\overline{U}} = -0.5625\ln\left(\frac{y}{R}\right) - 0.2422 \qquad \frac{600}{R^+} < \frac{y}{R} \le 0.15 \qquad (2.6)$$

$$\frac{U_{cl}-U}{U_{cl}-\overline{U}} = 1.7435\left(\frac{y}{R}\right)^2 - 3.503\left(\frac{y}{R}\right) + 1.7738 \qquad 0.15 < \frac{y}{R} \le 1 \qquad (2.7)$$

The centerline velocity U_{cl} is given: (Zagarola and Smits 1998)

$$\frac{U_{cl}}{u_\tau} = 5.269\log\left(Re^* f_f^{0.5}\right) + 3.742 \qquad (2.8)$$

where f_f is the friction factor.

2.3.1.2 Turbulent Kinetic Energy at the Pipe Inlet

The turbulent kinetic energy, k, at the inlet of the pipe was estimated using Equations 2.9, 2.10 and 2.11, as shown in Figure 2.11.

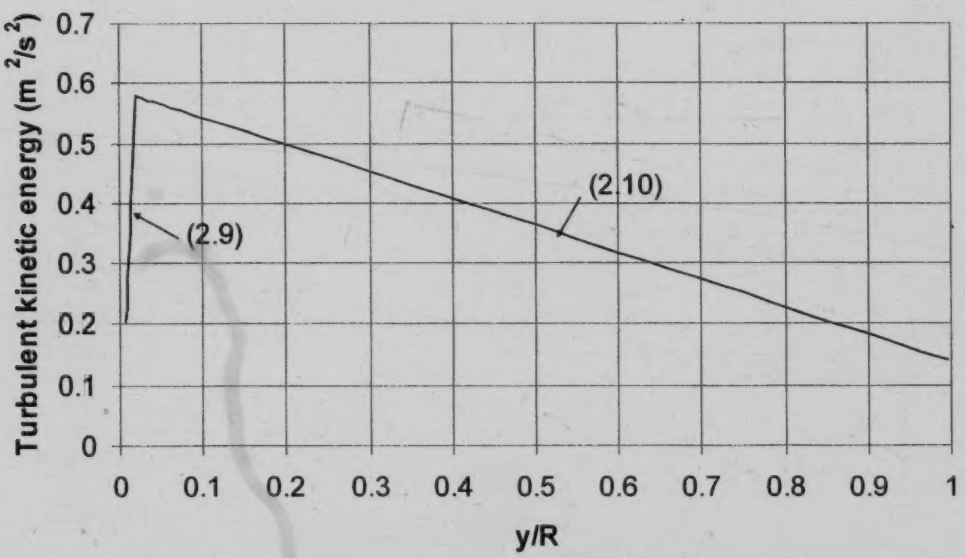

Figure 2.11: Profile of the turbulent kinetic energy as a function of the normalized distance from the wall at the pipe inlet. Numbers refer to the equations used.

Near the wall:

$$k = \frac{k_{nw} y^+}{500} \qquad y^+ \le 500 \qquad (2.9)$$

Outer region:

$$k = \frac{(k_{nw} - k_{cl})R}{r'} + k_{cl} \qquad y^+ > 500 \qquad (2.10)$$

$$r' = R - \left(\frac{500\mu}{u_\tau \rho}\right) \tag{2.11}$$

The turbulent kinetic energy near the wall, k_{nw}, and the turbulent kinetic energy at the centerline, k_{cl}, are given by Rodi (1984):

$$k_{nw} = \frac{u_\tau^2}{\sqrt{C_\mu}} \tag{2.12}$$

$$k_{cl} = \frac{3(\bar{U}I')^2}{2} \tag{2.13}$$

$$I' = 0.16(Re)^{-1/8} \tag{2.14}$$

where I' stands for the turbulent intensity (Spalding, 1974).

2.3.1.3 Rate of Dissipation of the Turbulent Kinetic Energy at the Inlet

The rate of dissipation of the turbulent kinetic energy, ε, in fully developed pipe flow was estimated using Equations 2.15 and 2.17 (Versteeg and Malalasekera, 1995), as shown in Figure 2.12.

Near wall:

$$\varepsilon = \frac{u_\tau^3}{\kappa y} \qquad y^+ \le 500 \tag{2.15}$$

Outer region:

$$\varepsilon = C_\mu^{0.75} \frac{k^{1.5}}{l} \qquad y^+ > 500 \tag{2.16}$$

$$l = R\left[0.14 - 0.08\left(\frac{r}{R}\right)^2 - 0.06\left(\frac{r}{R}\right)^4\right] \tag{2.17}$$

where κ is the Von Karman constant and l is the characteristic length in a pipe

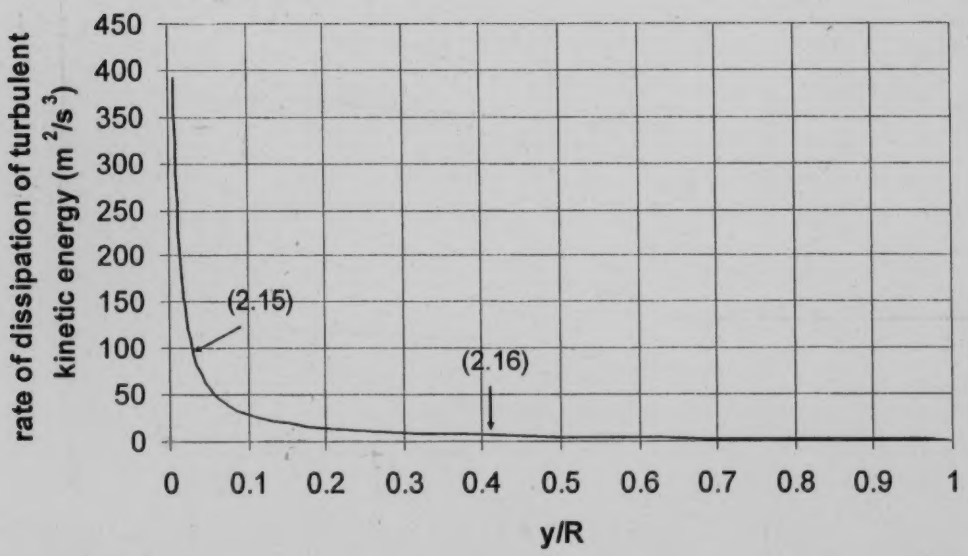

Figure 2.12: Profile of the rate of dissipation of turbulent kinetic energy as a function of the normalized distance from the wall at the pipe inlet. Numbers refer to the equations used.

2.3.2 Solid Wall Treatment

Wall, or no-slip, boundary conditions are used to bound solid and fluid regions. Since the flow near the wall is viscous, the no–slip condition at the wall was selected for the validation of the pipe flow. To bridge the solution variables from the near wall to the corresponding quantities at the wall, Launder and Spalding (1967) developed expressions for the flux of momentum and energy based on the log law of wall flows and the assumption that the rate of turbulent production is equal to the rate of dissipation at the near wall. Thus, the wall region was resolved using the empirical equations for the inertial layer Equation (2.4), and the eddy viscosity Equation (1.21) to give:

$$u^+ = \frac{1}{\kappa}\ln\left(Ey^+\right) \qquad 30 < y^+ < 500 \qquad (2.18)$$

where the constant E = 9.8, and the Von Karman constant, $\kappa = 0.436$.

The turbulent kinetic energy, k, and the rate of dissipation of turbulent kinetic energy, ε, at the wall are given in Equations (2.12) and (2.15), respectively.

2.3.3 Outlet

The outlet boundary condition requires two considerations: 1) the specification of the outlet condition in pipe flow should be consistent with the inlet boundary conditions, and 2) the location of the boundary condition plays a crucial role in the accuracy of the solution variables. In this study, a pressure of zero gauge was specified at the outlet. Ideally, the outlet surface should be placed 54 diameters downstream of the baffles to allow the flow to return to a fully developed state (Zagarola and Smits 1998). However, this condition demands more elements in the exit region than that in the lamp region (Figure 2.1). In reality, the outlet surface is placed at a distance equal or greater than 10 baffle heights downstream of the last baffle (Versteeg and Malalasekera, 1995).

The accuracy of the outlet condition (zero gauge pressure) was verified using a comparison of the expected pressure drop with the pressure drop computed by Fluent in an empty pipe. It was found that the CFD code computed a pressure drop equal to 36.0 Pa, which was close to the expected pressure drop of 37.5 Pa estimated with the Bernoulli equation and the Zagarola and Smits' friction factor relation for pipe flow. This new friction factor relation is similar to the Prandtl's, but has different constants to provide a more accurate representation of the velocity profile.

The location of the outlet surface was verified using the following: 1) a sensitivity analysis of the effect of the downstream distance on the interior solution, 2) gradients of

velocity, turbulent kinetic energy and the rate of the dissipation of the turbulent kinetic energy, which were computed in the flow direction, and 3) a comparison of the computed pressure drop over the last two baffle heights with the expected pressure drop for a pipe, for the same length of 0.3683m. Verification results led to the following conclusions: 1) insignificant variation of the velocity field was evident when the outlet was located at 10 baffle heights, 2) all the computed gradients approached zero as expected, and 3) the pressure drop over the last two baffle heights was 10 times greater than that for a pipe of the same length. Although the pressure drop was greater than expected, it had less effect on the velocity field in the lamp region. Therefore, the location of the outlet surface at 10 baffle heights downstream of the last baffle provided an acceptable solution of the velocity field.

2.4 Validation of the CFD Code for Pipe Flow

Validation of the velocity field predicted by Fluent 6.1 for a pipe 1.20 m in diameter was based on comparison with analytical or experimental results reported in the literature for both laminar and turbulent flow. For laminar pipe flow, analytical solutions can be applied for Reynolds numbers up to 2000. For turbulent pipe flow, the correlations developed by Zagarola and Smits (1998) for a pipe diameter of 0.13 m were extrapolated to the larger 1.20 m diameter pipe.

2.4.1 Laminar Flow in a Straight Pipe

The purpose of this simulation is to demonstrate that Fluent 6.1 is able to describe laminar flow in an empty pipe. Laminar flow was simulated using the flow properties given in Table 2.4 and a fully developed laminar velocity profile at the inlet given by:

$$U = U_{max}\left(1-\frac{r^2}{R^2}\right) \tag{2.19}$$

where U_{max} is the maximum velocity, r is the radial position and R is the pipe radius.

Zero gauge pressure was set as the outlet boundary condition and the no-slip condition was applied at the wall. The pressure at the inlet and the velocity field were computed by the CFD code. The UDF that was used to implement the laminar velocity profile in Fluent 6.1 is given in Appendix D.

Table 2.4: Fluid properties used to predict laminar flow in a pipe.

Fluid properties	**Value**
Density	1000 kg/m^3
Viscosity	0.01 kg/ms
Reynolds number	957
Pipe diameter	1.1971 m
U_{max}	1.6x10^{-2} m/s

The mesh selected was an unstructured hexahedral mesh of 798,914 elements, with refinement near the pipe wall (Figure 2.3). The velocity field was calculated using SIMPLEC, second order upwind differencing, and an upwind under relaxation factor of 1.0 for the body forces, viscosity and continuity. The convergence requirement was normalized residuals less than 1.0x10^{-6}.

The simulation results demonstrate that the velocity profile predicted by Fluent 6.1 at the outlet is the same as the user defined profile at the inlet. Figure 2.13 shows the axial velocity profiles as a function of the radial position. The pressure drop given by Fluent 6.1 is one percent lower than that computed with the Bernoulli equation (6.3×10^{-3} Pa).

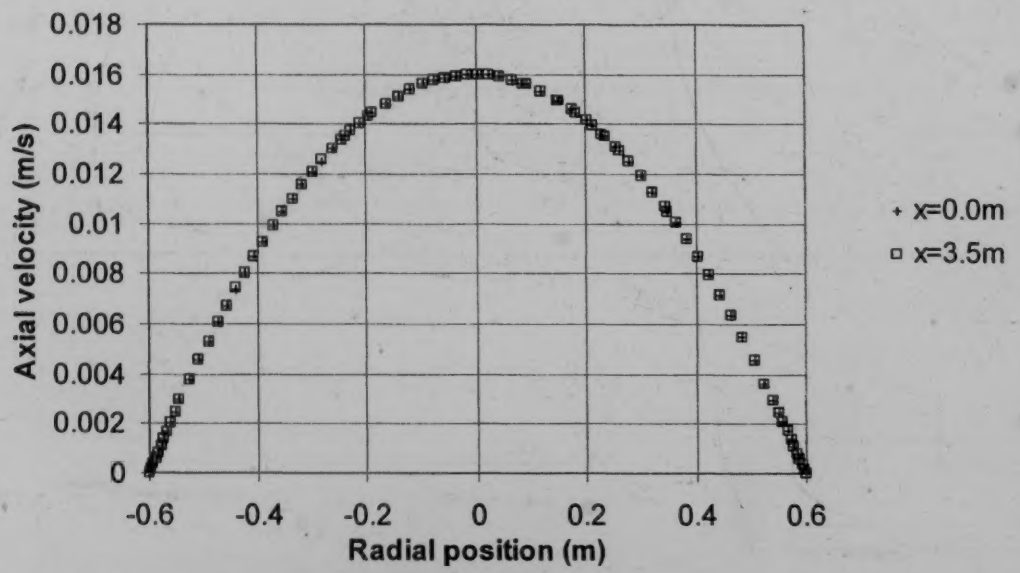

Figure 2.13: Comparison of the user defined velocity profile at the inlet for laminar flow with the velocity predicted by Fluent 6.1 at 3.5 m along the pipe for r = 0.5985 m. As expected, the velocity profile is constant along the pipe.

2.4.2 Turbulent Flow in a Straight Pipe

Simulations of the turbulent pipe flow proved that Fluent 6.1 can describe a fully developed pipe flow using both the k-ε and the RSM models. These simulations were set up using water properties (Table 2.5) and the velocity profile given in Equations (2.3) to (2.7) and turbulent kinetic energy and rate of dissipation of the turbulent kinetic energy profiles given in Equations (2.9) to (2.17) as the inlet boundary conditions. The outlet boundary condition was set to zero gauge pressure and the non-slip condition was specified at the wall.

Table 2.5: Fluid properties used for simulation of turbulent flow in a pipe.

Fluid properties	Value
Density	998.2 kg/m^3
Viscosity	$1.003x10^{-3}$ kg/ms
Temperature	293.15°K
Reynolds number	$1.83x10^6$
Friction factor	$1.1081x10^{-2}$
Friction velocity	$4.1677x10^{-1}$ m/s

The mesh used for this simulation was the same as that used for the initial laminar simulation, as shown in Figure 2.3, with the numerical parameters given in Table 2.2. The simulation was considered converged when normalized residuals reached $1.0x10^{-4}$ or less.

Both the k-ε and RSM turbulence models predicted the same fully developed velocity profile over the full 3.5 m length of pipe (Figure 2.14). They did not, however, predict the same turbulent kinetic energy (TKE) profiles. From Figure 2.15, it can be seen that both turbulence models give approximately the same maximum and minimum TKE values, and that both models damp out the TKE near the wall. Figure 2.16 shows that both turbulence models predicted an identical rate of dissipation of turbulent kinetic energy.

The simulations were repeated using an unstructured tetrahedral mesh. It was found that the numerical diffusion in the unstructured tetrahedral mesh flattens the velocity profile at the center of the pipe by approximately two percent (this results are not shown). Similar results have been reported by other authors (Slack and Prasad, 2000 and Mori and Razore, 2001).

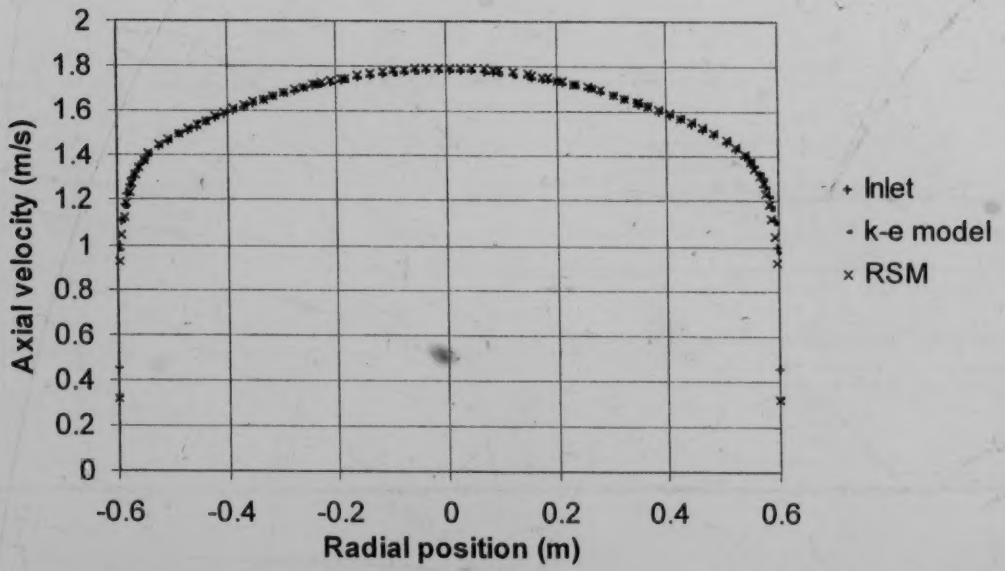

Figure 2.14: Comparison of the user defined velocity profile at the inlet with the k-ε and RSM model predictions at the outlet for Re = 1.8×10^6.

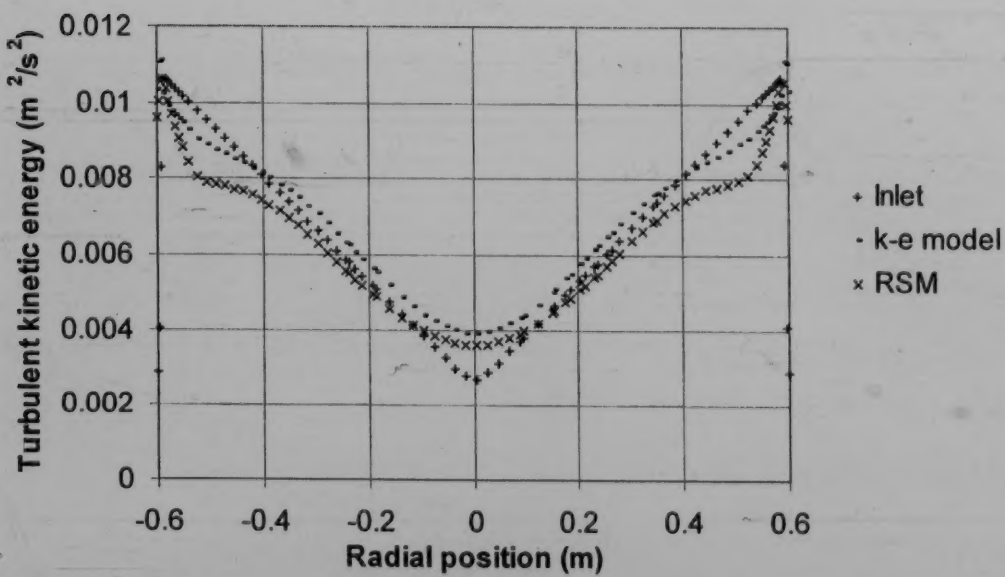

Figure 2.15: Comparison of the user defined TKE profile at the inlet with the k-ε and RSM turbulence model predictions at the outlet for Re = 1.8×10^6.

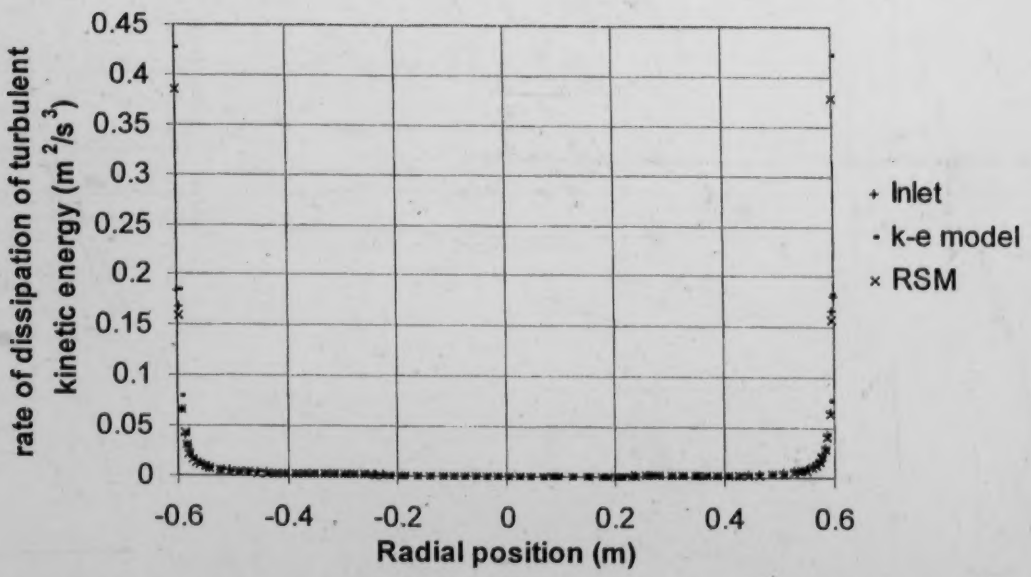

Figure 2.16: Comparison of the user defined energy dissipation rate profile at the inlet with k-ε and RSM model predictions at the outlet for $Re = 1.8 \times 10^6$.

2.4.3 Summary of the CFD Validation for Empty Pipe Flow

The results for laminar and turbulent pipe flow can be summarized as follows:

1. The k-ε and the RSM models combined with the numerical procedure maintained the fully developed turbulent velocity profile over the full length of pipe.
2. The k-ε model can be used as a primary model for the simulation of the UV reactor since the k-ε model predicted similar profiles of velocity, and required less computational time than the RSM model.
3. The unstructured hexahedral mesh should be used to predict the velocity profile in UV reactors since the unstructured tetrahedral mesh flattens the velocity profile by approximately 2 percent.

Due to the difficulty of measuring the flow field in a UV reactor the validation of simulation was performed in an empty pipe using Zagarola and Smits' velocity data. This

was based on the assumption that if the boundary conditions and numerical procedure worked well in a pipe, they would also work well in a UV reactor whose shape is similar to a pipe. It was found that the simulation was valid for an empty pipe; therefore, it was assumed that the model was valid for a UV reactor. However, a pilot test results should be conducted in the future to confirm the above conclusion or assumption.

2.5 Boundary Conditions for the Discrete Phase Model

The discrete phase model is used to simulate the path a microorganism follows through the UV reactor. This model requires boundary conditions for the particle at the inlet, solid walls and outlet. The initial conditions that must be specified for particle tracking are the starting position, diameter, velocity, temperature, and mass flow rate of the particle.

2.5.1 Initial Conditions

The initial conditions of the particles are identified as injection point properties in the discrete phase model. The location of the injection points must be defined by the CFD user before running the particle tracking. For the case of a UV reactor, it was assumed that 1) microorganisms in a pipe flow are distributed uniformly throughout the fluid on volumetric basis, and 2) the reactor cross section at the inlet was composed of m concentric rings of equal area. The number of particles in each ring volume, n_i, divided by the flowrate through the ring volume, Q_i, (Equation 2.20), is equal to a constant value C_1 (Equation 2.21).

$$Q_i = \int_{A_i} U_n dA_i = \int_{r_i}^{r_{i+1}} U(r) 2\pi r dr \tag{2.20}$$

$$\frac{n_p}{Q_t} = \frac{n_i}{Q_i} = C_1 \tag{2.21}$$

$$r_{i+1}^2 = \left(r_i^2 + \frac{A_t}{m\pi} \right) \tag{2.23}$$

where n_p is the total number of particles, Q_t is the total flowrate, r_i is the internal radius of cylinder i, and r_{i+1} is the external radius of cylinder i.

2.5.1.1 Starting Position of the Particles in Laminar Pipe Flow

The starting position of the particles in laminar flow was generated using the assumption that microorganisms in a pipe flow are uniformly distributed per unit volume of fluid. Substituting the laminar profile (2.19) and (2.21) into (2.20) and integrating gives:

$$n_i = \frac{n_p \pi U_{cl}}{Q_t} \left\{ r_{i+1}^2 \left(1 - \frac{r_{i+1}^2}{2R^2} \right) - r_i^2 \left(1 - \frac{r_i^2}{2R^2} \right) \right\} \tag{2.22}$$

The number of particles released as a function of the radius was then obtained, as shown in Figure 2.17. The spatial distribution of the particles in each ring was completed using a uniform random number generator (rand) as described in Equations (2.24) and (2.25)

$$r = r_i + (r_{i+1} - r_i) * \text{rand} \tag{2.24}$$

$$\theta = 360 * \text{rand} \tag{2.25}$$

where θ is the radial angle, which was converted to Cartesian coordinates by:

$$y = r * \sin\left(\frac{\theta\pi}{180}\right) \tag{2.26}$$

$$z = r * \cos\left(\frac{\theta\pi}{180}\right) \tag{2.27}$$

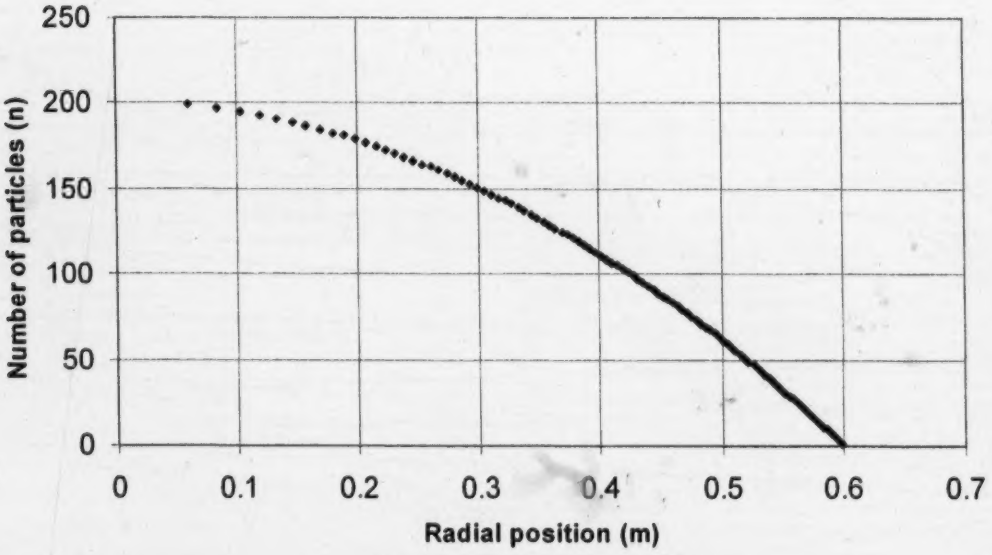

Figure 2.17: Distribution of particles as a function of radius for laminar pipe flow.

2.5.1.2 Starting Position of the Particles in Turbulent Pipe Flow

The starting position of the particles in turbulent flow was generated using the assumption that microorganisms in a pipe flow are uniformly distributed per unit volume of fluid. By substituting the equations for the radial velocity profile (2.3) to (2.7) and (2.20) into (2.21) and integrating, the following equations are obtained for the number of particles in each region:

In the viscous sublayer:

$$n_i = \frac{2n_p\pi u_i^2\rho}{Q_t\mu}\left\{\left(\frac{Ry_{i+1}^2}{2} - \frac{y_{i+1}^3}{3}\right) - \left(\frac{Ry_i^2}{2} - \frac{y_i^3}{3}\right)\right\} \tag{2.28}$$

In the buffer layer:

$$n_i = \frac{17.4 n_p \pi u_\tau}{Q_t \mu}\left(\frac{u_\tau \rho}{\mu}\right)^{0.137}\left\{\left(\frac{Ry_{i+1}^{1.137}}{1.137}-\frac{y_{i+1}^{2.137}}{2.137}\right)-\left(\frac{Ry_i^{1.137}}{1.137}-\frac{y_i^{2.137}}{2.137}\right)\right\} \tag{2.29}$$

In the inertial sublayer:

$$\begin{aligned} n_i = {} & \left(\frac{n_p \pi u_\tau}{Q_t}\right)\left(Ry_{i+1}-\frac{y_{i+1}^2}{2}\right)\left[4.587 * \ln\left(\frac{u_\tau \rho y_{i+1}}{\mu}\right)+12.3\right] \\ & -4.587\left(\frac{n_p \pi u_\tau}{Q_t}\right)\left[\left(Ry_{i+1}-\frac{y_{i+1}^2}{2}\right)+\left(Ry_i-\frac{y_i^2}{2}\right)\right] \\ & -\left(\frac{n_p \pi u_\tau}{Q_t}\right)\left(Ry_i-\frac{y_i^2}{2}\right)\left[4.587 * \ln\left(\frac{u_\tau \rho y_i}{\mu}\right)+12.3\right] \end{aligned} \tag{2.30}$$

In the core region for $\frac{600}{R^+} < \frac{y}{R} \le 0.15$

$$\begin{aligned} n_i = {} & \left(\frac{n_p \pi}{Q_t}\right)\left(Ry_{i+1}-\frac{y_{i+1}^2}{2}\right)\left[2U_{cl}+1.125\left(U_{cl}-\overline{U}\right)\ln\left(\frac{y_{i+1}}{R}\right)-0.4844\left(U_{cl}-\overline{U}\right)\right] \\ & -\left(\frac{n_p \pi}{Q_t}\right)\left(Ry_i-\frac{y_i^2}{2}\right)\left[2U_{cl}+1.125\left(U_{cl}-\overline{U}\right)\ln\left(\frac{y_i}{R}\right)-0.4844\left(U_{cl}-\overline{U}\right)\right] \\ & +1.125\left(U_{cl}-\overline{U}\right)\left(\frac{n_p \pi}{Q_t}\right)\left[\left(Ry_i-\frac{y_i}{4}\right)-\left(Ry_{i+1}-\frac{y_{i+1}^2}{4}\right)\right] \end{aligned} \tag{2.31}$$

In the core region for $0.15 < \frac{y}{R} \le 1$

$$\begin{aligned} n_i = {} & \left(U_{cl}-\overline{U}\right)\left(\frac{2n_p \pi}{Q_t}\right)\left(\frac{0.43587 y_{i+1}^4}{R^2}-\frac{1.7488 y_{i+1}^3}{R}+2.6384 y_{i+1}^2-1.7738 y_{i+1}\right) \\ & -\left(U_{cl}-\overline{U}\right)\left(\frac{2n_p \pi}{Q_t}\right)\left(\frac{0.43587 y_i^4}{R^2}-\frac{1.7488 y_i^3}{R}+2.6384 y_i^2-1.7738 y_i\right) \\ & +U_{cl}\left(\frac{2n_p \pi}{Q_t}\right)\left[\left(Ry_{i+1}-\frac{y_{i+1}^2}{2}\right)-\left(Ry_i-\frac{y_i^2}{2}\right)\right] \end{aligned} \tag{2.32}$$

The resulting number of particles as a function of the distance from the wall is shown in Figure 2.18. Similar to the laminar case, the distribution of the particles in each ring is made using a uniform random generator number (rand) as described in Equations (2.24) and (2.27). Appendix F, presents the C-code developed to assign the injection properties to each point for turbulent pipe flow.

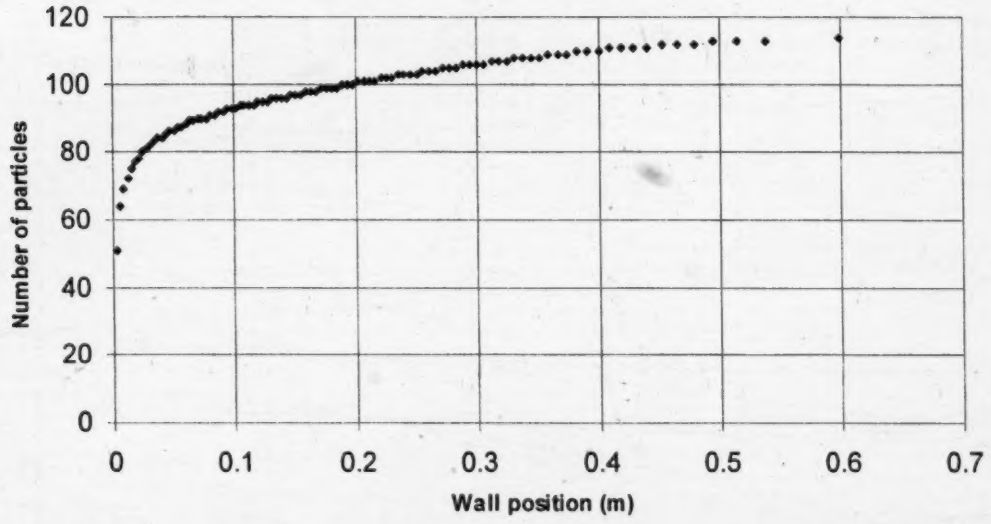

Figure 2.18: Distribution of particles as a function of distance from the wall in turbulent pipe flow

2.5.2 Particle Diameter

In this study, the size of a fluid particle was selected based on the following criteria:

1. Its diameter should be greater than $4x10^{-6}$ m for *Cryptosporidium oocysts* (Hanninen, 2002).
2. Its volume should be less than one milliliter to reduce the probability of more than one oocyst being contained per fluid particle. This was based on 10 cysts & oocysts per milliliter, which was the total concentration of *Giardia* cysts &

Cryptosporidium ***oocysts*** in primary treated wastewater (Hanninen, 2002). It should be emphasized that the concentration of cysts and oocysts in treated drinking water will be far less than reported by Hanninen (2002).

3. Its diameter should be smaller than that of the smallest eddies calculated by $\eta = (\nu^3/\varepsilon)^{1/4}$, which was 2.6×10^{-4} m for turbulent flow.
4. Its diameter should be greater than 3.0×10^{-5} m to minimize the computational time, but keep the similar accuracy of the computed particle path Han et al (2001).
5. Its diameter should be in the range of 1×10^{-5} to 1×10^{-3} m to provide satisfactory simulation results (Durst et al. 1984).

Based on the above criteria, 1×10^{-4} m was chosen as the size of a fluid particle in turbulent flow. This fluid particle size yields a particle volume of less than 1 mililiter, ensuring that each fluid particle contains no more than one oocyst.

Using a particle diameter of 1×10^{-4} m, the length scale used for the particle tracking is determined by the product of the relaxation time (Equation 1.36) and the average particle velocity for a low flow rate (0.75m/s). The estimated length scale of 2×10^{-4} m was computed using a half of the relaxation time of 5.5×10^{-4} s to ensure an accurate computation of the UV dose. The maximum number of steps (43500) was evaluated by trial and error until the number of parcels that escaped at the outlet was more than 98% of the injected particles in the domain. Appendix A presents step-by-step the CFD protocol for a UV reactor simulation.

Besides the starting position and diameter of the particle, the DRW model also requires an input file of velocity for laminar flow (Equation 2.19), turbulent flow (Equations 2.3 to 2.7), diameter (1.0×10^{-3}m), temperature (293.15 °K), and mass flow rate

(0.0 kg/s, set to zero since particles are massless) for each particle at the inlet. The computer programs developed to assign the injection properties to each point for laminar pipe flow and turbulent flow are presented in Appendix F and G, respectively.

2.5.3 Wall Treatment

The DPM in FLUENT 6.1 offers a variety of wall treatments ranging from "reflect" to "escape". The "reflect" condition assumes that the particle rebounds off the wall with a change in its momentum as defined by the coefficient of restitution. The normal (or tangential) coefficient of restitution defines the amount of momentum in the direction normal (or tangential) to the wall that is retained by the particle after the collision with the wall. The "escape" condition ends the trajectory calculation when the particle encounters the wall. For this work the "reflect" condition was used with a normal coefficient of restitution equal to zero and tangential coefficient of restitution equal to one. This assumes the collisions were elastic in the tangential direction only, and tangential velocity of the fluid dominates in comparison to the normal velocity of the particle.

2.6 Verification of the UDF Used to Compute the UV Dose

The UV dose absorbed by a particle was computed by integrating the particle position information with the fluence rate distribution, as described in Section 1.8.5. The DPM and DRW models were experimentally validated for neutrally buoyant particles by Domgin et al. (1997); however, the UDF used to compute the UV dose along the particle trajectory had to be verified as it is new for this work. This section pursues two objectives

1) to verify the User Defined Function (UDF) used to integrate the UV dose along the particle path, and 2) to estimate the effect of the Lagrangian integral time scale (τ_L) on the predicted dose distribution.

In the absence of experimental data to validate the computed UV dose, the predicted UV dose was compared to well defined ideal solutions for which the dose can be calculated exactly. The ideal cases used were 1) the laminar flow in an empty pipe, and 2) the turbulent velocity profile in an empty pipe with the velocity fluctuation set equal to zero.

To verify the UDF, a simple fluence rate distribution was assumed proportional to the velocity distribution according to:

$$E'(r) = E'_{max} * \frac{U}{U_{max}} \tag{2.33}$$

In which the fluence rate E'(r), is a function of the radius, r, and E'_{max} is the maximum fluence rate. Equation 2.33 was implemented as a UDF in Fluent 6.1 (Appendix H).

The UV dose was defined as the summation of the fluence rate along the time-space path traveled by a fluid particle (Equation 1.54). Thus, substituting Equation (2.33) into (1.54) gives:

$$D = \sum_{t=0}^{t=\infty} \frac{E'_{max}}{U_{max}} \frac{(U_{t-1} + U_t)}{2} \Delta t \tag{2.34}$$

where U_{t-1} is the velocity at previous time step and U_t is the velocity at current time step.

2.6.1 Verification of the UDF Used to Compute Dose in Laminar Flow

Laminar flow in a pipe was used as an initial test of the integrated UV dose computed by the UDF because the results can be directly compared with an analytical solution. In laminar flow the velocity field is given by Equation (2.19). Thus the time increment Δt is equal to the space increment divided by the velocity, which is constant at a certain radius. Since there is no radial dispersion ($U_{t-1}=U_t$) or velocity variation as the particle moves in laminar flow, Equation (2.34) simplifies to:

$$D = \sum_{L_i}^{L} \frac{E'_{max}}{U_{max}} \frac{U}{U} \frac{\Delta l}{U} = \frac{E'_{max}}{U_{max}} (L - L_i) \qquad (2.35)$$

where L is the distance from the particle starting position to the outlet and L_i is the starting position of a particle.

Verification of the discrete phase model for laminar flow was computed with the initial conditions given in 2.5.1.1 and the parameters listed in Table 2.6. The value for the ratio E_{max}/U_{max} was computed by assigning a UV dose equal to 400.0 J/m^2, L = 3.5 m and L_i = 0.0 m in Equation (2.35). Therefore, the UV dose computed for 9999 particles was compared to the expected dose of 400 J/m^2

Table 2.6: Particle tracking parameters for laminar pipe flow

Parameter	Value
E'_{max}/U_{max} (J/m^3)	114.12
D_p (m)	1.0×10^{-4}
L_i (m)	1×10^{-4}
L (m)	3.5052
Δl (m)	1.0×10^{-5}
Maximum Number of Steps	43,500
Particle temperature(°K)	293.15
Mass flow rate (kg/s)	0.0
Particle density (kg/m^3)	998.2
Particle velocity	Equation (2.19)

The simulation results for laminar flow in a pipe, shown in Figure 2.19, predict a dose distribution with a mean dose of 399.4 J/m^2 and a narrow standard deviation of 10.4 J/m^2. This is very close to the analytical result of 400 J/m^2 (Equation 2.35). In addition, the absolute axial velocity of the particles at the outlet, both in terms of velocity distribution and the maximum velocity of 0.016m/s, was maintained along the pipe.

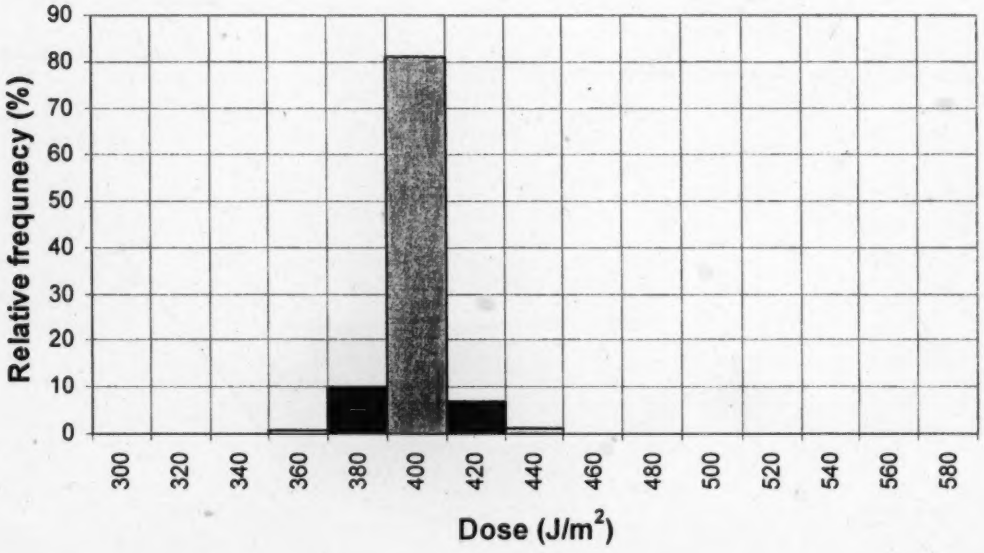

Figure 2.19: Predicted dose received by 9999 particles in laminar flow (mean = 399.4 J/m^2, s_D = 10.40 J/m^2).

2.6.2 Verification of the UDF Used to Compute Dose in Turbulent Flow

Verification of the UDF used to compute the UV dose received by a particle in turbulent flow in an empty pipe was divided into three steps: 1) particle trajectory based on the mean velocity (u = U), 2) particle tracking considering the instantaneous velocity (u = U + u'), and 3) particle tracking using different values for the Lagrangian empirical constant C_L.

Particle tracking for turbulent flow in an empty pipe was carried out using the mean velocity field and the boundary conditions defined in Section 2.5.1.2 and the parameters listed in Table 2.7. Since the velocity fluctuation has been ignored in the DRW model for this test, Equation 2.34 simplifies to Equation 2.35. Therefore, it is possible to verify the UV dose computed for turbulent flow as was done for laminar flow in Section 2.6.1. Figure 2.20 presents the predicted dose distribution with a mean dose of 399.9 J/m^2 and a standard deviation of 3.4 J/m^2. A comparison between Figure 2.19 and 2.20 shows that the dose distribution spread decreases as the particle velocity increases. This clearly shows that increasing the velocity near the wall leads to the reduction of round-off error, and provides better estimation of the dose received by a particle moving near the wall.

Table 2.7: Particle tracking parameters for turbulent pipe flow

Parameter	**Value**
E_{max}/U_{max} (J/m^3)	114.12
D_p (m)	$1.0x10^{-4}$
L_i (m)	$1x10^{-4}$
L (m)	3.5052
Δl (m)	$1.0x10^{-4}$
Maximum Number of Step	500,000
Number of Particles	9,999
Mass flow (kg/s)	0.0
Particle density (kg/m^3)	998.2
Particle velocity	Equation (2.3) to (2.7)

Particle tracking results where the fluctuating velocity is included in the DRW model are presented in Figures 2.21 to 2.24. The effect of the fluctuating velocities on the particle tracks is illustrated in Figure 2.21, where 10 simulations were performed for a single particle injection point to illustrate the potential paths predicted by the DRW model. By comparing Figure 2.20 and 2.22, it can be seen that the DRW model yields a wider dose distribution, but it does not change the mean of the dose distribution.

The final verification step for the discrete random walk model concerns the Lagrangian empirical constant C_L. This model constant determines the time period a particle is allowed to interact with an eddy and the velocity fluctuation during this period. The default values for the Lagrangian empirical constant in Fluent 6.1 are 0.15 and 0.30 for the k-ε and RSM models, respectively. These values are in the range given in Table 1.5. The effect of the model parameter C_L on the dose distribution was investigated by increasing C_L from 0.15 to 0.30. This increase caused an increase in the particle dispersion and a slightly wider dose distribution, as shown in Figures 2.23 and 2.24. This shows that the calculated dose distribution is robust with respect to the parameters chosen for the DRW model.

2.6.3 Summary of the Verification of the UDF Used to Compute Dose

Verification of the hydrodynamics models in an empty pipe produced five results:

1. The UDF used to compute the dose integration along the particle path is able to yield the expected UV dose.
2. The turbulent velocity profile yields a narrower dose distribution than the laminar velocity profile.
3. The effect of the turbulence component in the random walk model is to broaden the dose distribution without changing its mean.
4. The dose distribution is only broadened slightly by an increase in the Lagrangian empirical constant C_L.

These conclusions were used to define simulation conditions for the more complex flow in the full UV reactor geometry with lamps and baffles.

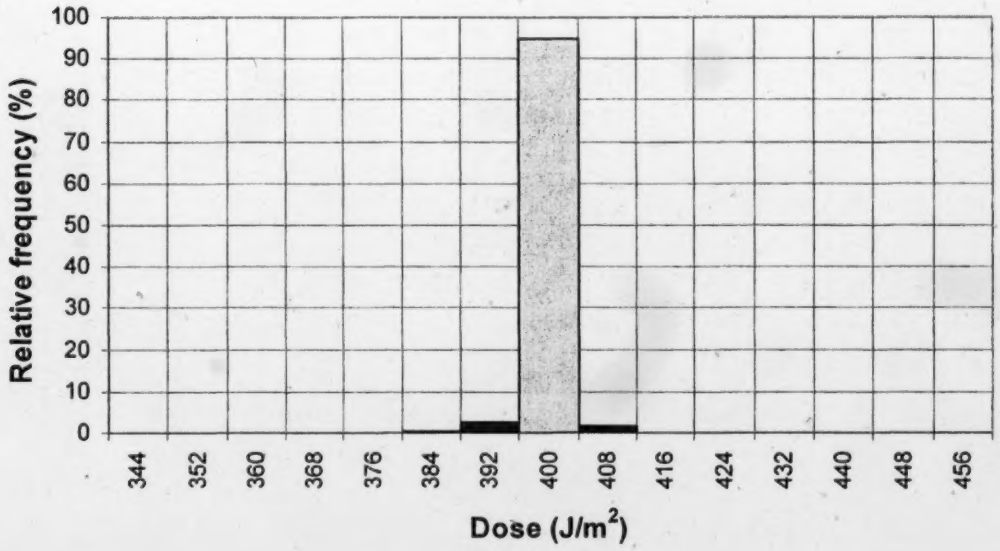

Figure 2.20: Predicted dose received by 9999 particles in turbulent flow u = U in an empty pipe (mean = 399.9 J/m^2, s_D = 3.4 J/m^2).

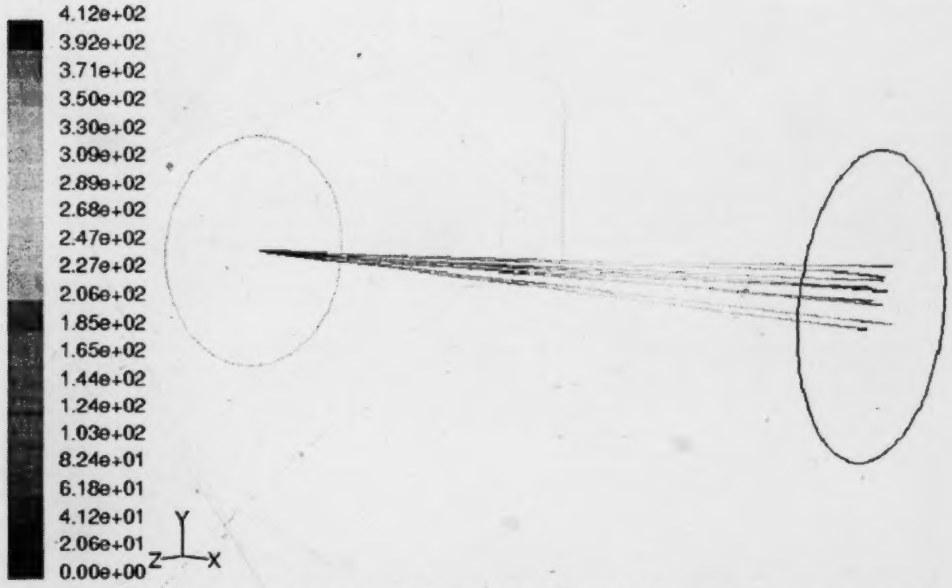

Figure 2.21: Particle tracks colored by UV dose (J/m^2) with C_L = 0.15 in an empty pipe.

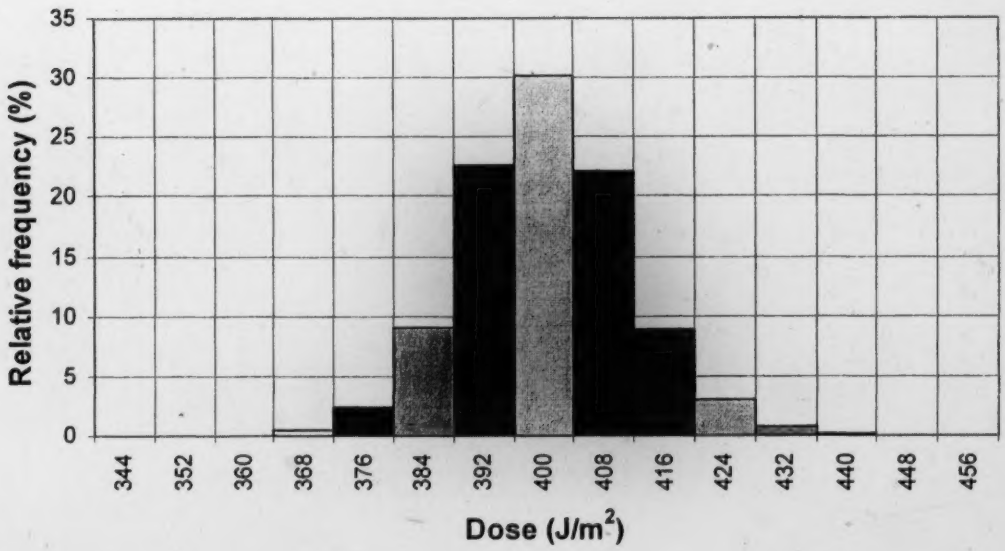

Figure 2.22: Dose received by 9999 particles $C_L = 0.15$ $\Delta l = 2.0 \times 10^{-4}$ m in an empty pipe (mean = 400.2 J/m^2, s_D = 10.8 J/m^2).

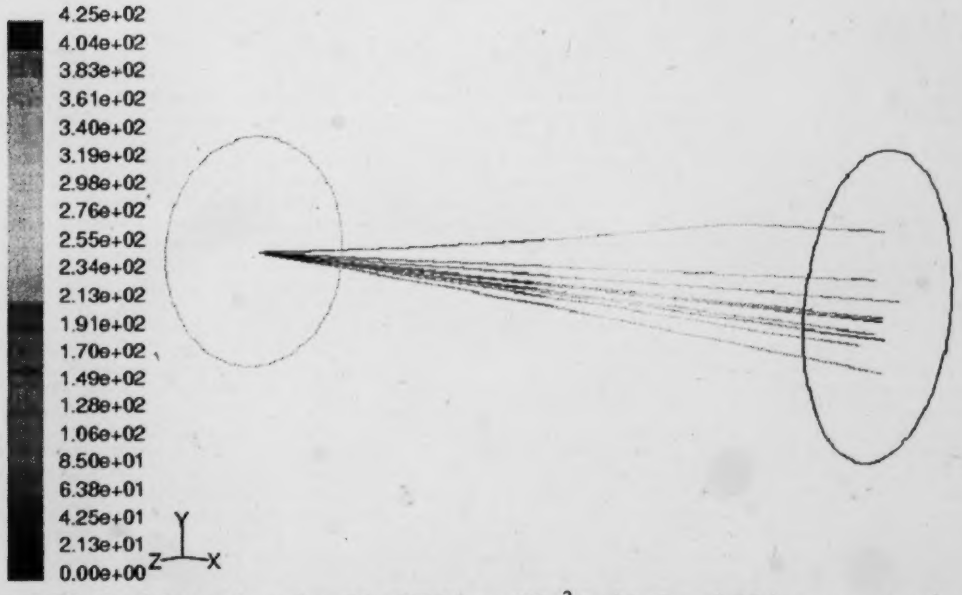

Figure 2.23: Particle tracks colored by UV dose (J/m^2) with $C_L = 0.30$ in an empty pipe

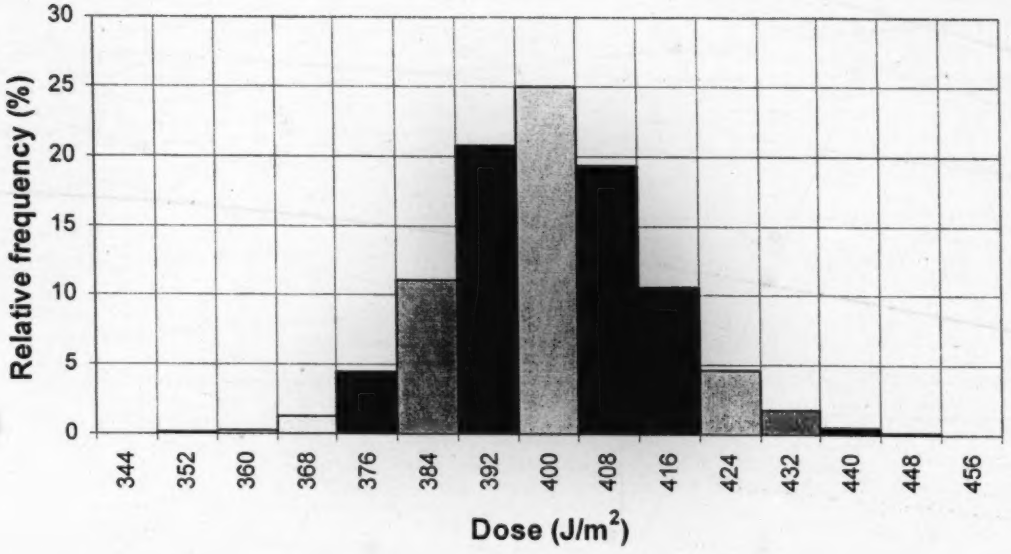

Figure 2.24: Dose received by 9999 parcels $C_L = 0.30$ $\Delta l = 2.0 \times 10^{-4}$ m in an empty pipe (mean = 400.1 J/m^2, s_D = 13.4 J/m^2).

2.7 *Verification of the Fluence Rate Distribution*

The fluence rate distribution computed with UVCalc3D_200 has been experimentally validated by Stefan et al. (2001) for a single medium pressure lamp in an annular UV reactor. However, the fluence rate distribution for a multiple lamp UV reactor has not been validated. Therefore, it is the objective of this section to 1) verify the fluence rate predicted with multiple lamps, and 2) characterize the fluence rate distribution of the SUVR at two transmittances.

2.7.1 Bolton Model Validation

Validation of the UV fluence rate model was performed in an annular reactor with a single lamp placed concentric with the axis of the reactor. Quartz spheres, prefilled by an

actinometer solution of KI/KIO_3, were arranged in various positions inside the UV reactor and the UV fluence was measured and compared with computations. It was found that the model predictions agree well with the experimental values for both low and medium pressure lamps (Rahn et al. 2000 and Stefan et al. 2001).

2.7.2 UVCalc Inputs

The integrated CFD approach uses UVCalc3D_200 (Bolton Photosciences Inc. Edmonton/Alberta) to compute the spatial fluence rate distribution from the medium pressure lamps. This program requires the inputs listed in Table 2.8, 2.9 and 2.10 as well as the centroid coordinates of the discrete control volumes or cells, which were generated and exported from Fluent 6.1 to UVCalc3D_200. Appendix I presents the UDFs that were developed and used to export or import data from or to Fluent. Appendix K presents an example of the input data used to compute the fluence rate.

Table 2.8: Inputs for the calculation of the fluence rate distribution for the SUVR.

Input	Value
Lamp power range (W)	6666 to 20000
Lamp power efficiency (%)	23.25
Maximum radius perpendicular to the lamp axis (m)	2.00
Lamp sleeve radius (m)	0.033782
Lamp length (m)	1.1971
Maximum full height parallel to the lamp axis (m)	2.5
Air refractive index	1.000
Water refractive index	1.372
Lamp sleeve refractive index	1.516
Lamp shadow effect	ON/OFF
Lamp refractive effect	ON/OFF

Table 2.9: Lamp orientation and coordinates of the SUVR.

Lamp ID	Lamp orientation	Lamp x coordinate	Lamp y coordinate	Lamp z coordinate
1	z	1.3495	-0.1778	0.000
2	z	1.3495	0.1778	0.000
3	z	2.0099	-0.1778	0.000
4	z	2.0099	0.1778	0.000
5	z	2.6703	-0.1778	0.000
6	z	2.6703	0.1778	0.000

Table 2.10: Input data for the calculation of a single MP lamp. [a] data provide by Epcor Water Services Edmonton, Alberta, [b] data provide by Bolton Photosciences Inc.

Band ID	Wavelength Band (nm)	UVT[a] (%)	Lamp emission[b]	Transmittance Sleeve[b] (%)	Germicidal Factor[b]
1	200-204	46.26	0.01662	0.60	1.26
2	205-209	66.94	0.02282	0.65	1.130
3	210-214	75.54	0.02991	0.69	0.910
4	215-219	79.23	0.03855	0.73	0.740
5	220-224	81.78	0.04341	0.77	0.520
6	225-229	84.54	0.04331	0.81	0.410
7	230-234	86.98	0.04029	0.85	0.420
8	235-239	89.10	0.04907	0.88	0.500
9	240-244	90.75	0.01906	0.90	0.630
10	245-249	91.75	0.06271	0.91	0.820
11	250-254	92.54	0.14524	0.92	0.970
12	255-259	93.21	0.08268	0.93	1.050
13	260-264	93.65	0.12616	0.94	1.060
14	265-269	93.73	0.04614	0.95	1.010
15	270-274	93.73	0.02683	0.955	0.890
16	275-279	93.60	0.07391	0.96	0.740
17	280-284	93.66	0.01263	0.965	0.560
18	285-289	93.75	0.02150	0.97	0.390
19	290-294	94.12	0.02119	0.975	0.220
20	295-299	94.82	0.07798	0.98	0.095

For the purpose of this research it was necessary to provide three ultraviolet water transmittance (UVT) spectra to evaluate the significance of the UVT over the log inactivation. The UVT spectra could be experimentally measured or scaled down from

the UVT spectra provided by Epcor Water Services Edmonton, Alberta (Figure 2.25). Scaled UVT spectra are used as an alternative to reduce the factors to study. Consequently, the following assumption was made to generate the distributions. If the UV transmittance is a function of the concentration of substances present in the water (Equation 1.5) then an upset in the water treatment plant will cause a concentration increase of these substances and therefore a proportional decrease in the UVT, as shown in Figure 2.25.

Three UVT transmittances were selected in this study: 98%, 93% and 80% UVT. The 98% UVT represents the highest transmittance that would be tested, 93%UVT is the minimum allowed UV transmittance that Calgon Carbon Corporation suggests to achieve a UV dose of 40 mJ/cm^2 for the Sentinel UV reactor working at 6469m^3/h, and 80% UVT represents the lowest transmittance that would be tested.

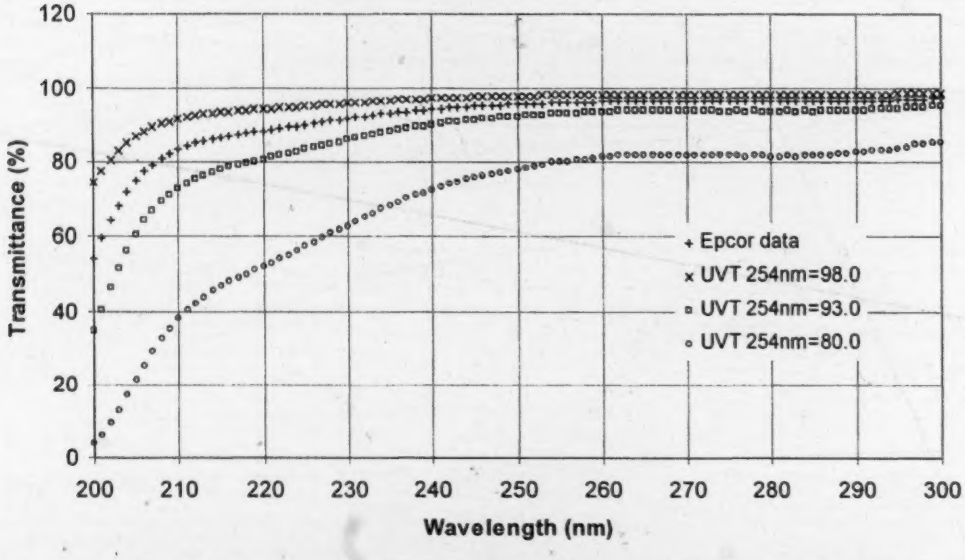

Figure 2.25: Scaled UV spectra based on the UV spectra of chlorinated filter water effluent from the E.L Smith plant, Edmonton, Alberta, provided by Epcor Water Services.

2.7.3 Numerical Verification of the Fluence Rate Distribution

UVCalc3D_200 is a very sophisticated program to compute a fluence rate distribution. In this study, a verification of the fluence rate calculated for a point located between the lamps was executed. Equation 1.13 was implemented in an Excel worksheet, neglecting the reflection and refraction. The results of excel calculation were verified using the Linear Sources Integration developed by Batchley (1997) assuming no absorption. The fluence rate received by a point located between the lamps with coordinates x = 2.0099 m, y = 0.0 m, z = 0.0 m (see Figure 2.1) was estimated using both Excel and UVCalc3D_200, and the input parameters given in Tables 2.8, 2.9 and 2.10. The results are summarized in Table 2.11.

Table 2.11: Fluence rate received by a point, located at x = 2.0099 m, y = 0.0 m, z = 0.0 m, estimated using UVCal3D_200 and Excel worksheet with the inputs given in Table 2.8 2.9 and 2.10. Reflection and refraction were neglected.

Lamp ID	Fluence rate (W/m^2)		Error (%)
	UVCalc3D_200	Excel worksheet	
Lamp 1	2.5	2.6	4.0
Lamp 2	2.5	2.6	4.0
Lamp 3	532.6	611.2	14.8
Lamp 4	532.6	611.2	14.8
Lamp 5	2.5	2.6	4.0
Lamp 6	2.5	2.6	4.0
Total fluence rate	1075.2	1232.8	14.6

Table 2.11 shows that the Excel worksheet gives a higher estimated fluence rate than that of the UVCalc3D_ 200 for points closer to the lamps. This is because the UVCalc3D_200 applied a correction factor to the calculation for points closer to the lamps. From the tests presented in Table 2.11, it can be concluded that UVCalc3D_200 provides a conservative estimation of the fluence rate.

2.7.4 Fluence Rate Distribution

A thorough literature search did not uncover any information regarding the fluence rate distribution in large UV reactor used for drinking water treatment, except for fluence rate distributions for a single lamp oriented parallel to the flow with a small output power. Therefore, the objective of this section is to characterize the fluence rate distribution for medium pressure lamps oriented perpendicular to the flow in large UV reactors using two water transmittances.

Examples of the fluence rate distributions predicted using UVCalc3D_200 are shown in Figures 2.26 and 2.28 for the SUVR at 93% and 80% UVT, respectively. These contours describe the fluence rate at various points in a plane that pass through the central axis of the reactor. The fluence rate calculated considers the radiant output from all point sources and all lamps. In addition, Figures 2.27 and 2.29 show the fluence rate as a function of the axial position at 93% and 80% UVT, respectively.

The fluence rate is greater near the lamps and becomes weaker as the distance from the lamps increases. This is illustrated in Figure 2.28, where the fluence rate at the surfaces of the quartz sleeves reaches a maximum of 9.31×10^3 W/m^2, and decreases to 1.1×10^3 W/m^2 between lamps 1 and 3 (see Figure 2.1 for lamp numbering). Similar behavior with a more rapid initial decrease can be observed for a fluence rate computed under a UV transmittance of 80%, as shown in Figures 2.27 and 2.29.

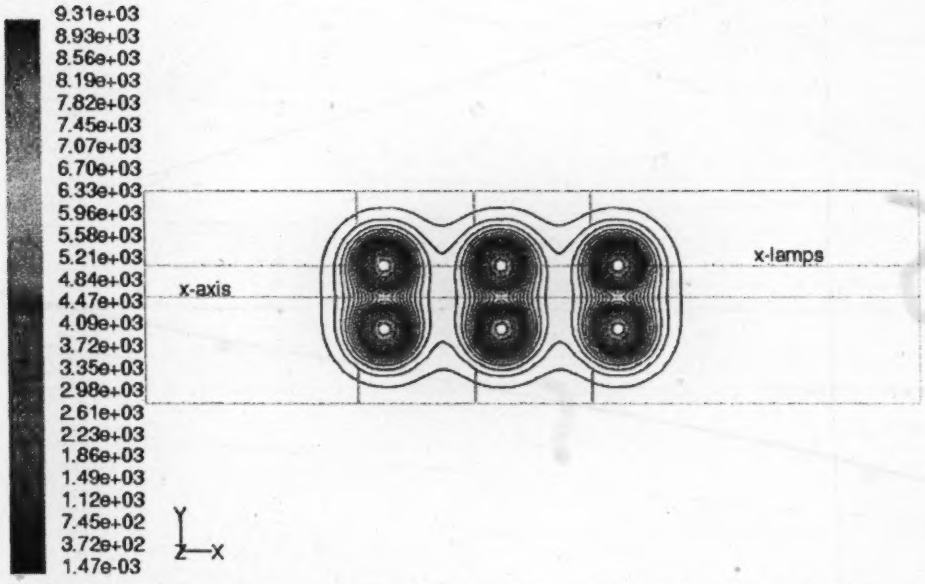

Figure 2.26: Contour of fluence rate (W/m^2) in an x-y plane with z = 0 m (UVT 93%, shadow effect ON and refractive effect ON)

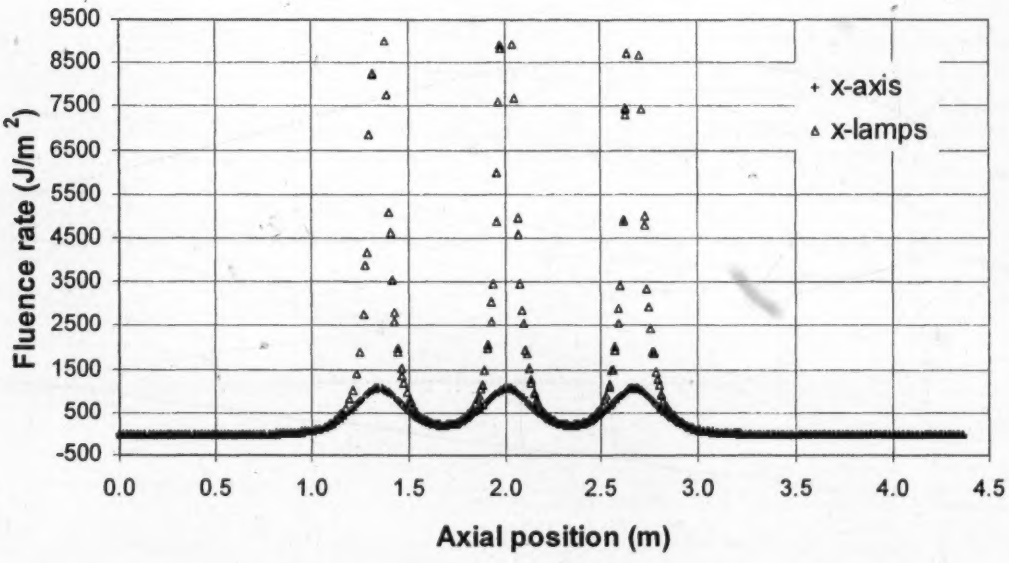

Figure 2.27: Fluence rate profile at the reactor x-axis and at the middle of the lamps 1, 3, and 5 (UVT 93% shadow effect ON and refractive effect ON). Location of the x-axis and x-lamps are shown in Figure 2.26.

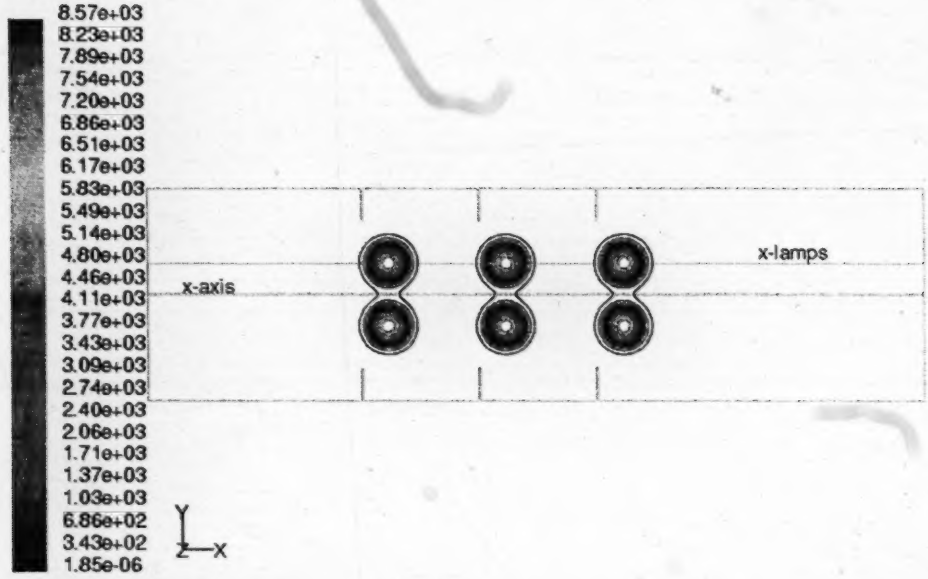

Figure 2.28: Contour of fluence rate (W/m^2) in an x-y plane with z = 0 m, (UVT 80% shadow effect ON and refractive effect ON)

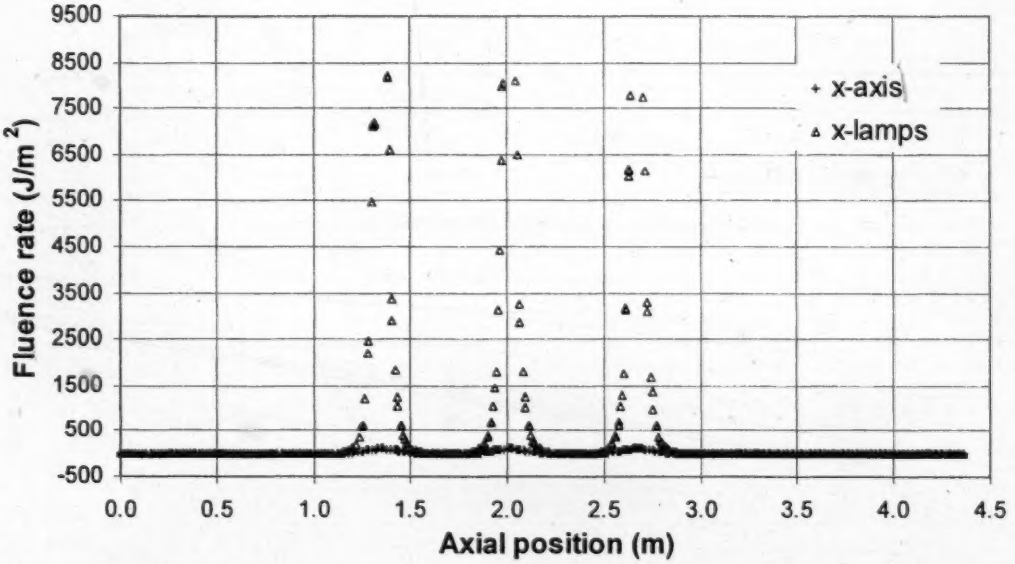

Figure 2.29: Fluence rate profile at the reactor x-axis and at the middle of the lamps 1, 3, and 5, UVT 80% shadow effect ON and refractive effect ON. Location of the x-axis and x-lamps are shown in Figure 2.28.

2.8 Verification of the Inactivation Program

A computer program written using C was developed to compute the inactivation in a UV reactor using inactivation Equations (1.55, 1.57, 1.58 and 1.64). This program was verified using an ideal dose case as discussed in section 1.6 and a computed inactivation reported in the literature. The computer program calculated inactivation by summation of the fractional survival ratio of each particle, which was computed from the dose received by each particle using a microorganism inactivation model. The equivalent dose was calculated using the microorganism inactivation model and the computed inactivation.

The computer program was verified by using an interesting feature of the first order kinetic model. If the inactivation constant k_r approaches zero (an organism very resistant to UV radiation), the equivalent dose approaches the mean dose of the distribution, regardless of the shape of the dose distribution (Wright and Lawryshyn, 2000).

The dose distribution shown in Figure 2.20 was selected to validate the inactivation program "Deqv.exe". This is because the true mean dose (400.0 J/m^2) is already known (see Section 2.6.2). For this validation, an inactivation constant (k_r = 0.01 m^2/J) in Equation (1.55) was chosen to provide an equivalent dose close to the mean dose of the distribution (400.0 J/m^2). The inactivation program provided an estimated equivalent dose of 399.94 J/m^2, which was close to the expected mean dose.

A separate evaluation of the inactivation program was performed using the UV dose distribution reported by Chiu et al. (1999). The dose distribution and kinetic parameters of the series event model (Equation 1.57) used by Chiu et al. (1999) were presented in Figure 1.1 and Table 1.6. The computer program, Deqv.exe, computed the same inactivation as Chiu et al (1999), who reported a value of 5.75 log. Therefore, it can be

concluded that the computer program, Deqv.exe, correctly computed the inactivation and equivalent dose.

2.9 Summary of the Validated Protocol

The protocol used for validation or verification of each model in turbulent pipe flow can be summarized as given in Table 2.12. This table also presents the protocol used to compute the dose distribution of the Sentinel UV Reactor. The protocols differ in the boundary conditions at the inlet and number of injected particles. The boundary conditions specified at the inlet of a UV reactor are the velocities, turbulent kinetic energy, and rate of turbulent dissipation of the turbulent kinetic energy computed with the k-ε model at the outlet of the empty pipe. The rationale to select the number of injected particles will be discussed in section 3.2.

Table 2.12: Summary of the validation protocol.

Turbulent model		
Model constants	Table 1.2 or Table 1.3	
Numerical procedure	Table 2.2	
Boundary conditions for the continuous phase		
Boundary	**Pipe flow**	**UV reactor**
Inlet	Eqs. (2.3) to (2.7), (2.9) (2.10) (2.15) and (2.16)	pipe profiles for Ui, k, and ε at 3.5 m
Outlet	Pressure outlet zero gauge	Pressure outlet zero gauge
Near wall treatment	Non-slip condition	Non-slip condition
Discrete Phase Model		
Particle diameter	$1.0x10^{-4}$ m	$1.0x10^{-4}$ m
Maximum number of Steps	43500	43500
Length scale	0.0002 m	0.0002 m
Lagrangian Empirical constant	0.15 or 0.30	0.15 or 0.30
Number of injected particles	10000	60000
Boundary conditions for the fluid particle		
Inlet	Equations (2.3) to (2.7)	
Outlet	Escape	
Near wall treatment	"Reflect" only for the tangential component	
Materials		
Particle density	998.2 kg/m^3	
Fluid properties	Table 2.5	
UV fluence rate model		
Initial conditions	Table 2.9, 2.10 and 2.11	
Microorganism inactivation model		
Kinetic equation	Equations(1.55), (1.57) and (1.54)	

3 Simulations and Sensitivity Study Results

This chapter presents a sensitivity analysis that identifies the most significant factors affecting CFD predictions for Sentinel UV reactor performance. Validations of UV reactor performance using CFD models conducted by either UV manufacturers or consultants revealed that the simulation results slightly over predict the results from biodosimetry (Wayne et al. 2002 and Rokjer et. al. 2002). In these studies, the difference between biodosimetry and CFD predictions could be attributed to the assumptions invoked in the CFD models. The aims of this chapter are to 1) ensure that the CFD predictions are consistent with expectations, and 2) investigate the effect of design, operational and computational factors and their interactions on the predicted performance of a UV reactor.

A second objective of this work was to provide insight into the design variables that can be used to improve UV reactor performance. A more uniform spatial dose distribution, and narrower dose distribution over a population of microorganism, can be achieved by 1) inserting baffles, and 2) increasing the number of lamps, thus reducing the spacing between lamps. Baffles provide mixing across UV fluence rate gradients but also increase the hydraulic pressure drop. A large number of lamps provide better spatial distribution of the fluence rate but increase the operational and maintenance costs. Several computational, operating and design variables were varied for the Sentinel UV Reactor (SUVR) to investigate the balance between these effects.

The work described in this chapter is divided into four phases: 1) preliminary analysis of the CFD predictions of the flow field, 2) optimization of the number of

particles required by the simulation to provide reliable results, 3) sensitivity analysis of the operational and computational factors of the SUVR, and 4) evaluation of modified reactor designs using different microorganism inactivation models.

3.1 Preliminary Analysis

The goal of the preliminary analysis was to select the turbulence model and the mesh to be used in subsequent simulations. The objectives of the preliminary analysis were to 1) compare the k-ε and RSM turbulence models for prediction of the steady-state flow field in the SUVR, 2) compare the k-ε and LES models for prediction of the periodic characteristics of the unsteady-state flow field, and 3) determine a mesh type and resolution that provides a good compromise between accuracy and computational effort. The selection of the k-ε, Reynolds Stress Model (RSM) and Large Eddy Simulation (LES) turbulence models for investigation was based on the following four arguments.

1) The steady-state k-ε model is considered capable of resolving the mean characteristics of the flow expected in the SUVR.

2) The RSM model provides a better description of inhomogeneous flows

3) The unsteady-state k-ε model has been used to describe periodic flow around bodies.

4) The LES model is often used for predicting complex unsteady-state flow.

The mesh definition for the SUVR was described in Table 2.3 and the spatial resolution of the meshes was illustrated in Figures 2.4 to 2.7. Two volumetric flow rates were evaluated, 75×10^6 and 150×10^6 m^3/d, which correspond to average superficial velocities, $\bar{U}$, of 0.77 m/s and 1.54 m/s, respectively (the average velocity was based on

flowrate divided by cross sectional area of the reactor). Due to the high flow rates, the flow regime in the SUVR was turbulent and the Reynolds number, Re, ranged between 9.18×10^5 and 1.83×10^6 (based on the reactor diameter). The numerical computations were carried out under the simulation conditions listed in Table 2.12. In each case, the simulation was run until the normalized residuals were less than 1.0×10^{-4}.

3.1.1 Steady-State Analysis

Steady-state analysis was conducted using both the k-ε and RSM models for two mesh geometries and two grid resolutions: 1) an Unstructured Hexahedral Coarse Mesh (UHCM) and an Unstructured Hexahedral Fine Mesh (UHFM) and 2) a Structured Hexahedral Coarse Mesh (SHCM) and Structured Hexahedral Fine Mesh (SHFM). The steady-state simulations provided a useful and somewhat heuristic approximation of the hydrodynamic behavior in the SUVR, which was characterized mainly by large eddies located behind each baffle and a wake region behind the lamps.

The RSM and k-ε models predicted the same general flow field for the SUVR with some minor differences near the wall. The flow fields predicted using the k-ε or RSM models with the UHCM are shown in Figures 3.1 and 3.2, respectively. These figures present the velocity contours for the SUVR. The results shown are only for an average velocity of 1.54 m/s, because the flow field patterns are essentially the same for both velocity studied. An identical dimensionless flow field is expected for turbulent flow because all of the velocities scale with some characteristic velocity. It should be emphasized that the model comparison was done using an UHCM and the same convergence criterion of 1.0×10^{-3}. The velocity contours are lines of constant velocity

magnitude over a selected plane. The velocity contours reveal that both models predict the same overall flow field characteristics, such as 1) vortices between the baffles (blue zone), 2) high velocity regions between the baffles and the lamps (red-yellow zone), and 3) a wake region downstream of the lamps (blue zone surrounded by the red-yellow zones). However, some minor differences between the k-ε and RSM models can be seen in the x-velocity profiles near the wall as shown in Figure 3.3. Using different mesh type did not significantly change the results, as shown in Figure 3.4.

The k-ε and the RSM models in conjunction with the SHCM did not provide mesh independence or satisfactory convergence (normalized residuals less than $1.0x10^{-3}$). The normalized continuity residuals converged to $1.0\ x10^{-2}$ for the both structured meshes (SHCM and SHFM) and to $1.0x10^{-3}$ for both unstructured meshes (UHCM and UHFM). The unsuccessful simulations for structured meshes were attributed to a periodic flow downstream of the lamps, which was identified by comparing consecutive velocity contour plots.

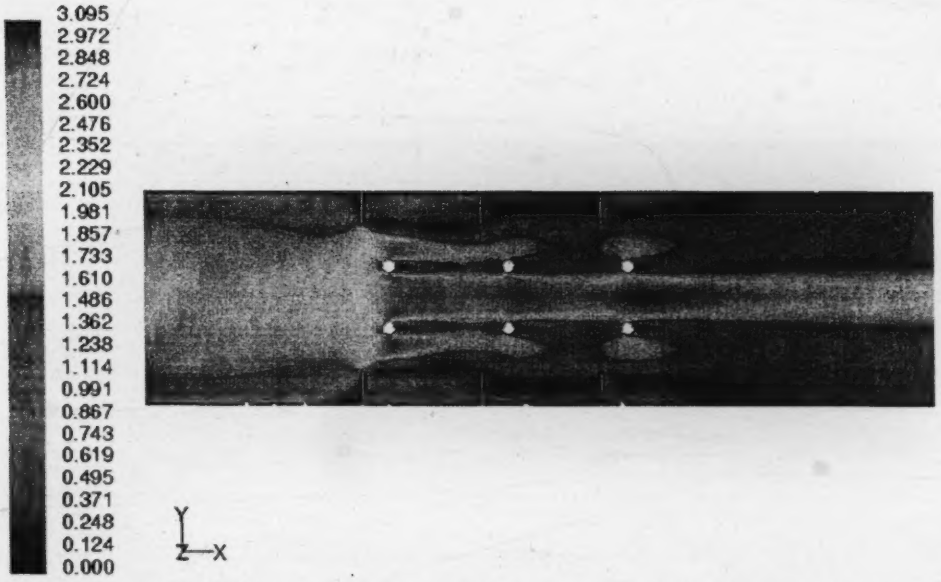

Figure 3.1: Velocity magnitude contours (m/s) in a vertical plane through the central axis of the reactor. Generated using the steady-state k-ε model and the UHCM. The direction of the flow is from left to right, Re = 1.83×10^6, $\bar{U}$ = 1.54 m/s.

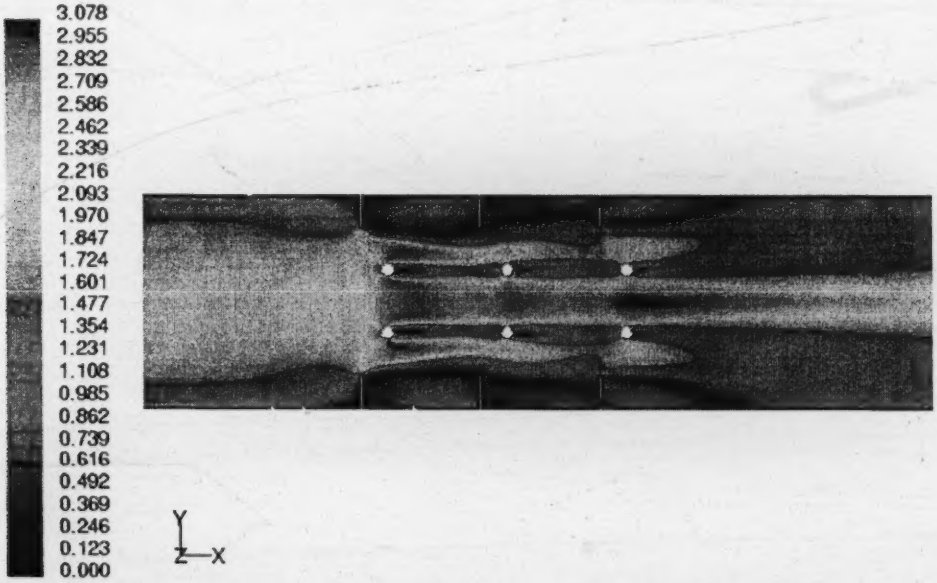

Figure 3.2: Velocity magnitude contours (m/s) in a vertical plane through the central axis of the reactor. Generated using the steady-state RSM model and the UHCM. The direction of the flow is from left to right, Re = 1.83×10^6, $\bar{U}$ = 1.54 m/s.

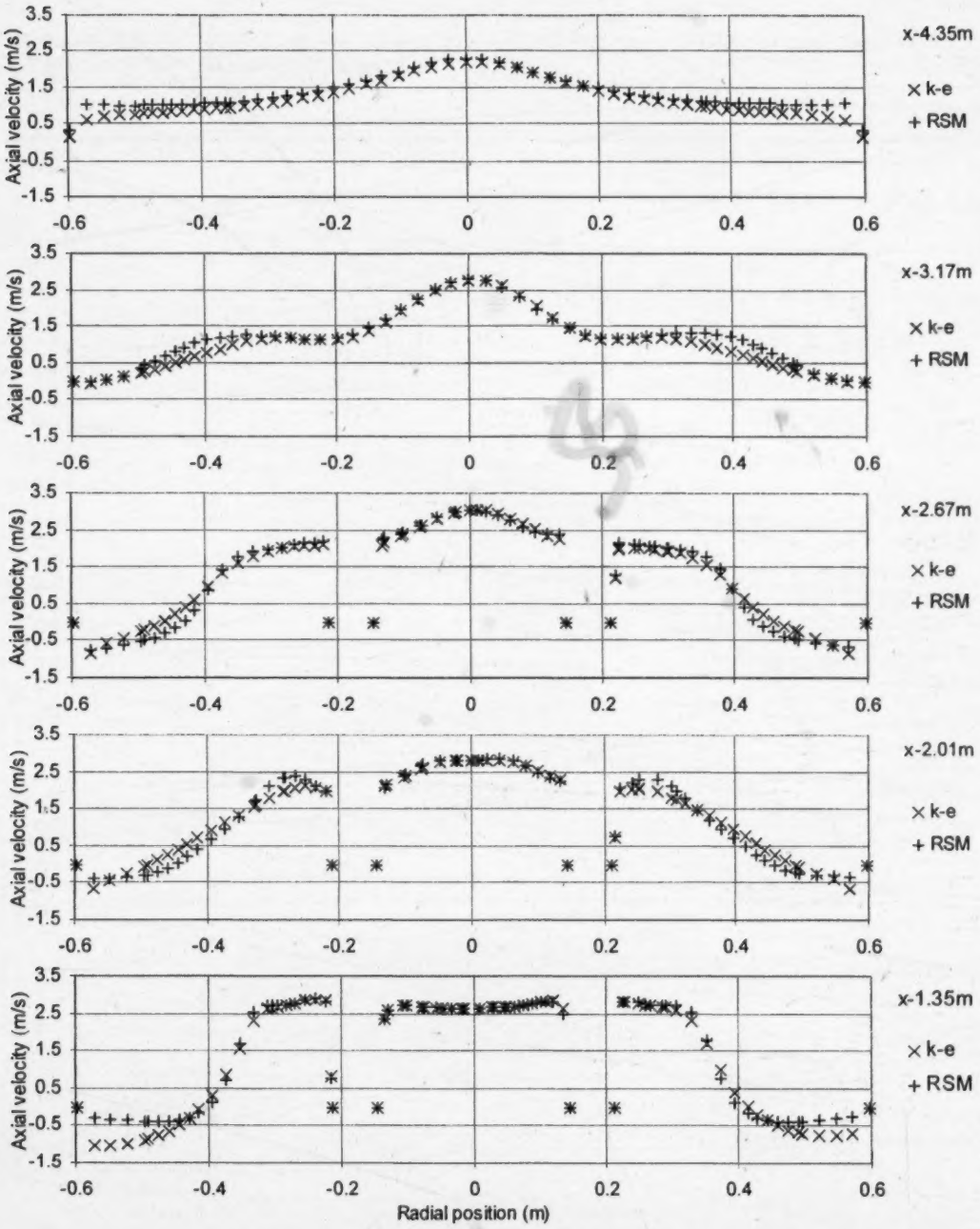

Figure 3.3: Axial velocity profiles in a plane through the central axis of the reactor and at various x-distances from the inlet of the reactor. Generated using the steady-state k-ε or RSM turbulence models and the UHCM. x is the location of these traverses on the reactor geometry. Continuity residual equals to $1x10^{-3}$, Re = $1.83x10^{6}$, $\bar{U}$ = 1.54 m/s.

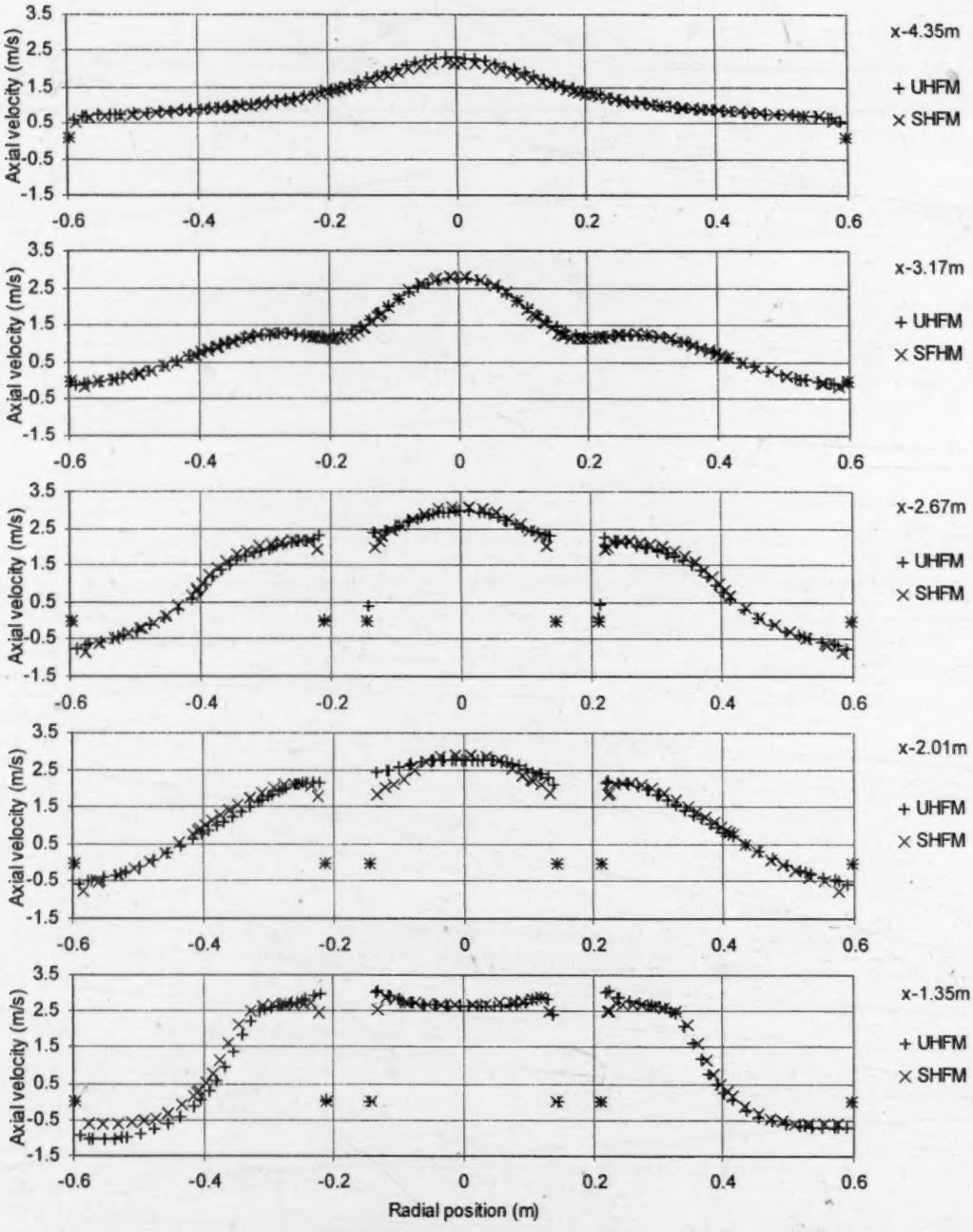

Figure 3.4. Axial velocity profiles in a plane through the central axis of the reactor and at various x-distances from the inlet of the reactor. x is the location of these traverses on the reactor geometry. Generated using the steady-state k-ε model, the UHFM and the SHFM.

Periodic flow in the SUVR was characterized by oscillation of the velocity in the y-direction in the wake region downstream of the lamp. Two questions were raised by observing y-velocity oscillation downstream of the lamps: 1) To what extent does the periodic flow affect the velocity field of the whole domain? 2) Could this phenomenon significantly change the dose distribution? The first question was addressed by performing unsteady simulations of the flow field. The second question was satisfactorily resolved after running the particle tracking simulation (Section 3.2). The final selection of the mesh and the turbulence model is deferred until the periodic results are examined. It can be concluded from the steady-state simulations that 1) the RSM and the k-ε model predicted similar velocity fields for the SUVR, and 2) the flow field patterns are similar for a set of Reynolds numbers simulated.

3.1.2 Unsteady State Analysis

Unsteady-state analysis was conducted to provide insight into the flow field characteristics due to the presence of periodic flow in the SUVR. Two turbulence models were used to accomplish the objective: 1) the unsteady-state k-ε model, and 2) the LES. The unsteady-state k-ε model was selected due to its numerical stability even though this model was not designed for non-equilibrium flow (the k-ε model does not account for non-local strain history and adverse pressure gradients). The LES model was selected because it is the most suitable model for unsteady-state flow, particularly when large structures are present.

A time step of 0.01 s was used to generate approximately 20 points in one oscillation period of 0.20 s. The oscillation period was estimated using Equation 3.1, and a experimental Strouhal number of 0.179 (Cantwell and Coles, 1983).

$$S_{tr} = \frac{fD_l}{U_\infty} \tag{3.1}$$

where

S_{tr} = Strouhal number

f = frequency, (Hz)

D_l = lamp diameter (m)

U_∞ = the flow free stream velocity

The time history of the y-velocity at a single point was recorded to quantify the periodicity of the flow. This point was located at three lamp diameters downstream of the first lamp (x = 1.55m, y = 0.178m, z = 0.0m). This point is located inside the wake but outside the separation region.

Simulations of the SUVR using the unsteady-state k-ε model showed a sinusoidal oscillation of the y velocity downstream of the lamps. Figures 3.5 and 3.6 present the predicted y-velocity as a function of the time for both the SHFM and UHFM using the unsteady-state k-ε model. Both figures show a sinusoidal oscillation of the y-velocity, which is more regular and of higher amplitude with the SHFM. Although a longer iteration time was used with the UHFM, it did not predict the maximum amplitude of ±1.25 m/s calculated with the SHFM. From Figure 3.5, an oscillation period of 0.17s was obtained. This corresponds to a Strouhal number of 0.22 which is greater than the experimental value of 0.17 reported by Cantwell and Coles (1983). The difference may be attributed to the sensitivity of the Strouhal number to the experimental conditions.

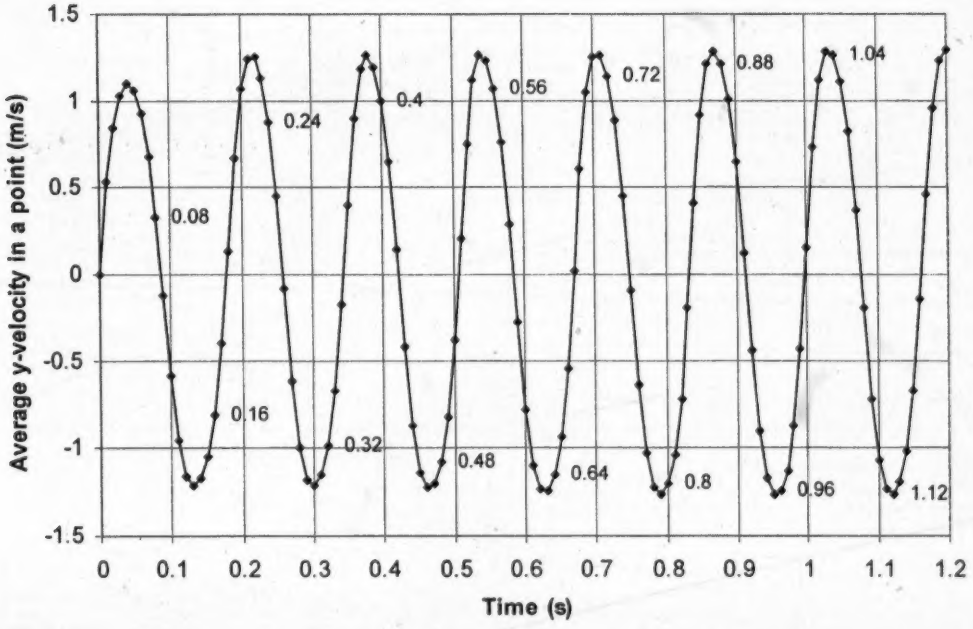

Figure 3.5: y-velocity as a function of time at a point located three lamps diameters downstream of the first lamp generated using the SHFM, unsteady-state k-ε model, Re = 1.8×10^6, and Time step = 0.01 s.

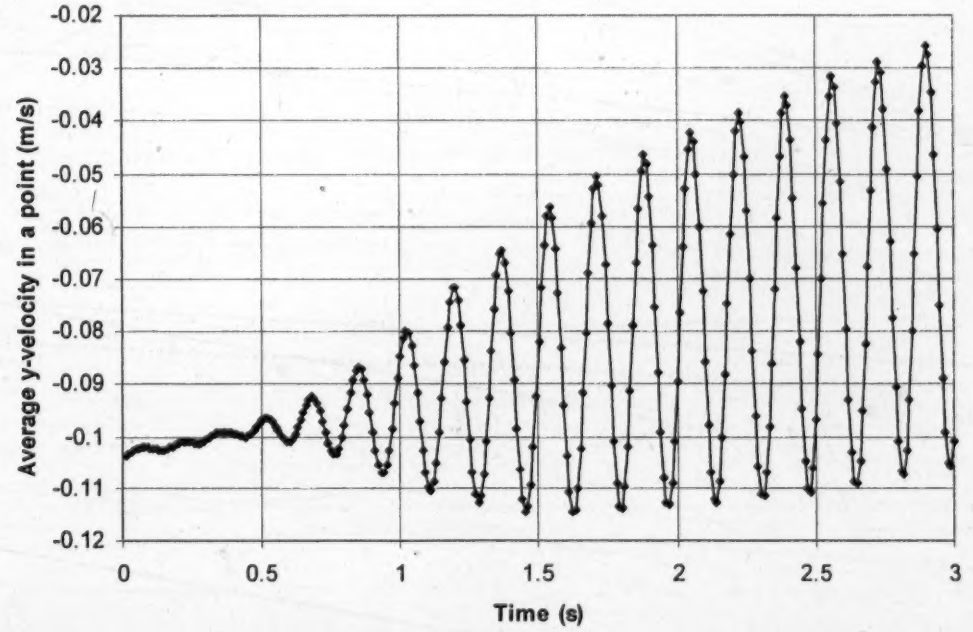

Figure 3.6: y-velocity as a function of the time at a point located three lamps diameters downstream of the first lamp generated using the UHFM, unsteady-state k-ε model, Re = 1.8×10^6 and Time step = 0.01 s.

Cantwell and Coles used a uniform velocity flow and circular endplates to isolate the flow over the cylinder ends. In the case of the SUVR, these ideal conditions cannot be satisfied due to the interactions between the flow around the lamps, the baffles, and the reactor wall.

It was found that the y-velocity oscillation downstream of the lamps correlated the axial velocity of the fluid between the lamps. Axial velocity contours and x-y velocity profiles shown in Figure 3.7 to 3.9 illustrate the relationship between the y-velocity oscillation and the x-velocity. The simulation times selected for these figures correspond to a half oscillation period starting at the high amplitude of 1.04 s and ending at the low amplitude of 1.12 s (Figure 3.5). It can be appreciated from these figures that the y-velocity oscillation downstream of the lamps is associated with changes of the x-velocity between the lamps (Figure 3.9).

Further unsteady-state simulations using LES were executed to provide flow field characteristics from a different perspective. The simulations using the unsteady-state k-ε model provided a different amplitude of the y-velocity oscillation depending on the mesh used. It was not possible to determine which simulation was more accurate due to a lack of experimental data for comparison.

The LES simulations predicted not only an oscillatory y-velocity downstream of the lamps, but also a complex flow field cycle in the domain (Figures 3.10 to 3.15). This complex cycle included vortex formation, vortex squeeze, vortex collapse, and vortex dissipation. A vortex was formed after a high-velocity parcel of fluid first struck the second baffle, then the reactor wall, and finally the velocity stream from which it originated. In this process a low-velocity parcel of fluid was trapped in the interior and

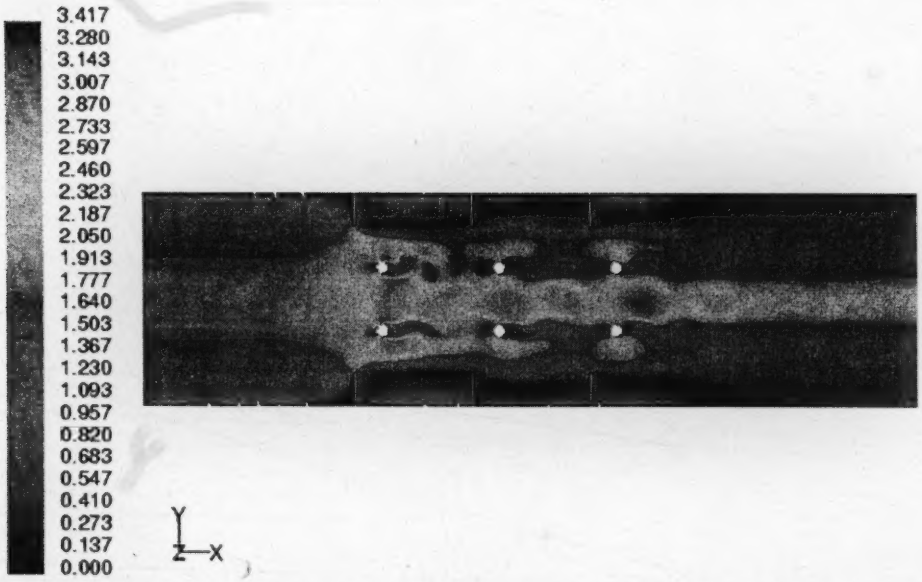

Figure 3.7: Velocity magnitude contours (m/s) in a vertical plane through the central axis of the reactor. Generated using the unsteady-state k-ε model and the SHFM, Re = 1.8×10^6 time = 1.04s.

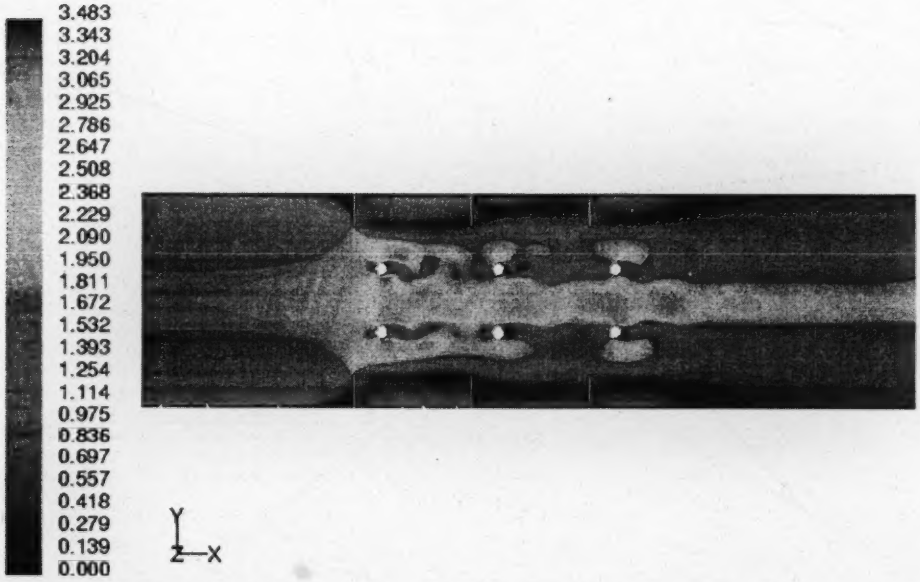

Figure 3.8: Velocity magnitude contours (m/s) in a vertical plane through the central axis of the reactor. Generated using the unsteady-state k-ε model and the SHFM, Re = 1.8×10^6 time = 1.12s.

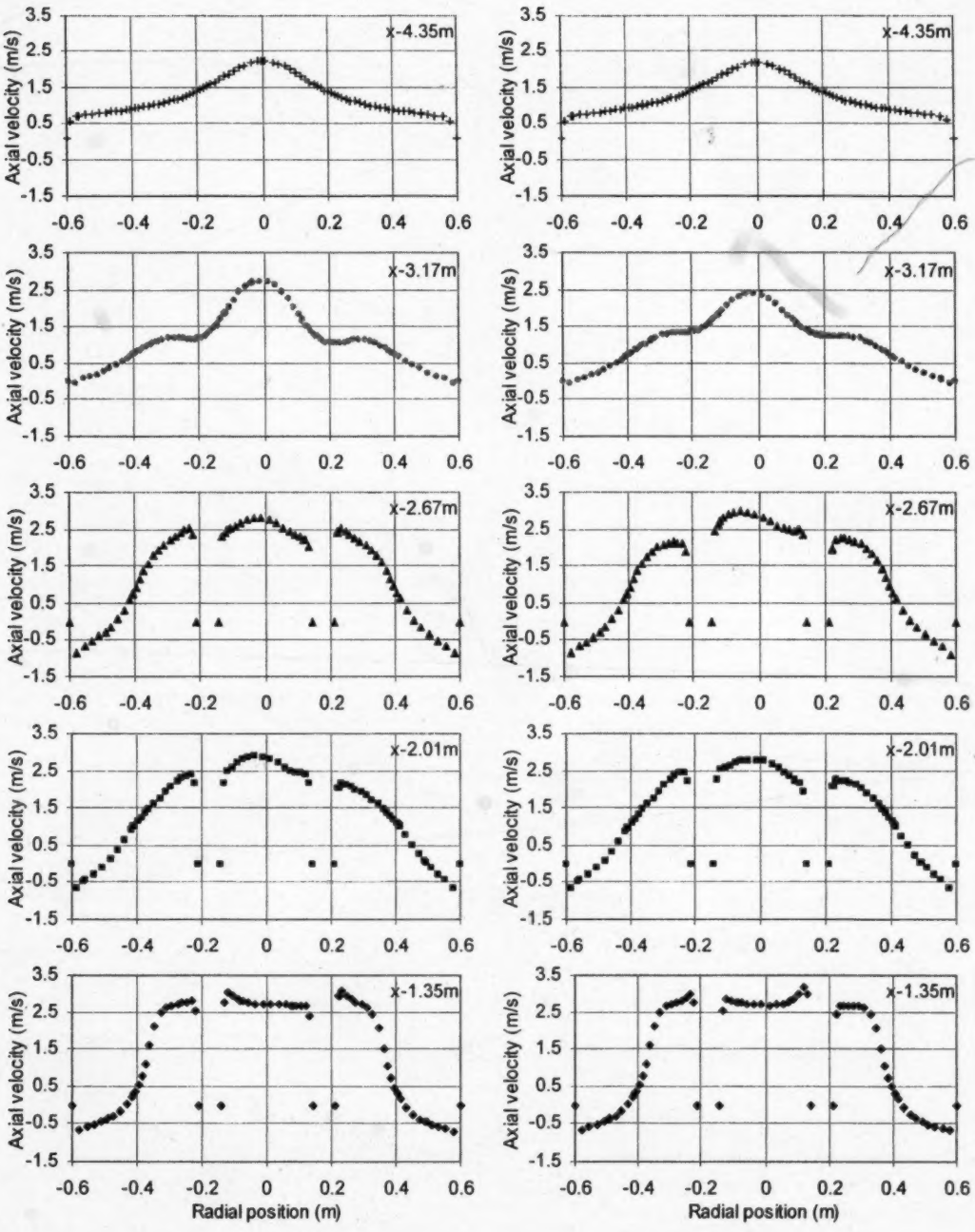

Figure 3.9: Axial velocity profiles in a plane through the central axis of the reactor and at various x distances from the inlet of the reactor. Generated using the unsteady-state k-ε model and the SHFM, Re = 1.83×10^6. Left column: time = 1.04s. Right column: time = 1.12s. x is the location of these traverses on the reactor geometry.

was surrounded continuously until it defined an independent structure called a vortex. Meanwhile the oscillatory wake region launched high-velocity flow parcels, which squeezed the vortex in the y-direction after several interactions between the vortex and the fluid parcels from the wake. This vortex collapsed with the vortex shedding from the lamps and struck the next lamp in the row where it dissipated. The domain underwent the above mentioned vortex cycle at each baffle, with the vortex cycles pattern changing as the fluid advanced through each reactor bank[8]. These vortex cycles were not synchronized between consecutive banks.

The flow field characteristics estimated by the LES model depended on the type of mesh used for calculation. For example, the combination of LES model and SHFM predicted a symmetrical flow field in the plane located at y = 0 m (Figures 3.10 to 3.12). The combination of LES model and UHFM predicted an asymmetrical flow field and a more complex vortex cycle pattern (Figure 3.13 to 3.15).

Using the LES simulations as a reference, it is more likely that the combination of the unsteady-state k-ε model and SHFM predicted the correct velocity field than the combination of unsteady-state k- ε model and UHFM. However, in the absence of experimental data it is impossible to make this a firm conclusion. The LES model predicted the y-velocity oscillation regardless of the mesh used for the SUVR simulations. In addition, the overall axial-velocity profiles at the lamps predicted by the two turbulence models followed similar trends (Figures 3.9 and 3.12).

[8] Bank refers to the reactor volumes between successive baffles and containing one set of lamps

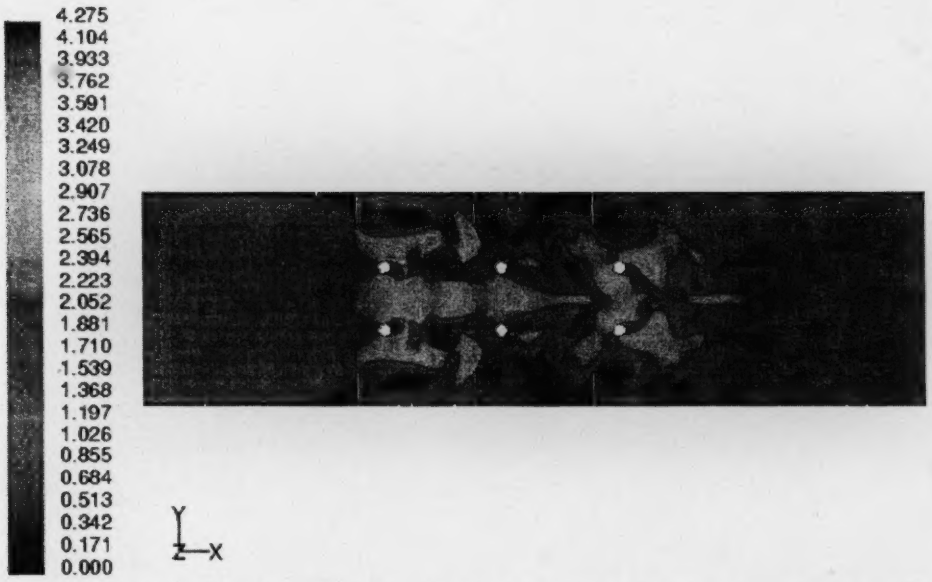

Figure 3.10: Velocity magnitude contours (m/s) in a vertical plane through the central axis of the reactor. Generated using the LES model and the SHFM at time step = 1.20s, Re = 1.83×10^6.

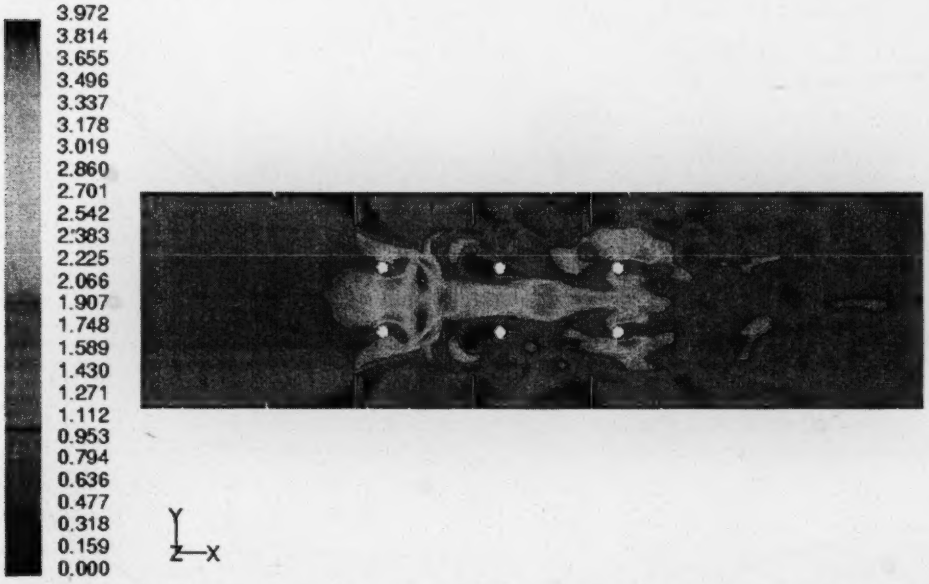

Figure 3.11: Velocity magnitude contours (m/s) in a vertical plane through the central axis of the reactor. Generated using the LES model and the SHFM at time step = 1.60s, Re = 1.83×10^6.

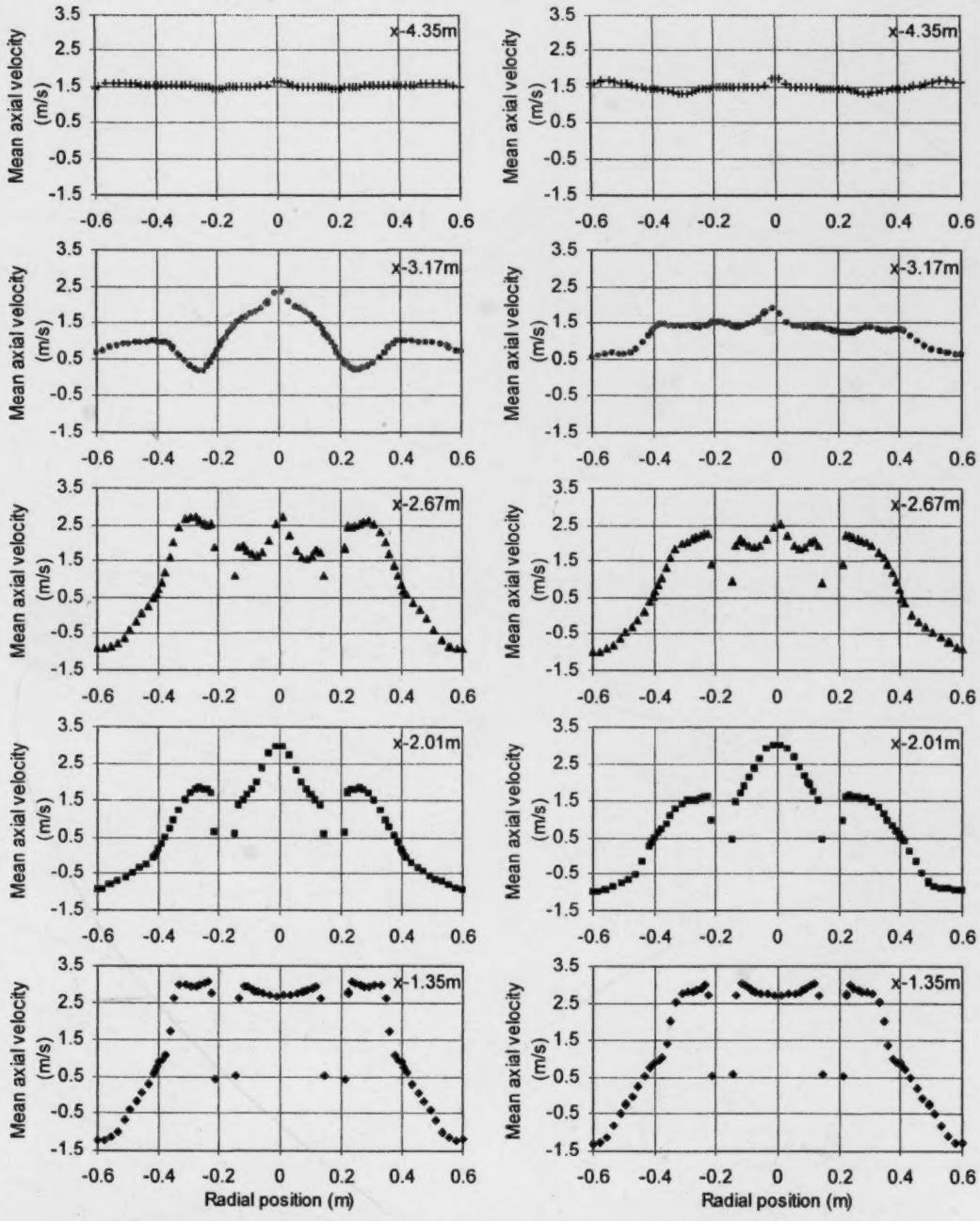

Figure 3.12: Axial velocity profiles in a plane through the central axis of the reactor and at various x distances from the inlet of the reactor. Generated using the LES model and the SHFM, Re = 1.83×10^6. Left column: time step = 1.2s. Right column: time step = 1.6s. x is the location of these traverses on the reactor geometry.

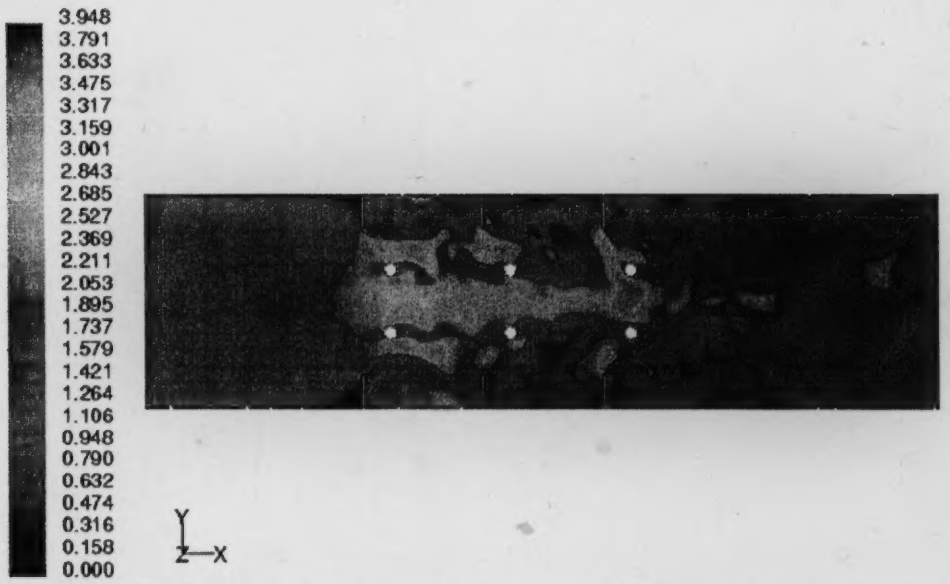

Figure 3.13: Velocity magnitude contours (m/s) in a vertical plane through the central axis of the reactor. Generated using the LES model and the UHFM at time step = 1.20s, $Re = 1.83 \times 10^6$.

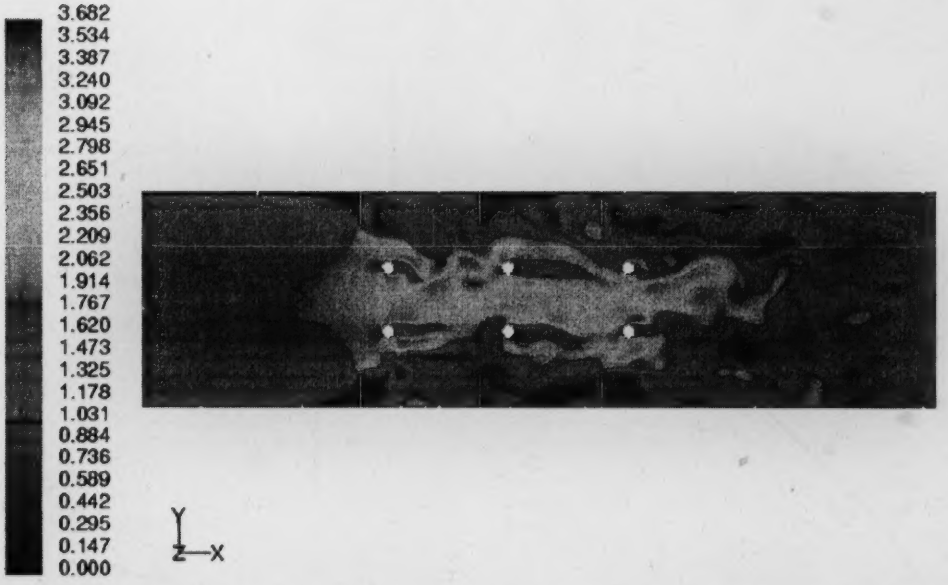

Figure 3.14: Velocity magnitude contours (m/s) in a vertical plane through the central axis of the reactor. Generated using the LES model and the UHFM at time step = 1.60s, $Re = 1.83 \times 10^6$.

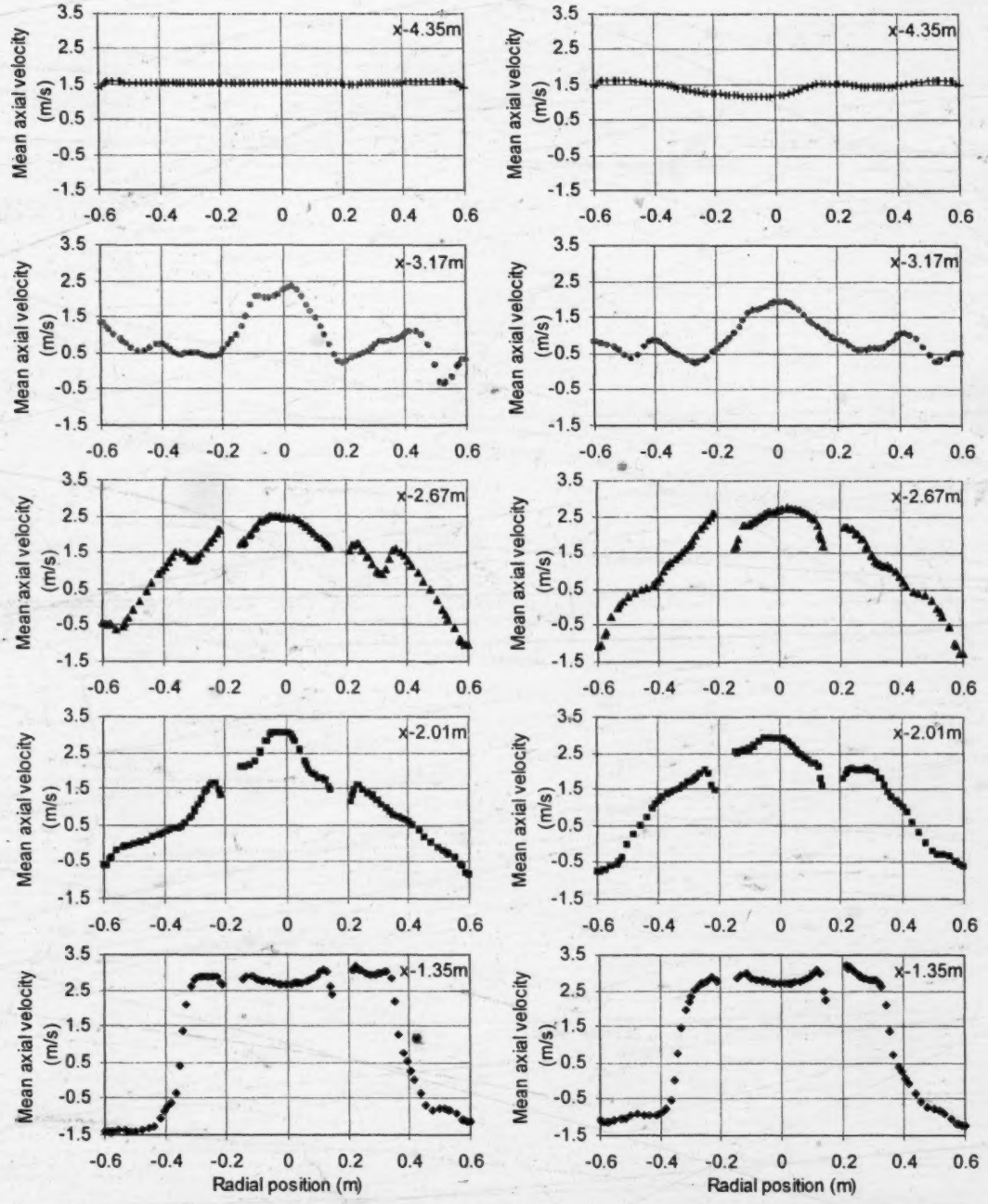

Figure 3.15: Axial velocity profiles in a plane through the central axis of the reactor and at various x distances from the inlet of the reactor. Generated using the LES model and the UHFM, Re = 1.83×10^6. Left column: time step = 1.2s. Right column: time step = 1.6s. x is the location of these traverses on the reactor geometry.

3.1.3 Summary

The preliminary investigation conducted above was critical for the numerical analysis of 3-D turbulent flow in the SUVR operated at a large Reynolds number. Three turbulence models were evaluated and compared; the standard k-ε, the RSM and the LES. The primary emphasis was on the prediction of expected flow characteristics such as large eddies near the baffles and vortices behind the lamps.

A comparison of the preliminary simulation results led to the following conclusions:

1. The steady state k-ε and RSM models can be used for subsequent simulations. Although both models predict a similar velocity field, it cannot yet be assumed at this point that they provide similar particle tracking due to the different assumptions used.
2. The UHFM will be used for subsequent steady-state simulations, because it provides satisfactory convergence with less computational effort than the SHFM.
3. The SHFM will be used for subsequent unsteady state simulations because it predicts a more stable y-velocity periodicity than the UHFM.
4. The LES model is clearly more suitable for calculating the complex flows in a UV reactor than the unsteady-state k-ε model. However, it demands a high computational effort and the differences in velocity profiles are small. Thus, it will not be used for further simulations.

The continuous phase analysis allows the number of computational factors to be included in the sensitivity analysis to be reduced. A similar approach was used to reduce the factors in the particle tracking calculations. The most important factor is the number of particles, which is addressed in the next section.

3.2 Optimum Number of Particles

When the DPM and the DRW models are used for particle tracking in a UV reactor, the number of particles must be large enough to produce a representative prediction of the dose distribution. As a general rule, the greater the number of particles, the more reliable the results. However, a larger number of particles requires greater computational effort. Therefore, users of the DPM and DRW models must determine the minimum number of particles required to obtain an accurate solution. The effect of the Lagrangian empirical constant, C_L, must also be determined.

Graham and Moyeed (2002) developed a general approach to estimate the number of particles required to simulate particle-laden air flows in a pipe expansion. They found that the variability of the results (concentration, flux, mean and RMS particle velocities) was proportional to $1/(n_p * n_s)^{0.5}$, where n_p is the number of particles in each simulation and n_s is the number of simulations. They defined variability as the maximum standard deviation of the quantity of interest. In order to characterize the variability of the results, the DPM and DRW models were run using the same number of simulations (n_s) with different numbers of particles per simulation (n_p) (mode 1) or the same number of particles per simulation with different numbers of simulations (mode 2).

The approach proposed by Graham and Moyeed (2002) was adapted in this work for UV reactor analysis. Since the distribution of UV doses received by the microorganism is not a normal distribution, it is necessary to invoke the *central limit theorem* (CLT) to justify the use of t-distribution to generate the confidence limits. This theorem states that for a given distribution with a mean, μ, and variance, σ^2, the sampling distribution of the mean approaches a normal distribution with a mean $\overline{X}$ and a variance σ^2/n_p as the

number of particles per simulation, n_p, increases. The sampling distribution of the mean is a theoretical distribution that is approached as the number of simulations, n_s, increases.

In the context of UV reactor simulation the significance of the central limit theorem is that regardless of the shape of the dose distribution, the distribution of the mean dose will tend to be normal as the number of particles per simulation, n_p, increases. Therefore, the distribution of the mean dose can be characterized in terms of a confidence interval based on the t distribution.

The result of a single numerical simulation with n_p particles was characterized in terms of the distribution of particle residence time and UV dose. For a given simulation, the UV dose distribution was characterized by either equivalent dose, D_{eqv}, determined using Equation 1.64, the UV dose response for MS2 coliphage, or the following statistical moments of the dose distribution: 1) the arithmetic mean of the UV dose distribution called the particle-mean dose, $\overline{D}$, and 2) the standard deviation of the particle-mean dose s_D. The particle residence time distribution was characterized by the following statistical moments: 1) the arithmetic mean of the particle Residence Time Distribution (RTD) called the particle-mean time, $\bar{t}$, and 2) the standard deviation of the particle-mean time, s_t.

The result of n_s simulations with n_p particles was reported in terms of the equivalent dose, particle-mean dose, and the particle-mean time. The particle-mean time demands less computational effort since it does not require computation of UV dose. The particle mean-dose demands an intermediate computational effort since it does not involve computing the microorganism response to the UV radiation. The equivalent dose requires the highest computational effort since it demands computation of both the dose and

microorganism inactivation. Therefore, the three parameters were compared to determine which level of computational effort should be applied to optimize the number of particles.

The particle-mean doses were characterized by the following statistical moments: 1) the arithmetic mean of the particle-mean doses called the simulation-mean dose, $\overline{\overline{D}}$, given by:

$$\overline{\overline{D}} = \sum_{i=1}^{n_s} \frac{\overline{D}_i}{n_s} \tag{3.2}$$

and 2) the standard deviation of the simulation-mean dose, $s_{\overline{D}}$, given by:

$$s_{\overline{D}} = \sqrt{\sum_{i=1}^{n_s} \frac{\overline{D}_i^2 - \overline{\overline{D}}^2}{n_s - 1}} \tag{3.3}$$

The variability of the particle-mean doses was expressed in terms of the 95% confidence interval:

$$\overline{\overline{D}} \pm t_{n_s-1,0.025} s_{\overline{D}} / \sqrt{n_s} \tag{3.4}$$

where, $t_{ns-1,0.025}$ was evaluated from the t-distribution. Similarly, the particle-mean times and the equivalent doses were characterized as the particle-mean doses as follows:

$$\overline{\overline{t}} = \sum_{i=1}^{n_s} \frac{\overline{t}_i}{n_s} \tag{3.5}$$

$$s_{\overline{t}} = \sqrt{\sum_{i=1}^{n_s} \frac{\overline{t}_i^2 - \overline{\overline{t}}^2}{n_s - 1}} \tag{3.8}$$

$$\overline{D}_{eqv} = \sum_{i=1}^{n_s} \frac{D_{eqv_i}}{n_s} \tag{3.9}$$

$$s_{D_{eqv}} = \sqrt{\sum_{i=1}^{n_s} \frac{D_{eqv_i}^2 - \overline{D}_{eqv}^2}{n_s - 1}} \tag{3.10}$$

where:

$\overline{D}_i$ is particle-mean dose of the ith simulation,

$\bar{t}_i$ is particle-mean time of the ith simulation,

$\overline{D}_{eqv,i}$ is the equivalent dose of the ith simulation,

$\bar{\bar{t}}$ is the simulation-mean time,

$s_{\bar{t}}$ is the standard deviation of simulation-mean time,

$\overline{D}_{eqv}$ is the simulation-mean equivalent dose, and

$s_{D_{eqv}}$ is the simulation equivalent dose standard deviation.

3.2.1 Effect of Number of Particles on the Dose Prediction

The effect of the number of particles on the predictions of UV dose is important in order to determine the confidence interval of the mean dose and thus the uncertainty in a UV reactor simulation. The simulations for the optimum number of particle analysis were performed under the conditions given in Table 3.1. The starting positions of the particles at the reactor inlet for each n_s simulation were randomized as described in Section 2.6.2.1.

The number of particles per simulation was selected based on a previously reported simulation, where 12,654 to 100,000 particles were used (Rokjer et. al. 2002, Graham et. al. 2002). In this study, 165, 333, 665, 999, 1332, 1667, and 2000 particles per simulation were evaluated. Each simulation was replicated 30 times for each number of particles, which resulted in 5000 to 70000 particles in total per test.

Figures 3.16 and 3.17 present the dose distributions for 163 and 2003 particles, respectively (not all the particle escape the reactor). It is evident that the overall shape of the dose distribution was similar in both figures; however, the statistical parameters varied as the number of particles increased and the tail of the distribution increased. The particle-mean dose increased from 837 to 847 J/m^2 and the equivalent dose decreased from 508 to 492 J/m^2 as the number of particles increased.

Table 3.1: Simulation conditions to evaluate the number of particles required

Condition	**Value**
Flow rate	6250 m^3/h (150x10^{6}L/d)
Number of lamps in operation	6
Lamp output power	100%
Water transmittance	93% UVT
Mesh type	Unstructured hexahedral fine mesh
Turbulence model	Steady-state k-ε model
Baffles	Yes
Simulation mode	Steady-state
Lamp shadow	On
MS2 coliphage UV dose response	$Log_{10}(N/N_o) = 0.00365D_i + 0.42$
Particle tracking parameters	
Particle diameter	1.0x10^{-4} m
Number of steps	43500
Length scale	0.0002 m
Lagrangian Empirical constant C_L	0.15

Analysis of the simulation results reveals that the size of the confidence intervals of $\overline{\overline{D}}$, $\overline{D}_{eqv}$ and $\bar{t}$ decreased as the number of particles per simulation increased. Figure 3.18 shows the simulation-mean dose, simulation-mean equivalent dose, simulation-mean time and their confidence levels as a function of the number of particles per simulation. As expected, the variability of all three decreases as the number of particles increases.

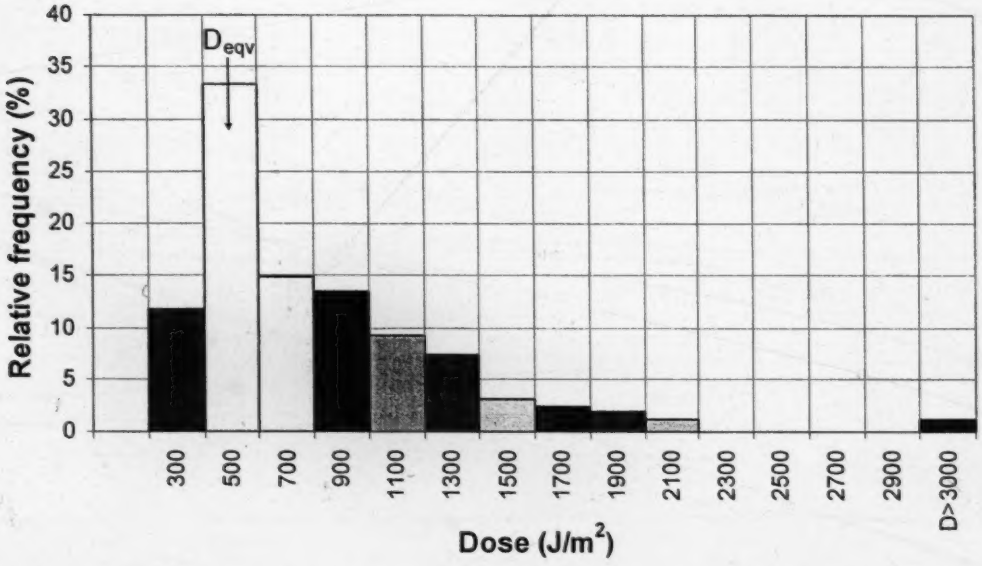

Figure 3.16: Distribution of the dose received by 163 particles for the Sentinel UV reactor under the conditions given in Table 3.1 ($\overline{D}$ = 837.3 J/m^2, D_{eqv} = 508.0 J/m^2, and s_D = 632.6 J/m^2).

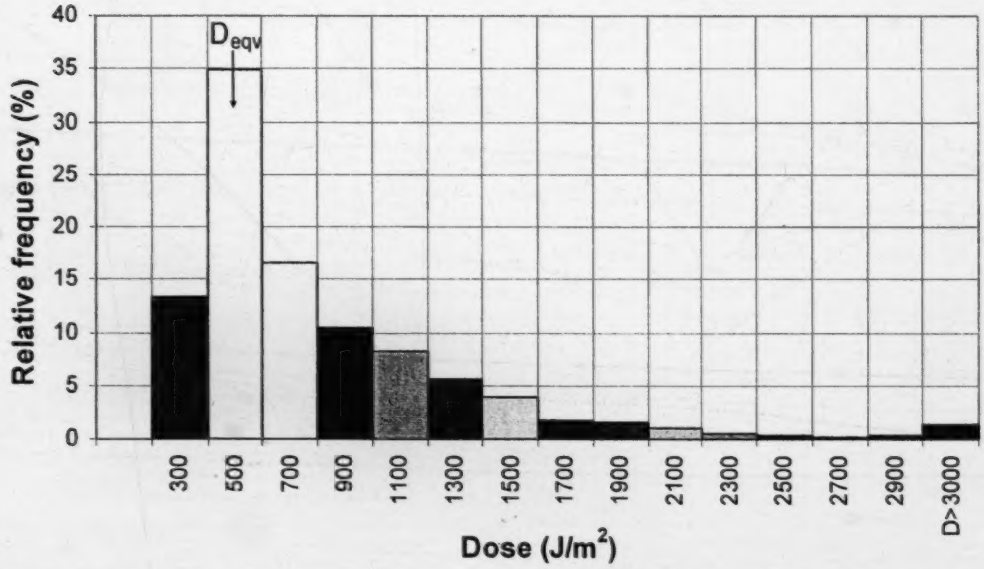

Figure 3.17: Distribution of the dose received by 2003 particles for the Sentinel UV reactor under the conditions given in Table 3.1: ($\overline{D}$ = 847.0 J/m^2, D_{eqv} = 492.7 J/m^2, and s_D = 1254.5 J/m^2).

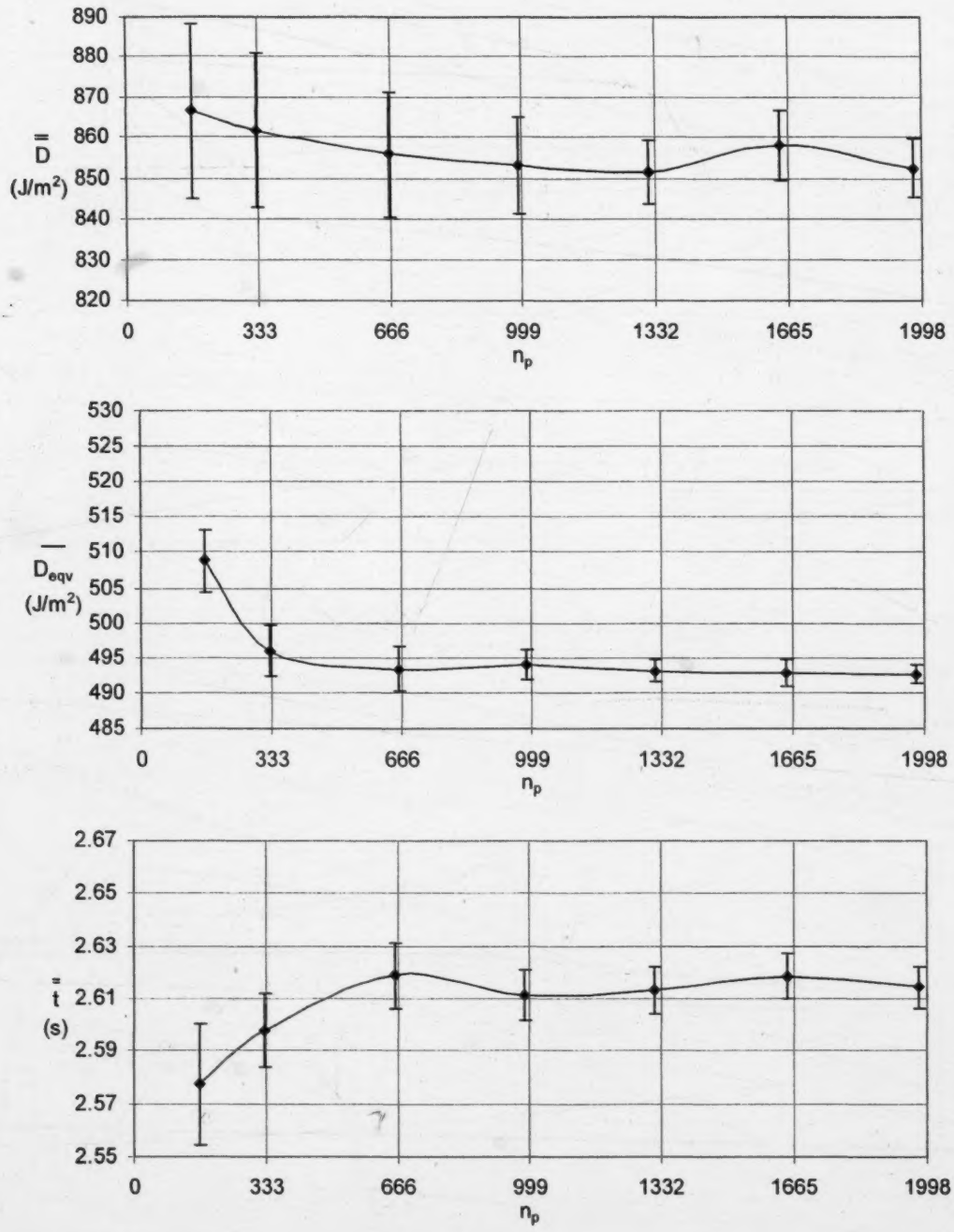

Figure 3.18: Simulation mean dose, $\bar{\bar{D}}$, (top) simulation equivalent dose, $\bar{D}_{eqv}$, (middle) and simulation mean time, $\bar{t}$, (bottom) as a function of the number of particles per simulation. The bar represent 95% confidence intervals at the UV reactor outlet resulting from 30 repeated simulations with $C_L = 0.15$.

A comparison of the pattern between $\overline{\overline{D}}$ and $\overline{D}_{eqv}$ shows that the variability in $\overline{D}_{eqv}$ is considerably lower than the variability in $\overline{\overline{D}}$. This is because the equivalent dose uses the inactivation rate constant, k_r, to weight the dose distribution. For a larger k_r the exponential term, $\exp(-k_r D_i)$, weights microorganisms that receive a lower dose more strongly than those which received higher dose (Wright and Lawryshyn, 2000). This tends to dampen the variability in dose. Consequently, the equivalent dose, D_{eqv}, should be used to estimate the number of particles required rather than the particle-mean time or the particle-mean dose.

3.2.2 Effect of the Number of Simulations on the Dose Prediction

Graham and Moyeed (2002) proved that the size of the confidence levels is not only a function of the number of particles per simulation, n_p, but also of the number of simulations, n_s. Therefore, a large number of simulations should provide a narrow confidence interval of the simulation-mean dose. However, a larger number of simulations require a longer simulation time and larger storage capacity in the computer as the results from each simulation are stored separately and processed. The objective of this section was to determine the minimum number of simulations beyond which no significant changes in the size of confidence interval of the simulation-mean dose are evident. The study was done by running 5, 15, 25, 35, 45, and 55 simulations with 1000 particles for each simulation (i.e., 5,000 to 55,000 particles in total).

Analysis of the simulations shows that the size of the confidence levels of $\overline{\overline{D}}$, $\overline{D}_{eqv}$ and $\overline{\overline{t}}$ decreased as the number of simulations increased. Figure 3.19 shows the simulation-mean dose, simulation-mean time and simulation-mean equivalent dose are

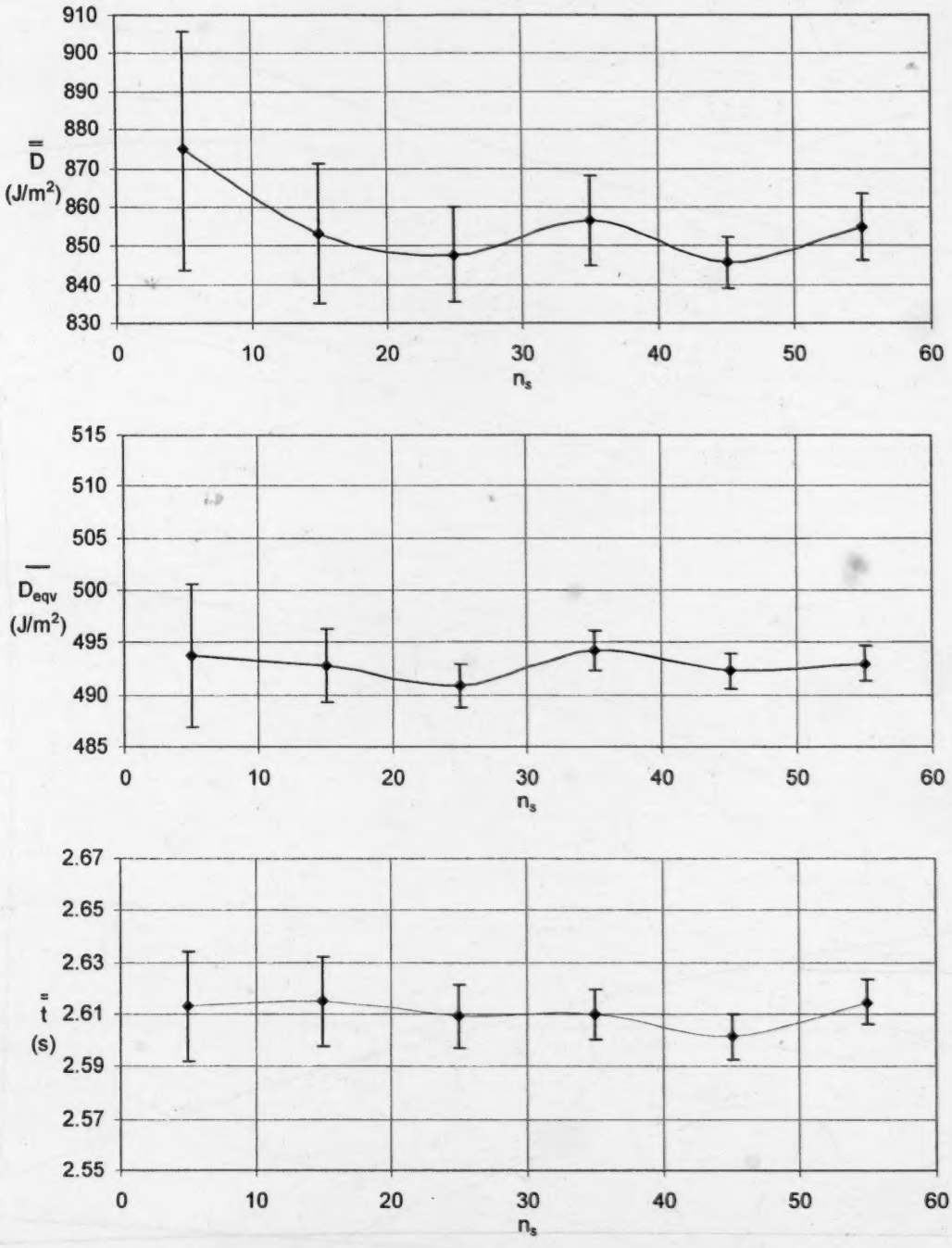

Figure 3.19: Simulation mean dose, $\bar{\bar{D}}$, (top) simulation equivalent dose, $\bar{D}_{eqv}$, (middle) simulation mean dose, $\bar{\bar{t}}$, (bottom) as a function of the number of particles per simulation. The bars represent the 95% confidence intervals at the UV reactor outlet resulting from n_s repeated simulations using a 1000 particles with $C_L = 0.15$.

functions of the number of simulations. From the figure, it can also be seen that the variability of three all decreases as the number of simulations increases.

3.2.3 Effect of the Total Number of Particles on the Dose Prediction

It is more convenient for a CFD user to do one simulation than several. A single simulation with n_p particles is appropriate if it can be demonstrated that the same variability can be expected by performing one simulation with n_p particles or n_s simulations with one particle.

In this study, the above demonstration was done by plotting the size of the confidence interval of the simulation-mean dose, $E_{\bar{D}}$, simulation equivalent dose, $E_{D_{eqv}}$, and simulation-mean time, $E_{\bar{t}}$, as a function of the total number of particles (n_p x n_s) under two different scenarios (Figure 3.20): one with n_s held constant at 30 and n_p varied; the other with n_p held constant at 1000 and n_s varied. The linear least-squares regressions for each set of the simulations were also plotted in Figure 3.20, which illustrates that variability was proportional to $1/(n_p \times n_s)^{0.5}$. This finding is consistent with that of Graham and Moyeed (2002).

The results presented in Figure 3.20 show that a single simulation can be performed with a number of particles determined based on the confidence interval the CFD user is willing to tolerate. For the remainder of this chapter, more than 55000 particles were used to provide the confidence interval given in Table 3.2.

The confidence interval of the equivalent dose is limited to the MS2 and cannot be extended to other microorganisms. This does not apply to the simulation mean dose or particle mean time, which are independent of the microorganism used for the simulations.

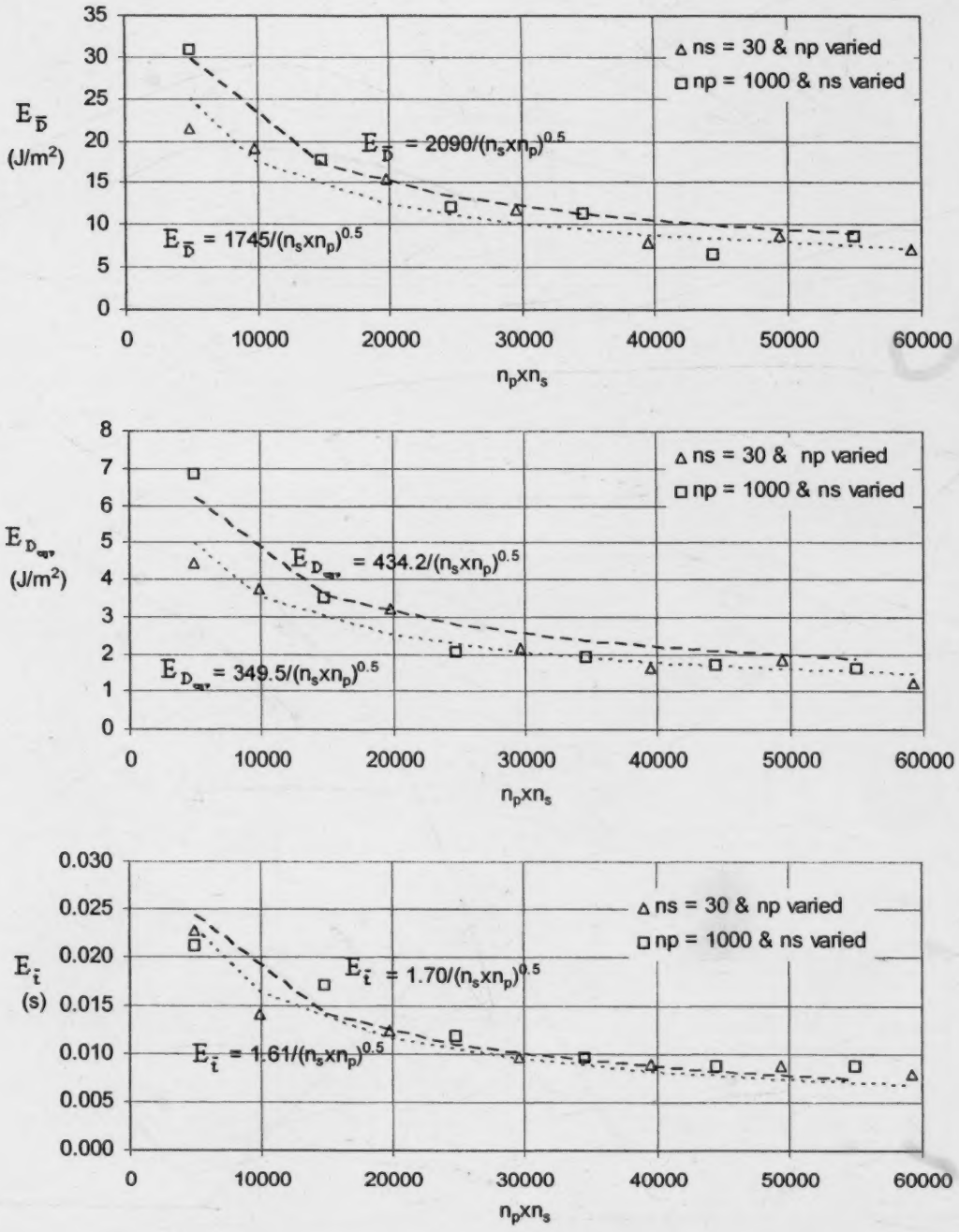
$E_{\bar{D}}$ (J/m²)
ns = 30 & np varied
np = 1000 & ns varied
$E_{\bar{D}} = 2090/(n_s x n_p)^{0.5}$
$E_{\bar{D}} = 1745/(n_s x n_p)^{0.5}$
$n_p x n_s$
$E_{D_{eqv}}$ (J/m²)
$E_{D_{eqv}} = 434.2/(n_s x n_p)^{0.5}$
$E_{D_{eqv}} = 349.5/(n_s x n_p)^{0.5}$
$E_{\bar{t}}$ (s)
$E_{\bar{t}} = 1.70/(n_s x n_p)^{0.5}$
$E_{\bar{t}} = 1.61/(n_s x n_p)^{0.5}$

Figure 3.20: Size of the confidence interval of simulation mean dose, $E_{\bar{D}}$,(top) simulation equivalent dose, $E_{D_{eqv}}$, (middle) simulation mean time, $E_{\bar{t}}$, (bottom) as a function of the total number of particles (n_p x n_s) with $C_L = 0.15$. The lines represent the linear least square regression for each set of the simulations.

Table 3.2: Confidence intervals and standard deviation expected for the SUVR under the conditions given in Table 3.1 with $n_p \times n_s = 55{,}000$ particles and $C_L = 0.15$. These values were computed using the linear regressions given in Figure 3.20 and Equation 3.4.

Variable	Size of the confidence interval	Standard Deviation	Variance
$\overline{D}_{eqv} = 492.7$ J/m^2	$E_{D_{eqv}} = \pm 1.49$ J/m^2	$s_{D_{eqv}} = 3.99$ J/m^2	$s^2_{D_{eqv}} = 15.92$ J/m^2
$\overline{\overline{D}} = 852.5$ J/m^2	$E_{\overline{D}} = \pm 7.44$ J/m^2	$s_{\overline{D}} = 19.93$ J/m^2	$s^2_{\overline{D}} = 397.2$ J/m^2
$\overline{\overline{t}} = 2.614$ s	$E_{\overline{t}} = \pm 0.007$ s	$s_{\overline{t}} = 0.019$ s	$s^2_{\overline{t}} = 0.0004$ s

From Figures 3.18 to 3.20, it can be concluded that the variability of the simulation mean dose, the equivalent dose and the simulation mean time are a function of the product (n_p x n_s). The number of particles selected to minimize variability in the results was 55,000.

3.2.4 Effect of the Lagrangian Empirical Constant on the Dose Prediction

As discussed in Sections 1.8.2 and 2.6, the Lagrangian empirical constant, C_L, is a computational parameter that determines the time period a particle is allowed to interact with an eddy, the velocity fluctuation during this period, and also indirectly determines the particle dispersion.

Two values of C_L, 0.15 representing level (-) and 0.30 representing level (+), were used for the following simulations, which are in the range given in Table 1.5. A comparison of the results presented in Figures 3.18 and 3.21 indicates that $\overline{D}_{eqv}$ decreases and $\overline{\overline{t}}$ increases with the increase of C_L level from 0.15 to 0.30. This finding was expected since increasing the C_L level results in greater particle dispersion and longer particle residence time, as shown in Figures 2.21 and 2.24. This is consistent with results reported by MacInnes and Bracco (1992) the random walk model with different Lagrangian time yields a different dispersion rate.

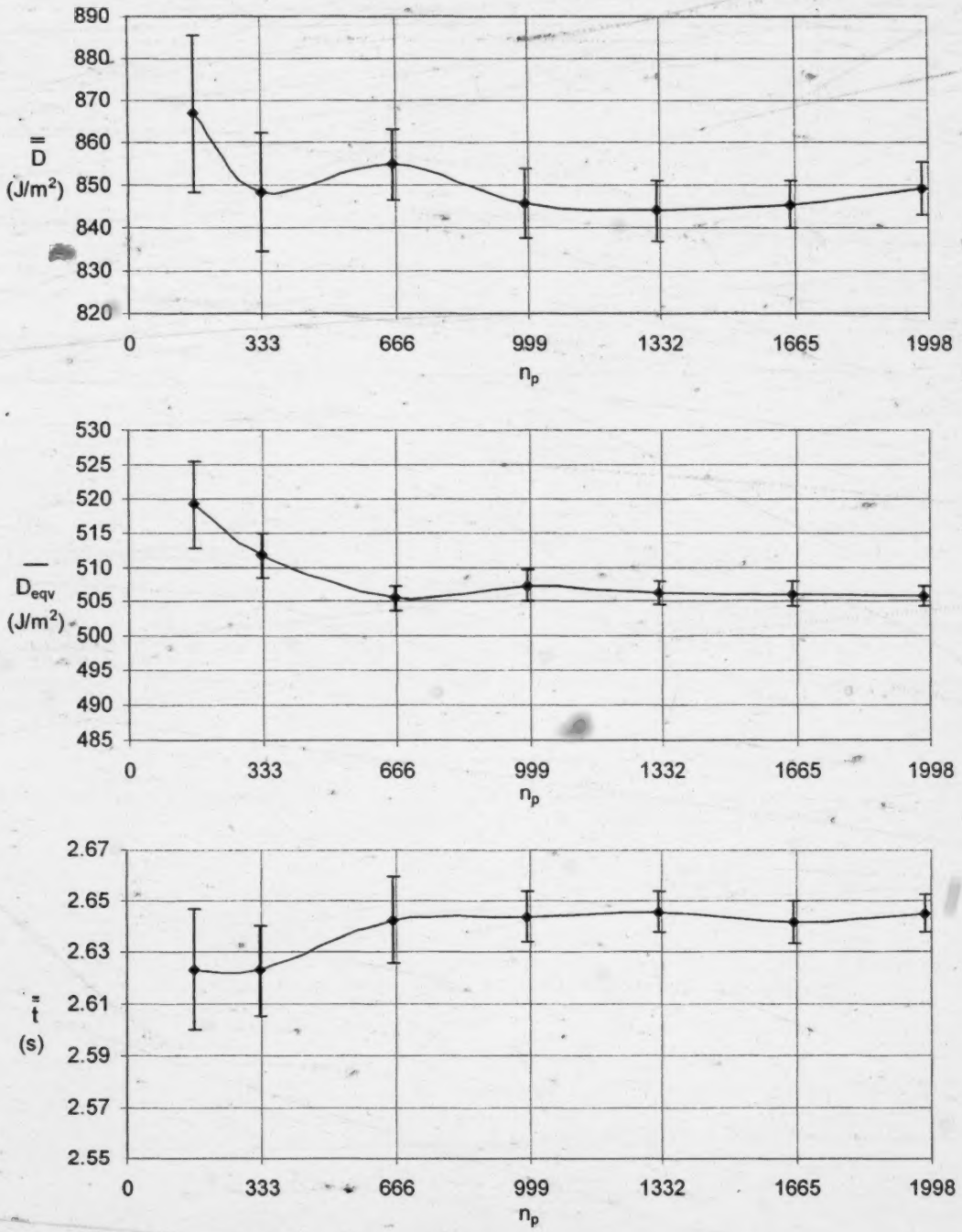

Figure 3.21: Simulation mean dose, $\bar{\bar{D}}$, (top) simulation equivalent dose, $\bar{D}_{eqv}$, (middle) and simulation mean time, $\bar{\bar{t}}$, (bottom) as a function of the number of particles per simulation. The bar represent 95% confidence intervals at the UV reactor outlet resulting from 30 repeated simulations with $C_L = 0.30$.

A statistical analysis of the simulation results shows that the C_L level has a significant effect on the prediction of the SUVR performance. The following null hypothesis was used for this analysis: the different C_L levels do not have any significance on the UV dose prediction, $(\eta^- - \eta^+)_o = 0$. To test the null hypothesis, it was assumed that the population variances, σ^2_{Deqv}, for levels (+) and (-) are, to an adequate approximation, equal. Thus the estimates in Tables 3.2 and 3.3 were combined to provide a pooled estimated of $s^2_{D_{eqv}}$ of this common σ^2_{Deqv}. This was done by using the following equation:

$$s^2_{D_{eqv}} = \frac{\sum\left(D^-_{eqv} - \overline{D}^-_{eqv}\right)^2 + \sum\left(D^+_{eqv} - \overline{D}^+_{eqv}\right)^2}{n^-_s + n^+_s - 2} = \frac{s^{2-}_{D_{eqv}}\left(n^-_s - 1\right) + s^{2+}_{D_{eqv}}\left(n^+_s - 1\right)}{n^-_s + n^+_s - 2} \qquad (3.11)$$

Substituting the estimate $s^2_{D_{eqv}}$ of 17.37 J/m^2 and $n_s^+ = n_s^- = 30$ on the Equation 3.12:

$$t_o = \frac{\left(\overline{D}^-_{eqv} - \overline{D}^+_{eqv}\right) - \left(\eta^- - \eta^+\right)_o}{s_{D_{eqv}}\sqrt{1/n^-_s + 1/n^+_s}} \qquad (3.12)$$

A p-value of less than 0.05% was obtained using a t distribution with 28 degrees of freedom. Thus, on the basis of this test, the null hypothesis was rejected. However, it should be noted that the magnitude of the difference was rather small (13.1 J/m^2). This suggests that a UV reactor designer should carefully select a C_L level. Further analysis of C_L for utilities with variable water transmittance and flowrate is provided in the next section.

Table 3.3: Confidence intervals and standard deviation expected for the SUVR reactor under the conditions given in Table 3.1 with n_p x n_s 55000 particles and $C_L = 0.30$.

Variable	Size of the confidence interval	Standard Deviation	Variance
$\overline{D}_{eqv} = 505.8$ J/m^2	$E_{D_{eqv}} = \pm 1.62$ J/m^2	$s_{D_{eqv}} = 4.34$ J/m^2	$s^2_{D_{eqv}} = 18.83$ J/m^2
$\overline{\overline{D}} = 849.2$ J/m^2	$E_{\overline{D}} = \pm 5.6$ J/m^2	$s_{\overline{D}} = 15.02$ J/m^2	$s^2_{\overline{D}} = 225.6$ J/m^2
$\overline{\overline{t}} = 2.645$ s	$E_{\overline{t}} = \pm 0.007$ s	$s_{\overline{t}} = 0.020$ s	$s^2_{\overline{t}} = 0.0004$ s

3.3 Sensitivity Analysis of the UV Disinfection Predictions

The main objective of a UV reactor designer is to propose a reactor configuration that is capable of delivering the highest hydraulic efficiency under different operating conditions. In other words, it is desirable that the equivalent dose be as close to the theoretical dose[9] as possible, regardless of the operational conditions. Thus the UV reactor designer needs to determine the factors that could cause variations in the predicted equivalent dose. If a CFD approach is used, several factors must be considered.

A total of 10 factors were examined in this study as listed in Table 3.4. The five design and operational factors are combined in three variables: 1) EED, 2) UVT and 3) baffles.

The number of lamps operating (NLO), lamp output power (Φ) and flowrate (Q) combine to give the Electrical Energy Dose (EED = (NLO*Φ)/Q), which is defined as the electrical energy (kW-h) consumed per unit of volume (e.g., 1 m^3) of water treated (Bolton, 2002). The EED levels selected were 0.0128 kW-h/m^3 and 0.0192kW-h/m^3 based on operational values provided by Epcor Water Services of Edmonton, Alberta.

The levels of the UV transmittance selected were 93 %UVT and 80 %UVT. The UV transmittance of 93% was selected as upper limit, which is the minimum allowed UV transmittance recommended by Calgon Carbon Corporation to achieve a UV dose of 40 mJ/cm^2 working at a flowrate of 6,469 m^3/h for the Sentinel 6x20kW reactor. The UV transmittance of 80% was arbitrarily selected as lower limit.

[9] The theoretical dose is defined as the average fluence rate in the reactor times the mean residence time. This definition assumes ideal plug flow with perfect radial mixing inside the reactor and no dose distribution (i.e. one well-defined dose).

The effect of inserting baffles on the computed UV dose distribution was determined by running simulations with and without the baffles.

Five computational factors were also considered. The levels of the Lagrangian empirical constant, C_L, represent the range of typical values reported in the literature (Table 1.5). The lamp shadow effect generated by the interception of the radiation by other lamps was considered to estimate its effect on the computed UV dose.

Table 3.4: Factors and levels used for investigating the Sentinel UV reactor. The bold variables were used in a full factorial design

Factors	**Level**	
Design factors	-	+
Electrical Energy Dose (EED) EED = (NLO*Φ)/Q	0.0128 kW-h/m^3 = (2*6.7kW)/3125m^3/h	0.0192 kW-h/m^3 =(6 *20kW)/6250m^3/h
UV transmittance (UVT)	80% at (254nm)	93% at (254nm)
Baffles	No	Yes
Computational factors	-	+
Lagrangian empirical const.(C_L)	0.15	0.30
Turbulence model	RSM	k-ε model
Simulation mode	Unsteady-state	Steady-state
Mesh type	UTFM	UHFM
Lamp shadow	Off	On

The effects of EED, UVT and C_L factors on the UV dose predictions for the SUVR were studied using a 2-level factorial design with 8 runs. Four additional runs were included in this analysis because there are two modes which can provide an EED of 0.0128 kW-h/m^3 at 3,125 m^3/h:

Mode 1: two lamps operating at 20 kW lamp output power (Φ = 2*20 = 40 kW).

Mode 2: six lamps operating at 6.7 kW lamp output power (Φ = 6*6.7 = 40 kW).

The effects of the turbulence model, simulation mode, mesh type and lamp shadow were analyzed by comparison with the base case used to estimate the number of particles

in section 3.2. This approach was used for the following reasons: 1) a 2 level factorial design with eight factors requires an unattainable number of simulations ($2^8 = 256$), 2) some simulations demand a high computational cost, and 3) some simulation cases do not represent realistic operating scenarios in water treatment plants.

3.3.1 Evaluation of EED, UVT and C_L in a Full Factorial Experiment

The effects of EED, UVT and C_L on the performance of the SUVR were studied using a 2-level factorial design. For this analysis 12 simulations were executed under the conditions presented in Tables 3.5 and 3.6. The simulation results are presented in Table 3.6, where runs 5 to 8 and 9 to 12 correspond to simulations of the SUVR operated under mode 1 and mode 2, respectively. In addition, the effect of various lamp on/off combinations was studied in a separate set of simulations (Table 3.7). These simulations were computed with 2 lamps operating at 20kW each and the conditions of each simulation are given in Table 3.5.

Table 3.5: Simulation conditions to evaluate the effect of EED, UVT and C_L on the performance of the SUVR

Condition	Level or Value
Mesh type	Unstructured Hexahedral Fine Mesh
Turbulence model	Steady-state k-ε model
Baffles	Yes
Simulation mode	Steady-state
Lamp shadow	On
MS2 coliphage rate equation	$Log_{10}(N/N_o) = 0.00365D + 0.42$
Particle diameter	$1.0x10^{-4}$ m
Number of steps	43,500
Length scale	0.0002 m
Total number of particles injected	60,000

Table 3.6: Matrix design and UV performance estimation for the Sentinel UV reactor under the conditions given in Table 3.5

Mode	ID	Electrical Energy Dose (kWh/m^3)				UVT (%)	C_L	$\bar{t}$ (s)	D_{min} J/m^2	D_{th} J/m^2	$\bar{D}$ J/m^2	Log_{10} (N/N_o)	D_{eqv} J/m^2	E_f
		NLO	Φ (kW)	Q(m^3/h)	EED									
	1	+	+	+	+	+	-	2.615	200.7	900.8	849.3	2.217	492.2	0.546
	2	+	+	+	+	+	+	2.647	197.2	900.8	844.2	2.264	505.3	0.561
	3	+	+	+	+	-	-	2.616	8.4	310.5	288.6	0.836	113.9	0.367
	4	+	+	+	+	-	+	2.652	7.7	310.5	287.9	0.860	120.5	0.388
Mode 1	5	-	+	-	-	+	-	5.228	139.2	600.0	581.0	1.731	359.1	0.598
	6	-	+	-	-	+	+	5.287	131.2	600.0	597.4	1.743	362.5	0.604
	7	-	+	-	-	-	-	5.235	5.3	206.8	204.7	0.735	86.3	0.417
	8	-	+	-	-	-	+	5.297	4.9	206.8	214.3	0.737	86.7	0.419
Mode 2	9	+	-	-	-	+	-	5.229	139.3	594.0	558.1	1.711	353.7	0.595
	10	+	-	-	-	+	+	5.297	133.1	594.0	559.7	1.749	364.1	0.613
	11	+	-	-	-	-	-	5.235	5.1	204.7	190.2	0.743	88.4	0.432
	12	+	-	-	-	-	+	5.297	5.3	204.7	190.8	0.760	93.3	0.455

Table 3.7: Matrix design and UV performance predictions for the SUVR operated with 2 lamps at 20kW in mode 1. Lamp on/off combinations are given under NLO (Figure 2.1)

ID	Electrical Energy Dose (kWh/m^3)				UVT (%)	C_L	$\bar{t}$ (s)	D_{min} J/m^2	D_{th} J/m^2	$\bar{D}$ J/m^2	Log_{10} (N/N_o)	D_{eqv} J/m^2	E_f
	NLO	Φ (kW)	Q(m^3/h)	EED									
5	1, 2	+	-	-	+	-	5.228	139.2	600.0	581.0	1.731	359.1	0.598
6	1, 2	+	-	-	+	+	5.287	131.2	600.0	597.4	1.743	362.5	0.604
5b	1, 4	+	-	-	+	-	5.229	114.5	608.8	585.7	1.645	335.6	0.558
6b	1, 4	+	-	-	+	+	5.297	115.1	608.8	585.8	1.644	335.2	0.558
5c	1, 6	+	-	-	+	-	5.235	101.1	600.6	557.1	1.612	326.7	0.544
6c	1, 6	+	-	-	+	+	5.297	88.0	600.6	565.5	1.591	320.8	0.534

Tables 3.6 and 3.7 present the outputs for each simulation, where:

$\bar{t}$ is the particle mean residence time as defined in section 3.2,

D_{min} is the minimum dose absorbed by a particle,

D_{th} is the theoretical dose,

$\overline{D}$ is the particle-mean dose as defined in section 3.2,

$Log_{10}(N/N_o)$ is the computed inactivation of MS2 coliphage,

D_{eqv} is the equivalent dose computed, and

E_f is the hydraulic efficiency defined as the ratio of equivalent dose to theoretical dose.

The hydraulic efficiency used herein should not be confused with the hydraulic efficiency used by Wright and Lawryshyn (2000). They defined hydraulic efficiency as the ratio of equivalent dose, D_{eqv}, to the particle mean dose, $\overline{D}$. This definition was not used because $\overline{D}$ decreases as C_L increases (see Table 3.6).

3.3.2 Effect of UVT, EED and C_L on the UV Dose Prediction

The fact that the UVT and EED have significant effects on the performance of UV reactors was used as an indirect method to validate the CFD model as whole. In the absence of experimental data, it is difficult to validate the CFD model; however, the physical principles could be used to test the plausibility of the CFD model. Therefore, the CFD model was assessed based on ability to predict the effect of EED and UVT on the inactivation level. In addition, these simulations were used to investigate the possibility of interaction between the effect of the C_L and operational design variables on the

prediction of UV reactor performance. A measure of these effects was quantified by regression analysis of the data in Table 3.6. The results are summarized in Table 3.8.

Table 3.8: Calculated effects for results of the 2^3 factorial design in Table 3.6. The effect were ordered from largest to smallest.

Effect	D_{min}	Effect	D_{th}	Effect	$\overline{D}$
UVT	160.7	UVT	490.8	UVT	466.2
EED	33.1	EED	204.3	EED	180.5
EED*UVT	30.2	EED*UVT	99.6	EED*UVT	92.2
C_L	-2.9	EED*UVT*C_L	0.0	EED*C_L	-5.0
UVT*C_L	-2.4	UVT*C_L	0.0	EED*UVT*C_L	-2.1
EED*UVT*C_L	1.1	EED*C_L	0.0	C_L	2.0
EED*C_L	0.7	C_L	0.0	UVT*C_L	-0.1

Table 3.8: Calculated effects for results of the 2^3 factorial design in Table 3.6. The effect were ordered from largest to smallest. (contd.)

Effect	D_{eqv}	Log 10	Effect	E_f	Effect	$\bar{t}$
UVT	326.35	1.191	UVT	17.39	EED	-2.630
EED	83.71	0.305	EED	-5.13	C_L	0.048
EED*UVT	55.16	0.201	C_L	1.5	EED*C_L	-0.014
C_L	7.29	0.026	EED*C_L	0.28	UVT	-0.004
UVT*C_L	2.67	0.009	EED*UVT	0.21	EED*UVT*C_L	-0.001
EED*C_L	2.55	0.009	UVT*C_L	-0.20	EED*UVT	0.001
EED*UVT*C_L	0.56	0.001	EED*UVT*C_L	-0.13	UVT*C_L	-0.000

Comparison of the computed effects in Table 3.8 suggests that:

- ✓ The CFD model correctly predicted the direction of the effect EED and UVT.
- ✓ The Lagrangian empirical constant and its interactions do not have any effects on the prediction of the SUVR performance in comparison to UVT and flowrate.
- ✓ The effect of the interaction between UVT and EED on the equivalent dose is greater as UVT decreases.
- ✓ The effect of increasing UVT is to increase the SUVR hydraulic efficiency.
- ✓ The effect of increasing EED is to decrease the SUVR hydraulic efficiency.
- ✓ The effect of increasing EED is to decrease the residence time of the organisms.

Analysis of the results in Table 3.8 shows that the CFD model is consistent with expected results. For example, UVT and EED are the most significant factors affecting the performance of UV reactors. The predicted UV dose of 492 J/cm^2 is in the same order of magnitude that Calgon Carbon Corporation suggested as minimum UV dose for the SUVR at 93 % UVT (400 J/m^2). The CFD model can be used to provide complete information on UV reactor performance in a short period of time (20 hours per simulation). The CFD model is a more powerful tool to validate large UV reactors than biodosimetry, which demands higher capital investment and time.

The factorial design analysis showed that the Lagrangian empirical constant has a small effect on the predicted efficiency of SUVR in comparison to the effect of UVT and EED (Table 3.8). Therefore, A UV reactor designer can select a value from 0.15 to 0.30 for this constant, as long as the reactor configuration and design factors range are similar to the Sentinel UV reactor. This conclusion should also be applicable for other reactors.

The effects of UV transmittance and EED should not be interpreted separately due to the large interaction between them, and can best be considered using the two-way table shown in Figure 3.22. The interaction arises because the equivalent dose is highly affected by the number of microorganisms receiving low doses when EED or UVT decrease. The effect of EED and UVT on the dose distribution can be better observed by comparing Figures 3.23 and 3.24. The shape of the dose distribution becomes increasingly skewed as UVT and EED decrease.

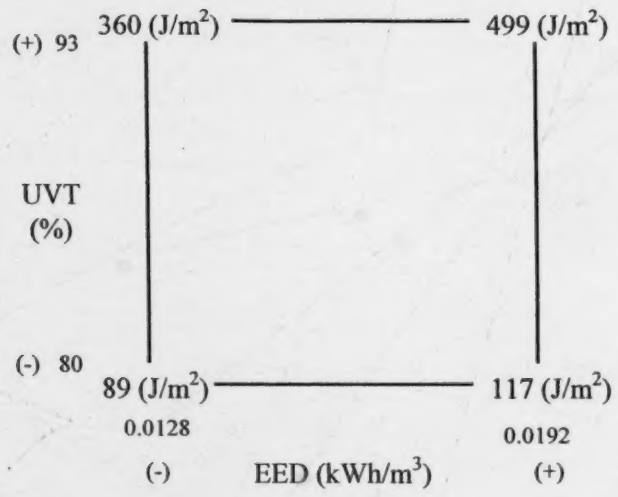

Figure 3.22: Effect of UVT and EED on equivalent dose.

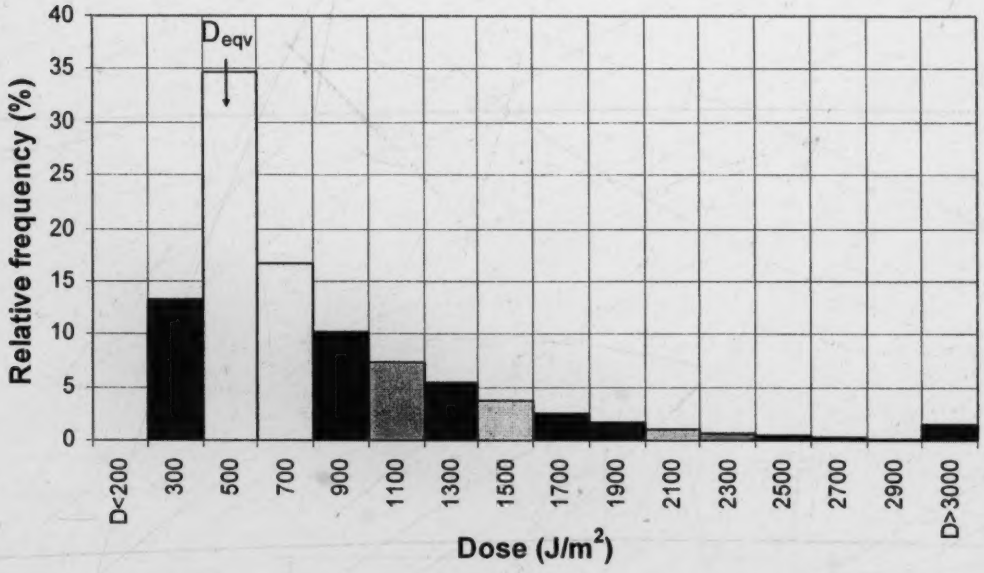

Figure 3.23: Dose received by 57,668 particles for SUVR with baffles under the conditions of run ID 1: EED = 0.0192, UVT = 93 % and $C_L = 0.15$ ($\overline{D}$ = 849 J/m^2, D_{eqv} = 492 J/m^2, D_{min} = 201 J/m^2, and s_D = 914 J/m^2)

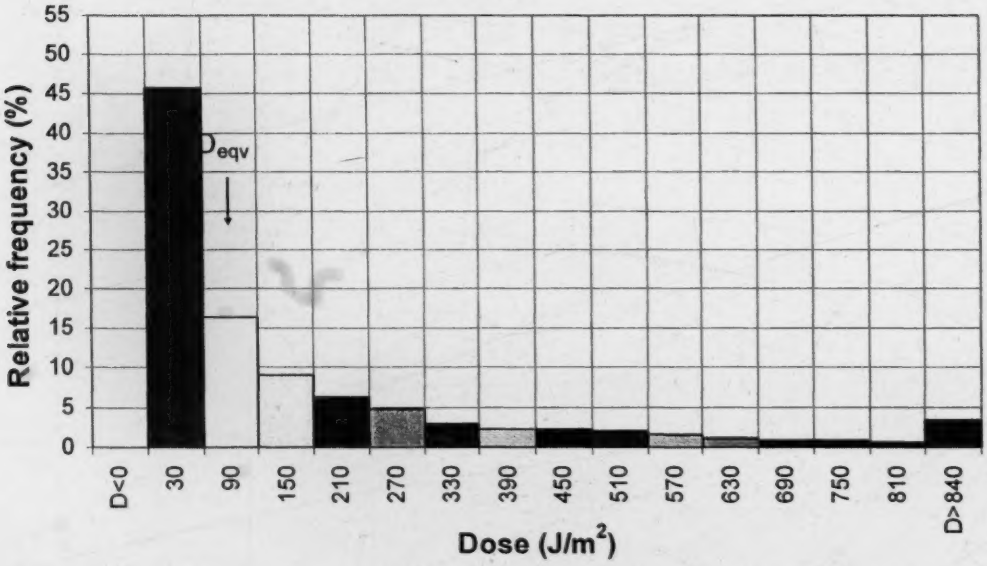

Figure 3.24: Dose received by 57,684 particles for SUVR with baffles under the conditions of run ID 7: EED = 0.0128, UVT = 80% and $C_L = 0.15$ ($\overline{D} = 289$ J/m^2, $D_{eqv} = 114$ J/m^2, $D_{min} = 8$ J/m^2, and $s_D = 664$ J/m^2)

The result with the most practical interest was the counter-intuitive behavior of the hydraulic efficiency in response to the EED. An increase of EED increased the equivalent dose but reduced the hydraulic efficiency (Figure 3.25). This could be attributed to the fact that less particles received doses lower than the equivalent dose when EED was increased; however, the theoretical dose increased more than the equivalent dose. Therefore, it can be concluded that an EED greater than 0.015 kW-h/m^3 should be supplied to ensure that the equivalent dose is greater than 400 J/m^2 (Calgon Carbon Corporation suggested 400 J/m^2 as minimum UV dose for the SUVR when UVT = 93%). This means that the EED can be used as a scale factor to determine the lamp output power to use when the flow rate varies in order to supply the same equivalent dose. For example, when the flowrate is decreased from 6250 to 3125 m^3/h, the lamp output power required is 60 kW rather than the 40 kW currently being used by Epcor, to provide the

same EED (0.0192 kW-h/m^3), equivalent dose (492 J/m^2) and hydraulic efficiency (0.546) as shown in Table 3.9.

Table 3.9: Correlation between EED and equivalent dose

Run ID	EED= 0.0192kW-h/m^3			$\bar{t}$ (s)	D_{min} J/m^2	D_{th} J/m^2	$\bar{D}$ J/m^2	Log_{10} (N/N_o)	D_{eqv} J/m^2	E_f
	NLO	Φ(kW)	Q(m^3/h)							
1	6	120	6250	2.614	203.4	900.8	852.5	2.218	492.7	0.547
13	6	60	3125	5.229	211.0	899.9	845.5	2.217	492.4	0.547

Run ID 13 was carried under the conditions given in Table 3.5, 93% UVT and C_L= 0.15.

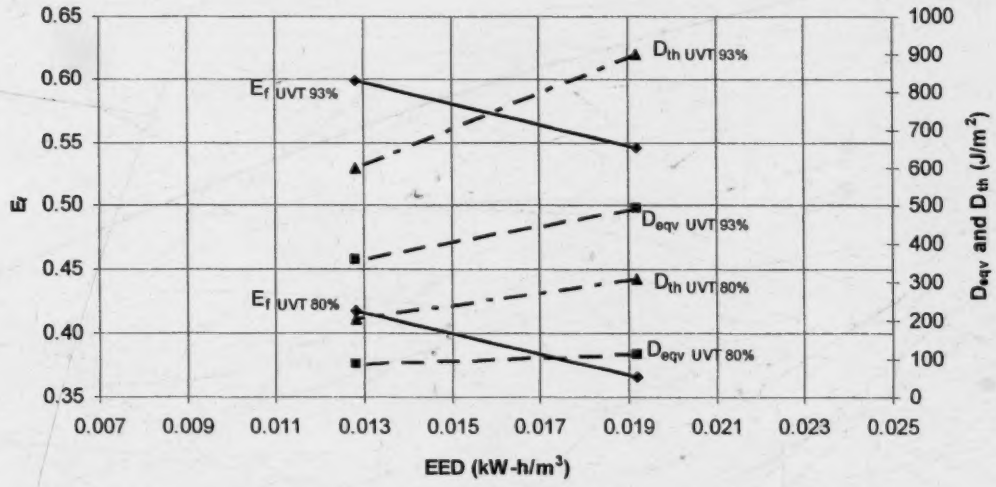

Figure 3.25: Effect of EED on the equivalent dose (D_{eqv}), theoretical dose (D_{th}) and hydraulic efficiency (E_f) for SUVR under the conditions of runs ID 1 and 5.

3.3.3 Effect of the Lamps on the UV Dose Prediction

Comparison of the results in Table 3.7 suggests that 1) the SUVR produces similar hydraulic efficiencies in both modes of operation; and 2) The SUVR when operated under mode 1 provides a higher hydraulic efficiency when the lamps operating are part of the same vertical bank.

Although two modes of operation were investigated in this study to operate the Sentinel UV reactor at low flow rate, only one mode offers a cost-effective operation.

The operational conditions of UV reactors change on a daily basis. When a UV reactor is operated at a low flow rate, it is economical to either reduce the power or turn off a set of lamps. The SUVR is typically operated with two lamps at 100 % of the output power (mode 1). Alternatively, it could be operated with six lamps at 33% of the output power (mode 2) at a low flow rate. A comparison of results in Table 3.6, runs ID 5 to 8 and 9 to 12 showed that similar hydraulic efficiencies could be reached by either mode. However, turning a set of lamps on and off will decrease the electrode life compared to simply reducing the power. It may be preferable to adjust lamp power even though the power supply required for power modulation could be more expensive than fixed power.

The simulation results also suggest that the predicted hydraulic efficiency of the SUVR operated under mode 1 was affected by which lamps operate. As discussed in Section 1.6 the total value of the fluence rate is the sum of the fluence rate for each of the lamps, which decreases as the distance between the lamps increases. Analysis of results in Table 3.7 shows that the combination of operating lamps affected the predicted hydraulic efficiency of the SUVR by more than 6 %. The combination of lamps 1 and 2 in operation resulted in a slightly higher predicted equivalent dose than the other combinations. This could be attributed to a higher overall fluence rate between two lamps located at the same vertical bank or a more uniform fluence rate in the irradiance zone. Therefore, to maintain operation at the highest hydrodynamic efficiency with two lamps in operation, the SUVR should be operated using any two lamps that are part of the same vertical bank of lamps rather than two lamps from different banks.

3.3.4 Effect of the Baffles on the UV Dose Prediction

Simulations were carried out to investigate the effects of baffles. These simulations were carried using the SUVR with and without baffles under the base case condition given in Table 3.1. The simulation results are presented in Table 3.10.

Table 3.10: Effect of the Baffles on the prediction of the SUVR performance.

ID	Factor	Level	$\bar{t}$ (s)	D_{min} J/m^2	D_{th} J/m^2	$\bar{D}$ J/m^2	Log_{10} (N/N_o)	D_{eqv} J/m^2	E_f
BC	Baffle	Yes	2.614	203.4	900.8	852.5	2.218	492.7	0.547
14	Baffle	No	2.733	47.4	900.7	807.2	1.395	267.1	0.296

BC. Base case study results given in Section 3.2

The simulation results in Table 3.10 show that the use of baffles improved the SUVR hydraulic efficiency by more than 25%. Baffles forced the fluid to flow towards the reactor center, which directed microorganisms towards the high fluence rate zones near the UV lamps. Meanwhile, stagnation zones behind the baffles reduced the effective volume of the UV reactor and trapped microorganisms for a longer time. On the other hand, baffles reduced the average residence time of microorganisms, and thus reduced the dose received by microorganisms traveling through the reactor center. Therefore, the location, size and arrangement of baffles should be optimized to reduce the number of microorganisms receiving a low UV dose.

The effect of baffles is to reduce the number of particles receiving low UV doses and can be better appreciated by comparing Figures 3.23 and 3.26. The relative frequency of particles receiving a dose less than 200 J/m^2 is 22% for the SUVR without baffles, whereas no particle receives a dose less than 200 J/m^2 for the SUVR with baffles. The 22% of particles that received a dose less than 200 J/m^2 decreased the equivalent dose by more than 225 J/m^2.

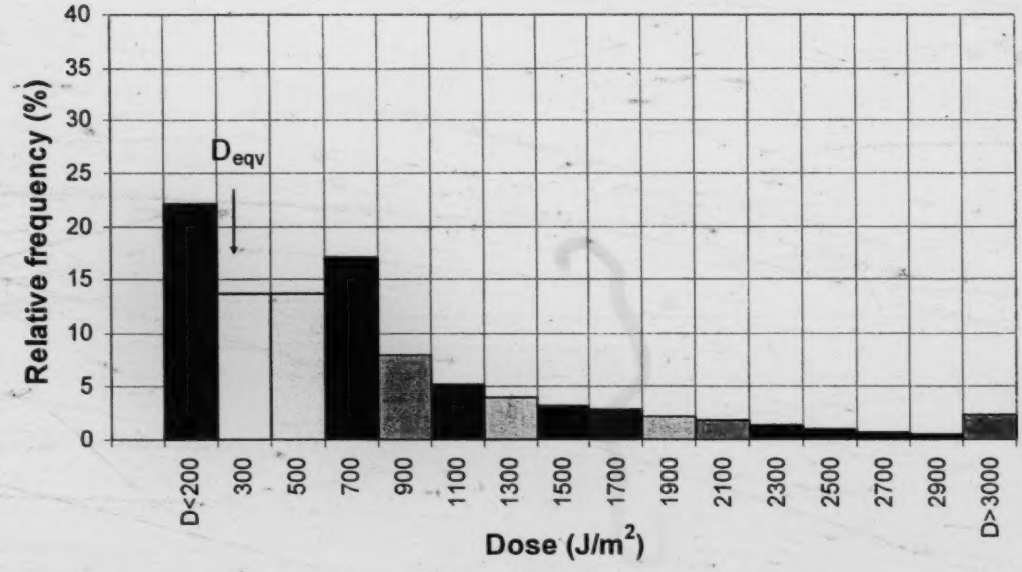

Figure 3.26: Dose received by 58,397 particles for the SUVR **without baffles** under the conditions of run ID 1. EED = 0.0192, UVT = 93% and C_L = 0.15 ($\overline{D}$ = 807.2 J/m^2, D_{eqv} = 267.1 J/m^2, D_{min} = 47.36 J/m^2 and S_D = 895.93 J/m^2)

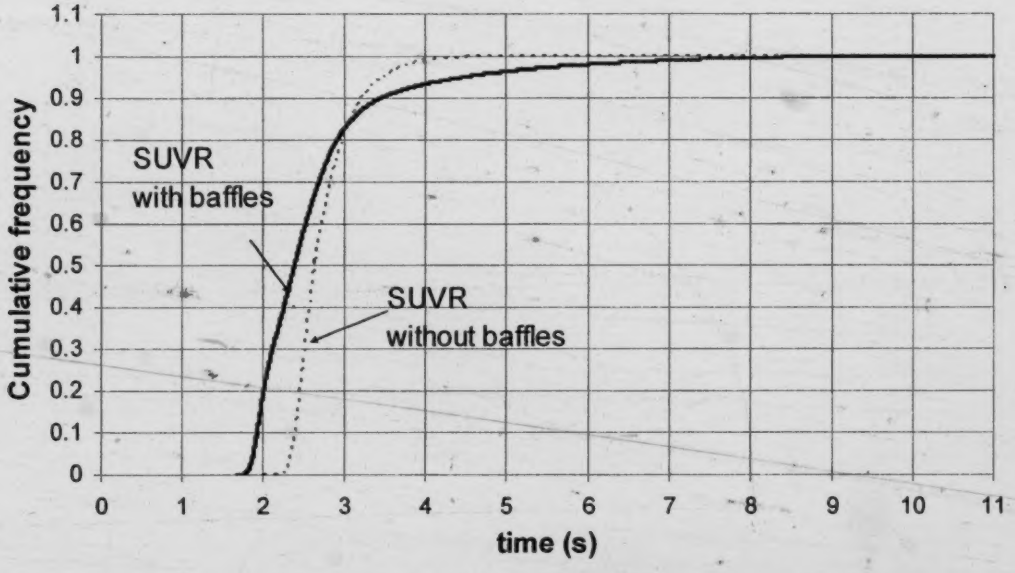

Figure 3.27: Cumulative relative frequency for the residence time of the SUVR **with baffles** ($\bar{t}$ = 2.61 s, t_{min} = 1.68 s and S_t = 0.939 s) and **without baffles** ($\bar{t}$ = 2.73 s, t_{min} = 2.12 s and S_t = 0.363s) under the conditions of run ID 1. EED = 0.0192, UVT = 93% and C_L = 0.15.

The insertion of baffles into a UV reactor has two main drawbacks: 1) increased pressure drop, and 2) increased dispersion of the residence time distribution (Figure 3.27). After installing baffles, the calculated pressure drop in the SUVR increased from 1 kPa (0.145psi) to 3 kPa (0.435 psi) at 6,250 m^3/h.

The increase of the pressure drop is attributed to the size of the baffles. The consequence of increasing the UV reactor head loss is that the available head is limited in water treatment facilities. Therefore, fitting the SUVR in a facility's hydraulic profile without the need for additional pumping can be a major issue especially for retrofits.

Baffles in the SUVR decrease the particle residence time and tend to accelerate the flow in the axial direction. Figure 3.27 shows that the use of baffles in the SUVR can 1) reduce the residence time of the particles, 2) increase the dispersion of the residence time distribution, and 3) decrease the minimum residence time. This implies that baffle size and location should be selected carefully to improve the hydrodynamic conditions of a UV reactor without reducing significantly the exposure time or the available head.

3.3.5 Additional Simulations

Additional simulations were carried out to investigate the effects of mesh type (unstructured hexahedral or unstructured tetrahedral), turbulence model (k-ε model or RSM), simulation mode (steady-state or unsteady-state), and lamp shadow (on/off) on the performance of the SUVR. As discussed in Section 2.2.1, an unstructured tetrahedral mesh was evaluated because it can quickly generate the complex geometry of the SUVR. However, an unstructured tetrahedral mesh can create other problems such as numerical diffusion.

Table 3.11: Additional simulations used to predict the SUVR performance.

ID	Mesh type	Turbulence model	Simulation mode	Lamp Shadow	Baffles	EED (kWh/m^3)	UVT (%)	C_L	$\bar{t}$ (s)	D_{min} J/m^2	D_{th} J/m^2	$\bar{D}$ J/m^2	Log_{10} (N/N_o)	D_{eqv} J/m^2	E_f
BC	+	+	+	+	+	+	+	-	2.61	203.4	900.8	852.5	2.21	492.7	0.547
15	-	+	+	+	+	+	+	-	2.63	226.8	898.3	872.7	2.34	527.7	0.587
16	+	-	+	+	+	+	+	-	2.58	206.0	903.2	786.8	2.15	475.3	0.526
17	+	+	-	+	+	+	+	-	2.60	186.3	900.2	964.0	2.19	485.4	0.539
18	+	+	+	-	+	+	+	-	2.61	204.4	902.0	853.9	2.22	493.6	0.547

BC. Base Case analysis given in Section 3.2.

A statistical analysis of the results presented in Table 3.11 using the base case as a reference shows that:

- ✓ The unstructured hexahedral fine mesh provided a more accurate prediction of the SUVR hydraulic efficiency than the unstructured tetrahedral fine mesh.
- ✓ The RSM under-predicted the SUVR UV dose in comparison to the k-ε model.
- ✓ The unsteady-state simulation has an appreciable effect on the UV dose prediction.
- ✓ The effect of lamp shadow on the SUVR UV dose prediction was insignificant.

3.3.6 Effect of the Mesh Type on the UV Dose Prediction

The Unstructured Tetrahedral Fine Mesh (UTFM) predicted a higher UV dose than the Unstructured Hexahedral Fine Mesh (UHFM). The equivalent doses of 492.7 J/m^2 and 527.7 J/m^2 were predicted by the UHFM and UTFM, respectively (Table 3.11). The following null hypothesis was used for this analysis: the different mesh type levels do not have any significance on the UV dose prediction, $(\eta^- - \eta^+)_o = 0$. To test the null hypothesis, it was assumed that:

1) a single simulation with more than 55,000 particles was equivalent to 30 simulations with 1833 particles,

2) The simulation equivalent dose variance for 30 simulations was 17.37 $(J/m^2)^2$ estimated in Section 3.2.4.

3) The population variances, σ^2_{Deqv}, for levels (+) and (-) are, to an adequate approximation, equal.

Using Equation 3.12 and the s^2_{Deqv} of 17.37 $(J/m^2)^2$ as external value of σ^2_{Deqv}, the significant level of less than 0.05% was computed. Based on this test, the null hypothesis was rejected. Over-prediction of the UV dose was expected because the UTFM under predicted the axial velocity at the center of the pipe by two percent in comparison to the Zagarola profiles. This provided longer exposure times and thereby predicted a greater equivalent dose. This result suggests that UV reactor designers should avoid using a tetrahedral mesh in CFD simulations, because it can cause over prediction of the UV reactor performance.

3.3.7 Effect of the Turbulence Model on the UV Dose Prediction

For the SUVR, the k-ε model predicted a higher UV dose than the RSM. The equivalent dose decreases from 492.7 J/m^2 using the k-ε model to 475.3 J/m^2 using the RSM (Table 3.11). This is because the RSM uses the Reynolds Stresses to compute the velocity fluctuation whereas the k-ε model uses a proportion of the kinetic energy (see Section 1.8.2). The following null hypothesis was used for this analysis: the different levels of the turbulence models do not have any significance on the UV dose prediction, $(\eta^- - \eta^+)_o = 0$. To test the null hypothesis, the same assumptions shown in section 3.3.6 were used. Using Equation 3.12 and the s^2_{Deqv} of 17.37 J/m^2 as external value of σ^2_{Deqv}, the significant level of 0.05% was computed. Thus, on the basis of this test, the null hypothesis was rejected. This suggests that the turbulence model should be selected carefully because its assumptions affect the UV dose.

3.3.8 Effect of the Simulation Mode on the UV Dose Prediction

The unsteady state flow predicted a lower UV dose than that using the steady state flow. Table 3.11 shows that the unsteady-state flow reduces the equivalent dose from 492.7 J/m^2 to 485.4 J/m^2. The following null hypothesis was used for this analysis: the different simulation mode levels do not have any significance on the UV dose prediction, $(\eta^- - \eta^+)_o = 0$. To test the null hypothesis, the same assumptions shown in section 3.3.7 were used. Using Equation 3.12 and the s^2_{Deqv} of 17.37 J/m^2 as external value of σ^2_{Deqv}, the significant level of 0.05% was computed. Thus, the null hypothesis was rejected. This suggests that the unsteady flow affects the UV dose prediction for the SUVR.

3.3.9 Effect of the Lamp Shadow on the UV Dose Prediction

Lamp shadow had only a small effect on the SUVR UV dose prediction. The shadow effect is generated by the interception of the UV radiation by other lamps. The predicted UV dose was 492.7 J/cm^2 considering the lamp shadowing and 493.6 J/cm^2 disregarding the lamp shadowing (Table 3.11). The following null hypothesis was used for this analysis: the different levels of the lamp shadow do not have any significance on the UV dose prediction, $(\eta^- - \eta^+)_o = 0$. To test the null hypothesis, the same assumptions shown in section 3.3.7 were used. Using Equation 3.12 and the s^2_{Deqv} of 17.37 J/m^2 as external value of σ^2_{Deqv}, the significant level of 20% was computed. Thus, the null hypothesis could not be rejected. This result was expected because the distance between consecutive lamps is large in medium pressure reactors. This factor may be important for low-pressure reactors because the lamps are spaced much closer together.

In summary, the computational factors become significant factors on the UV dose prediction, when the UVT and EED variabilities are small. Therefore, mesh type, turbulence model, and simulation mode should be selected carefully to increase the accuracy of the CFD approach. It is suggested that experimental studies should be conducted to determine which computational factors provide a more accurate UV dose prediction. It should be noted that although the statistical showed that mesh type, turbulence model, and simulation had a significant effect on the equivalent dose, they had only minor effect on the log inactivation of MS2 coliphage.

3.4 Investigation of Modified UV Reactor Designs Using CFD

The objectives of this section were: 1) to test a Modified UV Reactor (MUVR) configuration and compare the hydraulic efficiency and head loss to those of the SUVR, 2) to assess the predicted performance for both reactors using different operating conditions, and 3) to analysis the predicted performance for both reactors using more than one microorganism UV inactivation model to make sure the results are consistent for different microorganisms. The MUVR was initially evaluated under the conditions listed in Tables 3.5 and 3.12. The predicted performance for both reactors is summarized in Table 3.13.

Table 3.12: Factors and level used for the comparison of the SUVR and MUVR

Factors	**Level**	
	-	+
Electrical energy Dose (EED)	0.0128 kW-h/m^3	0.0192 kW-h/m^3
UV transmittance (UVT)	80% at (254nm)	93% at (254nm)
Baffles (B)	No	Yes

The MUVR is an enclosed pipe reactor with eight 15 kW medium pressure lamps arranged perpendicular to the bulk flow and perpendicular to each other as shown in Figures 3.28 and 3.29. Unlike the SUVR (Figure 2.2), The MUVR contains sixteen baffles located at a distance of 0.22 m from the lamps and oriented perpendicular to the flow. The distance between the first and the last set of lamps is the same as the SUVR.

This particular reactor configuration was selected because it is expected to provide a better spatial distribution of the fluence rate with lower pressure drop in comparison to the SUVR. The MUVR has some disadvantages. For example, the lamp arrangement may make it difficult to remove lamps for maintenance or replacement and the extra two lamps demand additional monitoring and mechanical cleaning systems.

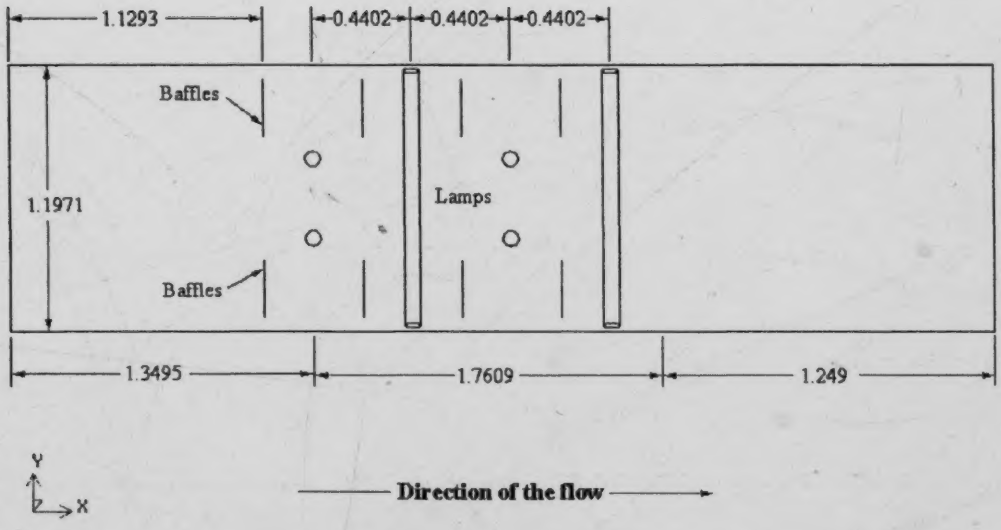

Figure 3.28: Elevation view of the Modified UV reactor (scale in meters).

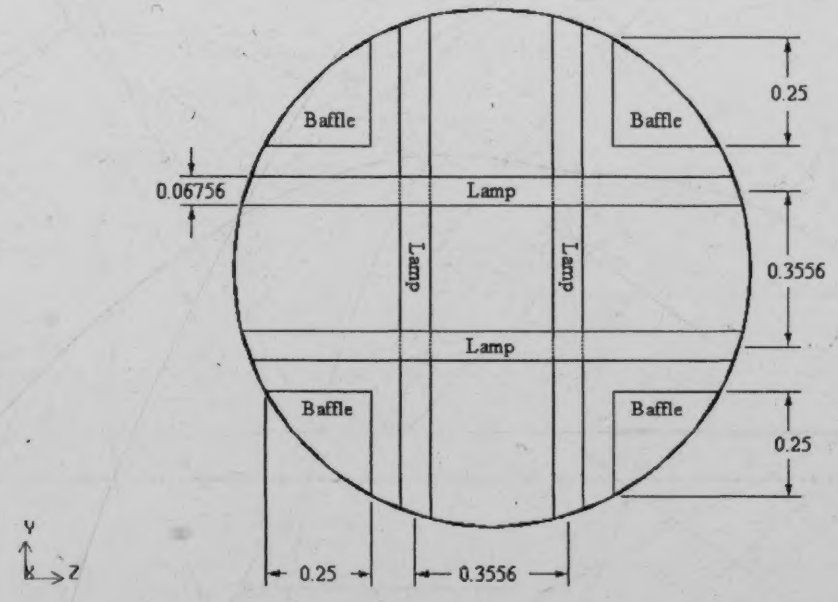

Figure 3.29: Cross sectional view of the Modified UV reactor (scale in meters).

Table 3.13: Matrix design and UV performance estimation for both UV reactors: the equivalent dose was estimated using the kinetic inactivation constant for MS2 coliphage

Sentinel UV Reactor													
ID	Electrical Energy Dose (kWh/m^3)				UVT (%)	B	$\bar{t}$ (s)	D_{min} J/m^2	D_{th} J/m^2	$\bar{D}$ J/m^2	Log_{10} (N/N_o)	D_{eqv} J/m^2	E_f
	NLO	Φ (kW)	Q (m^3/h)	EED									
1	+	+	+	+	+	+	2.615	200.7	900.8	849.3	2.217	492.2	0.546
3	+	+	+	+	-	+	2.616	8.4	310.5	288.6	0.836	113.9	0.367
5	-	+	-	-	+	+	5.228	139.2	600.0	581.0	1.731	359.1	0.598
7	-	+	-	-	-	+	5.235	5.3	206.8	204.7	0.735	86.3	0.417
17	+	+	+	+	-	-	2.733	47.4	900.7	807.2	1.395	267.1	0.296
Modified UV Reactor													
ID	Electrical Energy Dose (kWh/m^3)				UVT (%)	B	$\bar{t}$ (s)	D_{min} J/m^2	D_{th} J/m^2	$\bar{D}$ J/m^2	Log_{10} (N/N_o)	D_{eqv} J/m^2	E_f
	NLO	Φ (kW)	Q (m^3/h)	EED									
19	+	+	+	+	+	+	2.720	161.2	900.8	864.3	2.07	452.0	0.502
20	+	+	+	+	-	+	2.720	9.0	310.0	296.9	0.906	133.1	0.429
21	-	+	-	-	+	+	5.436	104.9	594.5	570.1	1.658	339.2	0.570
22	-	+	-	-	-	+	5.436	6.0	204.6	197.0	0.801	104.3	0.510
23	+	+	+	+	-	-	2.734	182.0	900.8	847.3	2.032	441.7	0.490

The results in Table 3.13 suggest that the predicted hydraulic efficiency for the SUVR is four percent larger than that for the MUVR at high UV transmittance (compare runs ID 1 & 5 vs. 19 & 21, Table 3.13). However, predicted hydraulic efficiency for the MUVR is six to ten percent larger than that for the SUVR at low UV transmittance (compare runs ID 3 & 7 vs. 20 & 22, Table 3.13). This is attributed to a higher percentage of particles receiving a low UV dose. For instance, more than six percent of the particles received a UV dose lower than 400 J/m^2 in the MUVR operated at high transmittance (compare Figures 3.23 and 3.30); similarly, more than eleven percent of the particles received a UV dose lower than 100 J/m^2 in the SUVR operated at low transmittance. These results reveal that the MUVR could provide a higher level of inactivation than the SUVR in a water treatment plant with low water transmittance.

Using baffles improves the predicted performance for both UV reactors. The hydraulic efficiency predicted for the MUVR without baffles is 20 % larger than that for the SUVR without baffles (compare runs ID 17 & 23, in Table 3.13). The insertion of baffles increases the predicted equivalent dose by more than 37 % for the SUVR and only 2 % for the MUVR. In addition, the head losses predicted for the SUVR with and without baffles were 3 kPa and 1 kPa, respectively. The head losses predicted for the MUVR with and without baffles were 1.8 kPa and 1.2 kPa, respectively. These results show that the performance of the SUVR is highly dependent on the insertion of baffles, which may be a disadvantage when limited head is available in a water treatment facility.

A thorough analysis and comparison of the UV reactor performance requires consideration of different microorganism inactivation models and operating conditions. Typically, the performance of a UV reactor is predicted using a non-pathogenic

microorganism (i.e. MS2 coliphage), which is described with a first-order inactivation curve (Equation 3.13 or 1.55). However, the UV inactivation characteristics of pathogens in water treatment facilities, (i.e. *Cryptosporidium parvum* and *Giardia lamblia*) are often non-linear characterized by tailing (Equation 3.14 or 1.58). The performance of the UV reactor for a pathogen microorganism is often based on the prediction of non-pathogenic microorganisms such as MS2 coliphage. This procedure may introduce a large error on the predicted equivalent dose for pathogen microorganism.

$$-\log_{10}\left(\frac{N}{N_o}\right) = k_r D \qquad \text{first-order inactivation curve} \qquad (3.13)$$

$$-\log_{10}\frac{N}{N_o} = \log_{10} C_k + k_{df} \log_{10} D \qquad \text{tailing inactivation curve} \qquad (3.14)$$

where

k_r = first order inactivation rate coefficient of the microorganism

k_{df} = empirical curve-fit parameter

C_k = intercept with the y-axis of the logarithmic data fit kinetic

To provide a proper comparison of the UV reactors, the Wright (2000) concept was extended to include microorganism inactivation curves that were characterized by tailing such as that of *Cryptosporidium parvum* and *Giardia muris*. Wright (2000) proposed an approach to compare the predicted hydraulic efficiency of several UV reactors for microorganisms that were characterized by first-order inactivation response to UV radiation (Equation 3.13 or 1.55). This approach was based on a plot of the hydraulic efficiency versus the UV resistance of the microorganisms, where the UV resistance was defined as the inverse of the first-order inactivation rate constant ($\text{Ln}(10)/k_r$).

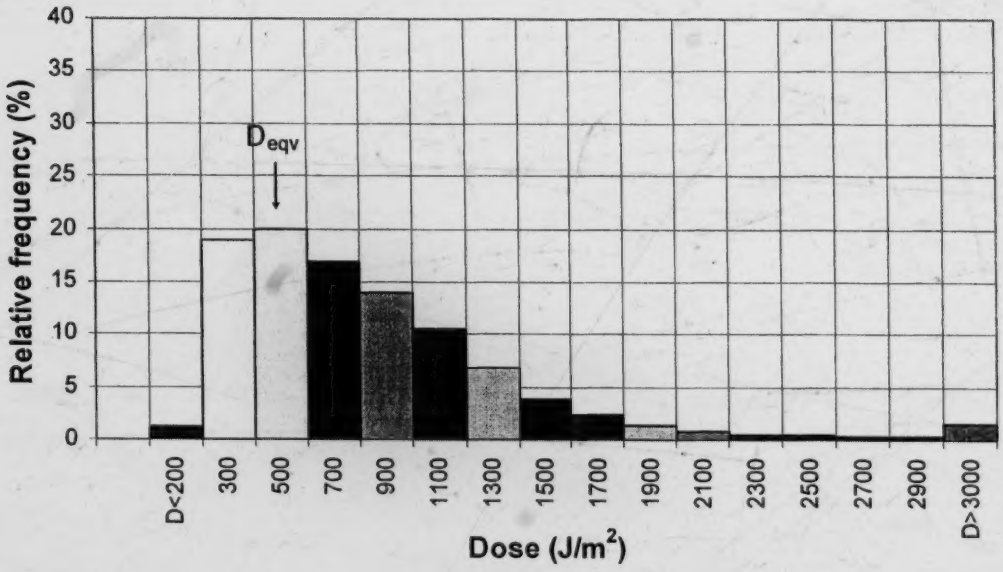

Figure 3.30: Dose received by 58,327 particles for the Modified UV Reactor **with baffles** under the conditions of run ID 19: flowrate of 6,250 m^3/h, eight lamps operating, lamps output power at 100%, water transmittance 93% UVT and $C_L = 0.15$ ($\overline{D}$ = 864.3 J/m^2, D_{eqv} = 452.0 J/m^2, D_{min} = 161.2 J/m^2, and s_D = 729.8 J/m^2).

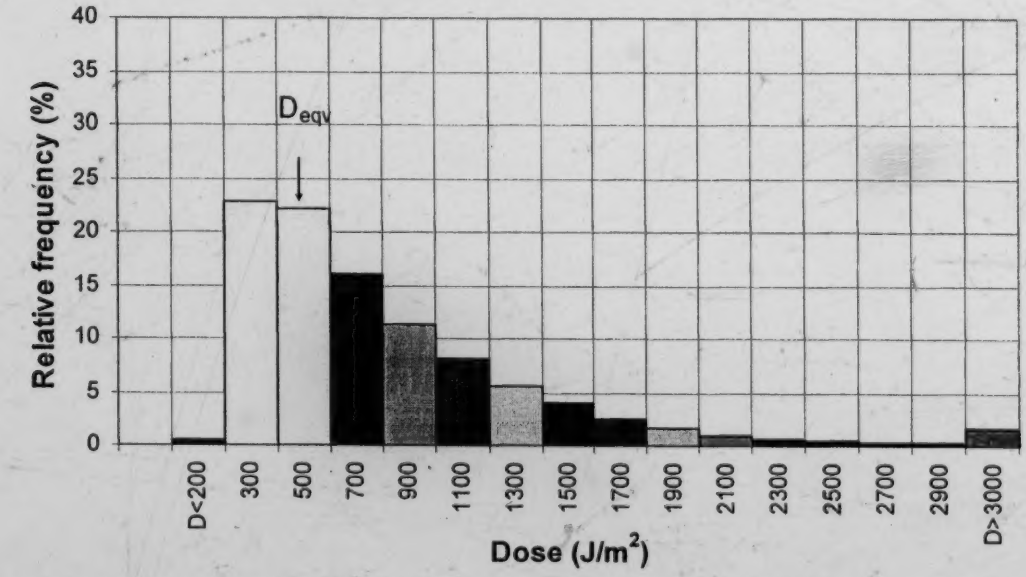

Figure 3.31: Dose received by 58,398 particles for the Modified UV Reactor **without baffles** under the conditions of run ID 23: flowrate of 6,250 m^3/h, eight lamps operating, lamps output power at 100%, water transmittance 93% UVT and $C_L = 0.15$ ($\overline{D}$ = 847.3 J/m^2, D_{eqv} = 441.7 J/m^2, D_{min} = 181.96 J/m^2, and s_D = 851.7 J/m^2).

The microorganism inactivation kinetic constants used in this analysis were listed in Table 3.14. The operational conditions used in this analysis were listed in Table 3.12 and additional operating conditions of 0.0128 EED and 98% UVT were included to provide a wider range of study.

Table 3.14: Microorganism inactivation kinetic constants.

Microorganism	First order model[a]		Non-linear model[b]		
	k_r (m^2/J)	$Ln(10)/k_r$ (J/m^2)	C_k	k_{df}	$1/k_{df}$
Giardia muris	0.063	36	1.9	0.6	1.666
Cryptosporidium parvum	0.059	39	1.5	1.6	0.625
MS2 coliphage[c]	0.009	256			

[a] Schmelling et al. (2003); the k_r values were estimated from Table 4 in this document.
[b] Craik et al. (2001).
[c] Blatchley et al. (2000).

Figures 3.32 and 3.35 show the effect of microorganism inactivation curve and UV resistance on the level of inactivation for both UV reactors at different sets of operational conditions. Figures 3.32 and 3.33 were plotted assuming several first-order inactivation rate constants. Figures 3.34 and 3.35 were plotted assuming 1) various empirical curve-fit parameters, and 2) the intercept with the y-axis of the logarithmic data fit, C_k, was equal to zero (Equation 3.14). This later modification was done to facilitate a comparison between inactivation models.

For the first-order inactivation curve, it can be seen from Figures 3.32 and 3.33 that:

1) The greatest change in inactivation occurs at values of UV resistance in the range of 30 to 300 J/m^2, which is the range of concern of pathogens.
2) Microorganisms with the least resistance are inactivated to the highest levels.
3) The predicted inactivation of low resistance microorganisms is more sensitive to operating conditions than predicted inactivation of high resistance ones.

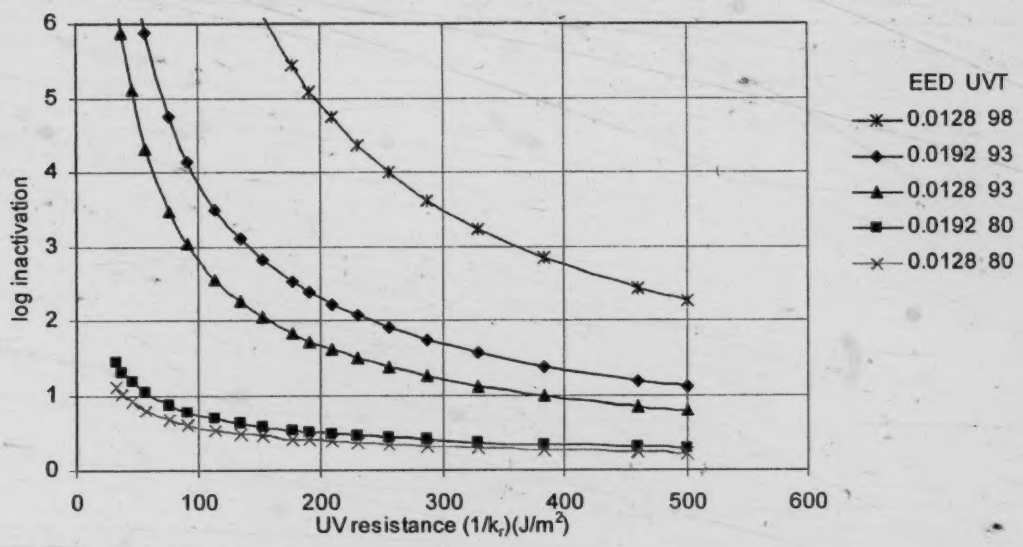

Figure 3.32: Effect of microorganism resistance on the predicted inactivation in the SUVR using a first order inactivation curve.

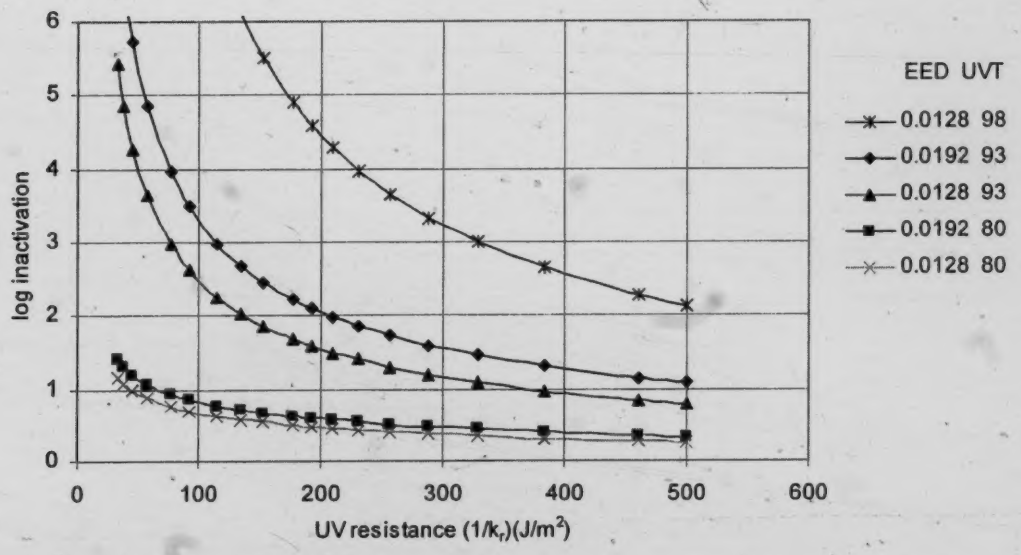

Figure 3.33: Effect of microorganism resistance on the predicted inactivation in the MUVR using a first-order inactivation curve.

For the non-linear inactivation curve with tailing, it was found from Figures 3.34 and 3.35 that:

1) The greatest change in inactivation occurs at values of UV resistance in the range of 0.5 to 2.0, which is the range of concern of pathogens.
2) The predicted inactivation is less sensitive to operating conditions using microorganisms with tailing than those with linear inactivation curves.
3) Both reactors provide a similar level of inactivation for microorganism with tailing inactivation curves.

Microorganisms with the least resistance are inactivated to the highest levels in both UV reactors. This is rather intuitive and can be explained using Equation 3.15, where the level of inactivation increases as the inactivation constant increases.

$$-\log_{10}\left(\frac{N}{N_o}\right) = -\log_{10}\left(\sum_{i=0}^{\infty} f_i\, e^{-k_r D_i}\right) \qquad (3.15)$$

where:

f_i is the fraction of particles receiving dose D_i.

The predicted inactivation with low resistance microorganisms and a first-order inactivation curve is more sensitive to operating conditions. This is attributed to: 1) the shape of the dose distribution that becomes more skewed for low UVT or EED (compare Figures 3.23 and 3.24), and 2) to the fact that the exponential term in Equation 3.15 weights strongly those microorganisms that received lower doses as the microorganism inactivation constant approaches high values (Wright and Lawryshyn, 2000).

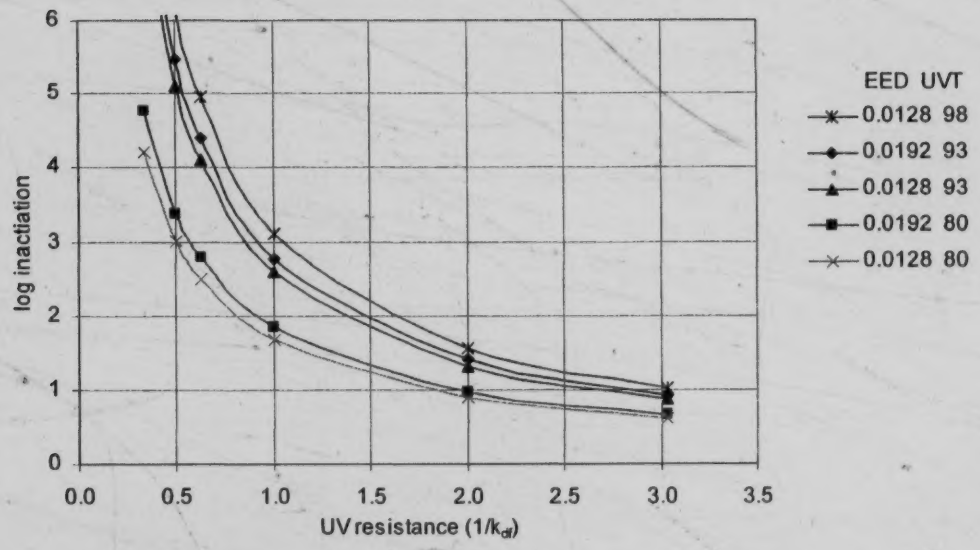

Figure 3.34; Effect of microorganism resistance on predicted inactivation in the SUVR using a tailing inactivation curve.

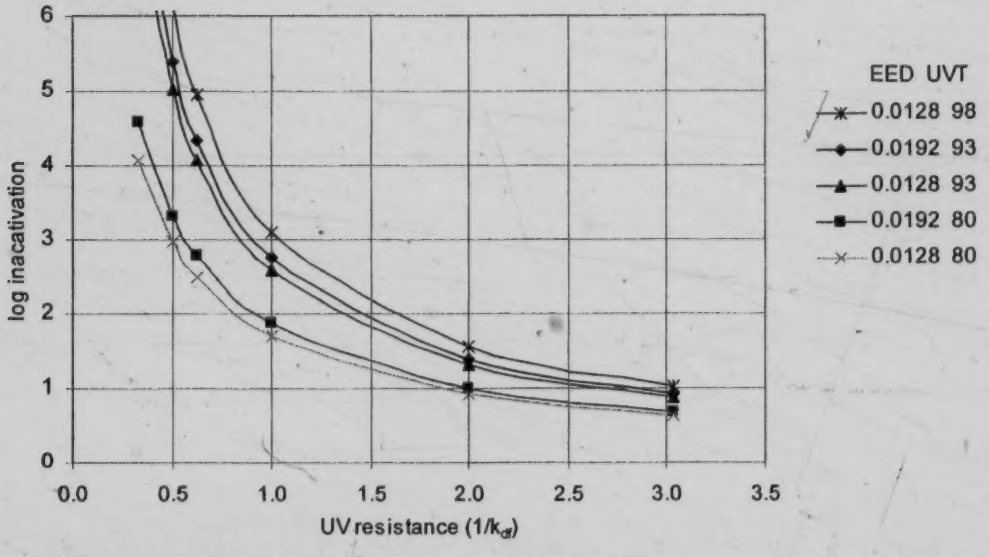

Figure 3.35: Effect of microorganism resistance on predicted inactivation in the MUVR using a tailing inactivation curve.

The predicted level of inactivation using a tailing inactivation curve is less sensitive to operating conditions than that using linear inactivation curves. Figures 3.36 and 3.37 illustrate that assuming a first-order inactivation curve for an organism like *C. parvum* instead of a tailing inactivation curve may result in an over or under prediction of the level of inactivation for the MUVR operated under the conditions of run ID 19 or 20.

This indicates that the level of inactivation estimated using a tailing inactivation curve is less affected by the shape of the dose distribution. This is because the predicted inactivation assuming a tailing inactivation curve is limited to a value less than a theoretical inactivation value. For *C. parvum* the theoretical inactivation value is 4.7 log. Therefore, the level of inactivation predicted using a tailing inactivation curve will be less sensitive to the hydrodynamics characteristics of the reactor.

By comparing Figures 3.34 and 3.35, it was found that both reactors provided similar levels of inactivation for microorganisms with tailing inactivation curves, although the SUVR can provide a greater level of inactivation than that of the MUVR at high transmittance. The differences in predicted inactivation are greater if a first-order inactivation curve is used for the computations. However, it should be emphasized that the pathogens of concern in water treatment plant are *Cryptosporidium parvum* and *Giardia lamblia*, which are described with a tailing inactivation curve. Therefore, UV reactors should be compared based on tailing inactivation curve rather than on a first-order inactivation curve.

Figures 3.38 to 3.41 present the hydraulic efficiency of both reactors as a function of microorganism resistance to UV radiation for first-order and tailing inactivation curves. These figures show an increase in the predicted hydraulic efficiency with an increase

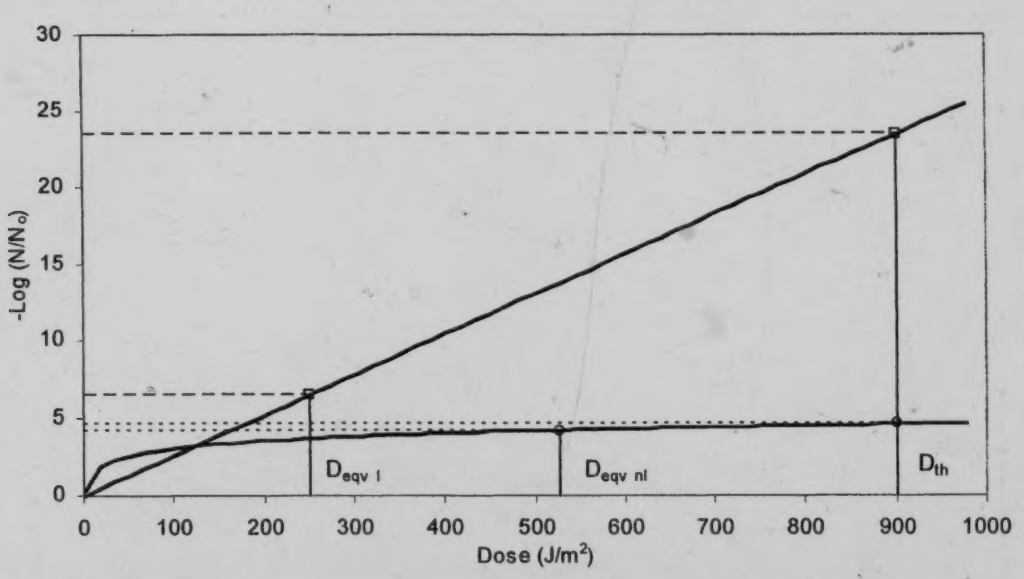

Figure 3.36: Effect of microorganism inactivation response to UV radiation on the predicted inactivation for the MUVR operated under the conditions of run ID 19 and the kinetic inactivation constants given in Table 3.14 for *Cryptosporidium parvum*. The sub indices beside the equivalent dose stands for linear (l) and non-linear (nl) model.

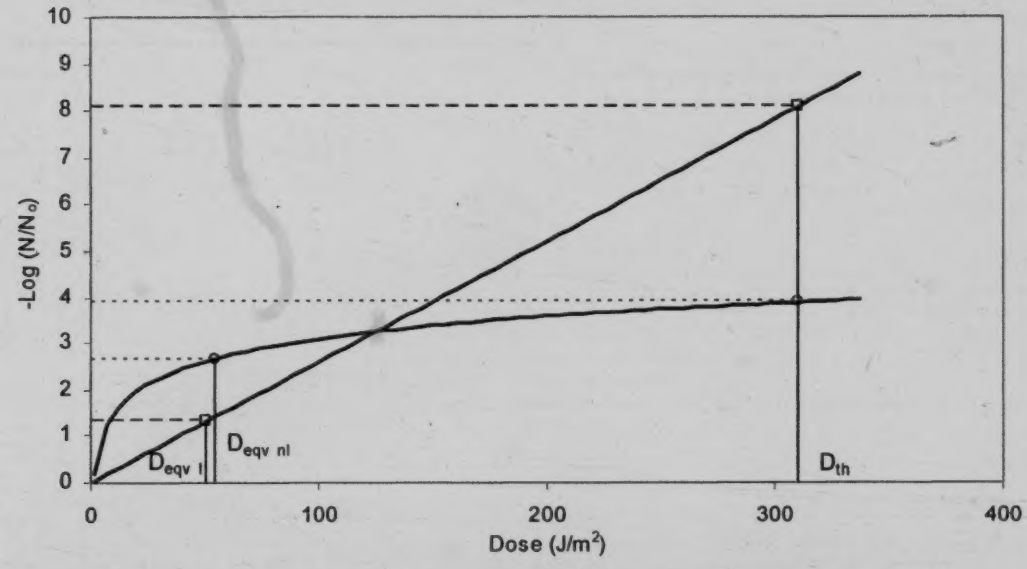

Figure 3.37: Effect of microorganism inactivation response to UV radiation on the predicted inactivation for the MUVR operated under the conditions of run ID 20 and the kinetic inactivation constants given in Table 3.14 for *Cryptosporidium parvum*. The sub indices beside the equivalent dose stands for linear (l) and non-linear (nl) model.

in the microorganism resistance. This effect is greater for microorganisms that exhibit first-order inactivation kinetics than for those that exhibit non-linear inactivation kinetics. This can be explained using Equation 3.16, that the greater the product of $k_r D_i$, the higher the hydraulic efficiency and the lower the effect of k_r or D_i on hydraulic efficiency.

$$E_f = \frac{D_{eqv}}{D_{th}} = -\frac{1}{D_{th} k_r} \ln\left[\sum_{i=0}^{\infty} f_i \, e^{-k_r D_i}\right] \tag{3.16}$$

The UV reactors are hydraulically more efficient for microorganisms with a tailing inactivation curve than those with linear inactivation curves. This could be attributed to the fact that the Equation 3.16 weights microorganisms that received lower doses more strongly than Equation 3.17. Therefore, the hydraulic efficiency estimated with a tailing inactivation curve is much higher than that estimated with a first order inactivation curve. The hydraulic efficiencies predicted with both inactivation curves approach each other, as the microorganisms become more resistance to the UV radiation.

$$\log_{10} D_{eqv} = \frac{1}{k_{df}} \log_{10}\left(\frac{1}{\sum_{i=1}^{\infty} \frac{f_i}{D_i^{k_{df}}}}\right) \tag{3.17}$$

The hydraulic efficiency curves reveal that using high flow rates does not necessarily improve the performance of UV reactors. From Figures 3.38 and 3.39, it can be appreciated that the slopes of the curves at different flow rates are similar for all the simulations. Moreover, for tailing inactivation curves, the efficiency curves overlap at 150 and 75×10^6 m^3/d as shown in Figures 3.40 and 3.41. This implies that the mixing across fluence rate gradients is the same for the two flow rates considered in this study.

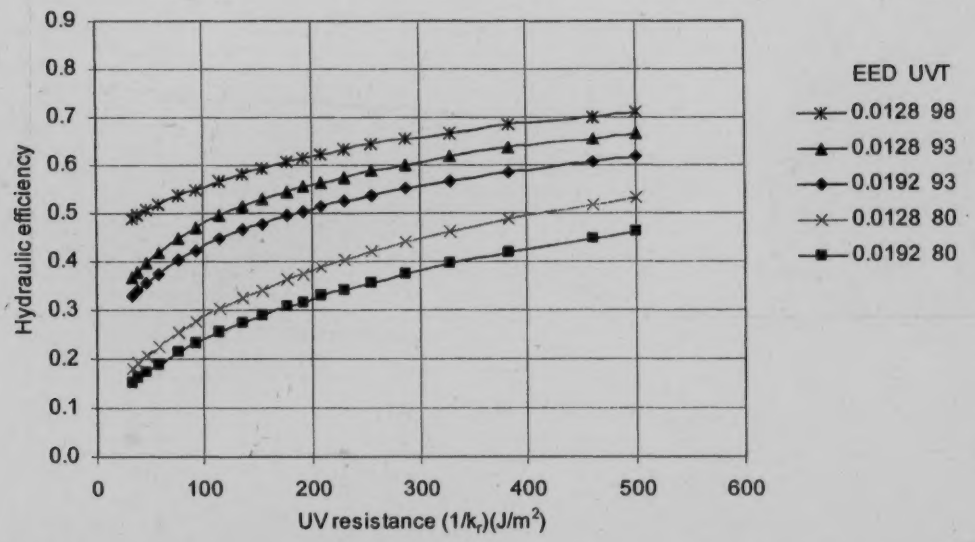

Figure 3.38: Effect of microorganism resistance on the hydraulic efficiency of the SUVR using a first order inactivation curve.

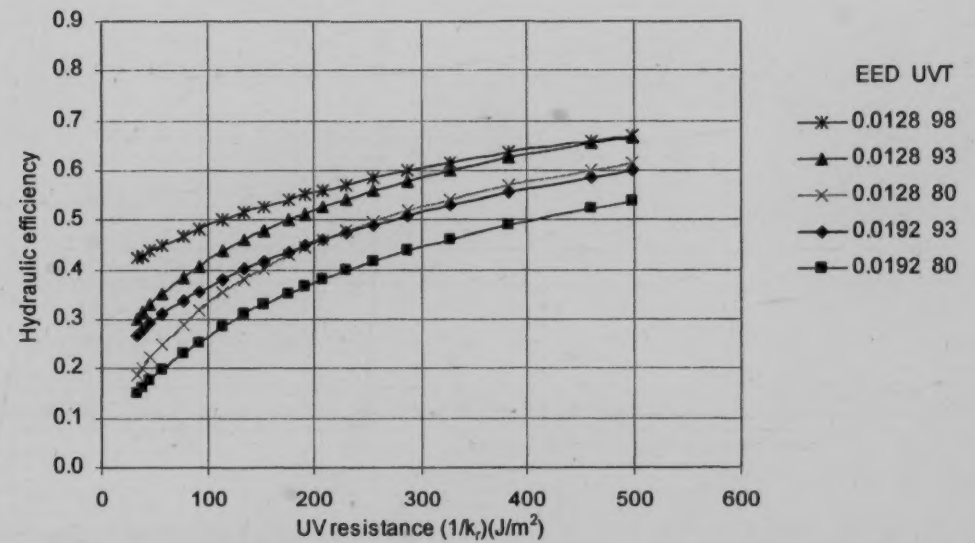

Figure 3.39: Effect of microorganism resistance on the hydraulic efficiency in the MUVR using a first order inactivation curve.

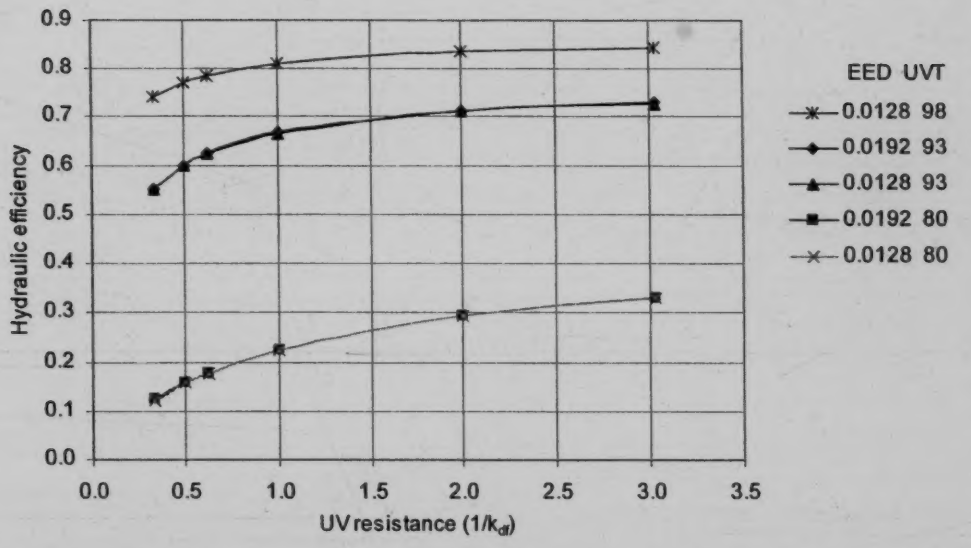

Figure 3.40: Effect of microorganism resistance on the hydraulic efficiency in the SUVR using a tailing inactivation curve.

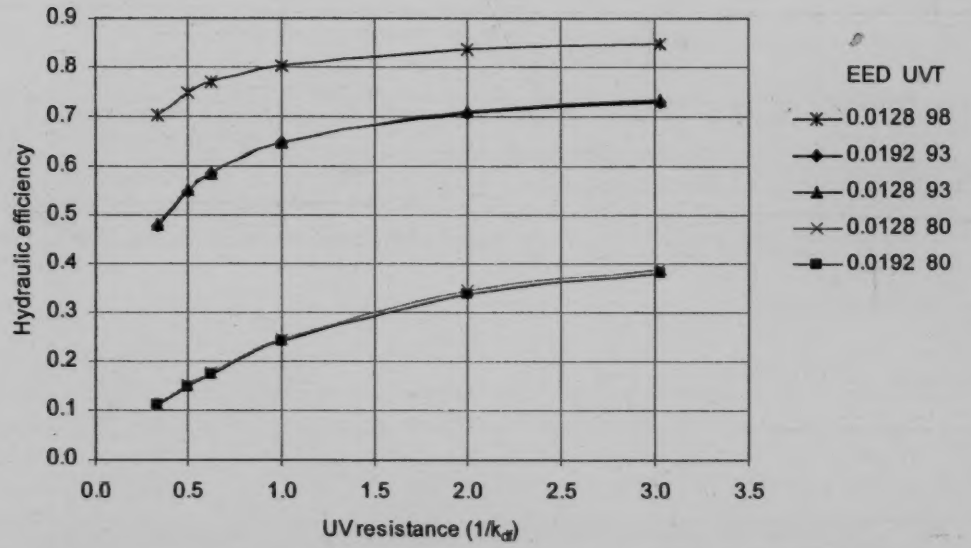

Figure 3.41: Effect of microorganism resistance on the hydraulic efficiency in the MUVR using a tailing inactivation curve.

4 Conclusions

This study demonstrates that it is feasible to predict the performance of large UV reactors using a three-dimensional CFD approach. The CFD approach was developed by integrating a computational fluid dynamic code (FLUENT), a fluence rate code (UVCalc3D_200) and a random walk model to compute the UV dose distribution. This distribution provides detailed information that is summarized in three statistics: the level of inactivation, the equivalent dose and the hydraulic efficiency. The level of inactivation states the ratio of infectious microorganisms before and after treatment on a logarithmic scale. The equivalent dose expresses the level of inactivation of a specific microorganism in terms of UV dose. The hydraulic efficiency relates the equivalent dose to a theoretical dose, which is the ideal equivalent dose that occurs when the standard deviation of the dose distribution approaches zero.

The real potential of the CFD approach lies in its capability to provide detailed information at a low cost and in shorter time than alternative experimental approaches such as biodosimetry. Unlike biodosimetry, which is only useful for surrogate microorganisms, the CFD approach can be used to predict the level of inactivation for any microorganism including pathogens. The CFD approach is advantageous because it allows UV reactor designers to: 1) identify any fundamental weakness of a UV reactor, 2) reduce inefficient use of power, 3) improve a particular UV reactor configuration, 4) speed the development of UV reactor prototypes, and 5) tailor a UV reactor for specific water characteristics or piping configurations upstream of the reactor.

The CFD approach was used to provide a better understanding of the effect of design factors on the performance of a UV reactor. Two design factors are available to increase

the hydraulic efficiency of a UV reactor; the use of baffles and the variation of lamp arrangement. Using baffles reduces the number of microorganisms receiving low doses by: 1) directing them towards high fluence rate zones near the UV lamps, 2) trapping them inside the vortices behind the baffles, and 3) reducing the effective volume of the reactor which the UV radiation must reach. The lamp arrangement increases the hydraulic efficiency by redistributing the fluence rate field. Selection of design factors to improve the performance of a UV reactor should consider limitations encountered in water treatment facilities. For instance, using baffles in a UV reactor could be inappropriate in facilities with limited head loss available. A complicated lamp arrangement could make it difficult to remove the lamps for maintenance or replacement in facilities with limited space. Water transmittance also plays a fundamental role in the selection of a design. The lamp arrangement could be a key design factor to improve the hydraulic efficiency of UV reactors operating at low transmittance because the lamp spacing becomes more critical as the UVT decreases. In contrast, using baffles could be a key design factor to optimize the performance of a UV reactor operating at high transmittance. As a result, the baffles and lamp arrangement should be selected carefully to suit the water characteristics and limitations encountered in a water treatment plant.

This study has produced charts which identify cost-effective methods for operating UV reactors:

1. Chart of the hydraulic efficiency and equivalent dose as a function of the electrical energy dose, and UV transmittance for a microorganism of interest (Figure 3.25).

2. Chart of the level of inactivation of different microorganisms as a function of UV resistance (Figure 3.32 or 3.34).

These charts allow UV-reactor operators to determine the lamp output power required to provide the same level of inactivation when the flow rate or UVT varies. It is recommended that the charts be developed for microorganisms of concern such as *Cryptosporidium parvum* or *Giardia lambia* rather than for a surrogate microorganism like MS2 coliphage. This is because the level of inactivation predicted for linear inactivation of MS2 coliphage is more sensitive to the hydraulic characteristics of the UV reactor and operating conditions than that for microorganisms with non-linear dose response. However, it should be emphasized that the tailing effect may be an artifact of the experimental conditions. If this were indeed the case, this analysis would not be valid.

This study has also identified two operating modes which provide the same level of inactivation when the flow rate decreases. In Mode 1 sets of lamps are turned on/off, and in Mode 2 the lamp output power is modulated. Although, these modes use the same EED, it is expected that one mode will offer a more cost-effective operation. Given cost data, charts of the operational cost as a function of EED and UVT could be generated to determine which operational mode is more economical in terms of power supply and lamp lifespan.

The CFD results have led to the following findings, which can be used to obtain a more accurate prediction of the performance of UV reactors. The ability of the CFD approach to produce accurate results depends on the correct specification of boundary conditions, the adequate spatial discretization of the domain, and an optimum number of particles. For water treatment facilities with stable UV transmittance and flowrate, it was

found that mesh type, turbulence model, Lagrangian empirical constant, and simulation mode have statistically significant effects on the UV dose prediction. However, for water treatment facilities with wide variation of the UV transmittance or flowrate, it was found that UVT and EED outweigh the computational factors. A statistical test used in this study showed that the k-ε model, steady-state flow, and unstructured tetrahedral mesh predict a higher UV dose in comparison to that of using the RSM, unsteady state and unstructured hexahedral mesh.

This study has demonstrated that the accuracy of the CFD approach depends on the number of particles simulated. Therefore, a strategy was developed to determine the number of particles that balance accuracy and computational effort. This strategy was based on an estimation of the variability of the equivalent dose that a UV reactor designer is willing to tolerate. It was demonstrated that the variability of the equivalent dose, measured in terms of the size of a confidence interval, is proportional to $1/(n_p*n_s)^{0.5}$. Therefore, the same variability can be expected by performing one simulation with n_p particles or n_s simulations with one particle. In this study the confidence interval of the equivalent dose was ± 1.5 J/m^2, which was achieved by using more than 55,000 particles.

It should be emphasized that the conclusions presented may be limited to the 6 x 20 kW Sentinel™ and the 8 x 15 kW Modified UV reactors. The main difference between those two UV reactors is the capability of the Sentinel UV reactor to deliver slightly higher hydraulic efficiency at high UV transmittance. However, the performance of the Sentinel UV reactor depends heavily on the use of baffles, which is a disadvantage when limited head is available in a water treatment facility.

5 Recommendations

1. Experimental studies are needed to validate, verify and calibrate the CFD approach and to corroborate the findings of this study. The completed study would provide the standardization required for regulatory agencies to incorporate CFD models as a validation tool; thus, leading to a faster implementation and development of more efficient UV reactors in water treatment facilities.
2. An experimental evaluation of the flow field is necessary to capture the outstanding features of the flow in a UV reactor. This evaluation consists of measuring velocity of the flow in a UV reactor using modern techniques such as Particle Image Velocimetry (PIV). Such a study would determine which turbulence model provides the best approximation to the actual flow field particularly downstream of the lamps.
3. It is recommended that a stochastic differential model be implemented in Fluent to track particle movement through the flow field. The implementation of a stochastic differential model would provide a more accurate model for estimating the dose received by a particle. This is because stochastic models provide a better representation of particle dispersion and uniform particle distribution than random walk models (MacInnes and Bracco, 1992).

References

Blatchley, E.R., Do-Quang, Z., Janex, M.L., & Laine, J.M. (1998). Process modeling of ultraviolet disinfection. Water Science and Technology. 38(6): 63-69.

Blatchley, E.R.,et al.(2000). Ultraviolet disinfection guidelines for drinking water and water reuse. National Water Research Institute and American Water Works Association Research Foundation. California, USA.

Bolton, J.R., Dussert, B., Bukhary, Z., Hargy, T., & Clancy, J. (2000). Inactivation of Crytosporidium parvum by medium pressure UV light in finished drinking water. Proceedings of AWWA annual conference: Texas, USA, Vol. A: 389-403.

Bolton, J.R. (2000). Calculation of ultraviolet fluence rate distributions in an annular reactor: significance of refraction and reflection. Water Research. 34(13): 3315-3324.

Bolton, J.R. (2000). Advanced oxidation UV treatment of organic pollutants in drinking water. International Ultraviolet Association Newsletter. 4(3): 16-19.

Bolton, J.R. (2000). Advanced oxidation UV treatment of organic pollutants in drinking water. International Ultraviolet Association Newsletter. 4(3): 16-19.

Bolton, J.R. (2001). Ultraviolet Applications Handbook. Bolton Photosciences Inc.

Broadkey, R.S. (1967). The phenomena of fluid motions. Massachusetts: Addison Wesley Pub. Co.

Cabaj A., Sommer, M. & Schoenen D. (1996). Biodosimetry: model calculations for U.V. water disinfection devices with regard to dose distributions. Water Research. 30(4): 1003-1009.

Calabrese R., & Middleman S. (1979). Dispersion of particles in a turbulent fluid. AIChe Journal. 25(6): 1025-1035.

Craik, S., Smith, D, Neumman, N., Kruithof, J., & Stafford, J., & Belosevic M. (2001). Effect of ultraviolet light on *Cryptosporidium parvum* oocysts and *Giardia Muris* cysts in various drinking waters. Proceedings of the first international congress on UV technologies, Washington, DC, June 14-16.

Chen, X.Q., & Pereira, J.C.(2000). Computational modeling of a dilute turbulent liquid – solid flow using a Eulerian-Lagrangian approach. International Journal of Numerical Methods for Heat & Fluid Flow. 10(4): 409-431.

Chiu, K., Lyn, D.A., Savoye, P., & Blatchley E.R. (1999). Integrated UV disinfection model based on particle tracking. Journal of Environment Engineering. 125(1): 7-16.

Domwey, D., Giles, D.K., & Delwiche, M.J. (1998). Finite elements analysis of particle and liquid flow through an ultraviolet reactor. Computer and Electronics in Agriculture. 21: 81-105.

Do-Quang, Z., Djebbar, R., Blatchley, E.R., & Laine, J.M. (1997). Computational fluid dynamics (CFD) modeling of UV disinfection reactor performances: optimization of the flow in vertical lamps open channel. CSCE/ASCE Environmental Engineering Conference. Edmonton, Alberta.22-26 July 1997: 1201-1212.

Franke, R., & Rodi, W. (1993). Calculation of vortex shedding past a square cylinder with various turbulent flows, in turbulent shear flows. 8 eds. U. Schumann et al., Springer Verlag.

Fluent 6 User's guide (2000). Fluent Incorporated, Lebanon, New Hampshire, USA.

Gosman, A.D., & Ioannides, E. J. (1981). Aspects of computer simulation of liquid-fuelled combustors. American Institute of Aeronautics and Astronautics (AIAA) Paper No 81-0323.

Hamada, M., & Hu, C.F. (2000). Experiments planning, analysis, and parameter design optimization. John Wiley & Sons, Inc. New York.

Hanninen, M.L.(2002). Microbial risk associated with drinking water; *Giardia* and *Cryptosporidium*. Finnish Research Programme on Environmental Health Sytty. Retrieved Nov, 2003 from http://www.ktl.fi/sytty/abstracts/hannim.htm.

Hardy, R.J., Lane, S.N. Ferguson, R.I. & Parsons, D.R. (2003). Assessing the credibility of a series of computational dynamic simulations of open channel flow. Hydrological Processes. 17: 1539-1560.

Havelaar, A.H., Meulemans, C.E., Pot-Hogeboom, W.M. & Koster, J. (1990). Inactivation of bacteriophage MS2 in wastewater effluent with monochromatic and polychromatic ultraviolet light. Water Research. 24(11): 1387-1393.

Hrenya, C.M., Bolio, E.J., Chakrabarti, D., & Sinclair, J.L. (1995). Comparison of low Reynolds number k-ε turbulence models in predicting fully developed pipe flow. Chemical Engineering Science, 50(12): 1923-1941.

Jacob, S.M., & Dranoff J.S. (1970). Light intensity profiles in a perfectly mixed photoreactor. AIChE Journal. 16(3): 359-363.

Jagger, J. (1967). Introduction to research in ultraviolet photobiology. Englewoods Cliffs, N.J: Prentice-Hall, Inc.

Janex, M.L., Savoye, P., Do-Quang, Z., Blatchley, E.R., & Laine, J.M. (1998). Impact of water quality and reactor hydrodynamics on wastewater disinfection by UV use of CFD modeling for performance optimization. Water Science and Technology. 38(6): 71-78.

Koobus, B., Farhat, C., & Tran, H. (2000). Computation of unsteady viscous flows around moving bodies using the k-ε model on unstructured dynamic grids. Computer Methods in Applied Mechanics and Engineering. 190: 1441-1466.

Launder, B.E., & Spalding, D.B. (1974). The numerical computation of turbulent flow. Computer Methods in Applied Mechanics and Engineering. 3: 269-289.

Kumar, V. & Pavithran S. (1999). Turbulent flow in two-dimensional U ducts: a computational study. ASME. 396: 65-78.

Lem W. (2002) Comparison of MS2 biodosimetry challenge results with computational fluid dynamics modeling for a UV disinfection reactor. Calgon Carbon Coorporation. Pittsburgh, PA.

Lyn, D.A., Chiu, K., & Blatchley E.R. (1999). Numerical modeling of flow and disinfection in UV disinfection channels. Journal of Environment Engineering, 125(1): 17-26.

MacInnes J. M., & Bracco, F. V. (1992). Stochastic particle dispersion modeling and the tracer-particles limit. Physic Fluids A. 4 (12): 2809-2824.

Martinuzzi, R., & Pollard, A. (1989). Comparative study of turbulence models in predicting turbulent pipe flow part I: algebraic stress and k-ε models. American Institute of Aeronautics and Astronautics (AIAA) Journal. 27(1): 29-36.

Martinuzzi, R., & Pollard, A. (1989). Comparative study of turbulence models in predicting turbulent pipe flow part II: Reynolds stress and k-ε models. American Institute of Aeronautics and Astronautics (AIAA) Journal. 27(12): 1714-1721.

Miller, L.H., & Quilici, A.E.(1986). Programming in C. New York: John Willey & sons

Mostafa A.A., & Elghobashi S.E. (1986). NASA Contractor report 175063.

Ornancey, A., & Martinon, J. (1984). Prediction of particle dispersion in turbulent flows. Physicochemical Hydrodynamics. 5(3-4): 229-244.

Paul, Atiemo-Obeng and Kresta, S. (2003). Handbook of Industrial Mixing. New York: Wiley Interscience.

Pope, S.B. (2000). Turbulent flow. Cambridge, UK: Cambridge University Press.

Press, W.H., Vetterling, W.T., Teukolsky S.A., & Flannery B.P. (1992). Numerical Recipes in C, Cambridge: Cambridge University Press.

Rahn, R.O., Stefan, M.I., Bolton, J.R. (2000) The iodine/iodate actinometer in UV disinfection: characteristics and use in the determination of the fluence rate distribution in UV reactors. Proceedings of the Water Quality and Technology Conference. Nov, 2000, Salt Lake City, U.T.

Rodi W., (1984). Turbulence models and their application in hydraulic - a state of art review. Karlsruhe: University of Karlsruhe.

Rodi W., (1998). Large eddy simulations of the flow past bluff bodies. JSME International Journal: 41(2): 361-375

Rogers, D.F. (1992). Laminar Flow Analysis. Cambridge: Cambridge University Press.

Rojiani, K.B. (1996). Programming in C with Numerical Methods for Engineers. New Jersey: Prentice Hall.

Rokjer, D., Valade, M., Keesler, D., & Borsykowsky, M. (2002). Computer modeling of UV reactor for validation purposes. American Water Works Association: Water Quality Technology Conference, 1-21.

Slack M., & Prasad R. (2000). Advances in cyclone modeling using unstructured grids. Chemical Engineering Research and Design. 78 (A8): 1098-1104.

Mori G, Razore S., Ubandi M., zunino P. (2001). Integrated experimental and numerical approach for fuel air mixing prediction in heavy duty gas turbine LP burner. Journal of Engineering for Gas Turbine and Power Transactions of the ASME. 123 (4): 803-809.

Schlichting, H. (1979). Boundary layer theory (7^{th} ed.). New York: McGraw-Hill

Schmelling, D. (2003). UV Disinfection Guidance Manual Draft. United States Environmental Protection Agency. Washington. D.C.

Sierra-Espinoza, F.Z., Bates, C.J. Bates & O'Doherty T.O. (2000). Turbulent flow in a 90° pipe junction Part1: decay of fluctuations upstream the flow bifurcation. Computers & Fluids. 29: 197-213.

Snyder W. H., & Lumley J. L. (1971). Some measurements of particle velocity autocorrelation function in turbulent flow. Journal of Fluid Mechanics. 48: 41-73

Speziale, C.G. (1991). Analytical methods for the development of Reynolds-stress closures in turbulence. Annual Review of Fluid Mechanics. 23: 107-157.

Tanka, T. & Tsuji, Y. (1991). In proceeding of the 4th International Symposium on Gas-Solid Flow. ASME FED. l(121): 123-128.

Tenneses, H., & Lumley, J.L. (1972). A first Course in Turbulence. Cambridge, UK: the Massachusetts Institute of Technology Press.
Van Doormal, J. P. and Raitthby, G. D. (1984). Enhancements of the SIMPLE method for predicting incompressible fluid flows, Numerical Heat Transfer. 27: 147-163.

Wayne, L. (2002). Comparison of MS-2 biodosimetry challenge results with computational fluid dynamics modeling for a UV disinfection reactor. Calgon Carbon Corporation. Retrieved January, 2003, from http://www.calgoncarbon.com/cces/ccc/tech/support/index.phtml ?mode=full&topic_id=12&document_id=35

Wright, N.G., & Hargreaves, D.M. (2001). The use of CFD in the evaluation of UV treatment systems. Journal of Hydrodynamics. 3(2): 59-70.

Yan Z.Y. (2000). Large eddy simulation of fully developed turbulent flow in a rotating pipe. International Journal for Numerical Methods in Fluids. 33(5): 681-694.

Yun, S., Yasukouchi, N., Hirosawa, Y., & Jotaki,T. (1978). Particle turbulent diffusion in a dust laden round yet. AICHE Journal. 24(3): 509-519.

Zagarola, M.V., & Smits, A.J., (1998). Mean-flow scaling of turbulent pipe flow. Journal of Fluid Mechanics. 373: 33-79.

Appendix A

CFD protocol for a UV reactor simulation

The CFD simulation for a UV reactor is developed as follow:

1. Eulerian Flow field generation
2. Cell-face centroids exportation from FLUENT to UVCalc
3. Fluence rate field computation
4. Fluence rate exportation from UVcalc to FLUENT
5. Dose distribution calculation
6. Log-inactivation estimation

Eulerian flow field

Once the FLUENT6.1 is opened in 3D version and the case file (gambit mesh file) has been read the next step should be following to generate the Eulerian flow field

1. Check the grid
   a. Grid → check,
2. Scale the grid from inches to meters
   a. Grid → Scale
3. Define the solver
   a. Define → model
   b. solver: segregated
   c. formulation: implicit
   d. space: 3D
   e. time: Steady
   f. formulation: absolute
   g. Gradient option: base cells
   h. Porous formulation: superficial velocity
4. Define the turbulence model to use
   a. Define → model → viscous
   b. model: k-e model
   c. model constants: default
   d. near wall treatment: Standard wall functions
   e. user define function: none
5. Define continuous phase material
   a. Define → materials
   b. Material database: Fluid materials:
   c. water liquid: copy
   d. change
6. Compile the user define function (to install the UDF, see the appendix UDF)
   a. Define → User Defined → Function → Compiled → libudf :load
   b. Copy boundary profile "pkehv" to the your working directory (Appendix E)

c. Read boundary profile
d. File→ read →profile→ boundary profile:type or browse "pkehv"

7. Define boundary condition for the continuous phase
a. Define → boundary conditions:
b. Inlet→ velocity inlet profile→ set:
c. Velocity specification method: components
d. Reference frame: absolute
e. Coordinate system: Cartesian
f. X-velocity: p-3.5 x-velocity
g. Y-velocity: p-3.5 x-velocity
h. Z-velocity: p-3.5 x-velocity
i. Turbulent kinetic energy: p-3.5 turbulent kinetic energy
j. Turbulent dissipation rate: p-3.5 turbulent dissipation rate
k. Outlet: pressure outlet
l. Aqua: water
m. Lamps and Baffles: wall

8. Reserve a user define memory for the fluence rate field
a. Define→ user defined→ memory
b. Number of user define memory locations=1

9. Define the numerical procedure
a. Solve → Control → Solution
b. under Relaxation Factors
c. pressure = 1
d. density = 1
e. body forces = 1
f. momentum = 0.7
g. turbulence kinetic energy = 0.7
h. turbulence dissipation rate = 0.7
i. turbulent viscosity = 1
j. discretization: second order upwind
k. pressure-velocity coupling: SIMPLEC

10. Define the convergence limit
a. Solve → Monitor → Residuals = 1E-04
b. Solve → Monitor → options→plot

11. Initialize the all the variables
a. Solve → Initialize → Initialize
b. X Velocity = 1.5425 m/s
c. turbulence kinetic energy = 0.01m2/s2
d. turbulence dissipation rate = 0.047m2/s3

12. Create planes and line for postprocessing purposes
a. Surface→ Plane or Line

13. Save the case and data file
a. File → Write → Case

14. Iterate the flow field
a. Solve → Iterate: Number of Iterations 400 iterations
b. File → Write → Case

Cell-face centroids exportation

There are two ways to export the cell centroids

If the centroids will be generated from a mesh file then open FLUENT6.1, type 3d version and read the case file (gambit mesh file)

1. Check the grid,
a. Grid → check,
2. Scale the grid from inches to meters
a. Grid → Scale
3. Compile the user define function (to install the UDF, see the appendix UDF)
a. Define → User Defined → Function → Compiled → libudf :load
4. Reserve a user define memory for the fluence rate field
a. Define→ user defined→ memory
b. Number of user define memory locations = 1
5. Initialize the all the variables
a. Solve → Initialize → Initialize
b. Do not change the default values
6. Execute your UDF on demand
a. Define → User Defined → Executed on Demand: centroid
b. Change the name file center.txt for a name that you consider more appropriate.

If the centroids will be generated from a case file then open FLUENT6.1, type 3d version and read the case and data.

1. Ensure that the user define library is compiled (libudf)
a. Define → User Defined → Memory
b. Number of user define memory = 1
2. Initialize the UDM field
a. Define → User Defined → Function Hook: browse "reset" code
3. Execute your UDF on demand
a. Define → User Defined → Executed on Demand: centroid
b. Change the name file center.txt for a file name that you consider more appropriate.

Fluence rate field computations

1. Load the reactor, Input and Output files
2. Select shadow ON
3. Select refraction ON
4. Run the calculation
5. Transfer the output file from Windows to Unix using FTP

Fluence rate data exportation from UVCalc to FLUENT

1. Before open FLUENT6.1 update the filename in your UDF,
2. Execute the "Makefile" by typing a command that begins with *make* and includes the architecture of the machine

a. make "FLUENT_ARCH=aix51"

3. Open FLUENT6.1 in 3D version and read the case and data file.
4. The next steps should be followed to read the fluence rate field
    a. Ensure that the user define library is compiled (libudf)
    b. Ensure that the number of user define memory =1
5. Execute your UDF on demand

a. Define → User Defined → Executed on Demand: browse the C code: addfluence:
b. The following message will be display
c. Filename: fluence.txt
d. Fluence set in udm-0
e. Execute on demand finish

Dose distribution calculation

Once FLUENT6.1 is open in 3D version and the case and data file has been read the next steps should be followed to generate the dose distribution

1. Ensure that the fluence rate field was loaded by plotting UDM contours

a. Contours→User Defined Memory
b. Select the surface and display

2. Define Discrete Phase

a. Define → Model → Discrete Phase
b. Tracking parameters:
c. Number of Steps 43500
d. Lengh scale (m) 0.0002
e. User Defined Functions
f. Scalar Update: Dose index (UDF Pdose)
g. Number of Scalars 1

3. Initialize the scalar update

a. Define → User Defined → Function Hooks
b. Initialization function: dose-setup

4. Define injection properties and computational parameters

a. Define Injections → Create → Set injection properties
b. Injection Type → File → browse the file injection (i.e.tur10th1.inj)
c. Partycle Type Inert
d. Laws → custom → First law inactive
e. Materials default
f. Point properties
g. Star time: select the actual time of the simulation
h. Stop time: select the actual time plus one time step
i. Turbulent dispersion

j. Stochastic tracking Stochastic model,
k. Number of Tries = 1,
l. Time scale constant = 0.15
m. Applied OK

5. Create the Discrete phase Materials
a. Define materials
b. material type Inert- particle
c. Name = MS2
d. Chemical formula virus
e. Properties Density 998.2 kg/m3
f. Press change/create

6. Define Boundary conditions
a. Define → Boundary conditions
b. Baffles wall reflect: Normal = 0
c. Lamps wall reflect Normal = 0
d. Section1 wall reflect Normal = 0
e. Section2 wall reflect Normal = 0
f. Section3 wall reflect Normal = 0
g. Outlet pressure outlet escape
h. Inlet velocity inlet reflect

7. Run the particle tracking to visualize the discrete phase see FLUENT guidelines
8. Run the sample report as follow
a. Report → Discrete phase → Sample
b. Boundaries: Outlet
c. Release from injections: select the injection
d. User Defined Function: select from the list dose-output or all-output
e. Change the file name of the output file

D_{eqv} computation

1. Transfer the output file from fluent directory to your desktop directory
2. Run the **Deqv.exe** code
a. Run the Deqv.exe
b. Enter the file root name (i.e. file name output1.dpm, enter output)
c. Enter the number of files (i.e file name output1.dpm, output2.dpm,..outputn.dpm, enter n)
d. Select the type of file
e. Press 1, if the file comes from fluent output
f. Press 2, if the file comes from experiments
g. Select the kinetic model (test microorganisms)
h. Enter the kinetic constants of the model see Table 1.6
i. Type any number to exit the code

Appendix B

C Code used to compute equivalent dose and inactivation, Deqv.exe (see CD).

Appendix C

UDF used to integrate the UV dose along the particle path (see CD).

Appendix D

UDF used to specify laminar velocity profile at the inlet of the SUVR (see CD).

Appendix E

UDF used to specify velocities, k and ε profiles at the inlet of the SUVR (see CD).

Appendix F

C Code used to assign injection properties to each particle in laminar flow (see CD).

Appendix G

C Code used to assign injection properties to each particle in turbulent flow (see CD).

Appendix H

UDF used to compute a simplified fluence rate function (see CD).

Appendix I

UDF used to export (import) centroid (fluence rate) from Fluent to UVCalc (see CD).

Appendix J

Journal files of the meshes generated in Gambit (see CD).

Appendix K

Files used to input data to UVCalc (see CD).